167

MARTIN MARIETTA ENERGY SYSTEMS LIBRARIES

3 4456 0365949 5

ORNL-3472
UC-20 – Controlled Thermonuclear Processes
TID-4500 (20th ed., Rev.)

THERMONUCLEAR DIVISION

SEMIANNUAL PROGRESS REPORT

FOR PERIOD ENDING APRIL 30, 1963

CENTRAL RESEARCH LIBRARY
DOCUMENT COLLECTION
LIBRARY LOAN COPY
DO NOT TRANSFER TO ANOTHER PERSON
If you wish someone else to see this document, send in name with document and the library will arrange a loan.

OAK RIDGE NATIONAL LABORATORY
operated by
UNION CARBIDE CORPORATION
for the
U.S. ATOMIC ENERGY COMMISSION

ORNL-3472

Contract No. W-7405-eng-26

THERMONUCLEAR DIVISION

SEMIANNUAL PROGRESS REPORT

For Period Ending April 30, 1963

DATE ISSUED

JUL 31 1963

OAK RIDGE NATIONAL LABORATORY
Oak Ridge, Tennessee
operated by
UNION CARBIDE CORPORATION
for the
U. S. ATOMIC ENERGY COMMISSION

MARTIN MARIETTA ENERGY SYSTEMS LIBRARIES

3 4456 0365949 5

Contents

INTRODUCTION vi

ABSTRACTING SUMMARY ix

1. DCX-1 PLASMA EXPERIMENTS 1
   - 1.1 Introduction 1
   - 1.2 Radio-Frequency Measurements 1
   - 1.3 Correlations Between Plasma Parameters and Radio-Frequency Signals 1
   - 1.4 Stabilization Experiments 3
   - 1.5 Containment Studies 4
     - 1.5.1 Measurements of Mirror Losses 4
     - 1.5.2 Effects of Magnetic-Field Perturbations 5
   - 1.6 Proton Trapping by Lorentz Dissociation of H_2^+ 6

2. DCX-2 9
   - 2.1 Plasma Density Measurements 9
   - 2.2 Energy Analysis of Escaping Fast Neutrals 11
   - 2.3 Gridded-Probe Measurements 13
   - 2.4 Radio-Frequency Studies 19
   - 2.5 End Electrodes 20
   - 2.6 Stabilizing Plasma Experiments 20
   - 2.7 High-Speed Current Amplifier 22

3. PLASMA PHYSICS 24
   - 3.1 Investigation of the Electron-Cyclotron Plasma in the Physics Test Facility (PTF) 24
     - 3.1.1 Introduction 24
     - 3.1.2 Neutrons 24
     - 3.1.3 Parametric Studies with Power 24
     - 3.1.4 Phase-Shift Measurements 25
     - 3.1.5 End-Collector Measurements 26
     - 3.1.6 Machine Modifications 27
     - 3.1.7 Parametric Study with Xenon Impurities 27
     - 3.1.8 Pinhole-Camera X-Ray Photographs 29
   - 3.2 Hot-Electron Plasma by Beam-Plasma Interaction 31
   - 3.3 Beam-Plasma Interaction Studies 37
   - 3.4 Electron-Beam Spreader 44
   - 3.5 Measurement of Ionic-Sound-Wave Velocity in Plasma by a Time-of-Flight Technique 45
   - 3.6 Automatic Converter for a Langmuir Probe 47
     - 3.6.1 Introduction 47
     - 3.6.2 Automatic Converter 48

4. VACUUM ARC RESEARCH 50

4.1 High-Density Deuterium Arc Analysis 50
4.1.1 Arc Potential Distribution 50
4.1.2 Electron Temperature from Plasma Power Balance 51
4.1.3 Electrode Power 51
4.2 Spectroscopic Investigations of the Gas-Fed, Magnetically Confined, High-Current, Carbon Arc – The Question of Ion Temperature 52
4.2.1 Introduction 52
4.2.2 Turbulence 52
4.2.3 Radio-Frequency Spectra from the Carbon Arc 53
4.2.4 Resonance Ion-Cyclotron Heating 53
4.2.5 Future Work 55
4.2.6 Acknowledgments 55

5. CROSS SECTIONS 56

5.1 Dissociation of H_2^+ in Hydrogen Gas 56
5.2 Dissociation of H_3^+ and HeH^+ in Hydrogen Gas 60
5.3 Formation of Neutral Atomic Hydrogen Beams 60
5.4 Production of H_2^+ in High-Vibrational Levels 63
5.5 Design and Fabrication of Crossed-Beam Apparatus 64
5.6 Photoionization of Atomic Hydrogen 64
5.7 Ionization of Excited States of Hydrogen by Electron Impact 65

6. PRODUCTION, ACCELERATION, AND INJECTION OF IONIC AND ATOMIC BEAMS 70

6.1 High-Current Ion-Beam Injection 70
6.2 Ion-Source Development 71
6.2.1 General Description 71
6.2.2 Operation of the Arc 72
6.2.3 Operation of the Ion Source 72
6.3 Neutral-Source Development 73
6.4 Negative Ions 73

7. PLASMA THEORY AND COMPUTATION 75

7.1 Instability Mechanisms 75
7.2 Bounds on Instability Growth Rates 76
7.3 Stability Investigation of Inhomogeneous Plasmas 77
7.4 Effect of a Finite Boundary on Ion-Cyclotron Instabilities 79
7.5 Impurity Radiation from Non-Maxwellian Spherical Plasmas 79
7.6 Beam-Electron Interaction in DCX-1 79
7.7 Relativistic Effects on Plasma-Density Measurements by Phase-Shift Analysis 81
7.8 DCX-1 Studies 82
7.9 DCX-2 Performance Curves 82

8. MAGNETICS AND SUPERCONDUCTIVITY 84

8.1 Current-Carrying Capacity and Transition State of Superconducting Solenoids 84
8.1.1 Discussion of the Models of Montgomery and of Chandrasekhar and Hulm 84
8.1.2 Currents and Fields in an Infinitely Long Ideal Superconductor Solenoid 85
8.1.3 Experiments with a Lead Solenoid (Quenching Current and Transition State) 86
8.1.4 Conclusion 87
8.2 Soft-Superconductor Proximity Effects 88
8.3 Cryogenic Current Input Apparatus 88
8.4 Metallurgy of Superconducting Materials 91

8.5 Micromagnetometers for Low Temperature 92
8.6 Thermal Protection of Water-Cooled Magnet Coils 103
8.7 Extended Work on New Computer Programs for Calculating Magnetic Properties of Current Systems 105
8.7.1 Program Based on Gaussian Integration of Elliptic Integrals 105

9. VACUUM SYSTEMS, TECHNIQUES, AND MATERIAL STUDIES 107

9.1 High-Vacuum Flange Test of a Bakeable Aluminum Wire Seal 107
9.1.1 Introduction 107
9.1.2 Test Facility and Procedure 107
9.1.3 Test Results 109
9.1.4 Summary and Discussion 112
9.1.5 Acknowledgments 114
9.2 Gaseous Desorption at Low Pressures and Liquid-Nitrogen Temperatures 114

10. FURTHER SPECULATIONS ON VERY HIGH ENERGY INJECTION INTO A MAGNETIC MIRROR 119

11. DESIGN AND ENGINEERING: NOTES 121

11.1 Corrosion-Erosion Tests on Internally Cooled Copper Conductors 121

12. DESIGN AND ENGINEERING: SERVICE REPORT 122

PUBLICATIONS, PAPERS, AND TRAVELING LECTURE PROGRAM 123

Introduction

A. H. Snell

During the past half year, the comparative docility of DCX-1 has continued, and its excellent experimental performance is attested by the extension of trapped-proton lifetimes to a minute or more. Details of the clustering "instability" in the storage ring continue to be examined (Sec 1.3), with confirmation of the supposition that the clustering is connected with the plasma spread, but that the interaction of the H_2^+ beam with the stored protons is probably not a contributing factor. There is further confirmation that the clustering takes place in the most ordered part of the trapped-proton population; an increase in disorder seems to increase stability (Sec 1.4). End plates had little effect, whether voltage-biased or not. Longitudinal injection of 420-v electrons seemed to shift the rf signals from the fundamental to higher frequencies (multiple clusters?), and this may be interpretable in terms of Harris theory (Sec 7.7). The clustering apparently leads to negligible loss of fast protons through the mirrors (Sec 1.5.1). Magnetic-field perturbations were harmful under some circumstances (Sec 1.5.2), but apparently in a way unconnected with the clustering.

The most important accomplishment on DCX-1, however, was the observation of substantial trapping by Lorentz dissociation of H_2^+ (Sec 1.6). Earlier attempts to find this had been directed to the usual conditions under which the H_2^+ ions were extracted directly from an ion source, and the results had been negative. More recently, following a practice originated at Aldermaston, the H_2^+ ions were derived from H_3^+, and the Lorentz dissociation under these circumstances was found to be important indeed. The potentialities are far-reaching, because by taking advantage of Lorentz dissociation, density can be accumulated simply by obtaining a better vacuum; this provides a new degree of freedom, unavailable with gas or arc dissociation. The arithmetic now suggests that with optimization of the neutralization cell, and with containment times no better than we have had before, an increase in density to the $10^{10}/cm^3$ range should be within reach; this should give us a good chance to see if there are new loss mechanisms waiting for us in that density range – an insight that we have long sought.

Profitable interplay has taken place between the DCX-1 effort and the groups concerned with the measurements of cross sections and with vacuum technology. The former has provided dissociation cross sections directly applicable to DCX-1, and contributes substantially in Sec 5 of this report. The latter has carried out some illuminating gas desorption studies (Sec 9.2) that point out the importance of a few degrees in the temperature of the nitrogen-cooled liner in obtaining low pressures.

Experience with DCX-2 is accumulating, and the DCX-2 performance is found to be sensitive and complicated. Trapped-proton densities are still in the range of $10^7/cm^3$, although the population has been distributed more evenly than before by careful smoothing of the magnetic field. Some phase correlations are sometimes found between rf signals at probes at similar azimuthal positions but different axial positions, although the plasma does not rotate as a whole at any frequency less than the proton-cyclotron frequency. Some interesting experiments have been performed by using the "backstream" of a lithium arc injected axially. This can have the result of reducing the frequency of the bursts of escaping fast ions that are seen on gridded probes; that is, the backstream has a stabilizing effect. The full lithium arc (100 amp) injected lengthwise through the apparatus increases the trapped-proton density to the $10^8/cm^3$

range, and also rather spectacularly increases the energy spread of the stored protons. An electron beam axially injected has a somewhat similar effect. There is still a lot to be learned about the performance of DCX-2, but our understanding and control will be clarified upon further investigation.

In the electron-cyclotron heating experiment a puzzle has arisen in that an electron density of $10^{11}/cm^3$ is indicated by a measured 30° phase shift shown by a 4-mm microwave interferometer, whereas all other measurements (diamagnetism, neutral-beam transmission, plasma pumping, $K\alpha$ radiation from introduced xenon) suggest 10^{12}. Furthermore, the microwave phase shift disappears after power turnoff about a thousand times faster than do the other signals. The discrepancy is described in Sec 3.1.4, and the question of a relativistic correction to the index of refraction formula is discussed in Sec 7.7. A correction is indeed found, but it does not seem to help sufficiently. The whole matter has to be studied further to effect a conciliation. Another odd observation is that a burst of neutrons appears about 50 msec after power turnoff (Fig. 3.1). Engineering preparations are being made for a scaleup of the electron-cyclotron heating experiment, using the vacuum and magnetic facilities available in the old Geneva tank that we call EPA, and we hope to study these matters under changed, and hopefully more favorable, conditions.

We have recently become interested in beam-plasma interactions, an immediate reason being the experiment described in Sec 3.2, in which a plasma electron temperature of 80 kev is apparently generated by injection of an electron beam of only 5 kev.[1] Naturally the question arises: to what extent can phenomena of this kind be used to heat ions in a controllable fashion? A lot of basic work in plasma physics will be needed to explore this avenue, as is suggested by Sec 3.3, where a start is made on a study of the interplay of ion sound waves and ion-cyclotron motions in one mode of beam-plasma interaction, and of electron-cyclotron backward wave and cavity oscillations in another mode. Meanwhile, smaller notes appear in these pages on a direct measure of ion-sound-wave velocity with the observation that the adiabatic compression coefficient γ is 3 for light gases and $5/3$ for heavy gases (Sec 3.6), on a shadow-graph method of measuring electron density by using evaporated gold (Sec 3.5), on the use of particle flows to anode and cathode of a deuterium arc to give an interrelated, self-consistent set of physical parameters for that arc (Sec 4.1), and on the influence of turbulence on Doppler broadening measurements in the carbon arc (Sec 4.2).

It may be gratifying to those who have difficulty in correlating the various types of plasma instabilities to see in Sec 7.1 that some of them can be brought together. Electrostatic velocity-space instabilities, including two-stream instabilities, can be thought of as caused by bunching, while pinch instabilities can be regarded as a magnetic analog. The reader is referred to the pertinent section for details, and to Sec 7.2 for some general remarks on instability growth rates in realistic geometries. Section 7.5 points out the ease with which impurity radiation losses from plasmas can be overestimated if one is not certain of the electron energy distribution and conversely introduces a note of caution for spectroscopic inference of electron temperatures by means of relative line intensities.

When ideally superconducting wire is wound into a solenoid, the Meissner effect forces a peculiar current distribution within the individual conductors; actually there are reversed currents in the wires, on the sides remote from the axis of the solenoid. This picture is developed in Sec 8.1, and an experimental test of the model is described for the case of a single-layer solenoid of lead wire, made "infinitely long" by end coils of niobium-zirconium. The critical current for onset of resistance agrees with that predicted by the model, within the approximation resulting from the use of round wire when square wire was envisaged in the model. Another experiment involving current distributions and the intermediate state for the basic case of two proximate wires is given in Sec 8.2. Matters concerned with the development of technique (small magnetometers, high-current leads for cryostats, wire testing) comprise more of the activities of our small group concerned with superconductivity. Our widely used codes for calculating the magnetic properties of current systems have been reformulated on the basis of elliptic integrals instead of zonal harmonics, with concordant results; the codes have been extended for use in plotting flux lines, even through the conductors (Sec 8.7).

[1] Similar observations have recently been reported from MIT in pulsed experiments, and other closely allied observations are in the literature.

Other matters pertaining to the development of technology, which is an inevitably important part of the controlled fusion program, are discussed throughout the report. They touch upon subjects such as vacuum technique, the protection and erosion of copper coils, ion-source development, and the handling of intense ion beams. Some may be interested in the use of the duoplasmatron ion source with reversed polarity, to serve as an electron source of high perveance (Sec 6.1).

The next six months at our Laboratory promise to be exceptionally interesting. DCX-2 will continue to provide fresh information, DCX-1 is at a more interesting stage than it has ever been in the past, and the scaleup of the electron-cyclotron heating experiment will take us into entirely new and essentially unpredictable territory. Au revoir until the next report.

Abstracting Summary

1. DCX-1 PLASMA EXPERIMENTS

The configuration of the DCX-1 facility and the basic operating parameters have remained relatively unchanged: the base operating pressure is normally still low in the 10^{-9}-torr range; the maximum H_2^+ beam is about 10 ma; and the maximum trapped-proton density is about $10^8/cm^3$. The longest containment time measured is 57 sec, registered by a detector on the median plane. The studies of correlations between plasma parameters and radio-frequency signals were extended, and more evidence was obtained on the influence of the ion-clumping instability on the Z extent of the plasma. Several techniques by which the plasma might be partially stabilized against the instability were investigated, but only slight increases in plasma density were noted. The effects of deliberate perturbations of the magnetic field were studied, and it was concluded that the containment properties of the facility were insensitive to the slight errors in magnetic-field shape that are now present in normal operation. The rates of proton trapping by the Lorentz dissociation of H_2^+ were investigated for H_2^+ obtained in the conventional manner (directly from a duoplasmatron source) and for H_2^+ obtained by dissociating an H_3^+ beam in the water-vapor cell. There was no evidence of Lorentz trapping of the beam formed by the first procedure (the observations fixed the Lorentz trapping fraction as less than 10^{-7}), but a substantial fraction (5×10^{-5}) of H_2^+ formed from H_3^+ was found to be trapped by this mechanism.

2. DCX-2

Surveying experiments designed to try to specify the most significant parameters affecting the trapped-proton plasma in DCX-2 were continued during this report interval. Experiments involving dissociation on the background gas were carried out at pressures as low as 7×10^{-7} mm Hg and with total beam currents generally up to 75 ma. From the neutral flux leaving the plasma, the energetic-particle density inside is generally in the range 10^6 to 10^7, with lifetimes in the range of 5 msec. By use of a faster amplifier, the initial decay of the neutral current could be examined and was found to be in the range of several hundred microseconds. The cause of this fast decay is not understood but may conceivably originate from precession and trapping of a fraction of the injected beam.

Energy spectra of the escaping neutral flux were taken and show both wide energy and angular spread of the trapped protons. Energy half-widths of the peak due to trapped protons (all expected to be at 300 kev) are approximately 80 kev. Detailed information on the "true" energy distribution awaits further experiments determining the effects of the required collimation for the detector.

The plasma potential was determined after the development of gridded probes which can be used to analyze the energy distribution of particles from the "cold" or "background" plasma. The plasma potential during background-gas dissociation experiments lay between 140 and 540 v. These probes could also be used in such a way as to bias out the "cold" plasma; under these conditions, bursts of fast ions are clearly evident out to radial distances as large as 10 in. Fast particles are not expected past the radial position of the injector, approximately 6 in. from the center, because of the rather rapid expected precession rate due to the radial gradient of the magnetic field near the mirrors. It has not yet been possible to determine the loss rate associated with these bursts, because of the unevaluated effect of other probes near the same radius. Despite the absence of detailed time correlation between two probes, a general gross correlation does appear to exist, and so the effect of one probe on the other is difficult to assess.

Radio-frequency studies were continued, with particular emphasis on trying to establish the phase relation of signals from probes azimuthally and axially displaced in the machine. Once again, difficulty in interpreting the data was encountered as a result of apparent "gross" correlation, but no detailed correlation, between signals on probes.

Experiments were carried out to determine if a greater stability of the trapped protons could be effected by potentials on end electrodes or a relatively cold, high-density plasma. The end-electrode potential had a marginal effect. The backstream from a lithium arc seemed to affect the trapped density and significantly reduced the frequency and current of bursts to radial probes. Similar effects were seen with a high-density lithium plasma column. Energy spectra observed in the latter case showed a significantly larger spread in the energy distribution. An electron gun, which could produce currents up to 5 amp at 3 kv in a $3\frac{1}{2}$-in. ring, approximately $\frac{1}{8}$-in. thick, was also used to produce a secondary plasma in DCX-2. Radio-frequency studies show intense oscillations, indicating that a beam-plasma interaction has occurred. The trapped density was again approximately 10^7 protons/cm^3. The protons again showed an abnormally large energy spread.

A high-speed current amplifier is described that was used with the foil-covered neutral-particle detector to observe the fast decay of the plasma. It has a rise time of approximately 1 μsec, an rms noise figure of 2×10^{-10} amp equivalent, and a gain of 10^{-7} amp/v.

3. PLASMA PHYSICS

In the electron-cyclotron heating experiment in the Physics Test Facility, measurements have been made of 4- and 8-mm microwave noise, phase shifts with a 4-mm microwave interferometer, neutral-beam transmission, plasma magnetic field, visible-light emission, x-ray emission, neutron emission, and the current to multigrid probes. Studies of the variation of some of these parameters as a function of 3-cm microwave power and as a function of xenon gas impurity are described.

A small-scale, hot-electron plasma generated by the interaction of an electron beam with the plasma of the beam, and contained between magnetic mirrors appears stable. The increased Debye length due to the high temperature may permit independent particle processes. Several experiments that will form hot-electron plasmas of DCX size are being prepared.

Preliminary beam-plasma interaction studies in the beta tank indicate the existence of two interaction modes. The first seems to be characterized by ionic oscillations, up to the fifth harmonic of the cyclotron frequency, and the second seems to be characterized by electronic oscillations, as reflected in the x-ray output. Measurements of plasma density and ion temperature and analysis of x-ray spectra have begun.

An electron-beam spreader or expander has been developed to dissipate the energy in a beam of power density of the order 200 kw/cm^2. Tests up to 150 kw/cm^2 indicate no apparent wearing on the target.

Ionic sound velocity has been measured directly in plasmas of the noble gases by a time-of-flight method. An automatic analog computer has been constructed to obtain electron temperature directly from Langmuir probe characteristics.

4. VACUUM ARC RESEARCH

Ideal-plasma calculations based on previous temperature and density measurements indicated that the plasma space potential, electron temperature, and arc electrode power might be calculated from power balance and calculated plasma particle flows. The resulting calculated electron temperatures are proportional to the arc power and have ranged from 5 to 35 ev for the deuterium arc. A plasma with a calculated temperature of 31 ev yielded a Langmuir-probe electron temperature of 45 ev. The agreement between calculated and measured electrode powers was good over a broad range of arc parameters.

The dependence of the observed ion temperatures on the charge state of ions in the gas-fed, magnetically confined, high-current carbon arc is discussed briefly in terms of turbulence phenomena and a possible resonance ion-cyclotron heating mechanism.

5. CROSS SECTIONS

The cross section for proton production by H_2^+ in H_2 gas has been remeasured in the energy range 40 to 200 kev. A comparison has been made for the cross sections obtained from H_2^+ ions from (1) a radio-frequency source, (2) a PIG source, and (3) H_3^+ dissociation. The results agree well with those of other investigators in this energy range.

Measurements have been made of the fraction of a hydrogen beam that exists in the neutral-charge state after passing H_3^+ and H_2^+ through hydrogen and water vapor for energies of 60 to 400 kev. The fraction of neutrals formed varied as Ae^{-Bv}, where A and B are constants for each gas and v is the particle velocity. Measurements of the H^0 spatial distribution indicate a half angle of divergence of 20 milliradians from the dissociation of 60-kev H_3^+ in water vapor.

Studies of H_2^+ ion formation in high vibrational states have been completed. H_3^+ ions were passed through water vapor in the energy range of 60 to 400 kev. The number of H_2^+ ions formed per incident H_3^+ ion was 0.14 at 60 kev and decreased to 0.105 at 400 kev.

A cross-beam facility has been designed and is being fabricated. Design parameters have been chosen such that the pressure in the collision chamber will be 10^{-10} to 10^{-11} torr with a pressure in the surrounding region of 10^{-9} torr. Performance tests have been conducted on the new metal-gasket-sealed Consolidated Vacuum Corporation and N.R.C. (National Research Corporation) ultra-high-vacuum, 6-in., oil diffusion pumps. The tests indicate that a base pressure of 10^{-9} torr should be obtainable in the outer region with the use of an N.R.C. pump and water-cooled baffle and a pressure of 10^{-10} torr in the inner region using cryo-titanium techniques.

Tabulated Gaunt factors for the bound-free transitions of atomic hydrogen [W. J. Karzas and R. Latter, *Astrophys. J. Suppl. Ser.* **55**, 167 (1962)] are used to derive photoionization cross sections for the nth state of atomic hydrogen ($1 \leqq n \leqq 15$). A modified Bethe approximation is used to convert these to electron-impact ionization cross sections from threshold to 200 ev. For the $1s$ state the results are in good agreement with experiment, but for the $2s$ and $2p$ states the maximum cross section lies about a factor of 4 below the Born approximation calculations [P. Swan, *Proc. Phys. Soc. (London)* **A68**, 1157 (1955)].

6. PRODUCTION, ACCELERATION, AND INJECTION OF IONIC AND ATOMIC BEAMS

The new accelerator tube with epoxy skirts is performing very satisfactorily on the DCX-2 injector system. The 600-kv H_2^+ ion current injected into the machine is limited to only 60 ma, although the total current is 150 ma. This same current limitation has been found with the High-Intensity Beam Facility. The cause of this current limitation has not definitely been resolved but appears to be a decreased relative production of H_2^+ in the ion source.

The duoplasmatron ion source has been evaluated both as a source of H_3^+ ions and electrons. Up to 36 ma of H_3^+ ions have been obtained with a total current of 89 ma. The maximum electron current obtainable has not been determined, but 1 amp of electrons was extracted at 20 kv with 0.4 amp arc current. A second electron gun has been built and tested up to 1500 v at 5 amp. Both of these electron sources will be tried for injecting along magnetic-field lines into DCX-2.

A neutral source composed of two hollow-cathode arc discharges, one used as ion source and one as converter, is still undergoing components testing. Some low-voltage insulation problems have arisen, but they are not believed to be serious.

Negative chlorine ion clusters have apparently been formed by the pressure-gradient arc (mode II).

7. PLASMA THEORY AND COMPUTATION

In a simplified discussion of velocity-space instabilities, it is shown that a "bunching" mechanism in response to the continuity condition and energy conservation causes all electrostatic growth of such modes. Further, the pinch effect, responsible for magnetic instabilities, is just a relativistic correction to bunching.

A method is presented for obtaining bounds on instability growth rates applicable to spatially nonuniform plasmas not amenable to conventional analysis. The growth rate is found to be small for equilibria near a stable state. For example, the streaming instability growth rate vanishes at least linearly with the streaming speed.

Stability of a spatially inhomogeneous plasma column and a slab of finite thickness is discussed.

The influence of the shape of the free-electron energy distribution on the steady-state de-excitation radiation resulting from electron collisions with not completely stripped impurity ions has been investigated. When the transition energy between impurity levels is large compared with the mean electron energy, the radiation rate is very sensitive, by orders of magnitude, to details of the high-energy tail of the electron distribution.

An electron stream passing through an idealized representation of the DCX-1 plasma is found to stabilize the lowest-frequency modes of the Harris type, but it introduces new unstable modes at higher frequencies.

For purposes of microwave interferometry, the index of refraction of a very hot electron plasma in a magnetic field, with polarization along the field, has been calculated relativistically. It is found that the cold-plasma result is valid for electron energies of tens of kilo-electron volts.

Numerical calculations of DCX-1 orbits for H^+, H_2^+, and H_3^+ beams are described.

An improvement in the mirror-loss formula in calculating DCX-2 performance curves has led to an increase in the predicted critical current.

8. MAGNETICS AND SUPERCONDUCTIVITY

The Gaussian integration code for calculating magnetic properties of current systems and a routine for tracing flux lines have been completed. A more general program for tracing lines of constant values of flux, axial field, or field magnitude is well under way. When the field values are supplied by the mentioned Gaussian integration code, both routines can trace lines even inside the winding space.

Tests made under well-reproducible thermal-transient conditions showed that the thermal protection of water-cooled magnet coils depends appreciably upon the position of the thermal switch on the coil conductor. An empirical rule for the best location of those thermal switches has been found.

Improvements were made on the cryostat current-input apparatus described in the last progress report. Newly developed feedthrough insulators proved to be able to withstand repeated exposures to large temperature changes. By use of a precooling nitrogen container with such bushings, the head of the current-input apparatus was completely redesigned and now allows pumping for achieving temperatures below 4.2°K.

A program for developing micromagnetometers for use at cryogenic temperatures is under way. The immediate motivation for these efforts was the continuation of the experimental work on soft-superconductor proximity effects. Preliminary experiments indicated that the magnetic field between the two wires of a long superconductor loop shows a "plateau" at the transition region from superconducting-to-normal state. Exact magnetic measurements could definitely remove the uncertainties of previous proximity-effect observations which are due to the limits of sensitivity of the instrumentation for measuring the voltage drop across the samples. Besides this special application, micromagnetometers are, of course, an important tool in many other investigations on superconductivity.

Experience shows that the current-carrying capacity of high-field superconductor magnet coils is often considerably smaller than that expected from short sample wire tests ("degradation effect"). An analysis of existing theories of the degradation effect is presented, which is also extended to the limiting case of an infinitely long, soft-superconducting solenoid. Experiments with a coil of simulated infinite length show the expected maximum field. Finally, tests have been made on the intermediate state of soft-superconductor coils with and without end compensation.

9. VACUUM SYSTEMS, TECHNIQUES, AND MATERIAL STUDIES

Leak-tight sealing of a 99% aluminum alloy wire gasket between plain flange surfaces is dependent on the mechanical properties of the alloy. Although the gasket was limited to a finite number of thermal cycles because of creep, it was possible to maintain vacuum closure for more than 18 thermal cycles between room temperature and 250°C with 4 hr per bake at the elevated temperature. The maximum loading force necessary to remain in the plastic, sealing, region is approximately $8\frac{1}{2}$ tons/in.^{2}, or 3000 lb per linear inch of gasket. Initial sealing of this 0.086-in.-diam gasket was achieved with approximately 0.028-in. gasket deformation and a force of 1500 lb/linear in.

Desorption behavior from a 30,000-cm^2 aged molybdenum surface has been studied as a function of temperature from 80 to 115°K. Heats of desorption have been determined for two desorption peaks found in the pressure-temperature data. Admission of three gases, CO, CH_4, and Ar, followed by a thermal adsorption have yielded isosteric heats of 3.0, 4.3, and 3.5 kcal/mole. The total quantity of gas desorbed, starting from a base pressure in the range of 2 to 4×10^{-10} torr, has been found to be a small fraction of a monolayer. An expression for a Henry's law isotherm has been derived, and a discussion of sorption speed at low temperatures and other desorption phenomena are discussed with reference to the derived isotherm.

10. FURTHER SPECULATIONS ON VERY HIGH ENERGY INJECTION INTO A MAGNETIC MIRROR

A brief discussion is given which points up some difficulties of attaining a very high density plasma by very high energy injection despite the large Lorentz breakup and grossly reduced charge-exchange losses.

11. DESIGN AND ENGINEERING: NOTES

Some additional tests to determine corrosion-erosion rates in copper tubing were conducted. Initial results indicate a high initial rate of weight loss; the rate of weight loss shows a gradual increase with increasing flow velocity and coolant temperature in the nonboiling range of temperatures.

12. DESIGN AND ENGINEERING: SERVICE REPORT

The activities of the Engineering Services Group are generally reported incidentally with the research efforts of other groups of the Thermonuclear Division. The Group executes or coordinates engineering design, shop fabrication, building operations, and maintenance.

1. DCX-1 Plasma Experiments

J. L. Dunlap
R. S. Edwards
G. R. Haste
L. A. Massengill
Herman Postma
R. G. Reinhardt
W. J. Schill
E. R. Wells

1.1 INTRODUCTION

During this report period only relatively minor changes were made in the mechanical configuration of the DCX-1 facility. A magnetic quadrupole lens was added to the H_2^+ beam injection system and has afforded some additional control on the beam focus in the trapping region. For experiments on Lorentz dissociation, a water-vapor cell was added between the source and the accelerator tube. It was determined that the two 14-in. oil diffusion pumps on the intermediate vacuum region were not contributing beneficially to the overall performance of the facility, and they were recently removed. The intermediate vacuum region is now pumped only by titanium evaporators and liquid-nitrogen-cooled conductances to the outer vacuum regions. Both of the inboard magnetic-field coils were replaced because of partial shorts internal to the coil windings.

The maximum H_2^+ beam that can be injected is still about 10 ma, and the base operating pressures in the plasma region are still low in the 10^{-9}-torr range. Containment times of tens of seconds are not uncommon; and in one series of runs at about 1×10^{-9} torr, centrally located detectors recorded charge-exchange-decay times of almost 60 sec. The maximum fast-proton densities have remained at about $10^8/cm^3$.

In the following sections, details are given of some experiments that are continuations of earlier work. Several new topics are introduced: direct measurements of mirror losses, investigations of the sensitivity of the containment properties to perturbations of the magnetic field, and proton trapping by Lorentz dissociation of H_2^+.

1.2 RADIO-FREQUENCY MEASUREMENTS[1]

Work continued on developing probes and techniques for separating the rf signals into the various electric- and magnetic-field components. Copious data have been obtained on the one feature of the rf signals that seems to be reproducible in fine detail, the initial buildup during the period of plasma accumulation at higher operating pressures (approximately 10^{-7} torr). The more general conclusions of this work have already been given.[2] Studies of these data are continuing, and it is expected that they will soon be the subject of a separate report.

During each of the other experiments described in this report, there was continuous monitoring of the amplitude of the rf signal from a single-loop probe mounted in the median plane just outside the plasma boundary. Details of these rf measurements are given in the other sections.

1.3 CORRELATIONS BETWEEN PLASMA PARAMETERS AND RADIO-FREQUENCY SIGNALS

At operating pressures in the 10^{-9}-torr range, the coherent rf signals, which are taken as indicating the appearance of the ion-clumping instability, occur in short intense bursts. Studies of the correlations between a number of plasma parameters and the appearance of this rf activity

[1]With C. E. Nielsen, consultant from Ohio State University.

[2]*Thermonuclear Div. Semiann. Progr. Rept. Oct. 31, 1962*, ORNL-3392, p 9.

(and hence, by inference, studies of the variation of these parameters in the presence and in the absence of the instability) have been reported.[3]

Efforts were made to extend these data to include direct measurements of the changes in the energy distributions of the circulating protons. A silicon surface-barrier detector was mounted in the median plane and was used in conjunction with a 256-channel analyzer to obtain the energy distributions of the charge-exchange neutral flux to that location. Energy spectra were obtained while operating in coincidence and then in anticoincidence with the rf signals, but no statistically reliable differences were noted. The possibility of directly measuring these energy changes with reasonable counting times is marginal; the charge-exchange signals are much more sensitive to variations in the energy distributions.

Studies of the correlation of the rf signals and scattering of the plasma away from the median plane have been more successful. Some data on this scattering during the buildup interval and during steady state have already been presented, and correlations have recently been noted during the decay interval. If the H_2^+ beam shutoff happens to occur during an rf burst, the rf signal usually persists to complete its normal time duration. This duration and hence the persistence interval is always much shorter than the plasma decay time; but with these decay times in the order of 10 to 20 sec the persistence intervals can be as long as 1 sec. For such an occurrence, expanded time-scale displays of the charge-exchange signals from the usual array of detectors show that during this persistence interval the central detectors indicate a density decay more rapid than normal, while the side detectors indicate a decay slower than normal. Figure 1.1 shows a pronounced example of this behavior, one in which the side-detector signals remain relatively unchanged during the persistence interval. For comparison, a set of detector decay traces is also given for a case in which the H_2^+ beam shutoff occurred when there was no strong rf signal present. These data indicate that the instability causes a scattering of the plasma from the more densely populated central region. Since the instability can persist for as long as 1 sec after H_2^+ beam shutoff, it seems highly unlikely that it

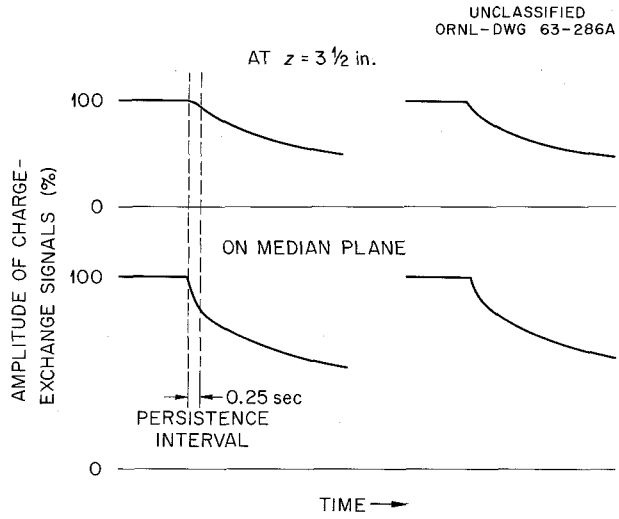

Fig. 1.1. Neutral-Particle-Detector Decay Traces Showing the Effect of an Instability During the Initial Portion of the Decay (5 ma H_2^+, 6×10^{-9} torr).

can be the result of an H_2^+ beam–plasma interaction. Additional evidence in support of this last point is given in Sec 1.6.

The Z scattering was also evident in the responses of the neutral-particle detectors during low-pressure runs with the movable end walls (Sec 1.4). With the walls well outside the plasma volume, the signals to these detectors show the usual increases during rf-burst intervals, with recovery back toward a steady-state level with a charge-exchange time constant. It has been argued[3] that these fluctuations are the result of an augmented charge-exchange loss rate due to increased energy degradation during the presence of the instability. When the end walls were brought as close as 6 in. to the median plane, a different sort of fluctuation became dominant at the end detectors (those at about the same Z locations). The fluctuations were still in coincidence with the rf signals, but the amplitude increases at these detectors were considerably larger, and at the end of the rf burst the signal levels dropped immediately (with the time constant of the recording equipment, some milliseconds) to almost the steady-state value. This rapid recovery time indicates that the signal increases in these detectors were associated with the direct loss of fast particles rather than with an enhanced charge-exchange loss rate. With the walls at symmetric positions with respect to the median plane, the

[3] *Thermonuclear Div. Semiann. Progr. Rept. Oct. 31, 1962*, ORNL-3392, pp 3–7.

fluctuations at the end detectors were also symmetric. Positioning one wall ½ in. closer to the median plane than the other resulted in about a factor of 2 increase in the amplitude of fluctuation of the detectors beneath the closer wall and in a reduction to almost zero amplitude at the detectors beneath the other end wall. We interpret these signal fluctuations as the result of almost-grazing collisions of circulating protons with the end walls while the protons are being Z-scattered by the instability. The fact that a slight asymmetry in the positions of the walls with respect to the median plane can affect the fluctuations in the manner observed indicates that the amplitudes of the Z oscillations grow slowly in comparison with the period for Z oscillation. (For small displacements from the stable orbit the frequency of Z oscillation is about 5 Mc.)

That the Z scattering is not particularly catastrophic is also supported by the fact that in the mirror-loss experiments (Sec 1.5), the mirror loss rate appeared to fluctuate at random and had no time correlation with rf-burst activity. The effect of the scattering on the plasma volume is described in the following section.

1.4 STABILIZATION EXPERIMENTS

For a "well-behaved" plasma, our calculations[4,5] indicate that the injected molecular-ion current and the proton containment time required for exponentiation may well be within the already demonstrated capabilities of the facility (the injection of 10 ma H_2^+ while maintaining a background pressure in the plasma region low in the 10^{-9}-torr range). Exponentiation has not been achieved, and the maximum fast-proton densities during this report period have again been about $10^8/cm^3$. The ion-clumping instability acts to make the conditions for exponentiation (the critical product of H_2^+ current and proton containment time) more difficult to achieve. When operating with the maximum H_2^+ beam at the lowest pressures, the instability appears to scatter the plasma so that it occupies a volume several times that expected on the basis of single-particle interactions and to change the proton-energy distributions so that the mean containment time is perhaps one-half that expected on the same basis. These considerations have prompted studies of several techniques by which the plasma might to some extent be stabilized. The details of these investigations are given in the rest of this section.

The previous progress report[6] described some results of changing the median-plane H_2^+ beam trajectory so as to deliberately increase the precessional motion of initially trapped protons. Evidences for partial stabilization of the plasma by this technique were reductions in the amplitude and repetition rate of the coherent rf signals associated with the presence of the instability, and reductions in the steady-state volume of the plasma (and hence corresponding increases in plasma density). Additional experiments of this nature were performed again at base pressures, and the studies were extended to include slight shifts of the H_2^+ beam trajectory relative to the median plane. The relative amplitudes and the repetition rate of the rf-burst activity could be modified by almost any change in the injection orbit, but the changes in other gross properties of the plasma (the amplitudes and Z distributions of the charge-exchange signals, the charge-exchange decay times, and the energy distributions of the charge-exchange neutral flux in the median plane) were usually modest and not consistently reproducible. Exceptions were the data obtained with the technique previously reported, that of first securing the normal beam trajectory at the normal or less-than-normal value of the containment field, and then operating at 5 to 10% above the normal field value. At the higher fields there was again a reduction of about 50% in the plasma volume at base pressure, the repetition rate of the rf bursts was again reduced about an order of magnitude, and there was some evidence for reduced proton-energy degradation.

The argument that increased disorder in the motion of trapped protons makes the plasma more stable is also supported by the results of an experiment which to some extent separated the effects of the more-ordered protons from those with less-ordered motions. An obstacle was arranged so that it could be swung into the plasma volume

[4] *Thermonuclear Div. Progr. Rept. Oct. 31, 1961*, ORNL-3239, pp 8–9.

[5] *Thermonuclear Div. Semiann. Progr. Rept. Apr. 30, 1962*, ORNL-3315, p 3.

[6] *Thermonuclear Div. Semiann. Progr. Rept. Oct. 31, 1962*, ORNL-3392, pp 7–8.

so as to intercept those protons moving between $R = \pm 1$ in. The gross plasma properties were measured with and then without this obstruction in place. The results showed that half the charge-exchange flux results from protons that precess through the central 1-in. region of the machine, that this precessing portion contributes in no discernible way to the generation of the ion clumps, and that most of the measured energy dispersion arises from the well-ordered protons.

When operating at reduced injection energy, it is possible to adjust the injection angle and the strength of the containment field so that the H_2^+ beam turns around either at the proton stable-orbit radius or at the axis of the containment field. The latter case represents the farthest departure from the standard injection orbit yet studied. For both 520- and 550-kev H_2^+ beams, the injection orbit was shifted back and forth between these two limits, and the effects on the charge-exchange signals and the rf were noted. The pressures were low (τ values of 8 to 15 sec), and the pressure and H_2^+ beam current were held constant. When shifting from the standard orbit to the other, an order-of-magnitude reduction in the repetition rate of the rf bursts was noted, and there were again indications of somewhat less proton-energy degradation. Only slight changes (about 10% variation) in the Z extent of the plasma were observed.

Other studies involved the use of metal end walls which were 10 in. in diameter and centered on the Z axis with their planes parallel to the median plane. These walls could be moved with respect to the plasma (the range $Z = 0$ to $Z = \pm 12\frac{1}{2}$ in. was investigated), and either wall could be grounded or biased up to ± 15 kv with respect to ground. The gross properties of the plasma at base pressure were examined as functions of the positions and potentials of the end walls. The optimum plasma density was obtained by having the walls at ground potential and positioned at least 6 in. from the median plane (there was evidence for direct loss of fast protons to the end walls at positions closer to the median plane). If the potentials were applied with the end walls positioned at Z greater than about 6 in., there seemed to be little effect on the plasma. With the end walls close enough to the median plane to intercept a portion of the plasma, the steady-state charge-exchange signals and the containment time decreased as the wall potentials were increased. The data were consistent with the interpretation that the rate of plasma loss to the walls increased.

Work by the Theoretical Group[7] had indicated that a convective electron current through the plasma might stabilize the system against lower frequency modes of the clumping instability, but that at the same time it might enhance higher modes. The electron gun previously described[8] in connection with electron-cyclotron heating was used in an investigation of this problem. Longitudinal electron currents (from 0 to 80 ma of 100-v electrons or 0 to 500 ma of 420-v electrons) were accelerated through the plasma but did not appear to lead to enhanced stability. Radio-frequency signals at the lower proton-cyclotron harmonics could be partially suppressed, but other signals appeared usually at greater than $3\omega_{ci}$ (the range 10 to 100 Mc was surveyed), apparently as the result of longitudinal current activity. The neutral-particle detector signals and the energy analyzer both showed that the proton-energy distributions were considerably degraded with electron currents greater than about 50 ma. Since the electron velocity is of considerable importance in the theoretical treatment of the problem, additional experiments with a higher voltage power supply are planned.

1.5 CONTAINMENT STUDIES

1.5.1 Measurements of Mirror Losses

Silicon surface-barrier detectors and a 256-channel analyzer were employed to measure the energy distributions and the flux of energetic particles ($E > 80$ kev) lost through each of the magnetic mirrors. These studies were made as a function of radius at $Z = \pm 25\frac{1}{2}$ in. and were performed at two values of azimuth at each Z location. The Z positions are such that the absolute containment zones for any 300-kev proton that can circulate in the median plane are unobstructed to that location. Measurements were made as a function of pressure, H_2^+ beam current, and H_2^+ injection orbit. A complete report is being prepared for internal distribution; only the more interesting results will be given here.

The most important conclusion was that the mirror losses of fast protons were from two to

[7] C. O. Beasley and E. G. Harris, "Beam-Electron Interaction in DCX-1," this report, sec 7.7.

[8] *Thermonuclear Div. Semiann. Progr. Rept. Oct. 31, 1962*, ORNL-3392, p 8.

possibly four orderc of magnitude less than the charge-exchange loss rate. Charge exchange thus remains the dominant loss mechanism.

About 40% of the protons formed in the trapping region have absolute containment zones that open through the mirrors. At one time it was thought that these protons would rapidly be lost out of the mirrors. The low measured mirror loss rate indicates that most of this class of protons are actually trapped long enough to charge-exchange even at pressures in the 10^{-9}-torr range. This conclusion is supported by the fact that the energy distributions of the mirror loss particles were not those of monoenergetic 300-kev particles, but rather they displayed the dispersion and degradation effects similar to the previously reported[9] distributions of trapped protons. Additional support was provided by studies of the effect of a movable radial obstruction on the charge-exchange signals. The radial distribution of the plasma derived from these studies agreed well with that calculated on the assumption that all protons formed in the trapping region were lost by charge exchange.

1.5.2 Effects of Magnetic-Field Perturbations

Interest in the effects of a θ-dependent perturbation of the midplane field was stimulated when Hall-probe scans showed that the two 14-in. diffusion pumps symmetrically mounted on the intermediate vacuum system were producing a perturbation of 20 gauss over the 3.25-in. proton stable-orbit radius. Studies were made of the effects on proton containment of the additional perturbation produced by rapidly moving a soft iron slug (2 in. long and 2 in. in diameter) along a radius in the median plane from large radii, where there was no noticeable change in the field along the stable-orbit radius, to $R = 9$ in., where the additional perturbation ranged from about 35 to 5 gauss. No effects of the additional perturbation were noted for plasma decay times less than about 0.1 sec. For longer containment times, insertion of the slug produced both a decrease in the steady-state charge-exchange reaction rate and a decrease in containment time. Both effects became more noticeable as the pressure was reduced. Since it had already been determined that the two 14-in. pumps were not contributing to lower base pressures in the plasma region or to the speed of pump-down, the pumps were removed. A check of the magnetic field then showed no measurable ($\lesssim$1 or 2 gauss) perturbation along the stable orbit, but the properties of the plasma appeared not to be affected by the change. The effects of introducing the perturbation of the iron slug were then reinvestigated. With containment times longer than 0.1 sec, insertion of the slug again reduced both the steady-state charge-exchange reaction rate and the containment time. At the lowest pressures achieved in these runs, the containment time without the perturbation was about 10 sec. Figure 1.2 shows the effects of introducing the perturbation under these conditions. The perturbation reduced the steady-state charge-exchange reaction rate by about one-half and the containment time for the remainder of the plasma by about one-fourth. The change in the steady-state reaction rate upon insertion of the slug occurred with a time constant of about 1 sec, which was several times longer than the time required to insert the slug.

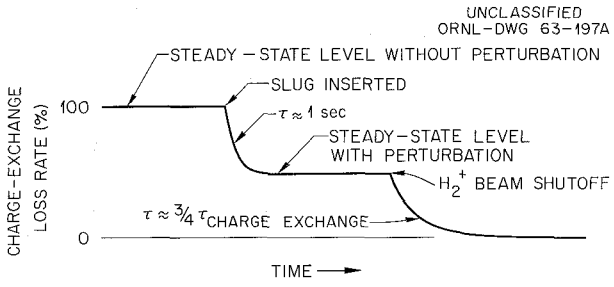

Fig. 1.2. Effect of a Magnetic-Field Perturbation on the Charge-Exchange Signals.

Under some circumstances the magnetization of ferromagnetic materials occurs with a time constant of seconds or more; so it was not initially clear whether the observed time constant was that for the perturbation to come to a steady state, or whether it was a measure of the time required for the plasma density to adjust to essentially a step-function perturbation. For the ferromagnetic effect, the time constant can be changed orders of magnitude by heating the material from room temperature to 100°C. The experiment was repeated with a hot slug, and the results were essentially the same. It appears then that the time constant is a measure of a real particle-orbit effect.

[9] *Thermonuclear Div. Semiann. Progr. Rept. Apr. 30, 1962*, ORNL-3315, pp 10–11.

Perturbing the field in this manner did not increase the rate at which fast particles were lost from the mirrors, nor did it appear to change the Z extent of the plasma. It is believed that the increased proton loss rates associated with the perturbation are the results of enhanced radial drift, though there has not yet been a successful measurement of the proton current to the wall.

In another series of experiments, separate current controls were arranged for the two coils that furnish the containment field so that these currents could be unbalanced. The only consequences of this action appeared to be some changes in the rf signals and increases in the Z extent of the plasma and in the rate of fast-particle loss out of the weaker mirror. With the maximum unbalance, the current through one mirror coil was 10% less than that through the other. For this condition (with 5-ma H_2^+ and containment times of about 7 sec), the extent of the plasma was not noticeably affected by the unbalance in coil currents, and the mirror loss rates were in the ratio of approximately 2:1. The total mirror loss rate was still two orders of magnitude lower than the charge-exchange loss rate. It was concluded that the containment properties would not be sensitive to the slight field unbalances that might be present during normal operation.

1.6 PROTON TRAPPING BY LORENTZ DISSOCIATION OF H_2^+

Calculations[10-12] have shown that substantial fractions of H_2^+ can be dissociated by strong electric fields, or equivalently by the Lorentz force experienced by the ions in a magnetic field, if the upper vibrational levels of the molecular ion were well populated. Experiments[13-16] have been described which in general confirm these calculations but disagree on the magnitude of the dissociation fraction for specific values of the electric field. Since the populations of the upper levels are presumably influenced by the manner in which the molecular ions are produced, it appears that a substantial portion of this disagreement is due to the use of different ion sources in the several experiments. The purposes of the experiments in DCX-1 were twofold: (1) to investigate various means of ion production in order to optimize the population of the excited states of interest and (2) to find out whether under our conditions the trapping of protons from Lorentz dissociation can be an effective mechanism for building up plasma densities in a controlled thermonuclear experiment.

The usual array of neutral-particle detectors in the DCX-1 measures a portion of the charge-exchange losses. Since all evidence indicates that the trapped protons are lost primarily by charge exchange, this measured portion can be related to the total charge-exchange loss rate and to the trapping rate as follows:

$$I(H_0) = GI_T(H_0) = GI(n\sigma L + \alpha) ,$$

where

$I(H_0)$ = current equivalent of the measured portion of the charge-exchange losses,

G = geometric factor for collection efficiency = 1/130,

$I_T(H_0)$ = current equivalent of the total charge-exchange loss rate,

I = injected current of H_2^+,

n = background neutral density,

σ = proton production cross section for collisions of 600-kev H_2^+ with background neutrals,

L = H_2^+ beam path length along which the resulting protons can be trapped = 35 cm,

α = fraction of the H_2^+ beam trapped by Lorentz dissociation.

By changing the background neutral density in the plasma region, one can distinguish between

[10] W. I. Linlor, UCRL COPJ-119-57 (Feb. 26, 1957) (unpublished).

[11] J. R. Hiskes, *Phys. Rev.* **122**, 1207 (1961).

[12] J. R. Hiskes, *Nucl. Fusion* **2**, 38 (1962).

[13] Selig Kaplan, G. A. Paulikas, and R. V. Pyle, *Phys. Rev. Letters* **7**, 96 (1961).

[14] A. W. Ehler, Informal AEC Research and Development Reports, Contract AT (04-3)-362, Hughes Research Laboratories (unpublished).

[15] A. C. Riviere and D. R. Sweetman, *Phys. Rev. Letters* **5**, 560 (1960).

[16] A. C. Riviere and D. R. Sweetman, *Ionization Phenomena in Gases*, vol II, p 1236, North-Holland Publishing Co., Amsterdam, 1962.

proton trapping due to gas dissociation and that due to Lorentz dissociation.

In the trapping region of the DCX-1, the 600-kev H_2^+ beam encounters Lorentz forces ranging from 6.5×10^4 v/cm at the outer edge of this region to 7.3×10^4 v/cm at the point of closest approach to the magnetic axis. The trapping rate due to Lorentz dissociation is then the difference between the total Lorentz dissociation fractions for these two electric-field values, and the critical-field value for prematurely dissociating molecules in all states of interest is 7.3×10^4 v/cm.

The Lorentz trapping fraction for H_2^+ taken directly from the duoplasmatron ion source was evaluated by two techniques: (1) by comparing the charge-exchange loss rates obtained at base pressures (10^{-9}-torr range) first with the source extractor potential adjusted for calculated (i.e., vacuum) fields in the extractor region 35% greater than the critical value, and then with the extractor potential adjusted for fields 45% less than the critical value; and (2) by examining the variation of the charge-exchange loss rate with pressure. Both high and low arc voltage modes of source operation were examined, but in none of these experiments was Lorentz trapping detected. The data were such as to fix the Lorentz trapping fraction $\alpha < 10^{-7}$. No other measurements of the Lorentz dissociation of H_2^+ from duoplasmatron sources appear to have been reported; so we are not able to make a comparison of these data with results obtained elsewhere.

Significant Lorentz trapping was observed when using H_2^+ from the dissociation of H_3^+ in a water-vapor cell. The manner in which this injection was accomplished is shown in Fig. 1.3. The water-vapor cell was 20 cm long, and a pressure differential was maintained by cooling the ends of the cell to liquid-nitrogen temperature. Using the data of Barnett and Ray,[17] the observed conversion efficiency of 3% indicates that the neutral areal density in the gas cell was about $4 \times 10^{14}/\text{cm}^2$. High pressures in the accelerator tube made it unadvisable to increase this density.

The charge-exchange current to the neutral-particle detectors and the proton containment time were measured as the background neutral density was varied with a helium leak. The results are

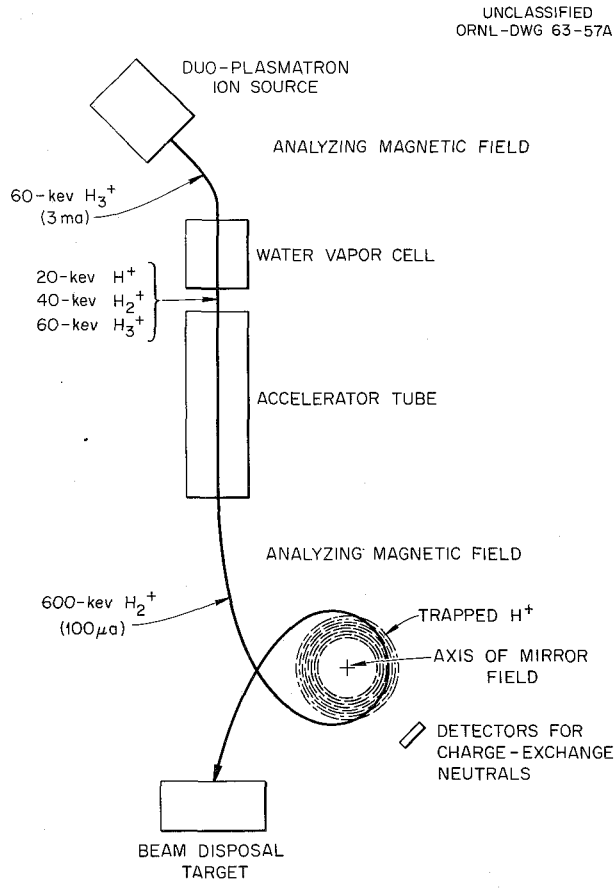

Fig. 1.3. Injection System for Lorentz Dissociation.

given in Fig. 1.4, which for comparison also shows some results obtained during injection of H_2^+ acquired directly from the ion source in the conventional manner. Since the reciprocal lifetime varies directly with background neutral density, curve *A* indicates that proton trapping is the consequence of gas dissociation in the case of conventional injection. In curve *B* the nearly constant value of the loss rate over a wide pressure range indicates a trapping mechanism that is independent of the background density and is evidence of Lorentz trapping.

It is possible to compute α from curve *B* in several ways. At base pressure the ratio of the total charge-exchange loss rate ($130 \times 400 \times 10^{-13}$ amp) to the input H_2^+ current (100 μa) yields $\alpha \approx 5 \times 10^{-5}$. Two calculations are based on projecting the 400×10^{-13} amp value to the point of intersection with the extension of the high-pressure (gas dissociation dominated) portion of the curve. The quantity α is then equivalent to the gas trapping

[17] C. F. Barnett, Mozelle Rankin, and J. A. Ray, "Production of H_2^+ in High Vibrational Levels," this report, sec 5.4.

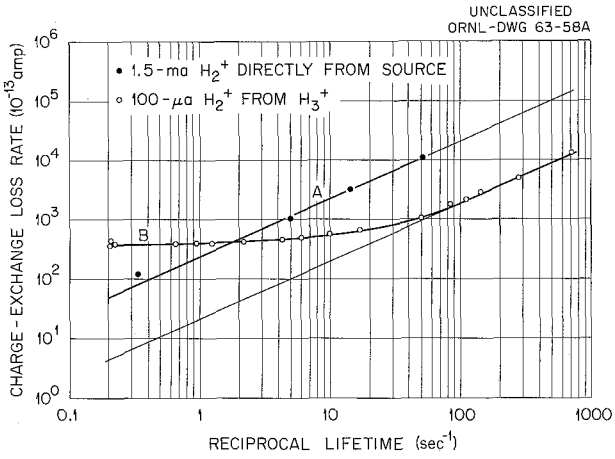

Fig. 1.4. Charge-Exchange Loss Rate as a Function of Reciprocal Lifetime.

fraction at that point. Using the τ^{-1} value at the point to calculate the density of helium atoms yields $\alpha = n\sigma L = 6.5 \times 10^{-5}$ (where the cross section for dissociation[18] was used rather than the proton production cross section, which does not appear to have been reported). Using the corrected ion-gage pressure at that point to determine the helium density yields $\alpha = n\sigma L = 7.5 \times 10^{-5}$. The observed Lorentz trapping fraction is thus in the order of 5×10^{-5}.

Riviere and Sweetman[16] have reported the total Lorentz dissociation fractions as a function of electric-field strength for H_2^+ formed from the dissociation of H_3^+ in a water-vapor cell. The difference of their dissociation fractions for field values of 7.3×10^4 and 6.5×10^4 v/cm is also about 5×10^{-5}.

[18]C. F. Barnett, *Proc. U.N. Intern. Conf. Peaceful Uses At. Energy, 2nd, Geneva, 1958* **32**, 398 (1959).

The importance of these observations will be stressed by several comments. At the base-pressure point of curve *B*, the density of the plasma established by the Lorentz dissociation of the 100-μa beam is equal to that which would have been established by the gas dissociation of a 10-ma H_2^+ input beam; that is, it is as dense a plasma as has been established in the facility at this pressure, about 10^8 fast protons/cm^3. With Lorentz trapping, reductions in pressure should increase the containment time but should not affect the trapping rate; so reductions in pressure should yield even higher densities. The base pressure during the runs of Fig. 1.4 was not particularly good; the containment time was 5 sec, whereas times of 20 to 30 sec are not uncommon. In addition, work is in progress to increase the amount of H_2^+ from the water-vapor cell by increasing the H_3^+ delivered to the cell and the efficiency of the conversion to H_2^+. It does not appear unreasonable to expect an increase of at least an order of magnitude in the total number of trapped protons at the very low pressures.

Worthy of mention is the fact that the gross characteristics of the plasmas observed in the runs of Fig. 1.4 seemed to be dependent only upon the proton densities and the background pressure. In particular, no effect seemed to have been caused by the variation of the ratio of H_2^+ density to trapped-proton density that accompanied the data of curve *B*. (This ratio is fixed at about one for trapping via gas dissociation and was about 0.01 for Lorentz trapping.) These observations serve to confirm our previous conclusion (Sec 1.3, this report, and ref 19) that H_2^+ beam–plasma interactions have little if any influence on the properties of the plasma.

[19]*Thermonuclear Div. Semiann. Progr. Rept. Apr. 30, 1962*, ORNL-3315, p 13.

2. DCX-2

P. R. Bell
L. J. Bledsoe
J. S. Culver
R. C. Davis
S. M. DeCamp
J. C. Ezell
R. A. Gibbons
G. G. Kelley
N. H. Lazar
O. B. Morgan
J. D. G. Rather
T. F. Rayburn
R. F. Stratton
J. C. Thompson
C. W. Wright
A. J. Wyrick

2.1 PLASMA DENSITY MEASUREMENTS

Surveying experiments in DCX-2 continued during this report period in an attempt to specify the most significant parameters which affect the trapped-proton plasma. For example, small variations in the magnetic field (<50 gauss) have been shown to have large effects on the apparent particle density in ring No. 7 (see Figs. 2.1*a* and *b* for identification of port locations), where a 1.7% dip in the magnetic field occurs, but to have only a lesser effect on the density in the "flat" portion of the field.

Pressure-variation experiments have been limited because of the rather high base pressures generally obtainable. With the beam on, the pressure in the liner generally has been between 1 and 2×10^{-6} mm Hg, even though the base pressure (with the beam off) may be as much as a factor of 2 lower. This high operating pressure, in general, is improved when the machine is held under vacuum for extended periods, especially if injection experiments are carried on during this time. During several runs the pressure was as low as 7×10^{-7} mm Hg with the beam on. The cleanup of the walls is slower than hoped for, and future operations will be preceded by an argon-arc bakeout. Although arcs have been used for this purpose for only rather short runs, and leaks (which have confused the issue) tend to plague a machine of this complexity, nevertheless, an arc bakeout (of approximately 6 hr) seemed to reduce significantly the operating time required to obtain a satisfactory pressure in the machine.

Beam current variations were carried out only over a limited range. For these runs, only approximate proportionality between total beam current and injected H_2^+ beam was obtained. Details of the experimental measurements of beam fractions as a function of current are given elsewhere.[1] The equilibrium densities determined from the charge-exchange neutral flux incident on the foil-covered detectors are given in Table 2.1 for beam currents of 25 and 50 ma for two runs on different days. A notable fact, still unexplained, is the significantly higher density obtained in the region of the dip at the west end of the machine (detector in port 7-8).

As explained in the previous progress report,[2] the amplitude of the current signal from the foil detectors is expected to drop to approximately nine-seventeenths of its equilibrium value when the beam is cut off, and then should decay almost exponentially (if the pressure is assumed to remain nearly constant) with a lifetime determined by the charge-exchange rate. Also shown in Table 2.1 is the ratio of the initial value of the apparent charge-exchange tail to the equilibrium current. The discrepancy of more than an order of magnitude between these figures and the value $^9/_{17}$ expresses, again, the enhanced loss rate of the trapped protons. Unfortunately, the rise time of the current amplifiers used for these measurements is approximately 200 μsec at these gains. If there were a

[1] R. C. Davis *et al.*, "High-Current Ion-Beam Injection," this report, sec 6.1.

[2] *Thermonuclear Div. Semiann. Progr. Rept. Oct. 31, 1962*, ORNL-3392, p 13.

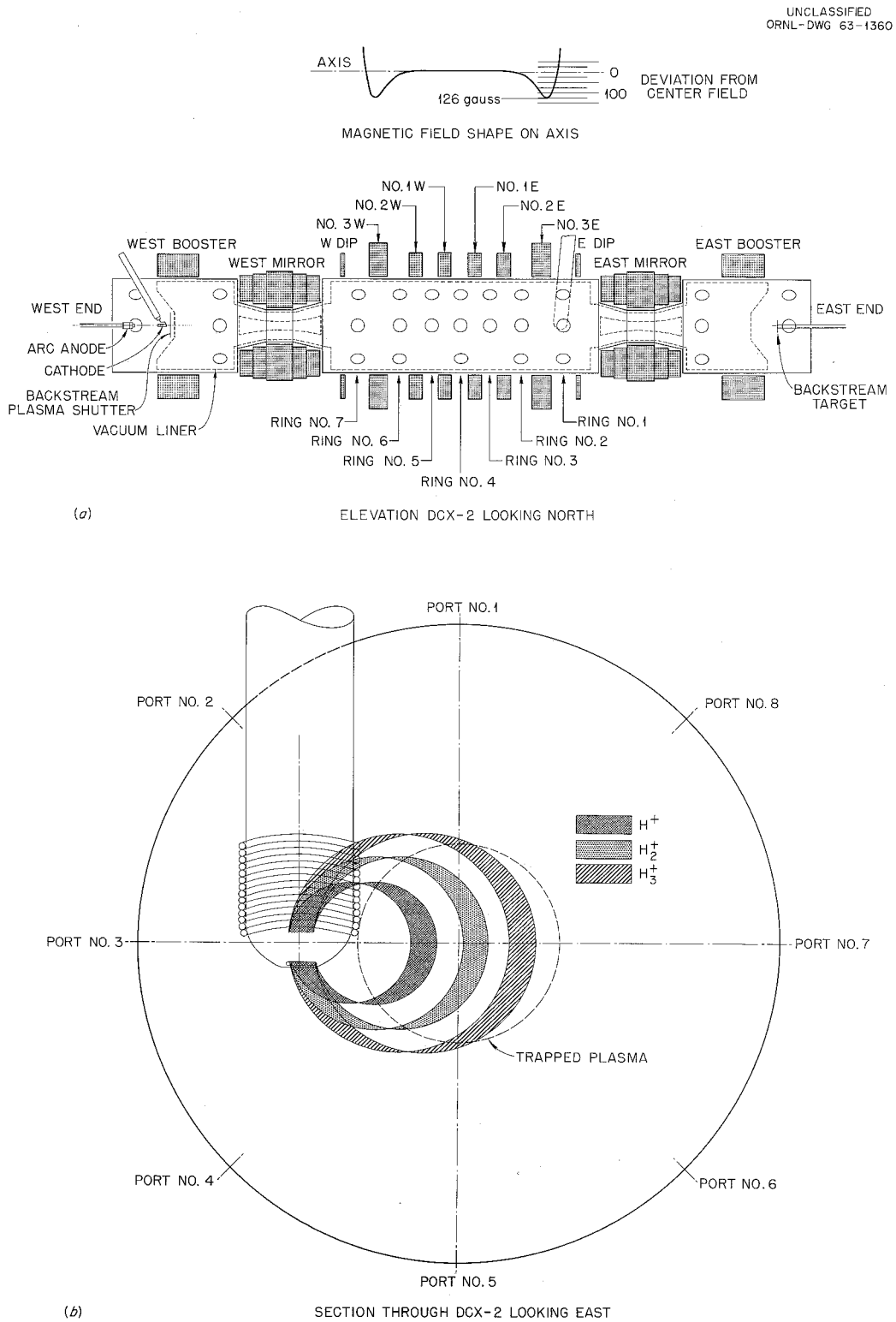

Fig. 2.1. (*a*) Elevation of DCX-2, Showing Port Ring Locations, Arc Electrodes for Backstreaming Plasma, and Magnetic-Field Profile Along the Axis; (*b*) Cross Section of DCX-2 Looking East, Showing Port Position Locations.

Table 2.1. Densities and Lifetimes of Trapped Plasma with Gas Breakup and "Flat" Field Conditions

I_{0cx}/I_{total} is the ratio of initial charge-exchange neutral current seen to the foil detectors.

Detector Position	n	τ (msec)	I_{0cx}/I_{total}
	Feb. 18, 1963; I_{beam} = 25 ma		
1-8	1.5×10^6	3.4	0.28
2-8	1.1×10^6	1.9	0.27
4-8	3.4×10^6	3.4	0.015
6-8	1.1×10^6	2.2	0.055
7-8	1.8×10^7	6.6	0.23
	Feb. 26, 1963; I_{beam} = 50 ma		
1-8	3.1×10^6	5.6	0.13
2-8	4.5×10^6	4.6	0.018
4-8	1.3×10^6	4.7	0.018
6-8	1.0×10^7	6.8	0.055
7-8	2.5×10^7	5.6	0.23

UNCLASSIFIED
PHOTO P-61703

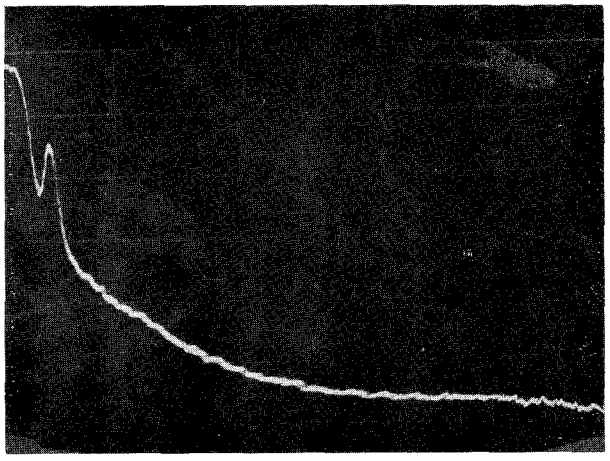

Fig. 2.2. Foil Neutral-Particle Detector Signal Using Fast Current Amplifier. The shoulder at the upper left shows the steady value of current with the beam on. The sweep speed was 50 μsec/cm, and the vertical sensitivity was 2×10^{-9} amp/cm. The spike just after turnoff was caused by a fault in the beam pulsing equipment.

significant energy spread of the trapped protons, their charge-exchange rate would be very much different from the value calculated from the cross section at 300 kev. In fact, since the charge-exchange cross section varies so rapidly with the energy in this range,[3] without knowing the particular energy distribution, it is not clear whether the average lifetime would be increased or decreased as a result of a spread. Recently, a fast amplifier (approximately 1-μsec rise time with a 10^{-7} amp/v sensitivity) was used in DCX-2, and the initial decay was found to be relatively fast (approximately 100 μsec; see Fig. 2.2). The ratio of the amplitude of the initial "charge-exchange current" to the equilibrium amplitude was $\frac{1}{2}$. This suggests that under certain circumstances, at least, the primary loss mechanism might well be through charge exchange with the background gas, rather than by radial bursts of the protons mentioned below.

[3]C. F. Barnett, W. F. Gauster, and J. A. Ray, *Atomic and Molecular Collision Cross Sections of Interest in Controlled Thermonuclear Research*, ORNL-3113 (1961).

2.2 ENERGY ANALYSIS OF ESCAPING FAST NEUTRALS

Energy analyzers have been constructed and used to survey two regions of the DCX-2 plasma. The energy-sensitive components are silicon barrier detectors which are placed at the position of the liner wall in ports 4-4 or 7-4. Energetic neutral particles, produced either by charge exchange of trapped protons or dissociation of energetic molecular ions, and which leave the plasma region at the proper angle, may enter the detector. The pulse height is then sorted in a 256-channel analyzer.[4] The resolution of the detectors is 35 and 25 kev respectively.

Collimation is used to restrict the flux into the detector so that distortion of the spectrum is not introduced by large counting rates. The collimation is shown in Figs 2.3*a* and *b*. It may be noted that the angle in the vertical plane is small enough to ensure that essentially none of the neutrals from dissociation may enter the detector from the expected molecular-ion orbits. The angle was made

[4]Nuclear Data Inc., model 100.

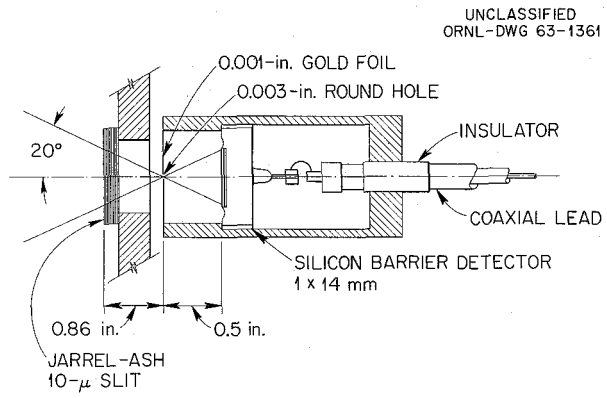

(*a*)

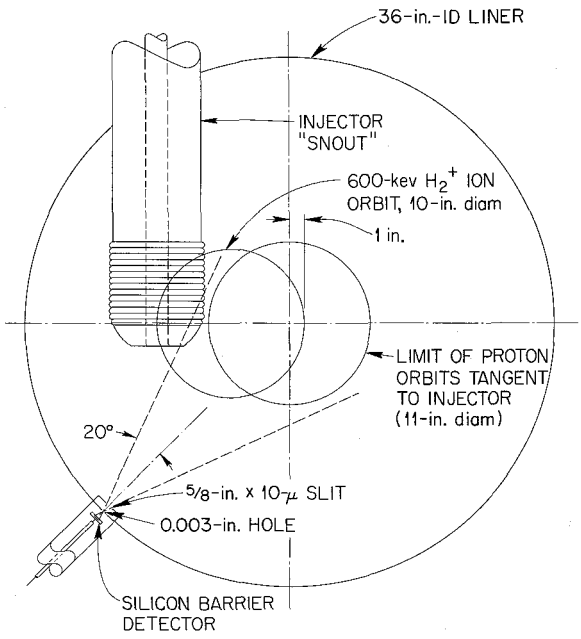

(*b*)

Fig. 2.3. (*a*) Section Through Fast Neutral-Particle Energy Analyzer; the Slit Assembly Used Was a Jarrel-Ash 82000 Optical Spectrometer Slit; the Silicon Barrier Detector Was an ORTEC No. 14A-25; (*b*) Section Through DCX-2, Showing Vertical Viewing Angle of Silicon Barrier Detector in Port 4-4.

as large as possible so as not to discriminate against the more energetic trapped particles, in the likely event that relatively they spend more time near the surface of the plasma (defined by the injector radius). With this arrangement a small percentage of what appear to be dissociation neutrals from precessed orbits is seen. Figure 2.4*a* shows a typical pulse-height distribution seen in the detector in port 4-4, and Fig. 2.4*b* shows the spectrum of trapped particles obtained from gas dissociation resulting from correction of the spectrum for the charge-exchange rate as a function of energy. As a result of the collimation in the horizontal plane, particles striking the detector must leave the plasma perpendicular to the axis with a pitch angle of less than ±0.2°. An attempt was made to determine whether this collimation also selected particles with nearly unmodified energy, since the molecular beam is expected to have a small pitch angle in spiraling down the machine. The collimating assembly and detector were therefore rotated about their axis to various angles. At 90° they could see 40° horizontally and only ±0.2° in the vertical plane. The resulting spectrum is shown in Fig. 2.5*a*. The counting rate taken with the slit aligned vertically (Fig. 2.5*b*) is similar; so apparently scattering is sufficiently great that the restricted acceptance angles may not result in a greatly distorted view of the plasma.

UNCLASSIFIED
ORNL-DWG 63-1362(*a*)

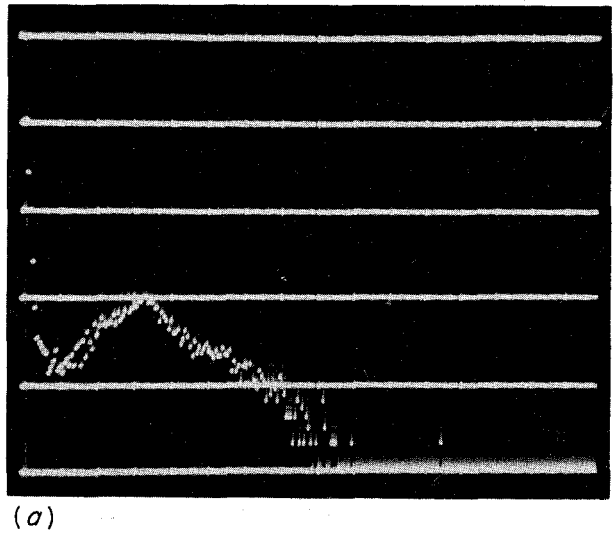

(*a*)

Fig. 2.4*a*. Typical Pulse-Height Spectrum from Fast Neutral-Particle Energy Analyzer in Port 4-4. Injection beam current is 25 ma, and the energy scale is approximately 3 kev per channel. Horizontal bars mark decades of total counts registered. The peak of the spectrum is at an energy of 150 kev, and the upper limit is at about 430 kev.

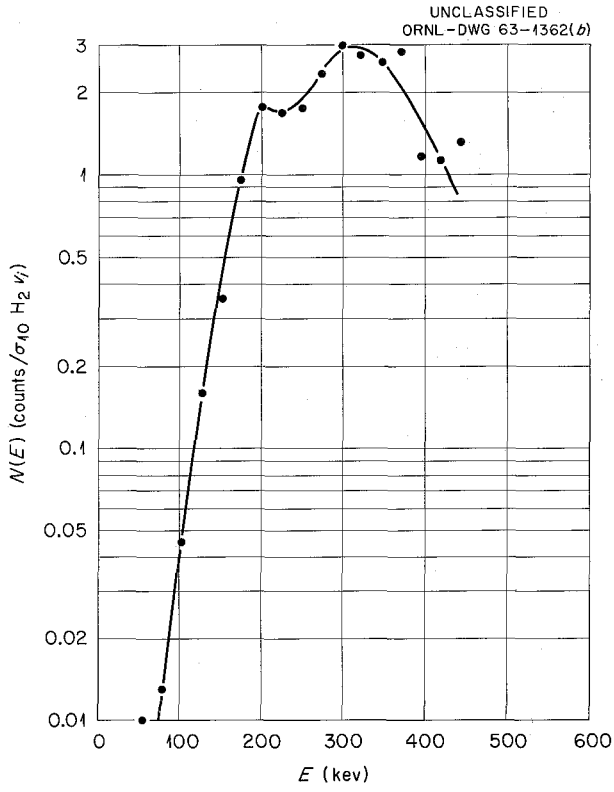

Fig. 2.4*b*. Spectrum of Trapped Particles Resulting from Correction of the Pulse-Height Distribution of Fig. 2.4*a* for the Charge-Exchange Rate as a Function of Energy. The satellite peak at 200 kev results from the presence of a small amount of H_3^+ in the injected beam.

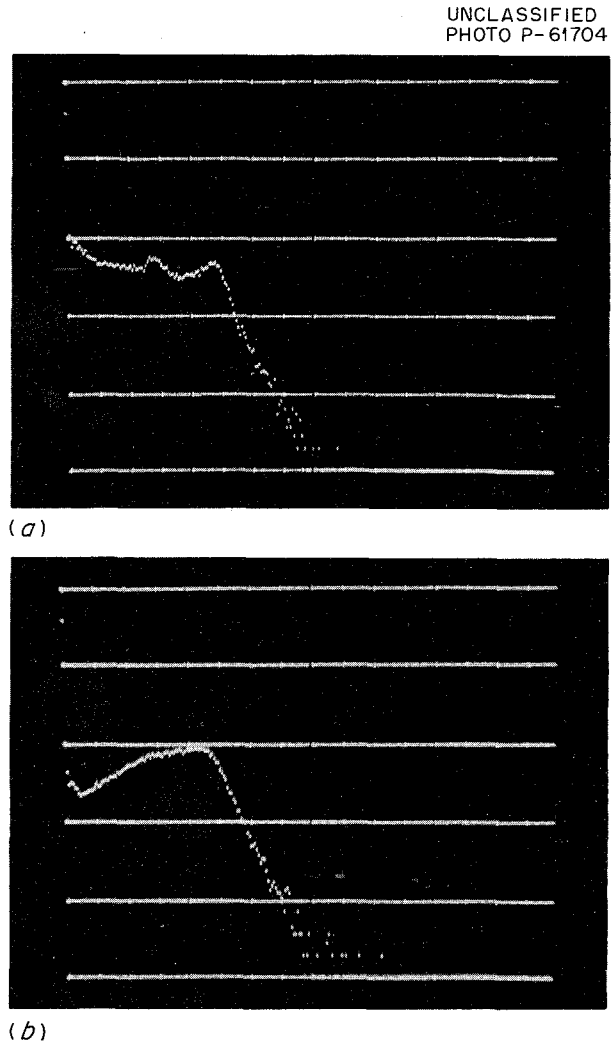

Fig. 2.5. (*a*) Pulse-Height Spectrum Found with the Analyzer Slit Horizontal (Parallel to Machine Axis); (*b*) Pulse-Height Spectrum Found with the Analyzer Slit Vertical (Perpendicular to Machine Axis). In these two spectra the energy zero was slightly suppressed.

One fact becomes obvious: the plasma particles are spread significantly in energy. The full width at half maximum of the main peak at 300 kev is 80 kev. The small satellite peak at 200 kev is connected with the presence of a small amount of H_3^+ in the beam. Experiments are under way in which a gating pulse is used to study the energy distribution during various intervals after the beam is turned on or off and will be reported in the future.

2.3 GRIDDED-PROBE MEASUREMENTS

Early measurements of current vs voltage on wires inserted into the plasma region radially and on axially located plates were of little value. It was found that the presence of a probe disturbed the plasma potential along lines of force passing through the probe. Apparently the electron lifetime in the machine is small compared with the time for cross-field diffusion over distances of the order of the dimensions of a probe. The plasma potential, therefore, adjusts itself locally to balance end losses against production rate.

The current of ions and electrons to an imaginary probe in the plasma would vary with probe voltage as shown in Fig. 2.6, if it is assumed that the probe does not disturb the distribution. The total current would be expected to vary as indicated by

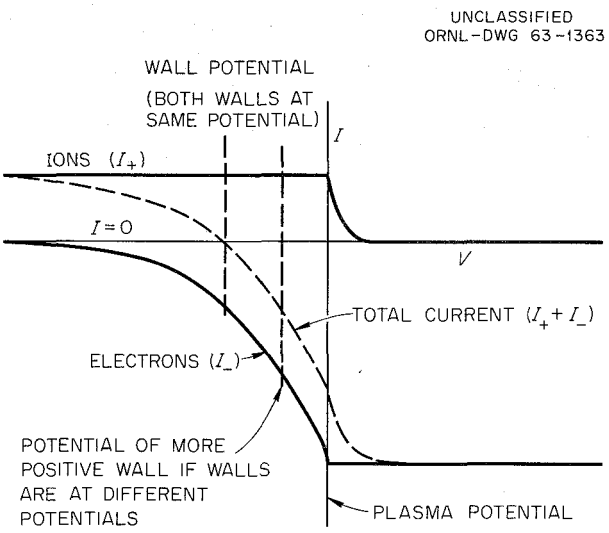

Fig. 2.6. Currents to an Imaginary Probe in a Plasma in Which Ions and Electrons Are Produced at the Same Rate.

the dotted curve. This curve is exponential with respect to voltage above and below the plasma potential, and its logarithm is a linear function of voltage, with slopes depending on the temperature of ions and electrons. The transition between electron temperature slope and ion temperature slope occurs at the plasma potential. When the probe is at this potential, it accepts all electrons and ions that are directed toward it. There is no electrostatic repulsion of either sign of particle. In an actual situation a wall or probe will determine the plasma potential. The plasma potential will then shift so that, with respect to the wall or probe, it is such that the electron current is equal to the ion current, since the production rates of electrons and slow ions are equal. If one surface which bounds a tube of flux is more positive than the other by a sufficient amount, it will receive essentially all the electron current but still only half the ion current. In this case the difference of potential between wall and plasma will shift so that the electron current received by this probe is twice as great as would be the case if both surfaces bounding the tube of flux were at the same potential. It may be seen that a simple wire probe will have a characteristic such as shown in Fig. 2.7. Since the probe now receives all the electrons from its tube of flux when it is very positive, the net current is equal to the positive ion current received when the probe was negative.

A gridded probe in which the collecting electrode is shielded from the plasma by a grid at wall potential can measure plasma characteristics without disturbing the potential of the plasma if the grid mesh is sufficiently fine. It is necessary that the reflected electrons diffuse during a small fraction of their lifetime far enough to cause their paths to intersect the grid. If the fraction of incident electrons that are reflected is small, this further reduces any probe effect upon the plasma. Electrons passing through the mesh of the grid will be collected if the potential of the collector permits or will be reflected and later will strike the grid. A second intermediate grid permits selection of the sign of particle which can reach the collector. Since only those particles with energy great enough to pass the grids can strike the collector, the current will be made up of portions of the curves shown in Fig. 2.8.

With a positive bias on the second grid sufficient to repel all ions, the electrons come through and appear at the collector with an unchanged energy distribution relative to the collector voltage. Likewise, if the second grid is made sufficiently negative, the ion portion of the characteristic in Fig. 2.8 appears, and the plasma potential can be determined at a glance by observation of the value of the potential at which the ion current begins to decrease. These results are modified by secondary emission – from the collector when it is less positive than G_2, and from G_2 when the collector is more positive. The effect is a downward step

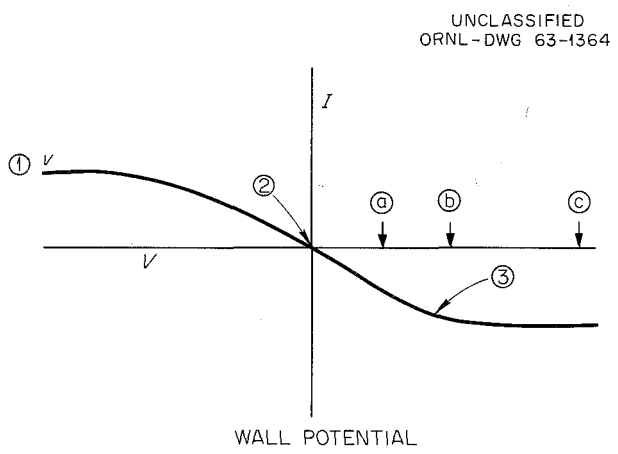

Fig. 2.7. Current to a Bare Probe as a Function of Voltage. The letters *a*, *b*, and *c* indicate the value of plasma potential corresponding to voltages 1, 2, and 3 respectively.

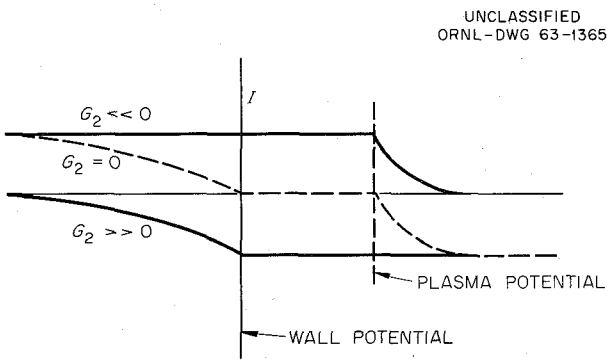

Fig. 2.8. Predicted Currents to a Gridded Probe with the Potential of Grid 2 (G_2) Positive, Zero, and Negative.

change in the proportionality factor between ion current and net collector current.

Two types of gridded probes have been used on DCX-2. The first type is shown in Fig. 2.9*a*. It consists of an array of three planar grids and a collector. The third grid is for electron suppression. It was connected to the collector by a 20-v bias battery during all measurements. Two of these probes have been used, inserted on axis from the ends of the machine. The second type of probe consists of electrodes from a type 4-65A vacuum tube. The arrangement is shown in Fig. 2.9*b* and the circuit diagram in Fig. 2.9*c*. A number of these probes are inserted radially at various ports into the central plasma region. The electrodes are coated with camphor black to minimize secondary electron emission.

Some of the probe characteristics obtained in DCX-2 under various conditions are shown in Fig. 2.10. Figures 2.10*a* and *b* are axial probe characteristics. Figure 2.10*a* shows the ion signals with the electrons suppressed. Despite the noisiness of the ion currents, the points of downward break can be seen. These vary from about +150 to +450 v, corresponding to plasma potential fluctuations between these values. The beam was being keyed with a 50% duty cycle, and the low slanting lines below, gradually merging into the horizontal axis, are the responses seen after the beam was turned off. Figure 2.10*b* is the response seen with cold ions suppressed. The electron current appears more noisy than the ion current, but despite the noisiness, an experimental tail having various slopes may be seen leading to the left. Careful examination of such photographs has shown a variation of these slopes of almost a factor of 3. The smoother traces near the axis also result from the period after beam turnoff.

The remainder of the pictures in Fig. 2.10 were obtained with radial probes. These probes show very low plasma potentials and low electron temperatures since they can be inserted only a short distance into the plasma region. Figure 2.10*c* shows the response with the cold ions suppressed at about 11.5 in. from the axis. Figure 2.10*d* was taken at 8.5 in. from the axis. The zero crossing was displaced about 0.5 cm because of a +100-v potential on the outer grid of the probe. Note the rather considerable current and large pulses of fast ions. Figure 2.10*e*, a similar picture with the probe at 6.5 in. from the center of the machine, shows a larger amount of fast ions and pulses. The two remaining pictures, *f* and *g*, were taken at different times while the lithium arc backstream was being used in the machine. These curves were obtained for conditions similar to those for *e*. Note the absence of fast-ion pulses, although some steady fast-ion current can be seen. Note also the steep break of the electron curve, indicating very low electron temperatures, and the considerably reduced noise in the electron current.

High-speed motion pictures were made of the probe characteristics. Individual traces have been analyzed for electron temperature. In most cases the electron repulsion curve has an exponential shape within the limits of accuracy of measurement, and typical values correspond to electron temperatures of 50 to 100 ev. The ion curves give values of plasma potential from 140 to 540 ev and ion energies from 45 to 130 ev. It is perhaps somewhat remarkable that the observed electron tail corresponds to a Maxwellian energy distribution. The energy equilibration time, assuming an electron density of $10^8/cm^3$, is about 0.1 sec, and the density is expected to be within an order of magnitude of this value. The lifetime of an electron in the plasma is expected to be very much shorter. Also, the electron temperature is observed to rise and fall in intervals at least as short as a few milliseconds after the start and stop of the beam. The presence of cooperative phenomena is clearly indicated.

It was found that when a bias is applied to G_2 to suppress ions, current pulses in the ion direction still appear at the collector. These pulses occur even at the maximum suppressor voltage which can be applied (about 2000 v) and apparently

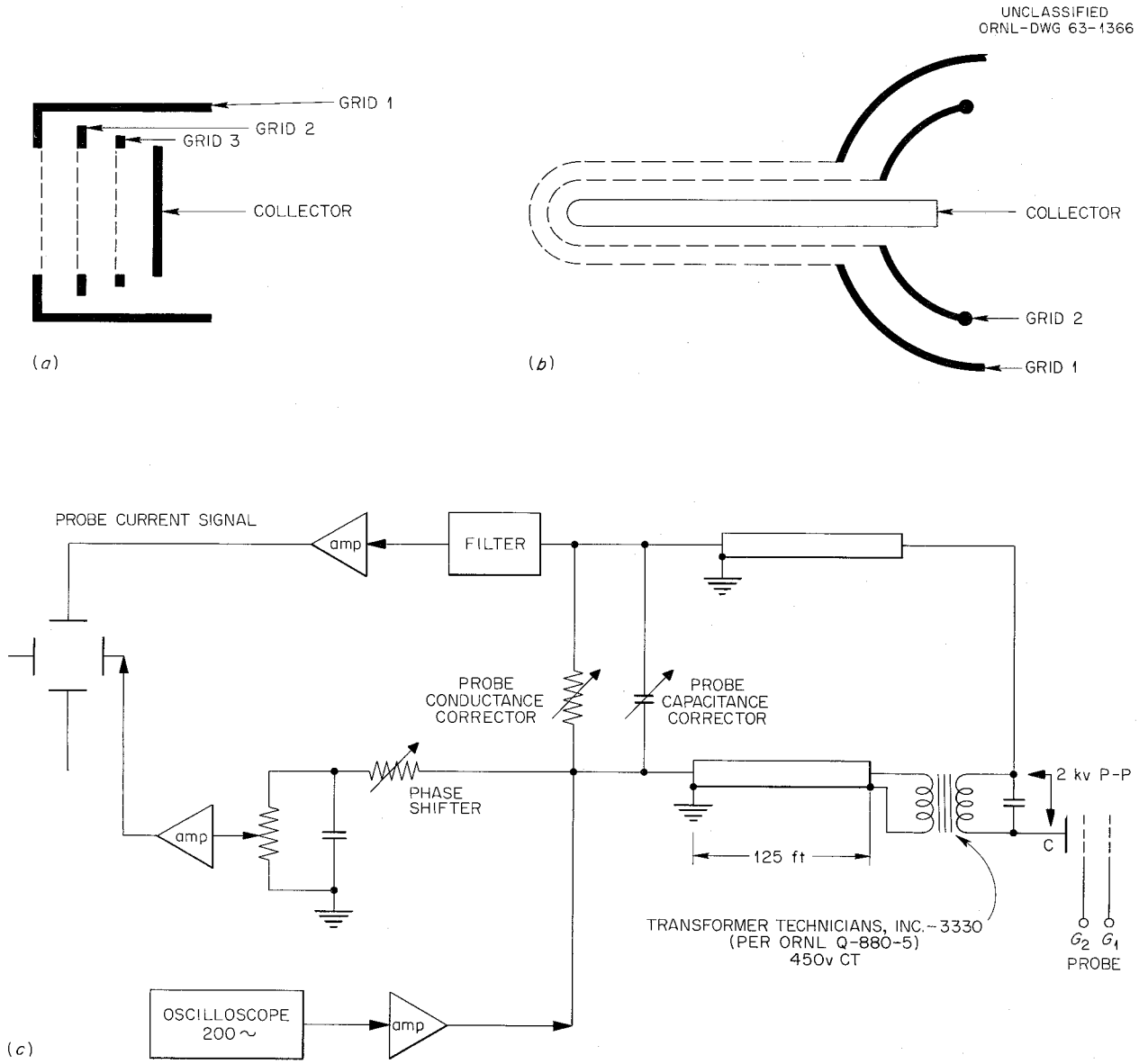

Fig. 2.9. (*a*) **Axial Gridded Probe;** (*b*) **Radial Gridded Probe;** (*c*) **Circuit for Obtaining Langmuir Probe Characteristics.**

UNCLASSIFIED
PHOTO P-61705 (PART 1)

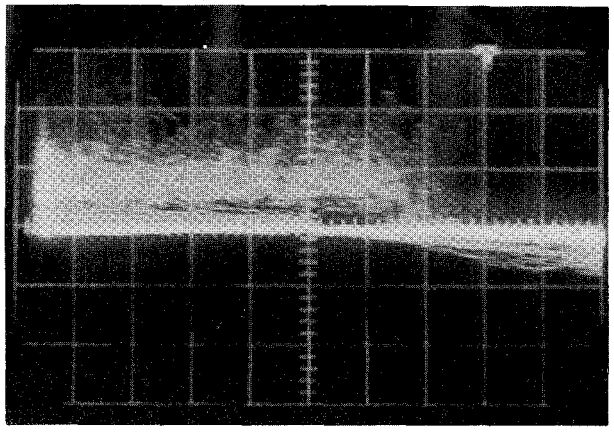

(*a*) AXIAL PROBE WITH ELECTRONS SUPPRESSED. VERTICAL SENSITIVITY 0.1 ma/cm, GRID G_2 VOLTAGE MINUS 1050 volts. INJECTION BEAM CURRENT 50 ma KEYED AT 10 cps WITH 50% DUTY CYCLE.

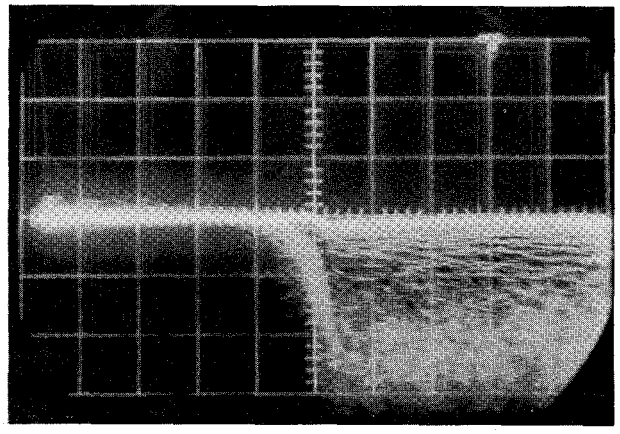

(*b*) AXIAL PROBE WITH IONS SUPPRESSED. VERTICAL SENSITIVITY 0.1 ma/cm, GRID G_2 VOLTAGE PLUS 1050 volts.

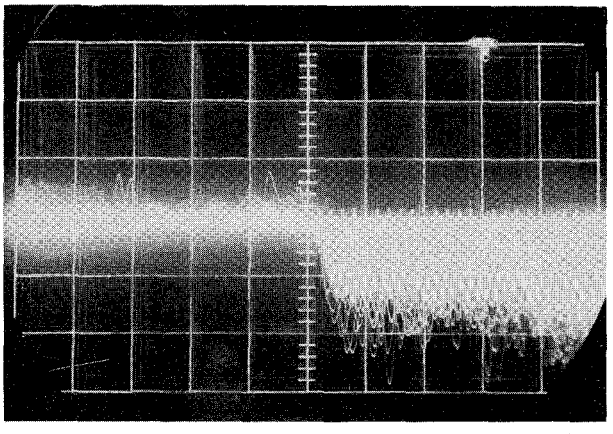

(*c*) RADIAL PROBE WITH IONS SUPPRESSED. VERTICAL SENSITIVITY 0.2 ma/cm, GRID G_2 VOLTAGE PLUS 850 volts. PROBE TIP 11.5 in. FROM DCX-2 AXIS.

Fig. 2.10. Gridded-Probe Characteristics in DCX-2 Plasmas. Sinusoidal sweep voltage at the collector is 200 cps with ±1000 v peak value.

UNCLASSIFIED
PHOTO P-61705 (PART 2)

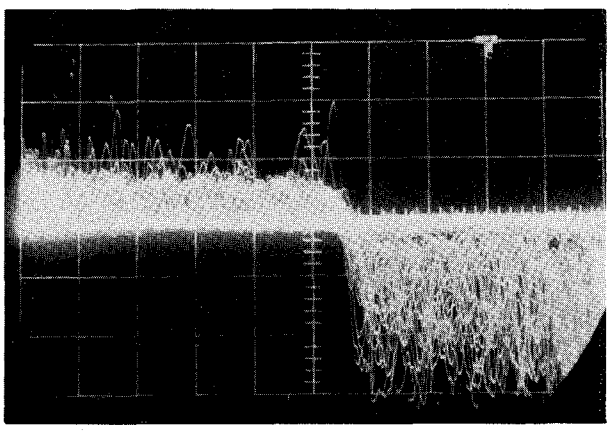

(*d*) RADIAL PROBE WITH IONS SUPPRESSED. VERTICAL SENSITIVITY 0.05 ma/cm, GRID G_2 VOLTAGE PLUS 850 volts. PROBE TIP 8.5 in. FROM THE AXIS. IN THIS CASE A POSITIVE VOLTAGE OF 100 volts WAS APPLIED TO GRID G_1 PRODUCING AN INCREASE OF PLASMA POTENTIAL RESULTING IN A 0.05-cm DEFLECTION TO THE RIGHT.

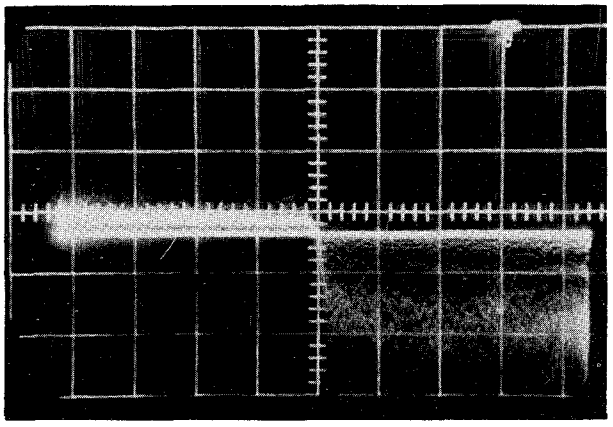

(*f*) RADIAL PROBE CHARACTERISTIC WITH IONS SUPPRESSED IN PRESENCE OF LITHIUM ARC BACKSTREAM. INJECTION BEAM CURRENT 25 ma. VERTICAL SENSITIVITY 0.2 ma/cm, GRID G_2 VOLTAGE PLUS 600 volts. PROBE TIP 7.5 in. FROM AXIS.

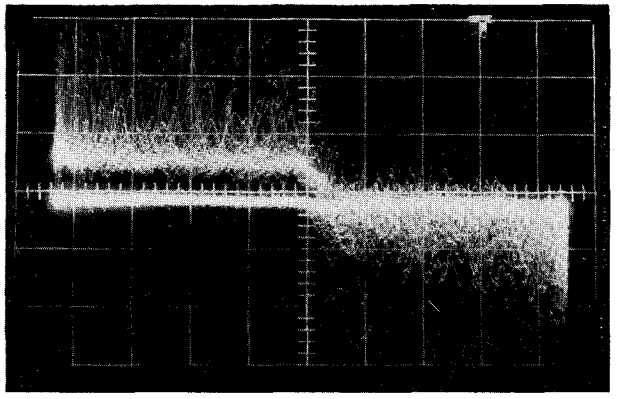

(*e*) RADIAL PROBE WITH IONS SUPPRESSED. VERTICAL SENSITIVITY 0.05 ma/cm, GRID G_2 VOLTAGE PLUS 850 volts. PROBE TIP 6.5 in. FROM MACHINE AXIS.

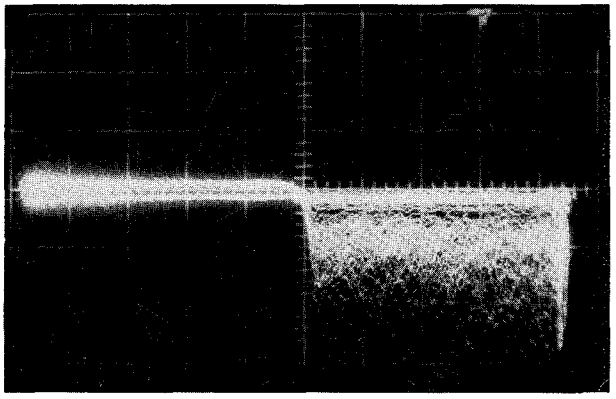

(*g*) RADIAL PROBE WITH IONS SUPPRESSED IN PRESENCE OF LITHIUM ARC BACKSTREAM. INJECTION BEAM CURRENT 50 ma. VERTICAL SENSITIVITY 0.5 ma/cm, GRID G_2 VOLTAGE PLUS 1500 volts. PROBE TIP 7 in. FROM AXIS. PLASMA REGION PRESSURE 7.5×10^{-7} mm Hg.

Fig. 2.10 (continued). Gridded-Probe Characteristics in DCX-2 Plasmas. Sinusoidal sweep voltage at the collector is 200 cps with ±1000 v peak value.

are produced by trapped energetic ions. These pulses represent a loss process for the fast ions; however, it is not easy to assess their total contribution to the ion loss rate, because some shielding effect of one probe on another has been noted. That is, the pulses of fast ions seen are considerably reduced by the insertion of another probe at the same azimuthal position. The snout, of course, is also a very large probe at the expected plasma edge, so that there seems to be no straightforward method of determining whether the fast-ion pulses account for a major fraction of the plasma loss. The pulses are found out to a radius of 10 in., which is much greater than the expected 6-in. radius defined by the injection snout. The frequency of occurrence at 10 in. with an injected beam current of 10 to 15 ma is about 4000 pulses/sec, with an average amplitude of 0.8×10^{-9} amp and an average duration of 40 μsec. The frequency and amplitude increased rapidly with decreasing radius. This current is somewhat in error due to secondary emission by these energetic ions, perhaps as much as a factor of 2. A search was made for time correlation between the fast-ion pulses of various probes and between fast-ion pulses and the rf pulses also seen on the outer grids of these probes. Detailed correlation was not found, although a sort of correlation does exist.

2.4 RADIO-FREQUENCY STUDIES

Radio-frequency signals at the proton-cyclotron frequency and its harmonics are received at the detectors and under some conditions have a periodically varying amplitude. The period typically is about 200 μsec. Under these conditions it was found that this intensity variation is in phase on all probes in the machine; also, there is time correlation with probes biased to reject everything except fast ions. Under other conditions of operation, these regular fluctuations in rf intensity do not occur. Under these conditions there is still a correlation between rf intensity in various parts of the machine, but only a gross correlation between the ion bursts and rf activity.

The study of the phase relationship between rf signals at various places in the plasma region was continued.[5] In both the Z and θ directions the phase between signals fluctuated with time. The signals from two probes were placed on the X and Y deflection plates on an oscilloscope and observed at various times during a beam pulse by intensifying the scope only for certain intervals with respect to the start of the pulse. When the observation interval was rather long (100 μsec to 1 msec), there was a good average value of the relative phase. When the observation interval was short ($\sim$1 μsec), it was found that for large amplitudes of signals the phase was generally well defined at each pulse, but varied from pulse to pulse. Time exposures of the X-Y pattern show a roughly constant value of the ratio of the rf signals of maximum amplitude (Fig. 2.11). Attempts were made to exhibit the detailed time correlation apparently shown by this result; however, no exact correlation could be seen. Figure 2.12 is a typical example, although longer time intervals do show more correlation (see Fig. 2.13.) This general correspondence in amplitude and phase, despite the lack of detailed time correlations, reflects a real time correlation. Study of the X-Y correlations indicates that there is no plasma rotation at periods below the ion-cyclotron frequency, confirming our observations in the previous report.

[5] *Thermonuclear Div. Semiann. Progr. Rept. Oct. 31, 1962*, ORNL-3392, p 23.

UNCLASSIFIED
PHOTO P-61706

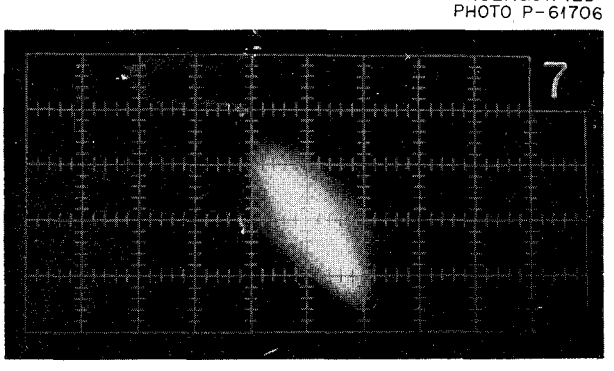

Fig. 2.11. Electrostatic Pickup from Probes in Ports 4-8 and 5-8 Displayed on the X and Y Deflection Plates of an Oscilloscope. Bandwidth in both channels is about 40 Mc. The apparent 180° phase shift is instrumental.

UNCLASSIFIED
PHOTO P-61707

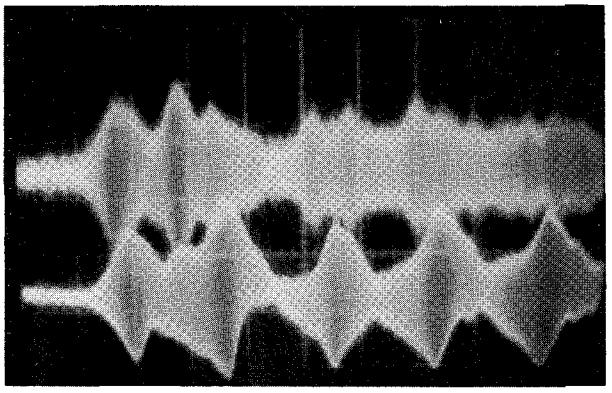

Fig. 2.12. Electrostatic Signals from Radial Probes in Ports 4-3 and 4-7. The beam was turned on at the beginning of the sweep and the sweep speed was 100 μsec/cm.

UNCLASSIFIED
PHOTO P-61708

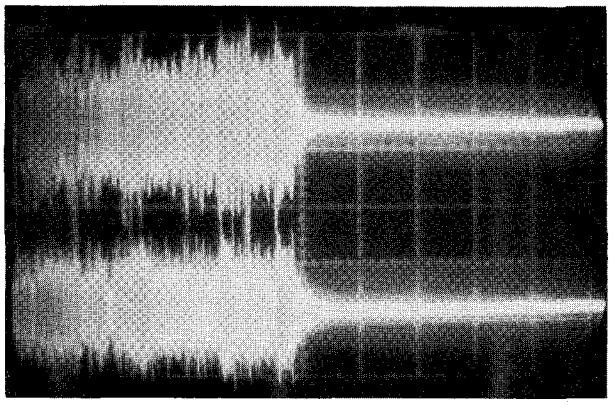

Fig. 2.13. Electrostatic Signals from Radial Probes in Ports 4-7 and 4-5.

2.5 END ELECTRODES

When it was found that bursts of electrons were coming out of the machine on axis, it was thought that the stability of the plasma might be improved by providing end electrodes which were at ground potential for direct current but which could change potential momentarily with the arrival of a small charge. A positive potential on the ends, of 1 to 2 kv, apparently does decrease somewhat the loss rate of fast ions, but the special end plates showed no improvement over simple electrodes.

2.6 STABILIZING PLASMA EXPERIMENTS

The backstream plasma from a vacuum lithium arc[6] was permitted to run through the mirrors in DCX-2 and produce a plasma in the region where the energetic protons are trapped. The density in the plasma column was expected to be less than $10^{11}/cm^3$, but was not measured. A cooled shutter could be inserted past the cathode as shown in Fig. 2.1 to stop essentially all of the backstream plasma. The arc was run at currents ranging from 50 to 100 amp in the voltage range 150 to 250 v. The color of the plasma in the region between the mirrors was green, indicating the substantial absence of neutral lithium in the plasma.

The intent of the experiment was to determine if a relatively cold, high-density plasma improves the stability of the trapped protons. Several foil detectors were able to view the plasma, although in the initial experiments there were none in position 4-1 which might have given us additional information concerning the dissociation from the plasma column. Nevertheless, the densities obtained in the presence of the backstream plasma are shown in Table 2.2. One striking fact, observed under some conditions, was the substantial reduction in burst pulses seen on a gridded probe inserted radially. By moving the shutter, part of the backstreaming plasma could be interrupted while the burst pulses were being monitored. An optimum could be seen in the burst frequency, with no apparent variations of the foil-detector signals (Fig. 2.14). The energy distribution of the neutral particles leaving the plasma was measured, and the trapped proton-energy distribution was extracted from them. The energy spread was only slightly modified from that seen with no backstream plasma.

During two short runs, the full lithium arc was run through both mirrors. This arc, run at approximately 100 amp, is expected to have a density approximately 10^{13} to $10^{14}/cm^3$ in the region of the injected beam. Foil-detector signals were obtained, and the densities are given in Table 2.2. The energy analysis gave the spectrum shown in Fig. 2.15. In view of the large energy spread, it is questionable that a single lifetime should be ascribed to the trapped protons.

[6] *Thermonuclear Div. Progr. Rept. Oct. 31, 1961,* ORNL-3239, p 49.

UNCLASSIFIED
PHOTO P-61721

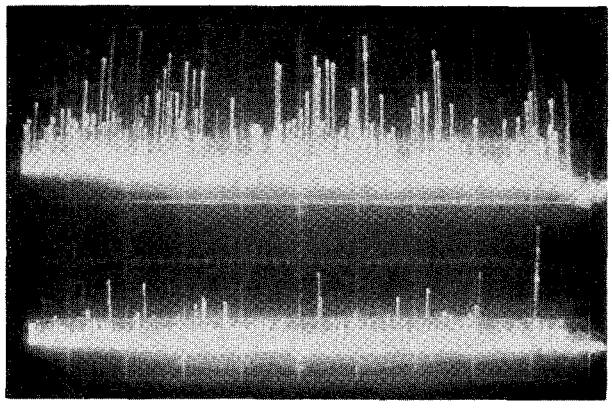

(*a*) FULL BACKSTREAM

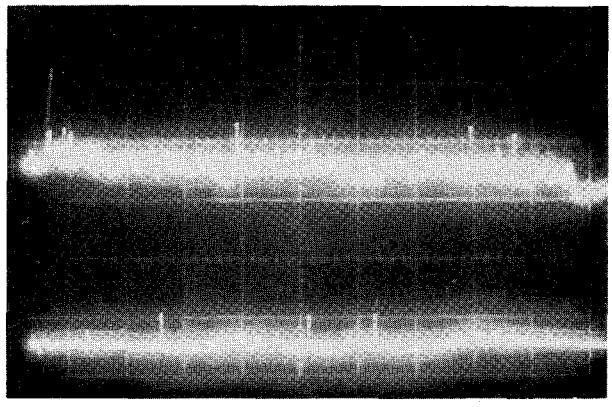

(*b*) SHUTTER INSERTED FOR OPTIMUM REDUCTION OF BURSTS

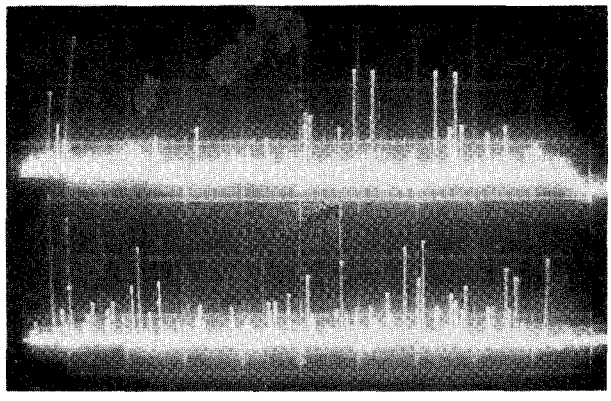

(*c*) SHUTTER FULLY INSERTED—NO BACKSTREAM

Fig. 2.14. Effect of Arc Backstream on Fast-Ion Bursts Received by Radial Gridded Probes. Sweep speed is 0.5 msec/cm. Upper trace was obtained at position 4-5, lower at 7-7. Beam current was 75 ma with 40 ma into the plasma region.

UNCLASSIFIED
ORNL-DWG 63-1367

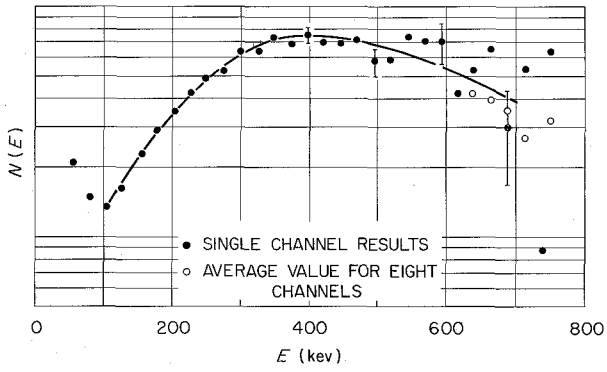

Fig. 2.15. Trapped-Proton-Energy Distribution as Derived from the Pulse-Height Distribution of Neutrals Striking a Silicon Barrier Detector in Port 4-4 with Full Lithium Arc. Beam current was 30 ma.

UNCLASSIFIED
PHOTO P-61709

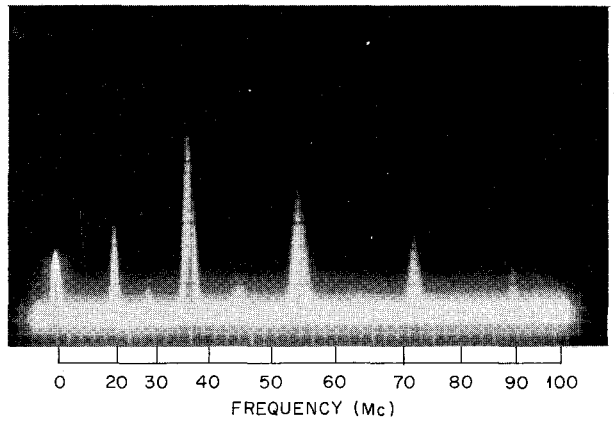

(*a*) TYPICAL SPECTRUM WITH NO ELECTRON BEAM

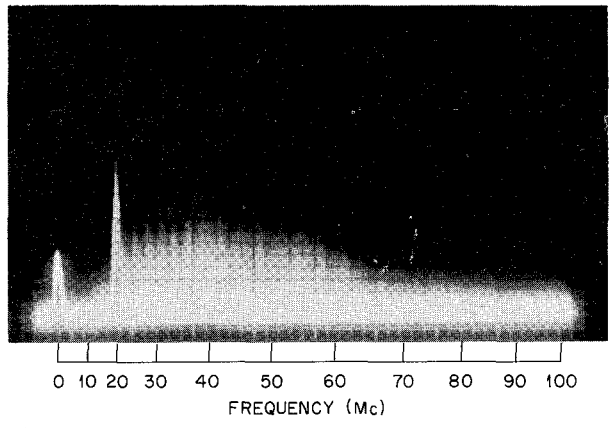

(*b*) EFFECT OF AXIAL ELECTRON BEAM OF 3.2 amp AT 2 kv

Fig. 2.16. Radio-Frequency Spectrum as Received on an Electrostatic Probe in the Plasma Region, Port 5-3.

Table 2.2. Densities, Lifetimes, and Ratio I_{0cx}/I_{total} for Various Beam Currents into DCX-2 with Backstream or Main Plasma from Vacuum Lithium Arc

Detector Position	n	τ (msec)	I_{0cx}/I_{total}
Lithium Arc Backstream; I_{beam} = 10 ma			
1-8	5.8×10^6	8.5	0.19
2-8	1.5×10^7	6.9	0.14
4-8	5.6×10^7	8–10	0.19
6-8	1.4×10^7	6.9	0.23
7-8	1.0×10^8	11	0.15
Lithium Arc Backstream; I_{beam} = 50 ma			
1-8	7.1×10^6	6.9	0.10
2-8	2.1×10^7	6.3	0.065
4-8	6.1×10^7	6.8	0.022
6-8	1.9×10^7	9.5	0.065
7-8	2.6×10^8	10.8	0.13
Lithium Arc Backstream; I_{beam} = 75 ma			
1-8	1.6×10^7	10.0	0.12
2-8	2.2×10^7	5.6	0.038
4-8	5.9×10^7	6.0	0.038
6-8	2.4×10^7	6.3	0.105
7-8	2.5×10^8	10.0	0.11
Full Lithium Arc; I_{beam} = 12 ma			
1-8	2.6×10^7	0.85	
	1.4×10^7	5.3	
2-8	2.9×10^8	4.8	
4-8	1.8×10^8	2.7	
6-8	5.2×10^7	1.0	
	3.5×10^7	4.4	
7-8	4.3×10^7	1.2	

An intense electron beam has also been allowed to pass through the mirrors of DCX-2 into the trapping region. Steady electron-beam currents as high as 5 amp at 3 kv from a thin ring filament, 3.5 in. in diameter, were produced. The beam was run space-charge-limited, since attempts at emission limiting to obtain higher electron energies resulted in discharges and nonsymmetric beams. Radio-frequency spectra, foil-detector signals, and energy analyses were obtained. Preliminary results showed a very large energy spread of the trapped particles and a density of $\sim 10^7$ ions/cm^3. Radio-frequency spectra showed a wide distribution of relatively white noise, plus only the atomic ion-cyclotron fundamental (see Fig. 2.16).

2.7 HIGH-SPEED CURRENT AMPLIFIER

Until recently, all the neutral-particle-detector signals were amplified by a modified Philbrick model P-2 operational amplifier. The modification consisted of the addition of a complementary emitter-follower output stage to permit driving a line to ±10 v. These amplifiers have a rise time too great to permit observation of the faster features of the neutral-particle-detector signals. At a sensitivity of 10^{-7} amp/v, the rise time is 200 μsec and the rms noise is about 10^{-10} amp. A new amplifier has been developed to operate in the range of currents found in the detectors in DCX-2. It normally has a fixed gain of 10^{-7} amp/v and will drive a 91-ohm line to ±1 v. The rise time is slightly better than 1 μsec, and the rms noise corresponds to a signal of about 2×10^{-10} amp. It uses two 4-v mercury cells and has a current drain of 3.8 ma. The amplifier is designed to fit into a $2\frac{1}{8}$-in.-diam probe housing and plugs into a socket directly behind the foil neutral-particle detectors. Figure 2.17 shows the mechanical arrangement, and Fig. 2.18 is the circuit diagram.

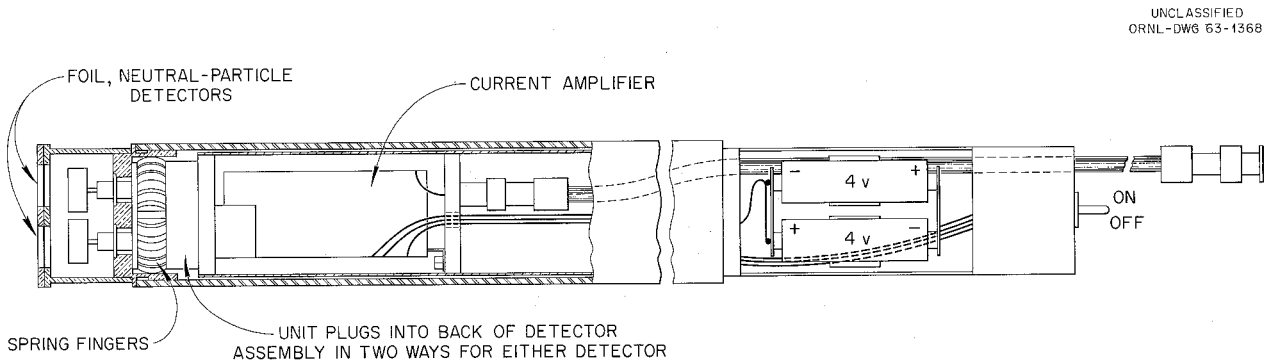

Fig. 2.17. Mechanical Arrangement of Neutral-Particle Detector and Fast-Current Amplifier.

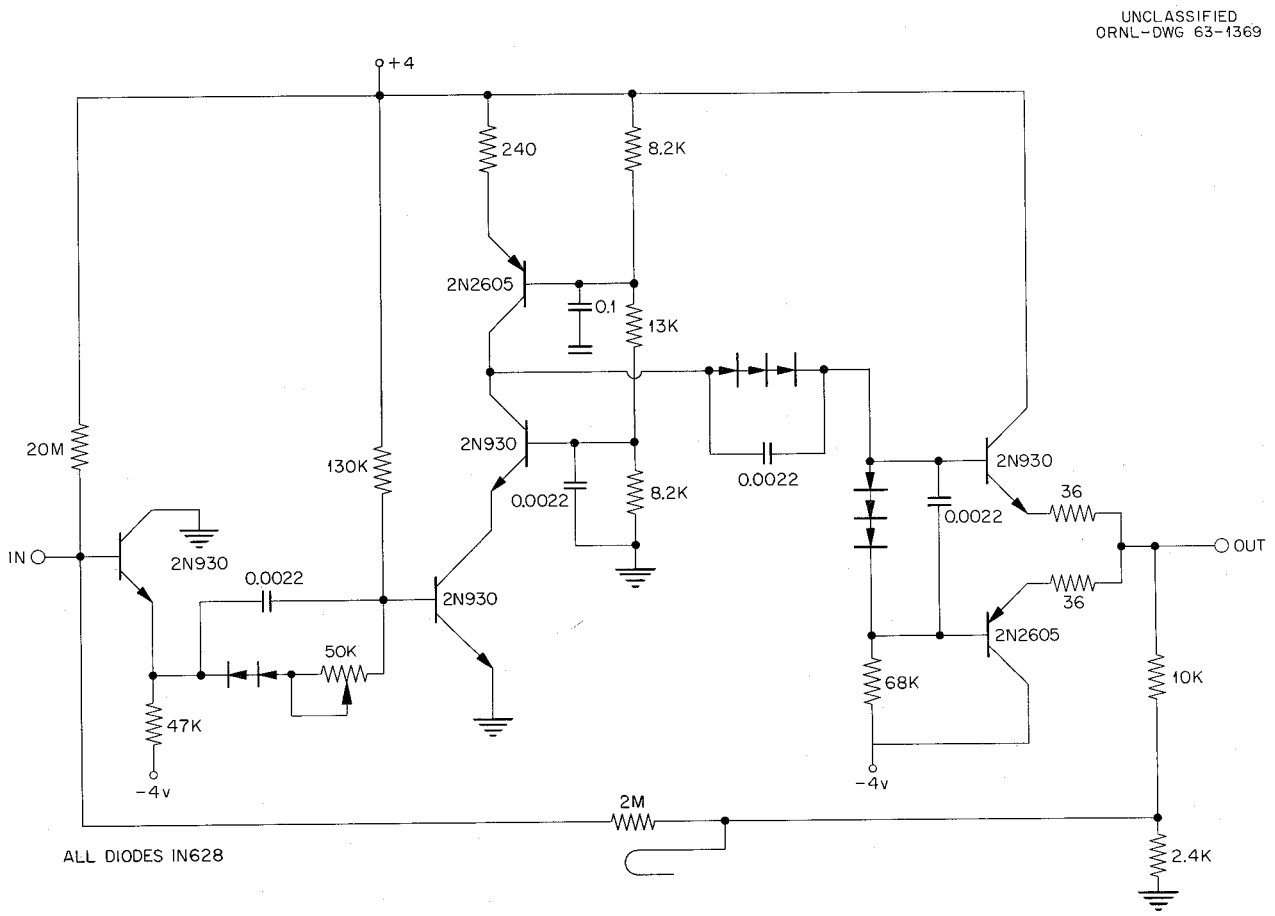

Fig. 2.18. Circuit Diagram of Fast-Current Amplifier.

3. Plasma Physics

3.1 INVESTIGATION OF THE ELECTRON-CYCLOTRON PLASMA IN THE PHYSICS TEST FACILITY (PTF)

W. B. Ard
M. C. Becker
R. A. Dandl
H. O. Eason
A. C. England
R. J. Kerr

3.1.1 Introduction

During the period of this report, further investigations have been made on the electron-cyclotron plasma (ECP)[1-4] heated by the 5 kw, 10.6 gc (gigacycle) klystron power supply mentioned in the last semiannual report.[4] In particular, measurements have been made of 4- and 8-mm microwave noise, phase shifts with a 4-mm interferometer, neutral-beam transmission, plasma magnetic fields, visible-light emission, x-ray emission, neutron emission, and the current to multigrid probes. A study has been made of some of the effects of adding a high-Z impurity to the plasma. Also additional pumping speed was added, several new cavities were investigated, and several variations in microwave feed have been tried.

3.1.2 Neutrons

Further studies of the Coulomb-dissociation neutrons[4,5] from the ECP were made during microwave-power turnoffs in order to correlate the neutron and x-ray decay times. The interesting observation was made that after turnoff the neutron emission first increased before decaying. Figure 3.1 shows the neutron emission and hard-x-ray emission as a function of time at turnoff. It is observed that the neutron emission increases by a factor of 10 after power turnoff, while the x-ray emission shows a burst, a sharp drop, and then a rise. The x-ray-emission rise and the neutron-emission peaks both occur about 50 msec after turnoff, and both emissions have a characteristic decay time of $\sim$130 msec. Considerations of plasma-energy storage and ion temperature rule out all mechanisms for the neutron production after turnoff except Coulomb dissociation of deuterium ($e + d \rightarrow e + n + p$). The mechanism producing the neutrons after turnoff apparently involves an increase of the electron population over 2.22 Mev by a plasma-energy-exchange mechanism. This mechanism preferentially accelerates a small plasma-electron component at the expense of the large number of lower-energy electrons. The lifetime of neutrons in the room is measured in tens or hundreds of microseconds and does not represent a systematic error in the neutron-production lifetime measurements.

3.1.3 Parametric Studies with Power

Several studies have been made of the variation of a number of parameters with microwave power. The results of one study are given in Fig. 3.2, which shows the 8- and 4-mm microwave-noise amplitude, the Hall-probe signal, and the density as determined by the neutral beam.[2] The density as determined by the neutral beam appears to

[1] *Thermonuclear Div. Semiann. Progr. Rept. Jan. 31, 1961*, ORNL-3104, sec 3.1.

[2] *Thermonuclear Div. Progr. Rept. Oct. 31, 1961*, ORNL-3239, sec 3.1.

[3] *Thermonuclear Div. Semiann. Progr. Rept. Apr. 30, 1962*, ORNL-3315, sec 3.1.

[4] *Thermonuclear Div. Semiann. Progr. Rept. Oct. 31, 1962*, ORNL-3392, sec 3.1.

[5] W. B. Ard *et al.*, *Phys. Rev. Letters* **10**, 87 (1963).

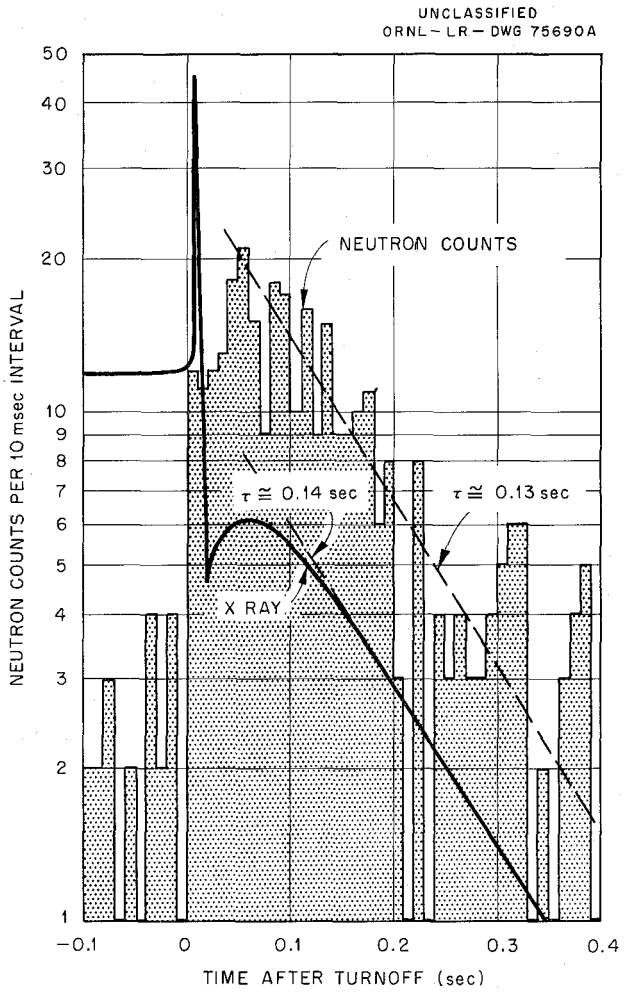

Fig. 3.1. Neutron Counting Rate and X-Ray Intensity from the PTF at Microwave-Power Turnoff. The hard-x-ray counter is shielded from the plasma by 2 in. of lead. Neutron counts from 25 turnoffs were summed for improved statistics.

vary linearly with applied microwave power. The signal from the Hall probe, which measures a quantity proportional to the plasma energy density, varies roughly as the square of the microwave power. Thus the temperature should appear to change linearly with power. Both 4- and 8-mm microwave-noise amplitudes appear to change proportionally to the square of the microwave power rather than to change linearly with power. This would indicate either that the microwave-noise amplitudes are not proportional to the plasma temperature or that the concept of temperature is not valid for this plasma. This parametric study involved microwave power levels only up to 2.5 kw.

The results of another study are shown in Fig. 3.3, which gives the 8-mm microwave-noise amplitude, the Hall-probe signal (labeled diamagnetism), the neutron emission rate, intensity of D_β (4861 A), and intensity of Cu I (3247 A). The D_β light is from the D_2 gas bled into the cavity, while the Cu I light is from copper sputtered from the cavity walls; both are viewed axially in a restricted region.

It is clear that a limit is reached at about the 3-kw level. At this point the three parameters dependent on plasma energy and/or density reach a plateau. The D_β light continues to increase, indicating an increasing amount of dissociation and excitation (from low-energy electrons) and recombination. The Cu I light continues to increase, indicating more sputtering. The Cu II light is not seen, which would imply that the sputtered copper is quickly ionized and forced out by the space potential.

3.1.4 Phase-Shift Measurements

A 4-mm microwave interferometer was constructed in order to measure the plasma density. Cast metallic-gold lenses were mounted on opposite sides of the cavity, with the usual microwave interferometer equipment external to the machine. The lenses produced a microwave beam less than 1 in. in diameter at the axis of

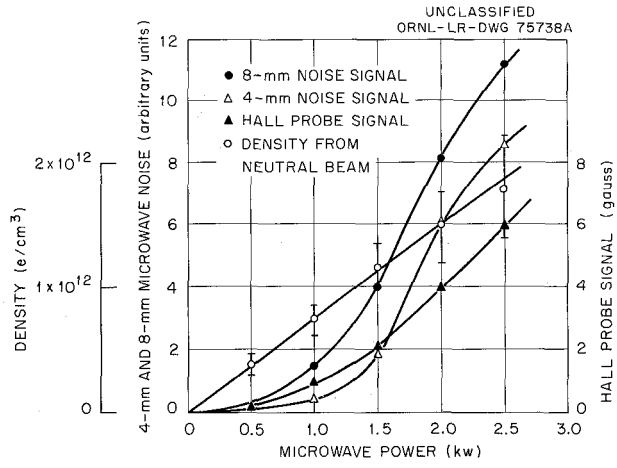

Fig. 3.2. Parametric Study of the Electron-Cyclotron Plasma with Microwave Power to 2.5 kw.

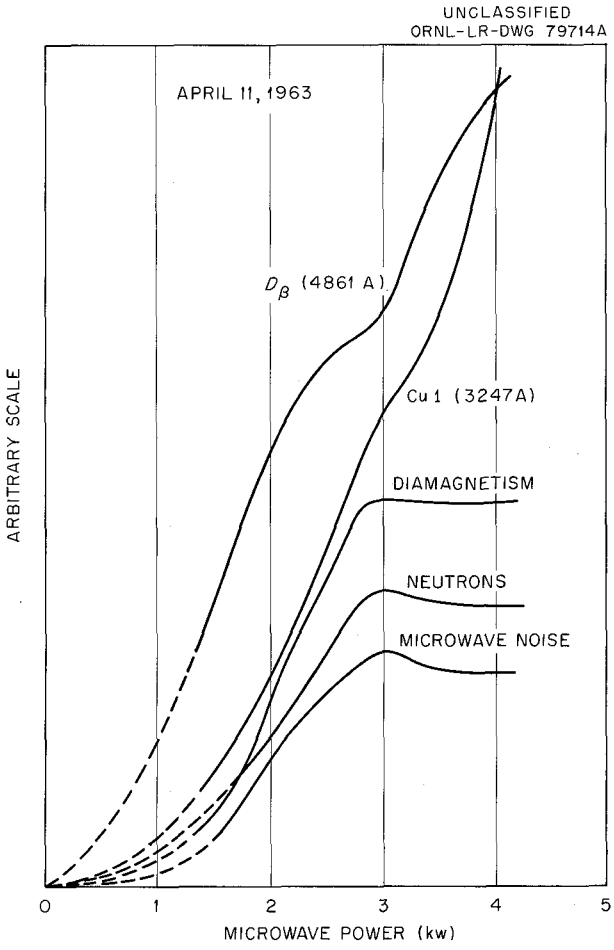

Fig. 3.3. Parametric Study of the Electron-Cyclotron Plasma with Microwave Power to 4 kw. The three parameters (diamagnetism, neutron counting rate, and microwave-noise amplitude) which depend on plasma density and/or temperature reach a plateau at 3 kw.

the cavity. The wave was launched with the microwave electric field parallel to the static magnetic field.

Measurements were made of phase shift and attenuation by nulling the interferometer with and without plasma. The time dependence of the phase shift and attenuation could also be measured.

The phase shift produced by the plasma increased as the heating power was increased, reaching about 30° at 3-kw power input. The attenuation increased at low power, reaching a maximum of about 2 db at 0.5 kw. Above 0.5 kw, the attenuation decreased with increasing power, and at 3 kw of heating power the transmitted 4-mm beam was about 1 db greater with plasma than without plasma. The increase in the transmitted beam might be due to the refraction of the beam in the plasma. Since the lenses produce a converging beam, the divergence produced by the plasma could produce a better or worse coupling between the lenses, depending on which way the lenses were out of focus.

The 30° phase shift would correspond to a density which is an order of magnitude less than that given by other measurements (e.g., the neutral-beam measurements). In addition, measurements of the phase-shift change with microwave power turnoff indicated decay times of ~ 100 μsec, which are smaller by a factor of 10^3 than other decay times (e.g., microwave noise, x rays, and neutrons). So far no explanation has been found for the apparent discrepancy between the interferometer measurements and the mass of other data.

The only other decay time which is shorter than 100 msec is that of the visible light. The light decays in a characteristic time of ~ 3 msec, longer than the interferometer measurement by more than a factor of 10. This 3-msec decay time has been measured both for visible light from a single spectral line (as measured by a spectrometer) and for visible light of all wavelengths (as measured by a photodiode and by a high-speed-framing camera).

3.1.5 End-Collector Measurements

Two Faraday-cup detectors were made with multiple grids to measure the properties of the plasma flowing out of the mirrors. The first detector had four grids and was fixed on the machine axis. The second detector had three grids and could be moved radially from the machine center line outside the mirror. Both detectors gave the same information and were subject to the same difficulties. Due to the flux of very-high-energy electrons escaping out of the mirror, both detectors were unable to completely bias out the electron component of the escaping plasma.

Measurements were made of the ion component by biasing the second grid negative to repel electrons. The first grid (facing the plasma) was grounded. The third grid was used with a

variable positive voltage, and the ion current to the collector was measured as a function of this voltage. From the measured curves an ion temperature between 10 and 15 ev could be inferred.

Figure 3.4 shows a number of parameters at microwave turnoff. The end-collector current is seen to take a sharp drop, but collects a highly erratic current for a few hundred milliseconds. As mentioned before, the x rays show a sharp drop, an increase, and then a decay with a time constant of ~130 msec. The 8-mm microwave noise often shows a sharp drop, as indicated in this figure, followed by a characteristic decay time of a few hundred milliseconds. The Hall-probe signal shows a two-component decay (discussed in detail in a previous semiannual report[3]) which may be indicative of a steady-state two-component plasma or may be indicative of the plasma-energy-exchange decay mechanism discussed above.

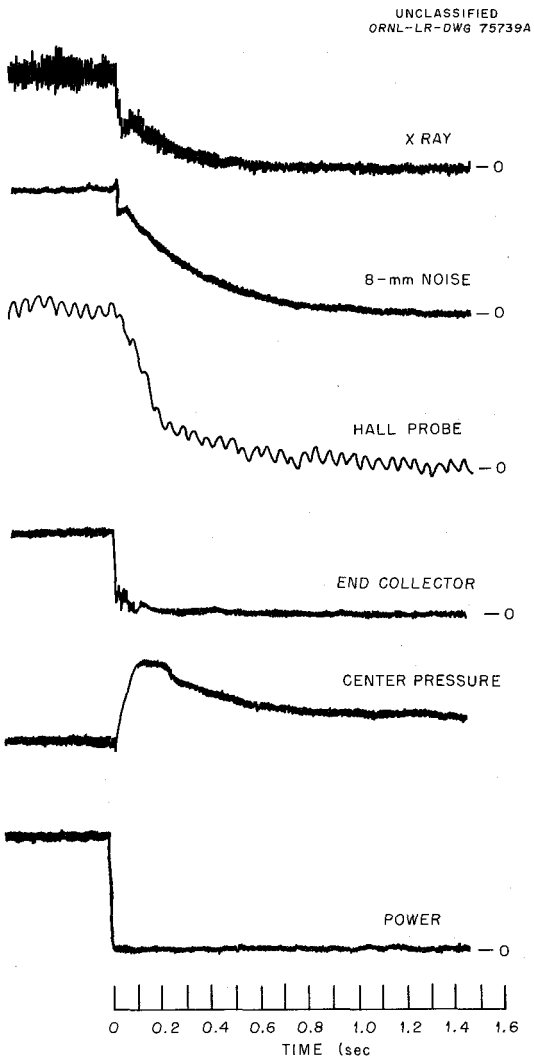

Fig. 3.4. A Number of Plasma Parameters at Microwave Turnoff.

3.1.6 Machine Modifications

Figure 3.5 shows the PTF after modifications for improved end pumping. Two 10-in. diffusion pumps were mounted on each end of the machine. This modification increased the gas-handling capacity by a factor of approximately 6 over the original capacity of a single 6-in. pump on each end. The purpose of this modification was to attempt to prevent contamination of the hot plasma by recycling of impurities sputtered from the walls.

Also, a new support for the lead x-ray shield was added. This new support can carry a 4-ton lead shield which has a minimum thickness of 1 in. and which completely surrounds the machine.

3.1.7 Parametric Study with Xenon Impurities

In an attempt to ascertain the effect of high-Z impurities on the plasma, the PTF was operated with a combination of D_2 and xenon gas. A parametric study was made of the effects of varying the xenon concentration. Figures 3.6 and 3.7 show the relative variations of the following quantities with increasing xenon concentration: amount of neutral copper in the plasma [intensity of the Cu I (3247 A) line], amount of ionized xenon in the plasma [intensity of Xe II (4844 A)], neutron emission from Coulomb dissociation [counting rate of an He^3 counter], decay time of 8-mm microwave noise, decay time of soft x rays [decay time of dc current from a phototube viewing a scintillator], 8-mm microwave-noise amplitude, x-ray intensity [steady-state current from a phototube viewing a scintillator], and intensity of Xe $K\alpha$ x rays [counting rate of photomultiplier-scintillator x-ray detector with a single-channel pulse-height selector set for ~30 kev].

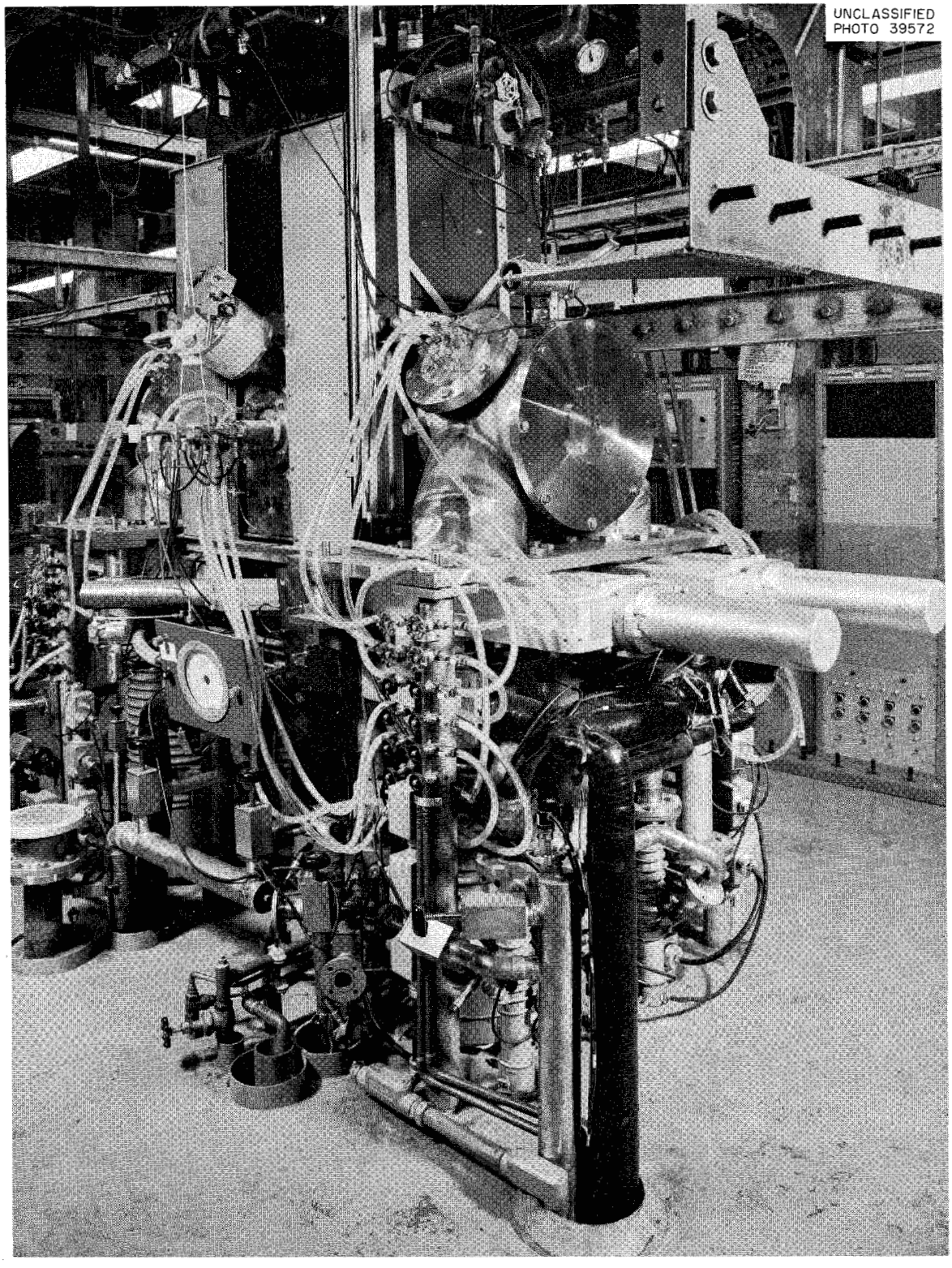

Fig. 3.5. The PTF After Modification for Improved Pumping.

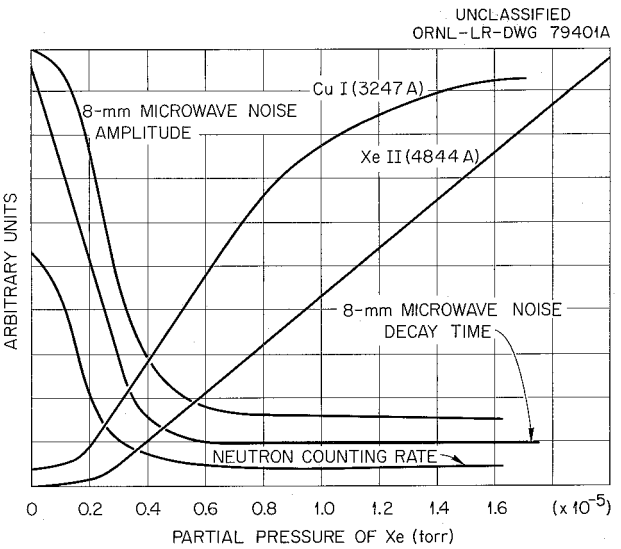

Fig. 3.6. Variation of a Number of Parameters with Xenon Pressure.

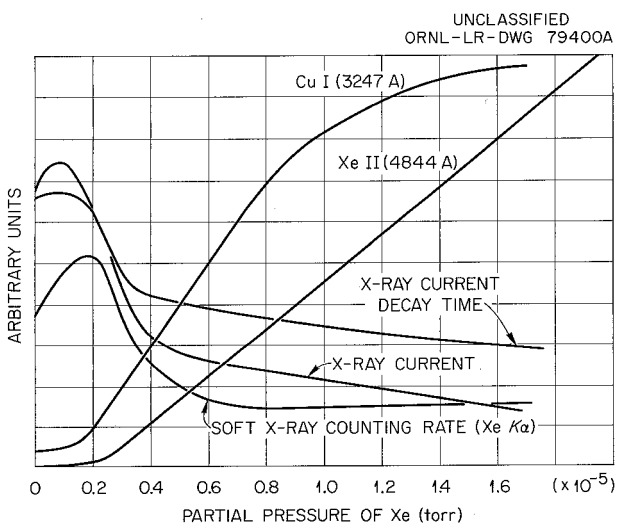

Fig. 3.7. Variation of a Number of Parameters with Xenon Pressure.

From the figures several conclusions may be drawn: (1) the amount of copper sputtered from the walls strongly depends on the partial pressure of xenon, (2) the neutron emission is reduced to near background when the partial pressure of xenon reads 5×10^{-6} torr, (3) the 8-mm microwave-noise amplitude and decay time are reduced by a factor of ~ 6 at a xenon pressure of 5×10^{-6} torr, (4) the Xe $K\alpha$ x-ray counting rate first rises and then drops as the xenon pressure is raised, indicating first a rise in the amount of xenon in the plasma and then a decrease in the number of hot electrons available for producing Xe $K\alpha$ excitation.

To summarize from the figures, it is clear that the presence of xenon strongly reduces the mean electron energy and the number of relativistic electrons.

3.1.8 Pinhole-Camera X-Ray Photographs

Pinhole-camera x-ray photographs of the plasma in the PTF were attempted on both the end and the midplane of the machine. With the normal cavities used, the end pinhole photographs showed only the structure of the copper pumping tubes on the end of the cavity. The x rays emanated from the surfaces of these copper structures and were due to bombardment of the ends by high-energy electrons that escaped from the mirrors.

The pinhole photographs taken from the midplane of the machine also suffered the handicap of viewing the plasma through the perforated copper cavity wall. However, these walls are not strong x-ray sources, because the main high-energy electron loss is out of the mirrors. Figure 3.8 shows a typical photograph taken from the midplane. There appears to be a diffuse x-ray source at the center of the cavity with a diameter of 3 to 4 in. The faint vertical lines at the sides are due to the film holder.

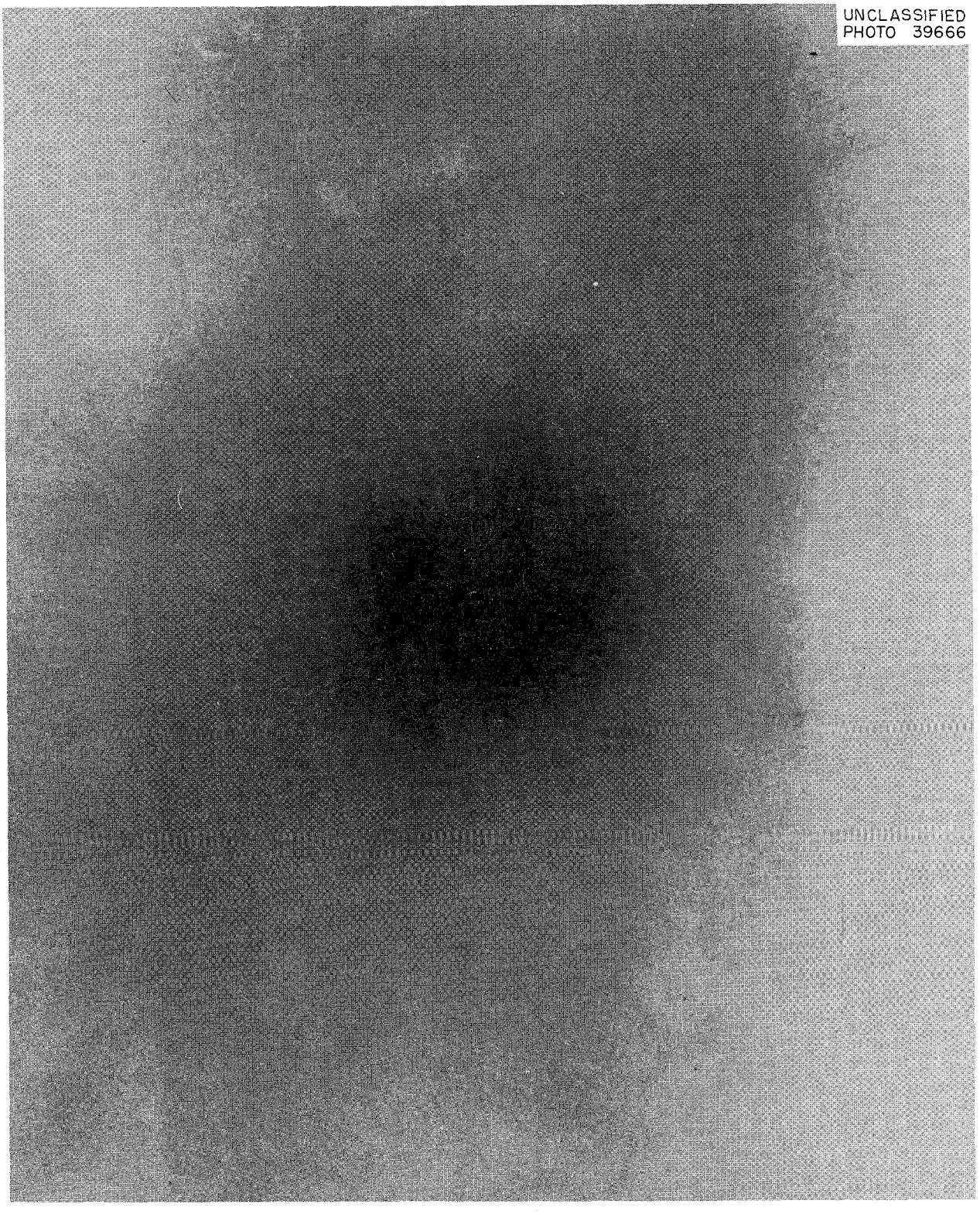

Fig. 3.8. A Pinhole-Camera X-Ray Photograph of the PTF Plasma Taken from the South Side of the Midplane. The faint vertical lines are due to the film holder. The darkened region corresponds to a plasma ball about 4 in. in diameter.

3.2 HOT-ELECTRON PLASMA BY BEAM-PLASMA INTERACTION

Igor Alexeff R. V. Neidigh W. F. Peed

This is a report of experimental progress in plasma heating by beam-plasma interaction. Some heating of plasma electrons by this method has been reported by others,[6,7] and a preliminary report of our work has been published.[8] A 7-kv, 100-ma, direct-current electron beam on the axis of a magnetic-mirror machine (4500:1500:4500 gauss) is used. The electron beam interacts with a plasma of deuterium or helium generated by the beam and formed between the magnetic mirrors. The temperature of the plasma electrons was found to be about 80 kev and the electron density to be about $10^{11}/\text{cm}^3$ for an average beta ($\beta = 8\pi nkTB^{-2}$) in excess of 0.1.

The plasma was photographed (Fig. 3.9) and appears to occupy about the same volume in the photograph as it did to the eye. The diameter at the midplane was about 3 in., even though the electron beam which generated the plasma was limited in the mirror throat and should have a diameter less than $\frac{1}{2}$ in. in the midplane, Clearly, an extensive secondary plasma forms which extends beyond the initial collimation of the electron beam.

A schematic diagram of the apparatus is shown in Fig. 3.10. Both the plasma and the electron beam were formed by apparatus similar to that used for the pressure-gradient arc, sometimes called mode II (ref 9, 10). The pressure gradient is produced by feeding gas into the aperture in the anode, which defines the electron beam, producing a local region with a pressure of about 10^{-3} torr. The pressure between the mirrors is generally a factor of 100 lower. The electron beam (up to 100 ma) forms, in the mirror throat, a dense plasma which may extend beyond the anode into the region between the magnetic mirrors. Previous experiments have shown that this plasma may be traversed by ionic sound waves[10] and may emit ions random in energy and direction. When deuterium gas is used, the secondary plasma has been shown to contain trapped deuterium ions of about 70 ev.[11]

X rays were first observed without the copper liner surrounding the plasma region as shown in the figure, but the addition of the enclosure enhanced the x-ray photon yield by about a factor of 100. The increased yield was thought to be due to a cavity resonance with the rotating electrons, as explained later. However, the liner is not a microwave cavity in the strict sense. No effort was made to retain a high Q. More than half the cylindrical portion of the cavity was later removed for photographic and visual observation without noticeably lowering the plasma temperatures. Perhaps the resulting additional neutral-gas pumping in the plasma region compensated for the lowered Q.

Electrons may be heated by a resonance which occurs between a cavity frequency and the electron-cyclotron frequency.[8] For example, the lowest frequency of a fundamental cavity mode was 0.76×10^9 cps, measured experimentally. Many other modes with higher frequencies were possible. The electron-cyclotron frequency at the midplane of the apparatus was about 4×10^9 cps. As the frequencies of the cavity modes are increased by the presence of the plasma, it is conceivable that even a fundamental mode of the cavity is in resonance with the electron-cyclotron frequency. A resonance with the plasma frequency $(n_e e^2/\pi m_e)^{1/2} = 5 \times 10^9$ cps is also possible.

X-ray photographs of the plasma region were made by a pinhole camera technique. A camera used outside the vacuum chamber was a cube 25 cm on a side and was made of sheet lead. The "pinhole" was $\frac{1}{4}$ in. in diameter. Another x-ray photograph was made inside the vacuum chamber. Here, the "pinhole" was $\frac{1}{8}$ in. in diameter. Sheet lead covered the copper enclosure. The film (Eastman type AA x-ray film) was suitably shielded from heat and light.

---

[6] L. D. Smullin and W. D. Getty, *Phys. Rev. Letters* **9**, 3 (1962); W. D. Getty *et al.*, Fourth Annual Meeting, Division of Plasma Physics, American Physical Society, Atlantic, City, N.J., Nov. 28–Dec. 1, 1962, paper No. O8 (unpublished).

[7] I. F. Kharchenko *et al.*, *Proceedings of the Salzburg Conference on Nuclear Fusion*, Paper CN-10/230/A, Salzburg (1961).

[8] Igor Alexeff *et al.*, *Phys. Rev. Letters* **10**, 273 (1963).

[9] R. V. Neidigh and C. H. Weaver, *Proc. U.N. Intern. Conf. Peaceful Uses At. Energy, 2nd, Geneva, 1958* **31**, 315 (1959).

[10] Igor Alexeff and R. V. Neidigh, *Phys. Rev.* **129**, 516 (1963).

[11] Igor Alexeff, R. V. Neidigh, and E. D. Shipley, *Phys. Fluids* **6**, 450 (1963).

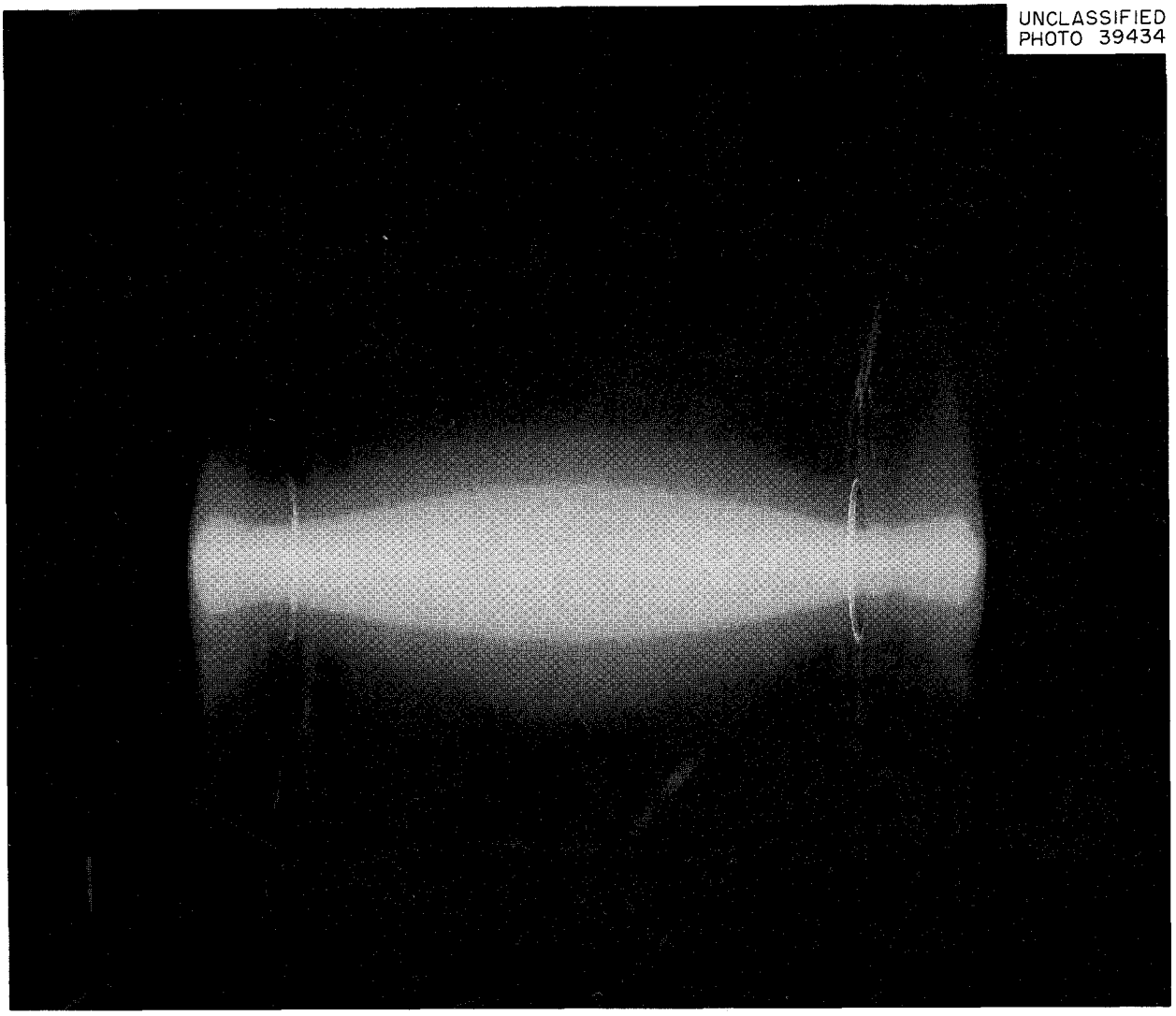

Fig. 3.9. Deuterium Plasma Between Magnetic Mirrors. The visible plasma diameter in the midplane is about 8 cm.

Several x-ray exposures are shown in Fig. 3.11. A geometrical analysis of the x-ray photographs indicates that the central elliptical area corresponds to x rays emitted from the volume of the plasma. The two x-ray sources at the ends of the plasma coincide with the entrances to the mirror coils. These x rays probably result from the bombardment of the metal walls by energetic electrons which are outside the boundary defined by the plasma x rays. The photographs showed that the x-ray flux from the plasma region was as dense as that from the walls.

The total photon flux from just the plasma and its energy spectrum were measured by a sodium iodide scintillation crystal, photomultiplier, amplifier, counter, and multichannel analyzer. A photon spectrum is shown in Fig. 3.12. A calibration spectrum of a Cs^{137} source is shown for comparison. Note that the energy distribution is exponential over three decades and that some electrons have energies greater than $\frac{1}{2}$ Mev. An additional check by an x-ray absorption technique supported the general features of the energy spectrum. By assuming a point source and isotropic

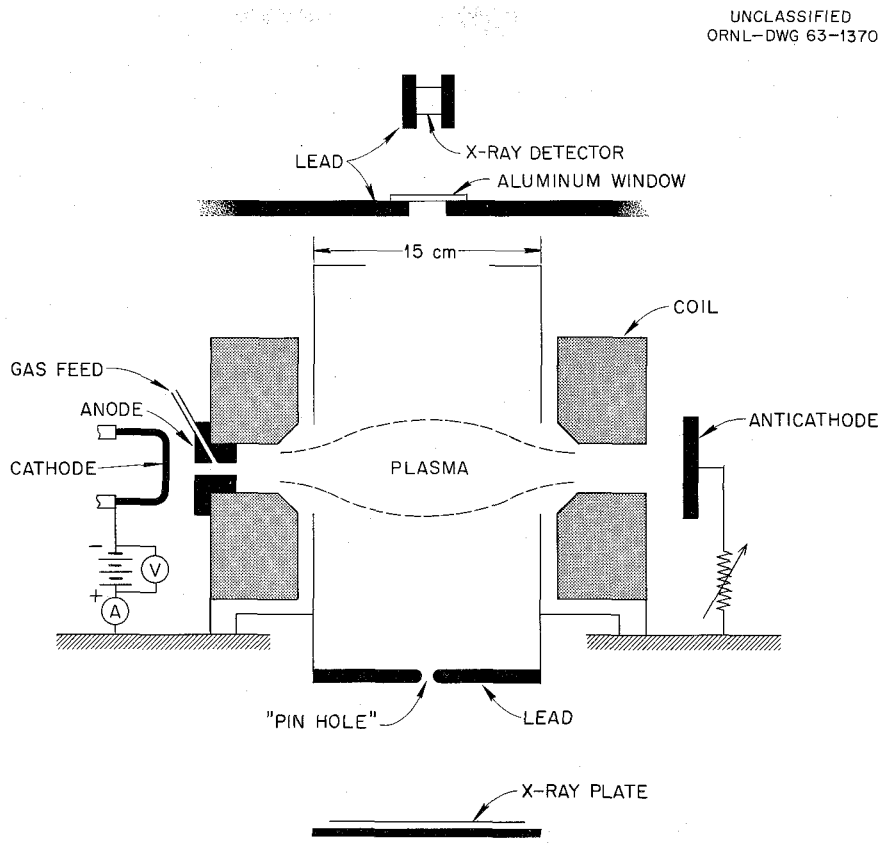

Fig. 3.10. Schematic Diagram of the Apparatus for Producing the Hot-Electron Plasma. Helium gas gave results similar to those described for deuterium. The cavity is cylindrical, 30 cm in diameter and 15 cm long; other dimensions may be scaled approximately.

distribution, the total photon flux was conservatively estimated to be 10^{10} photons/sec.

Electron temperatures may be calculated from the x-ray spectrum by use of known formulas[12] if the plasma is fully ionized. The exponential section of the x-ray spectrum extends over a factor of 10^3 in intensity; if its slope is associated with $-h\nu/kT_e$, the derived electron temperature is $T_e = 80$ kev.

The electron density can be inferred from the foregoing data[12] by use of the relation $\epsilon = 1.42 \times 10^{-27} \times Z^3 n^2 T_e^{1/2}$, where the rate of energy emission ϵ takes the value 12 ergs cm^{-3} sec^{-1}, as indicated by the source strength and the energy spectrum (n is in cm^{-3}, and T_e in °K). Inserting $Z = 1$ (deuterium) and a plasma volume of 100 cm^3 as derived from the pinhole image, together with $T_e = 80$ kev, we obtain a density value of about $n = 10^{11}/cm^3$. Contaminants with Z higher than 1 and lack of complete ionization may make this a slight overestimation.

An additional measurement of the density of the hot electrons was made by evaporating gold from a filament on one side of the plasma and measuring the density of the deposited gold in the "shadow" of the plasma on the opposite side. A sketch which illustrates the method is shown in Fig. 3.13. The deposit was analyzed by light transmission, x-ray fluorescence, and weight of equal areas. Typical distributions of the light transmission and x-ray fluorescence are shown. All methods of analysis gave, for the electron density of the most dense region of the plasma, a value of $10^{11}/cm^3$, within a factor of 2.

[12] L. Spitzer, Jr., *Physics of Fully Ionized Gases*, 1st ed., chap. 5, p 88, Interscience, New York, 1956.

UNCLASSIFIED
PHOTO 39328

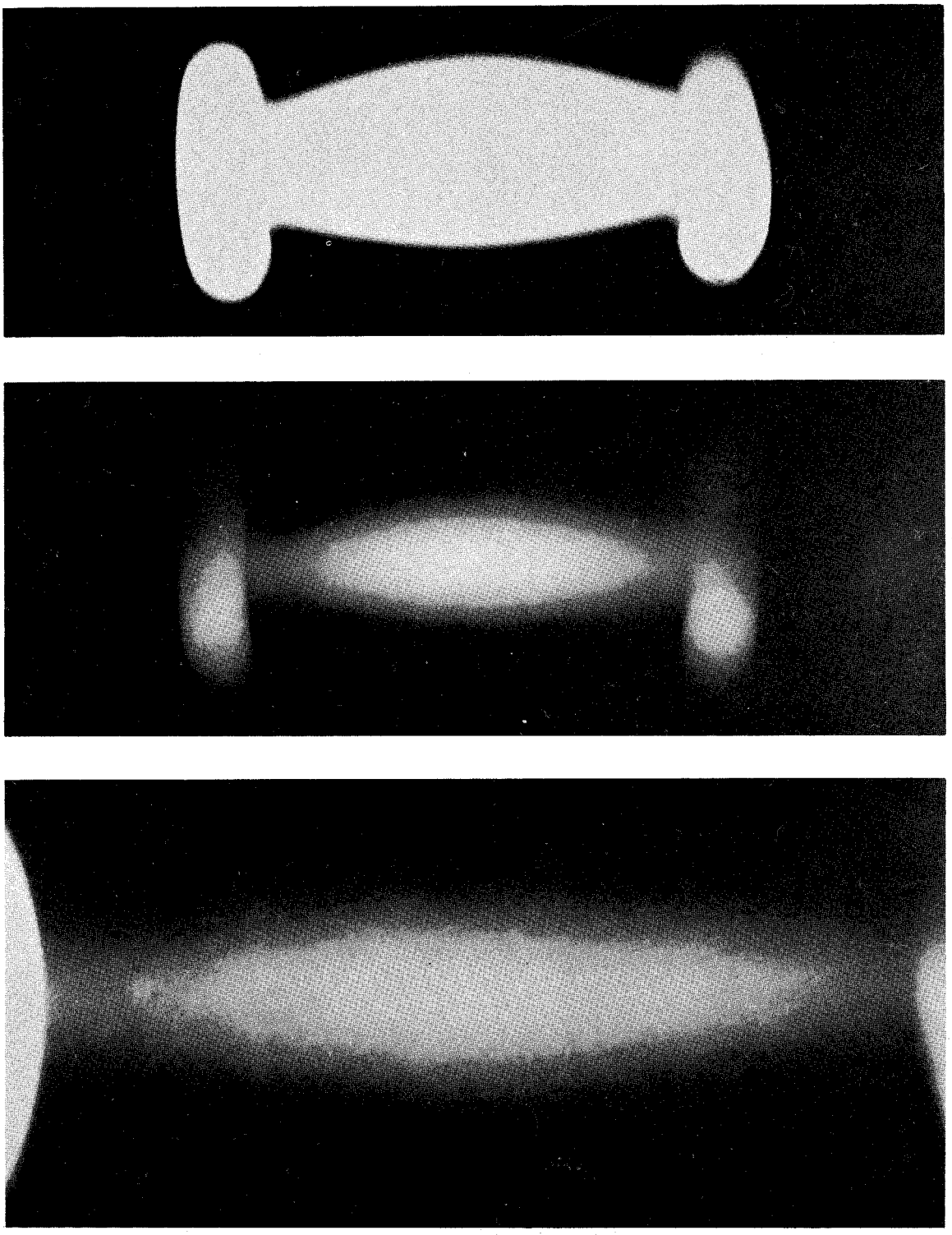

Fig. 3.11. X-Ray Photographs of the Plasma. The upper two photographs were made with the "pinhole" camera outside the vacuum chamber and represent different exposure times. The lowest photograph was made inside the vacuum chamber as diagramed in Fig. 3.10.

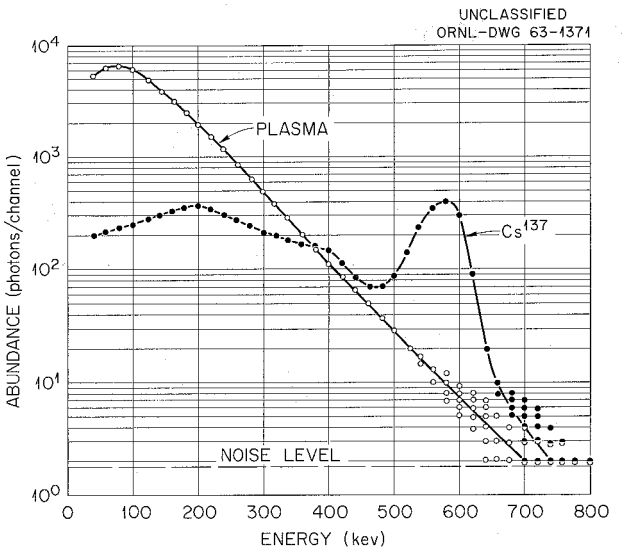

Fig. 3.12. Energy Distribution of X Rays from the Plasma and from a Cs^{137} Source for Calibration.

The light-transmission method proved to be the quickest. In this case the electron density N_e was calculated from the equation

$$N_e = \frac{V_m}{\sigma_e V_e D} \log \left[\frac{\log(i_0/i_1)}{\log(i_0/i)} \right],$$

where

N_e = average electron density,

V_m = thermal velocity of metal vapor,

σ_e = cross section for ionization by electrons,

V_e = velocity of electrons,

D = diameter of plasma,

i_0 = light transmission of plate where baffle has blocked metal vapor,

i_1 = light transmission of plate and deposit where there is no attenuation by plasma,

i = light transmission at any point such as center of deposit.

All units are expressed in the cgs system, and all logarithms are to the base e.

A direct measurement of the diamagnetic effect was made. A 100-turn electrostatically shielded loop was placed around the plasma at the midplane. In principle, the voltage developed in the loop after electron-beam turnoff is a measure of the rate of magnetic-field change due to the decaying plasma. The two photographs at the left in Fig. 3.14 show this plasma decay rate ($\tau = 0.003$ sec). Since the diamagnetic effect is proportional to $n_e T_e$, the density may be calculated by assuming T_e to be known from the photon-energy distribution. Again the electron density is found to be about $10^{11}/cm^3$.

The upper traces on the photographs at the right in Fig. 3.14 are the fluctuating voltages developed in the loop while the electron beam is on. A direct calibration of the fluctuating magnetic field in the loop can be made by comparing the voltages developed in the loop by the ripple in the current which supplies the mirror coils. The lower trace

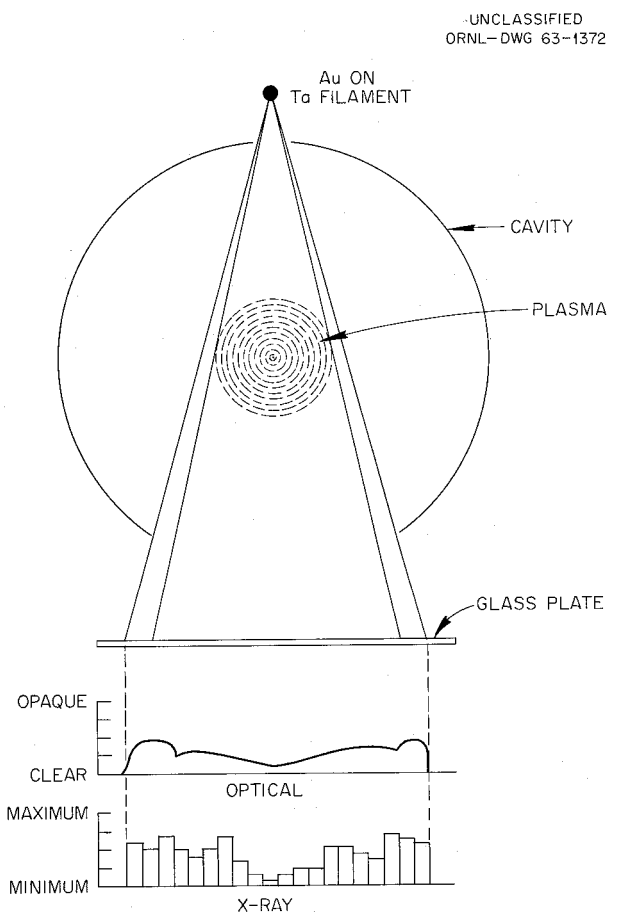

Fig. 3.13. Method of Gold Evaporation for Determination of Electron Density. The gold deposit was measured optically and by x-ray fluorescence. Typical results are shown.

UNCLASSIFIED
PHOTO P-61710

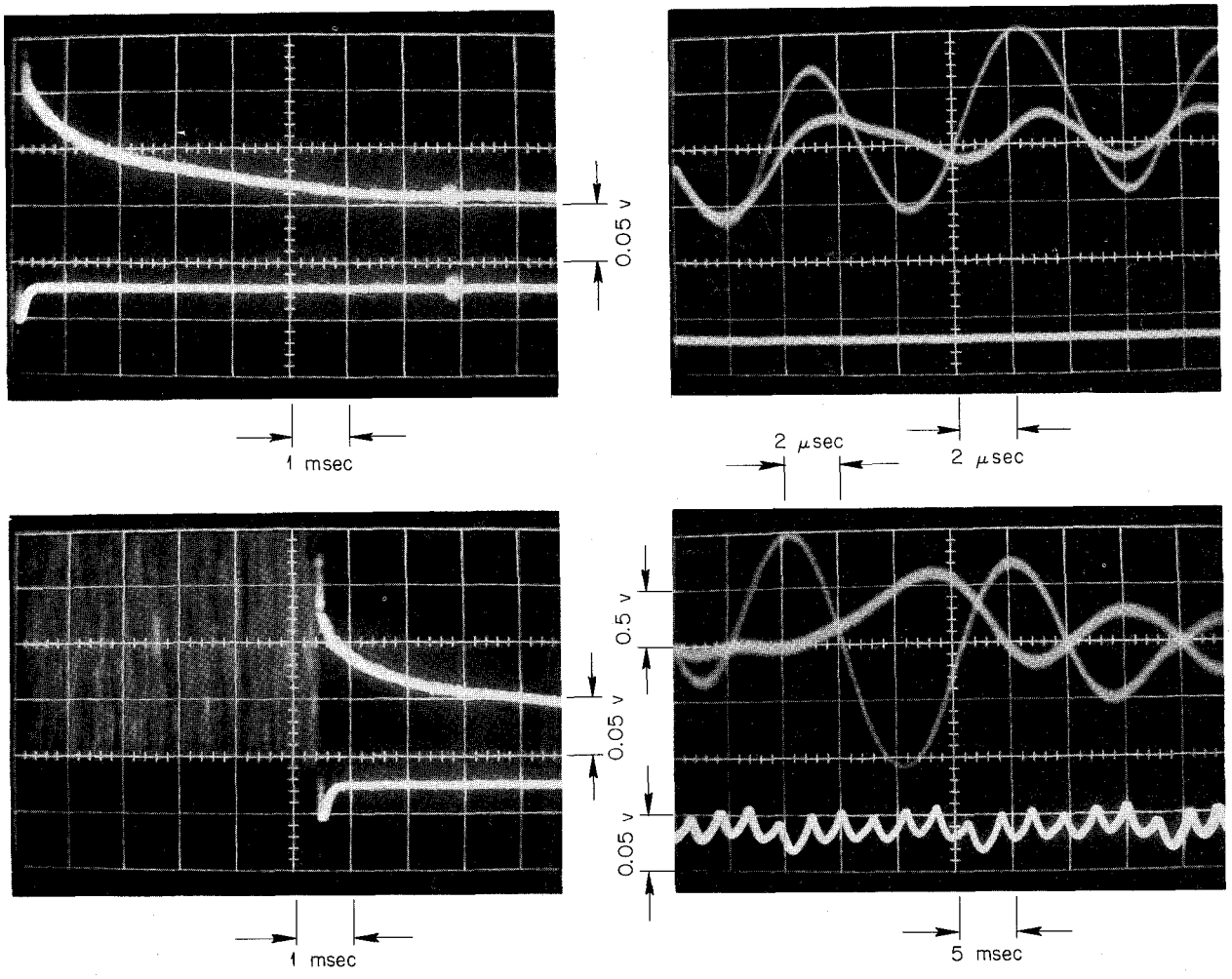

Fig. 3.14. Plasma Diamagnetic Effect. Upper trace in each photograph is the voltage developed across a 100-turn loop around the plasma at the midplane.

of the lower right photograph of Fig. 3.14 is the ripple voltage. The fluctuating field at the loop with the electron beam on is about 0.01 the maximum field strength at the midplane. Apparently the plasma is "breathing" or "sloshing" about the magnetic axis in the steady state. The breathing corresponds to a $\Delta\beta \approx 0.01$, and since this must be smaller than the true β, one derives as a lower limit $n_e > 10^{10}$ electrons/cm^3.

The decay of the photon output was observed after turnoff of the electron beam. The results are in Fig. 3.15. The photographs on the left are typical. The beam turnoff point is at the start of the trace. The photons could be counted in the lower trace as well as in several others. The decay was exponential, with a τ equal to about 0.016 sec. The photographs at the right indicate decrease by a factor of about 10 in photon output in less than a millisecond after beam turnoff. It is the remaining plasma which has the 0.016-sec decay constant. The τ of 0.016 sec is nearly equal to the theoretical decay constant ($\tau = 0.020$ sec) for electrons scattered off neutrals and lost through the mirrors. Apparently the plasma is quite stable after the initial loss at beam turnoff.

An explanation for this apparent stability may be found in the electron temperature. The Debye shielding distance $[6.9(T_e/n_e)^{1/2} \approx 0.6$ cm], where

UNCLASSIFIED
PHOTO P-61711

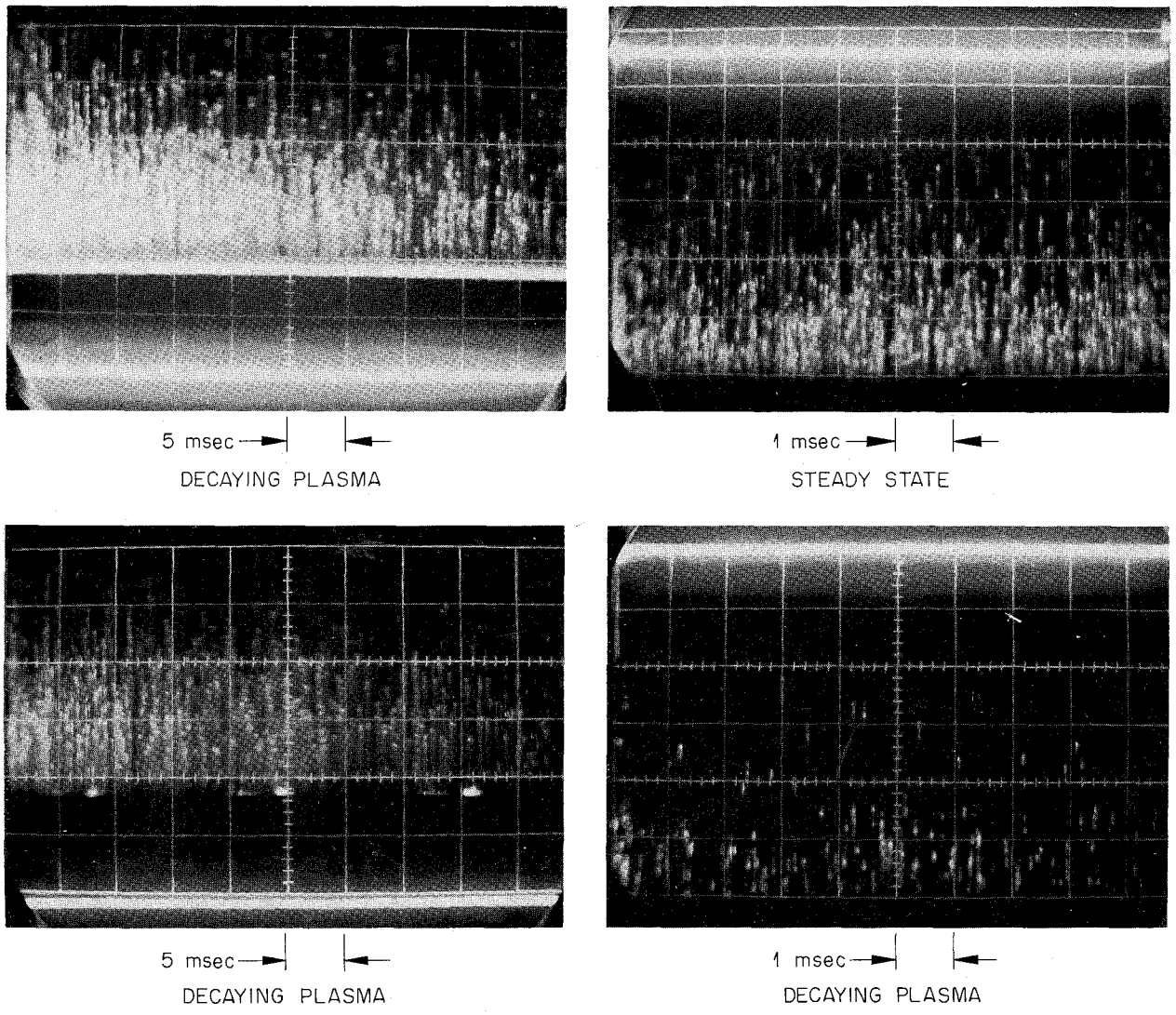

Fig. 3.15. X-Ray Photons from the Plasma After Electron-Beam Turnoff. A plasma decay constant ($\tau \approx 0.016$ sec) was determined by counting the photons.

T_e is expressed in °K and n_e in cm^{-3}, is a large fraction of the diameter (2 cm) of the dense central region. Therefore this part may not be a true plasma but may behave as a collection of independent particles. The outer, cooler, portions of the plasma may shed quickly after beam turnoff, while the central region with the longer Debye distance may be quite stable. This would account for the sudden drop in x-ray intensity after turnoff and the subsequent, apparently stable decay in the remainder of the plasma.

3.3 BEAM-PLASMA INTERACTION STUDIES

E. Earley[13] V. J. Meece W. L. Stirling

Preliminary results have been obtained from an experiment in which an electron beam interacts with a plasma created by the beam. This experiment is actually a dc version of the experiments

[13]On loan from Y-12 Plant.

of Kharchenko,[14] Smullin,[15] and many others which employed pulsed beams. Discussion of another dc beam-plasma experiment involving the mode II arc discharge can be found in the preceding section of this report.

In all work reported to date, the secondary plasma is created by the primary beam which ionizes the background gas. The secondary plasma receives energy from the beam through a coherent beam-plasma interaction, which increases the plasma density and heats the plasma as well. The rf radiation starts somewhat above the electron-cyclotron frequency

$$f \cong (f_{ce}^2 + f_{pe}^2)^{1/2} ,$$

where f_{ce} is the electron-cyclotron frequency and f_{pe} is the plasma frequency, and steadily increases until blowup or strongly enhanced diffusion of the beam occurs.

Kharchenko reports that nonlinear effects permit strong coupling between the longitudinal plasma oscillations and the transverse oscillations at $f_{ce} \cong f_{pe}$. In addition, his measurements have shown that $E_z = 0$ and E_r and E_θ are maximal when the cyclotron and plasma frequencies are equal.

The primary objectives of this experiment are (1) to produce a coherent beam-plasma interaction employing a dc electron beam, (2) to study what plasma heating occurs, if any, under the resonance condition of $f_{ce} \cong f_{pe}$, and (3) to investigate the possibility of producing beam-plasma interactions which might lead to direct energy transfer to the plasma ions.

Figure 3.16 shows a schematic of the experimental apparatus. The total axial extent of the apparatus is limited to about 28 in., since the

[14] I. F. Kharchenko *et al.*, *Proceedings of the Salzburg Conference on Plasma Physics*, Paper 230/A, Salzburg (1961).

[15] L. D. Smullin and W. D. Getty, *Phys. Rev. Letters* **9**, 3 (1961); W. D. Getty, *Investigation of Electron-Beam Interaction with a Beam-Generated Plasma*, Technical Rept. 407, MIT, 1963.

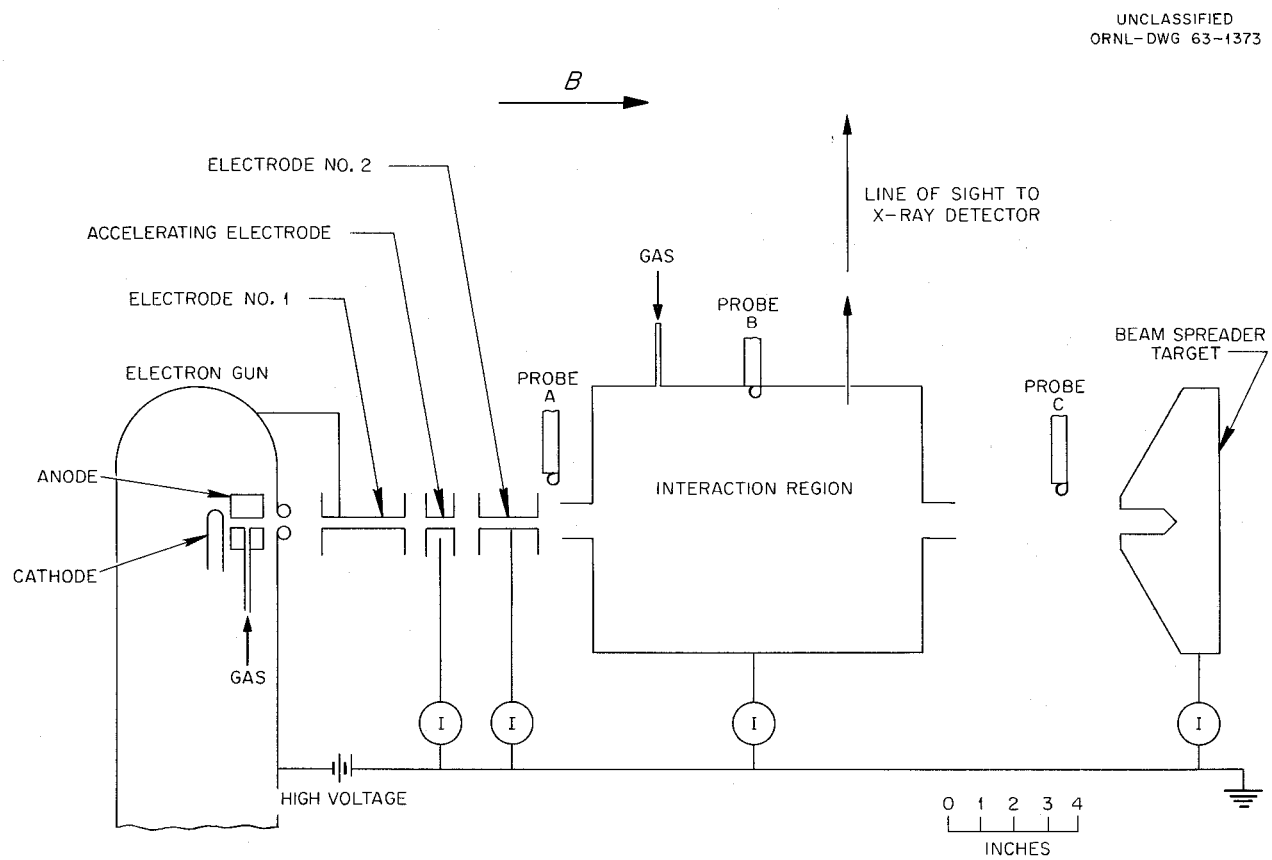

Fig. 3.16. Schematic of Apparatus for Beam-Plasma Interaction Studies.

equipment is housed in the 32-in.-wide C tank of the Beta Tank facility.

The electron gun is a gas-supported arc with gas feed into a 0.180-in.-ID hollow cylindrical anode. The cathode, of thoriated tungsten, is resistance-heated. The electrode next to the gun, No. 1, is electrically tied to the gun and serves as a shield against ion bombardment on the gun. The accelerating electrode is spaced $\frac{1}{2}$ in. from electrode No. 1 and $3\frac{1}{4}$ in. from the interaction region. The high-voltage supply is a 50-kv 2-amp supply. Electrode No. 2 is a ground-potential electrode which may be moved axially between the accelerating electrode and the interaction region. The interaction region is bounded by a right-circular copper cylinder at ground potential. The purpose of the cylinder is twofold: (1) to serve as a means of producing a localized high-pressure region and (2) to act as resonant cavity in a transverse magnetic mode compatible with the desired resonant condition, $f \cong \sqrt{2}\, f_{ec}$, thus possibly enhancing the rate of plasma heating. The beam-spreader target is described in the next section of this report.

Experimental measurements made thus far fall into two categories. The first is low-frequency measurements from probes placed as shown in Fig. 3.16. The second is x-ray intensity measurements made with a 1-in. NaI-crystal x-ray spectrometer mounted to look perpendicular to the magnetic field or plasma column. The data indicate at least two different beam-plasma interactions.

The first is the least productive of the x rays, and the associated rf spectrum is shown in Fig. 3.17. This picture was taken with a model SPA-3 Panoramic Analyzer. The spectrum was monitored on probe B, and the frequency sweep width is 500 kc from the left to the right markers. Operation in this manner is difficult because of the extreme sensitivity to gas flow into the interaction region. This spectrum was taken at a magnetic field of 2800 gauss with an argon gas feed into the gun at a rate of 1 atm cc in 38 sec and deuterium gas into the cavity at 1 atm cc in 2 sec. The beam voltage is 20 to 22 kv with a power delivery to target of about 9 kv. The target electron current pegged the meter at 1.5 amp. This reading is true for all interaction modes and serves as an indication of when the apparatus is performing properly.

From the known frequency calibration, Fig. 3.17 yields peaks at about 100, 180, 280, 360, and 440 kc. These numbers are roughly 1 × 90, 2 × 90, 3 × 90, 4 × 90, 5 × 90 kc. The magnetic field is 2800 gauss, and the ion-cyclotron frequency for singly ionized argon is about 100 kc.

One can compare the observed frequency and harmonics with those to be expected for ionic sound waves. From the relation

$$f = \frac{1}{2L}\sqrt{\frac{3kT_e}{m_i}}\ ,$$

where

L = length of plasma column,

k = Boltzmann's constant,

T_e = electron temperature,

m_i = ion mass,

a value of 110 kc is obtained by use of the values T_e = 17 ev (ref 16) and L = 4.7 cm. There is then relatively good agreement between the values for the ionic cyclotron, sound, and the lowest observed frequency of 90 kc. The observed frequencies indicate the likelihood of resonance up to the 5th harmonic.

The geometry of the system is consistent with that necessary to establish standing ionic sound waves. Electrode No. 2 has a length of 4.75 cm, and the length of the interaction region is 31 cm, or about 7 × 4.5 cm. The effect of varying the

[16] Igor Alexeff *et al.*, *Thermonuclear Div. Semiann. Progr. Rept. Jan. 31, 1961*, ORNL-3104, p 31.

UNCLASSIFIED
PHOTO P-61712

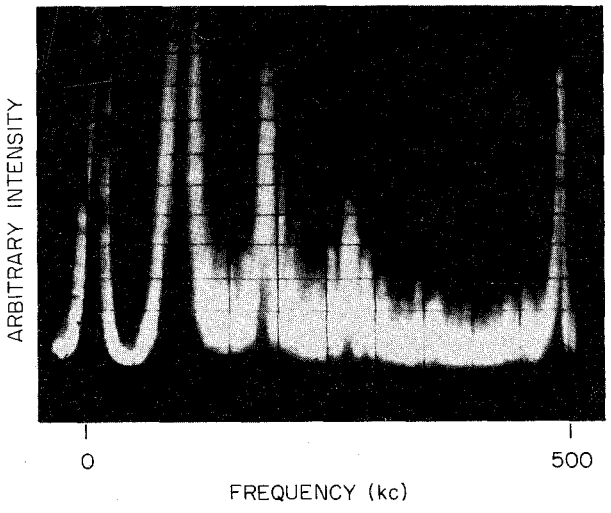

Fig. 3.17. Low-Frequency RF Spectrum on Probe B with an Argon-Deuterium Gas Mixture.

separation between electrode No. 2 and the cavity is unpredictable. Sometimes it destroys the spectrum, and sometimes it has negligible effect.

The presence of deuterium can also be seen by observing the frequency range from 500 kc to 3 Mc (Fig. 3.18). The ion-cyclotron frequency is about 1 Mc for D_2^+ and 2 Mc for D^+. Using the electron temperature and plasma column length given above, one would expect molecular deuterium to have an ionic sound frequency of about 550 kc, and atomic deuterium about 850 kc. The frequencies indicated in Fig. 3.18 (above 400 kc) are 500 kc, 800 kc, 1 Mc, 2 Mc, and 3 Mc. One notes that both the ion-cyclotron and ionic sound frequencies for deuterium are observed, even though they are not in resonance as in the case of argon. Initial attempts to achieve resonance between the deuterium ionic sound and cyclotron frequencies by lowering the magnetic field have not been successful.

Frequency observations of probe A are identical with those of probe B. However, probe C yields only a low-intensity noise spectrum below 500 kc. The presence of the target beam spreader produces a mirror effect in the magnetic field in the region between the aperture of the beam spreader and the cavity where probe C is located. Magnetic-field values quoted in this report are the axial values in the middle of the cavity. However, the field is 1.7 times greater at the beam-spreader aperture. Those ions which approach the region of probe C are either turned around by the mirror effect of the increasing magnetic field or they no longer experience a synchronization between their ionic sound and cyclotron frequencies. Either effect would tend to reduce the signal on probe C.

Data similar to those in Fig. 3.17 have been obtained during operation with argon gas alone and with nitrogen gas alone. Operation with deuterium alone is very poor, as the filament in the gun becomes contaminated.

Figure 3.19 shows a typical pattern on probe B for nitrogen gas alone. The observed frequencies are about 90, 170, 250, 325, and 400 kc. These frequencies are approximately 1 × 80 kc through 5 × 80 kc. The ion-cyclotron frequency is about 235 kc under the conditions for which this picture was taken; the ionic sound frequency is about 90 kc. Thus the conditions for resonance are approximately satisfied between the 3d harmonic of the ionic sound and the cyclotron frequency. Whether or not the approximate equality of the ion-cyclotron and sound frequencies produces any heating of the ions remains to be seen. An attempt will be made to observe a Doppler shift in appropriate optical spectra.

The second type of beam-plasma interaction fits a description which characterizes the interaction

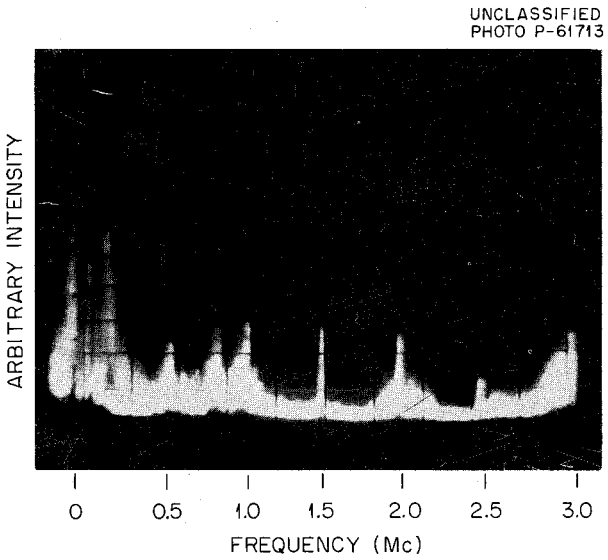

Fig. 3.18. Intermediate RF Spectrum on Probe B with an Argon-Deuterium Gas Mixture.

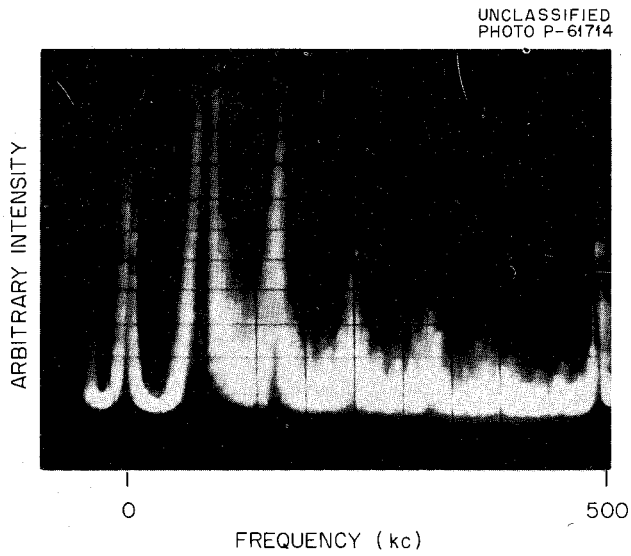

Fig. 3.19. Low-Frequency RF Spectrum on Probe B with a Nitrogen Gas Feed.

with respect to electron oscillations rather than ion oscillations. In general, the integrated x-ray intensity is a factor of 100 greater than that obtained when the interaction meets the ion resonance conditions discussed above.

When the experiment proceeds in the second mode, the low-frequency probe spectrum for argon looks like Fig. 3.20, a decreasing noise continuum above a well-defined minimum of about 80 to 100 kc. There is some noise between 0 and 80 kc, but of very low intensity. This is in sharp contrast to Figs. 3.17 and 3.18. These data were taken with a beam voltage of 25 kv, the field was 2200 gauss, and the power on the target was 16 kw. Gas flow of argon into the gun was 1 atm cc in 25 sec, and the argon flow into the cavity was 1 atm cc in 16 sec; the operating pressure (in the vacuum chamber) was about 1.5×10^{-5} torr.

Besides having a relatively high x-ray intensity, the counting rate varied by a factor of from 5 to 20 at different positions of electrode No. 2 from the interaction region.

Figure 3.21 shows a plot of the count-rate meter output in which the intensity varied by a factor of about 5. Such well-defined peaks are suggestive of an interaction which produces a wave that travels back toward electrode No. 2 and for which electrode No. 2 is resonant. At spacings of about $\frac{3}{8}$ and 1 in. from the cavity, electrode No. 2 operates to bunch the electrons in the proper

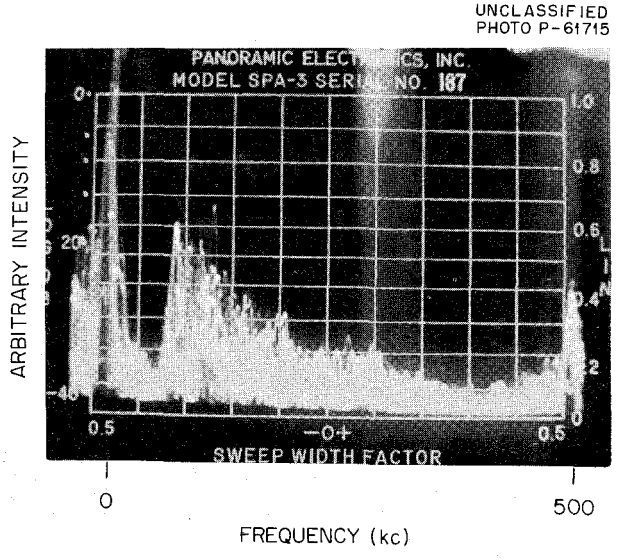

Fig. 3.20. Low-Frequency RF Spectrum on Probe B with an Argon Gas Feed; Second Mode of Operation.

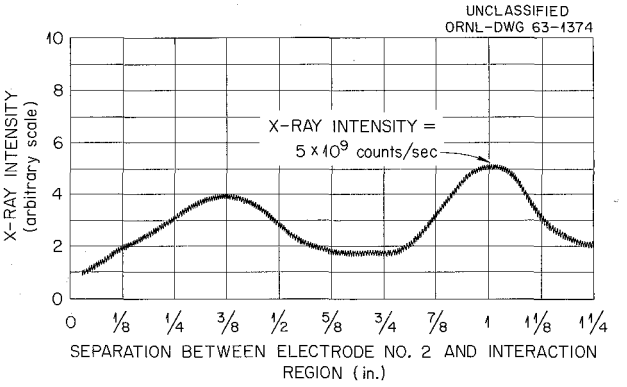

Fig. 3.21. Illustration of Beam Bunching at Electron-Cyclotron Frequency.

phase to help drive the beam-plasma interaction. Thus from Fig. 3.21 one can estimate the wavelength of the oscillation bunches on the beam as about $\frac{5}{8}$ in. With a beam velocity of 10^{10} cm/sec, the frequency of the backward wave turns out to be 6.4×10^9 cps. The magnetic field at this time was 2200 gauss, which yields an electron-cyclotron frequency of about 6.2×10^9 cps. The difference is less than 5%. One can compare the geometrical length of electrode No. 2 with the wavelength of the backward wave. The former (Fig. 3.16) is 4.75 cm; the latter is calculated to be 4.7 cm. This suggests the presence of a longitudinal standing wave in electrode No. 2.

Figure 3.21 has been repeated many times with argon gas feed only, nitrogen only, and argon (in gun) and deuterium (in interaction region) mixture. On two occasions with argon, the apparatus was adjusted so that the oscillation frequency (indicated by the x-ray intensity peaks) was within 10% of being equal to twice the electron-cyclotron frequency. Figure 3.22 is an example of the x-ray intensity output for this type of operation. The electron-cyclotron frequency is 6.6×10^9 cps, and the backward wave frequency is about 12×10^9 cps. The accelerating potential is 25 kv.

In general, the operation of the apparatus in this mode of interaction is quite stable for field values between 2200 and 2400 gauss. Figure 3.23 shows four pictures of the x-ray pulse-height spectrum taken with the aid of a Tektronix 535 oscilloscope. All parameters were held constant except the magnetic field, which varied from 2200 to 2500 gauss as indicated. The beam voltage was

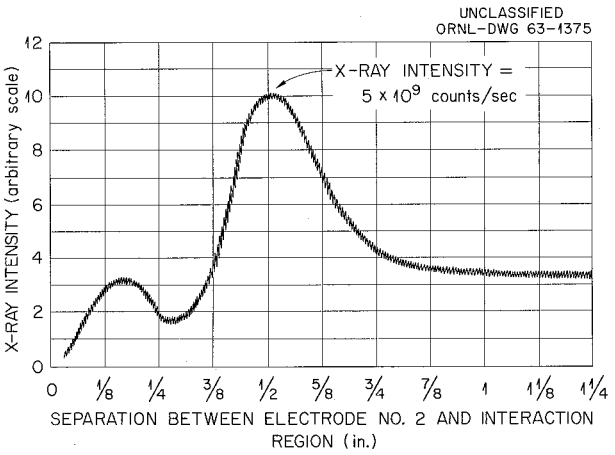

Fig. 3.22. Illustration of Beam Bunching at Approximately Twice the Electron-Cyclotron Frequency.

25 kv. The argon gas feed into the gun was 1 atm cc in 25 sec and into the cavity was 1 atm cc in 20 sec. The largest pulse heights are obtained at 2400 gauss, but the highest x-ray intensity occurs at 2200 gauss. The x-ray intensity is practically nonexistent at fields of 2000 gauss and lower or 2600 gauss and above.

Figure 3.24 shows the 36-kev, Cs^{137} *K* x ray taken at the same amplifier gain as the pictures in Figs. 3.22 and 3.24. It is characteristic of the model DD2 amplifier to have both positive- and negative-voltage swings for each trace. The amplitude is limited by the scope.

Figure 3.25 shows the variation of the x-ray spectrum as a function of beam voltage. The magnetic field is fixed at 2400 gauss; the argon gas feed into the gun is 1 atm cc in 25 sec and

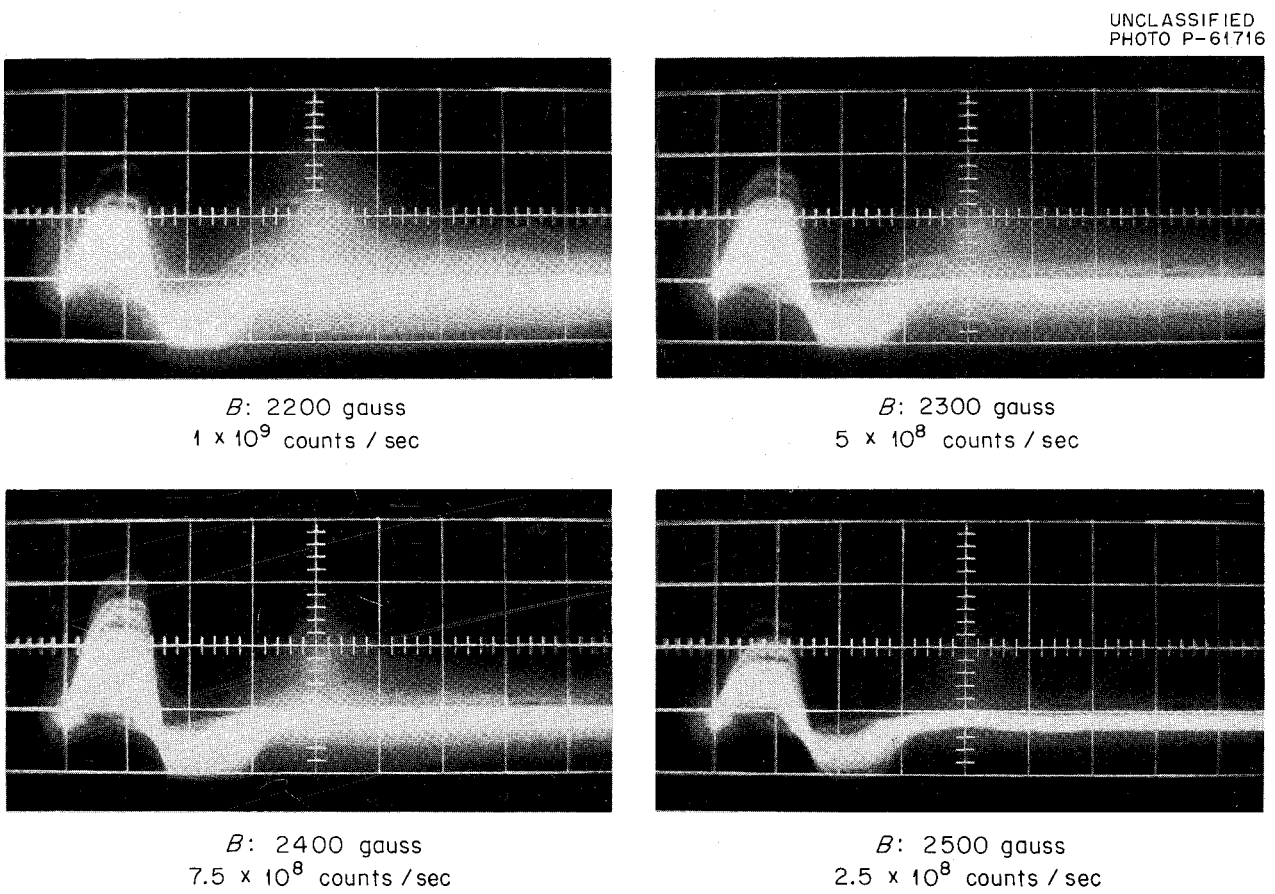

Fig. 3.23. Variation of X-Ray Pulse-Height Spectra with Magnetic Field.

UNCLASSIFIED
PHOTO P-61717

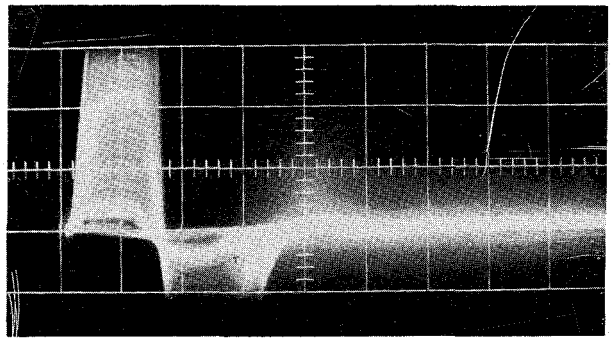

Fig. 3.24. Cs^{137} K X Ray.

into the cavity is 1 atm cc in 15 sec. Both the x-ray intensity and energy increase with increasing beam voltage. Comparison with Fig. 3.24 shows that the maximum x-ray energy is between 175 and 200 kev. It is believed that the line structure in the pictures is statistical in nature and not due to the x-ray origin. The origin of the x rays is known not to be the target. The solid angle seen by the NaI crystal, $d\Omega/4\pi = 5 \times 10^{-7}$, does not include any portion of the target. A quantitative pulse-height analysis will determine the true nature of these x-ray lines.

It is not possible at this point to say very much about the nature of the beam-plasma interaction observed in the second mode of operation. Smullin and Getty[15] concluded that the interaction mechanism which explained their observations was the one existing at synchronism between the slow cyclotron wave of the beam and the backward or negative dispersion wave of the plasma circuit. However, they observed no relation between the interaction and the geometry of the system. This experiment, of course, exhibits a marked dependence of the interaction on the position of electrode No. 2. With reasonable certainty, one can describe the interaction observed in this experiment in the following manner: Under certain conditions of beam velocity and density it is possible for a coherent interaction to exist in the cavity between the beam and the secondary plasma created by the beam. Such an interaction is characterized by a self-modulation or bunching of the beam in the proper phase to transfer energy from the beam to the plasma. Consequently, the plasma density increases and the self-bunching frequency of the beam changes accordingly. The role of electrode No. 2 can be explained by assuming that the interaction produces a wave which travels in a direction opposite to that of the beam. At a given frequency, the backward wave experiences resonance in electrode No. 2, which results in premodulation of the beam. By adjusting the position of electrode No. 2, the bunches produced by it can be made compatible with the phase of the beam bunches produced by self-modulation,

UNCLASSIFIED
PHOTO P-61718

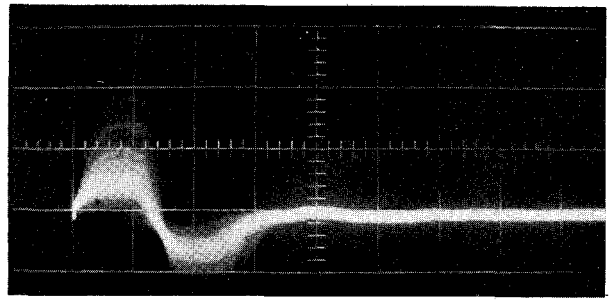

VOLTAGE: 20 kv
5.5×10^8 counts/sec

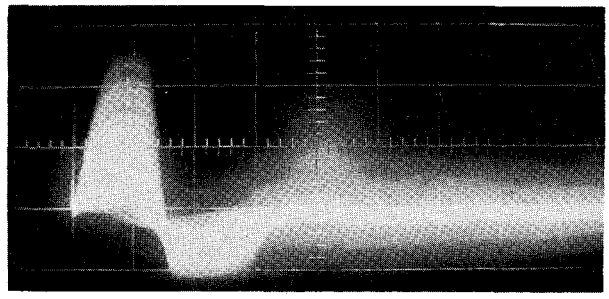

VOLTAGE: 25 kv
4.5×10^9 counts/sec

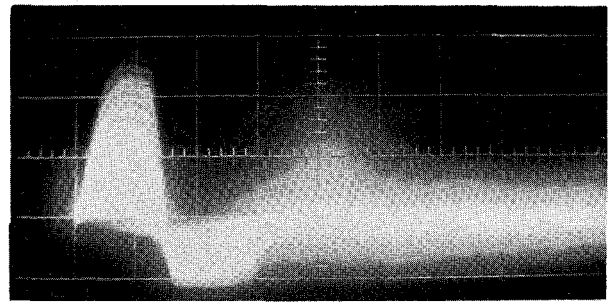

VOLTAGE: 28 kv
5.6×10^9 counts/sec

Fig. 3.25. Variation of X-Ray Pulse-Height Spectra with Beam Voltage.

thereby enhancing the interaction. The magnetic field, or electron-cyclotron frequency, plays a major role because the interaction is tuned through observation of the x-ray intensity; the x-ray intensity is a function of the electron velocity component perpendicular to the magnetic field.

Because of the x-ray production and the existence of beam bunching at a frequency equal to the electron-cyclotron frequency, it is tempting to assume that the electron-cyclotron and plasma frequencies are about equal. In Fig. 3.20 the density turns out to be, for $f_{ec} \cong 6.4 \times 10^9$ cps,

$$f_{ec} \cong f_{ep} = 8.97 \times 10^3 \, n_e^{1/2} ,$$

$$n_e = 5 \times 10^{11} \text{ electrons/cm}^3 .$$

There are disadvantages to assuming that $f_{ec} \cong f_{ep}$. First, some mechanism must exist which will limit the plasma density in order to satisfy the equality. Second, a small-signal theory (postulated by Smullin and Getty) is invalid in the range of approximate equality between f_{ec} and f_{ep}.

It is not clear why the system operates best at a magnetic field of 2200 to 2400 gauss or f_{ec} in the neighborhood of 6.5×10^9 cps unless f_{ec} must also be a standing wave of electrode No. 2. To check this, electrode No. 2 will be replaced with other geometries, including a helix, to see if the interaction will proceed at higher magnetic fields and, possibly, higher plasma densities. Independent measurements of plasma density will be made in order to check the assumption $f_{ec} \cong f_{ep}$. In addition, direct observation of the kilomegacycle frequency range will be made, as will pulse-height analysis of the x-ray spectra.

3.4 ELECTRON-BEAM SPREADER

E. Earley[17] V. J. Meece W. L. Stirling
J. N. Luton, Jr. C. E. Parker

The experiments described in the preceding section were carried out in the Beta Tank facility, and they have required the development of an electron-beam spreader in order to distribute the energy in the electron beam over a large area. The power in the beam is often in the 20- to 25-kw range, with an average power density between 100 and 200 kw/cm^2. A spread in the beam by a factor of 100 in cross-sectional area lowers the power density to about 1 to 2 kw/cm^2, which can be easily dissipated.

Figure 3.26 shows a schematic of the beam spreader. Testing and operation are being performed in vacuum tank C, which is 32 in. wide and which has a maximum steady-state field of about 3500 gauss.

The soft-iron shield approximates a truncated cone with an altitude of $2\frac{5}{8}$ in. The larger face is 4 in. in radius, and the small one is $2\frac{1}{8}$ in. in radius. A 1-in.-diam axial hole provides the field reduced region in which the water-cooled copper target cup is positioned.

The inside diameter of the target cup is about 0.730 in.; the copper wall thickness is about 0.030 in. The minimum cross-sectional area of the cooling-water passage is equivalent to the cross-sectional area of a 0.5-in.-diam water line. A water flow of about 25 gpm is maintained with an inlet-to-outlet water pressure differential of 80 psi.

Figure 3.27 shows the variation of the magnetic field along the axis of the beam spreader. This curve was taken with a 3-mil Mylar film (approximate) separating the device from the magnetic pole piece. The Mylar film electrically insulates the assembly from ground and thus permits the target current to be monitored. The maximum reduction in magnetic field inside the target cup is seen to be about a factor of 150. The magnetic field falls off a little faster at the radius of the inner copper surface of the target cup than it does at corresponding points along the cup axis.

The maximum beam power tested so far is 24 kw. With a cooling-water flow of 25 gpm, the water temperature rise is about 3.6°C. It is estimated that the target surface temperature is about 325°C.

[17] On loan from Y-12 Plant.

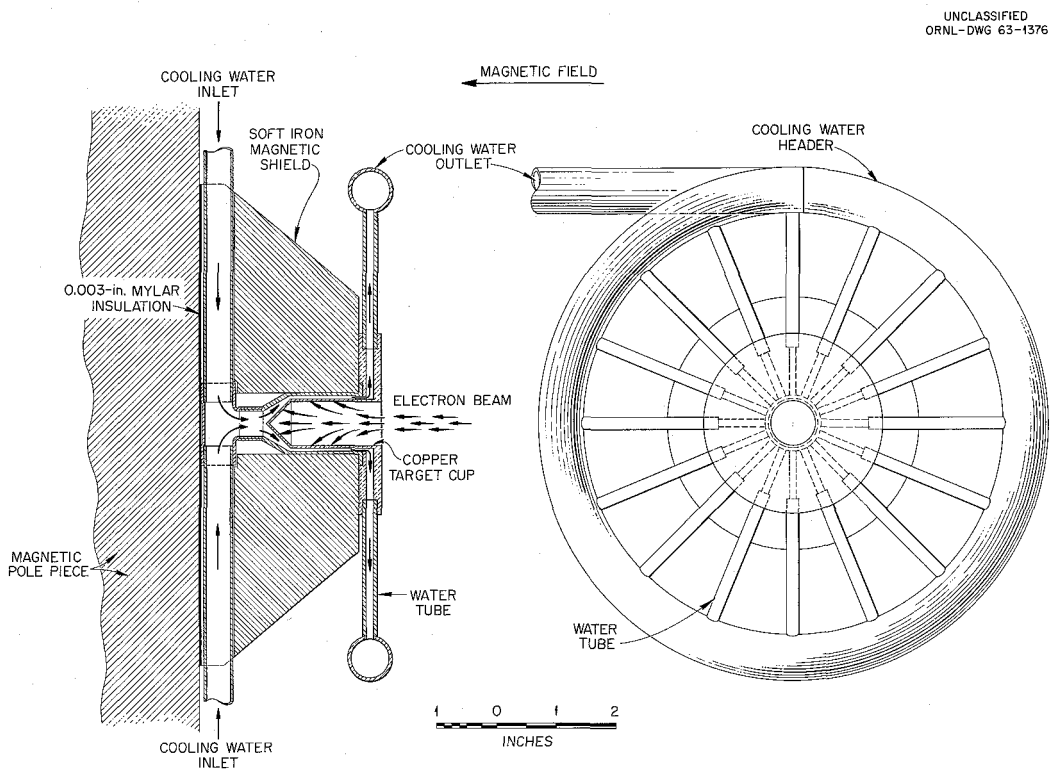

Fig. 3.26. Magnetic Beam Spreader.

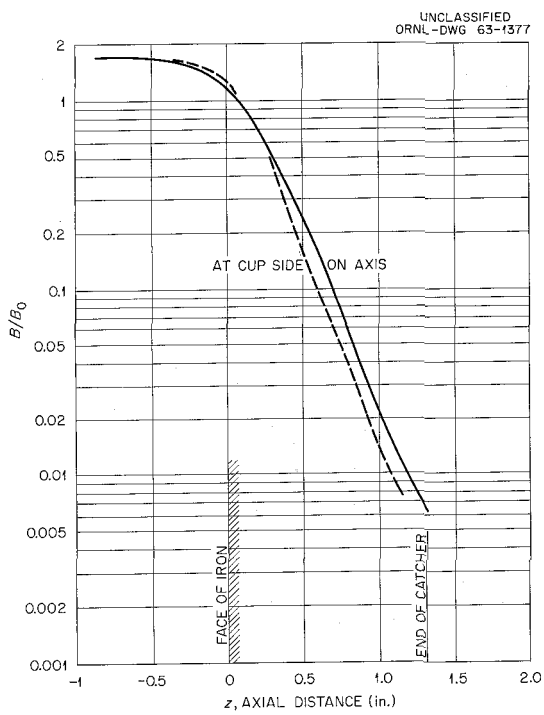

Fig. 3.27. Field Reduction in Beam Expander. B_0 = **undisturbed field (3530 gauss).**

3.5 MEASUREMENT OF IONIC-SOUND-WAVE VELOCITY IN PLASMA BY A TIME-OF-FLIGHT TECHNIQUE

Igor Alexeff W. D. Jones

The velocity of ionic sound waves in a plasma[18] has now been measured directly by a time-of-flight technique instead of being inferred from the frequency and wavelength of a standing-wave system.[19]

The apparatus used is shown in Fig. 3.28. A discharge tube is run in an ordinary glow mode. The tube is filled with gas at about 10^{-2} torr pressure. An electron stream flowing from the heated-tungsten cathode to the anode ionizes some of the gas to provide the plasma. A Langmuir probe is provided both to measure the plasma electron temperature and to measure the floating probe potential during the time-of-flight studies.

[18] L. Tonks and I. Langmuir, *Phys. Rev.* **33**, 195 (1929).

[19] Igor Alexeff and R. V. Neidigh, *Phys. Rev.* **129**, 516 (1963).

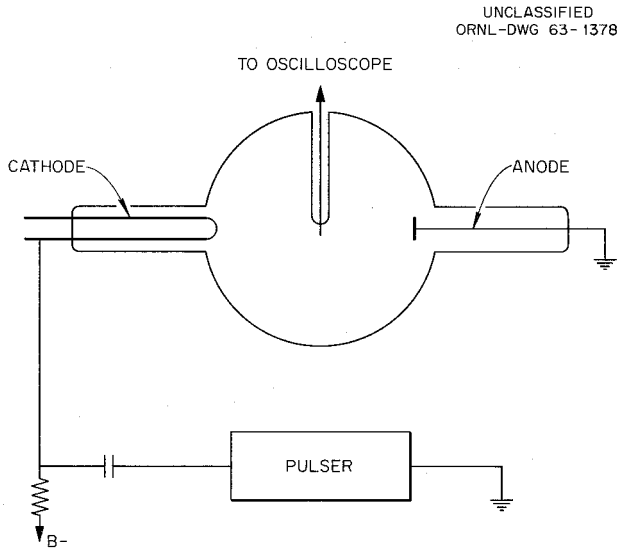

Fig. 3.28. Discharge Tube Used for Time-of-Flight Studies.

Ion waves are generated in the tube by a pulser, which increases the anode-cathode potential for a period of a few microseconds. Presumably, ionic sound waves are thereby produced by sheath interactions at the anode and cathode. Now, if the cathode is operated in a space-charge-limited regime, the floating potential of the plasma is observed to go suddenly negative after an appropriate delay, as shown in Fig. 3.29. Presumably, an ion wave from the anode arriving at the cathode neutralizes the cathode space-charge sheath and causes a drastic increase in cathode emission. This negative pulse is very strong and is easily observed above the background noise level of the discharge. The time delay between the initial and the response pulse is proportional to the distance between the anode and the cathode, as would be expected if a wave of constant velocity were propagating between them.

The velocity of the ion wave is computed from the following formula: $v = D/t$, where v is the velocity in cm/sec, D is the spacing of the anode and cathode in cm, and t is the time delay observed between the driving pulse of the pulser and the negative response pulse of the discharge tube. However, in some cases the pulse shows strong dispersion, and the time-of-flight of the pulse as a whole is not well defined (see Fig. 3.30). In this case, the time is measured to the point at which the response pulse just begins to appear. In other words, one measures the time-of-flight of the most rapidly propagating components of the pulse – those components propagating with the signal velocity of the medium.

The experimentally measured signal velocity of ionic sound waves in the plasma has been compared with the theoretically computed signal velocity. This theoretical signal velocity has the same form as the Tonks-Langmuir formula for phase velocity,

$$v = (\gamma k T_e)^{1/2} m_i^{-1/2} ,$$

where v is the wave velocity in cm/sec; γ is the adiabatic compression coefficient of the electron

UNCLASSIFIED
PHOTO P-60796

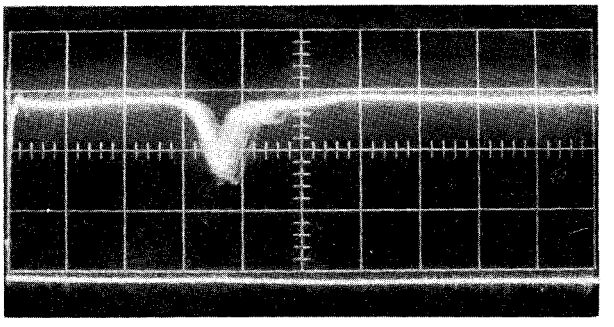

Fig. 3.29. Response of System Containing Argon Plasma. Horizontal scale, 10 μsec per large division. (Note the pickup from the driving pulse at $t = 0$.)

UNCLASSIFIED
PHOTO P-61758

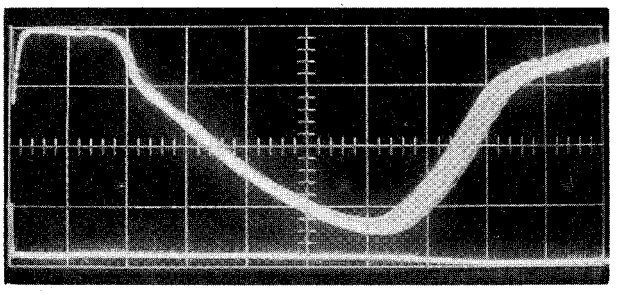

Fig. 3.30. Response of System Containing Helium Plasma. Horizontal scale, 5 μsec per large division. (Note the extreme dispersion of the pulse.)

gas, which has the permitted values of 1, $5/3$, and 3; k is Boltzmann's constant in ergs/°K; T_e is the electron temperature in °K; and m_i is the ion mass in grams. Since k and m_i are known and since v and T_e can be measured experimentally, it is perhaps possible to determine γ.

Experimental results which appear to reveal the correct value for γ are shown in Fig. 3.31. In this graph, the measured velocities for a variety of different atoms are plotted as a function of atomic mass. Each measured velocity has been normalized to an electron temperature of 1 ev, so that only the velocity dependence on ion mass is present. This normalization is accomplished by multiplying the measured velocity by $T_e^{-1/2}$, where T_e is the electron temperature which was measured during that specific run. The normalized experimental ion wave velocities are compared with the theoretically possible ion wave velocities computed for $T_e = 1$ ev, which are represented by the three straight lines in Fig. 3.31.

The comparison between the experimentally measured and the theoretically computed ionic-sound-wave-signal velocities in Fig. 3.31 reveal two basic facts. First, the experimental velocity agrees in general with the computed velocity. Second, the lighter atoms appear to have $\gamma = 3$, while the heavier atoms have $\gamma = 5/3$.

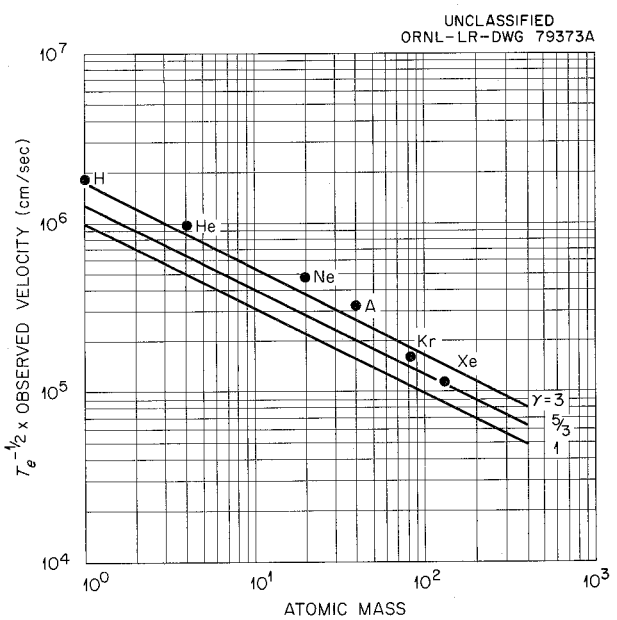

Normalized Observed Wave Velocity vs Atomic Mass.

Fig. 3.31. Graph of Normalized Observed Wave Velocity vs Atomic Mass.

The observed dependence of γ on ion mass is actually quite reasonable. The value of $\gamma = 3$ corresponds to the wavefront of the ion wave passing a given point in the plasma in a time short compared with the time required for the plasma electrons to scatter appreciably from the background un-ionized gas atoms in the system. Conversely, $\gamma = 5/3$ corresponds to the wavefront passing a given point in a time long compared with the time required for electron–gas-atom scattering. Now, for the lighter atoms, the value $\gamma = 3$ is more probable than for the heavier atoms for two reasons. First, as shown by Eq. (1), the ion wave velocity is higher when the ion mass is smaller. Second, at the electron temperatures being studied (about 4 ev) the electron–gas-atom scattering cross section is much smaller for the lighter atoms. Thus, for the lighter atoms, the electron–gas-atom scattering time is longer. Both the higher wave velocity and the longer electron-atom scattering time for the lighter gas atoms tend to make $\gamma = 3$ for the lighter atoms and, conversely, $\gamma = 5/3$ for the heavier ones.

Thus, in conclusion, measuring the ionic-sound-wave velocity directly by a time-of-flight technique is apparently quite easy. The wavefront appears to make itself observable by perturbing a cloud of electrons surrounding a hot cathode operating in the space-charge-limited regime. The observed wave velocity apparently agrees quite well with the computed wave velocity. Finally, one can tentatively compute the adiabatic compression coefficient, γ, of the electron gas, and also observe that γ varies in a predictable fashion with the type of gas atom used in forming the plasma. However, both the picture of the wave perturbing the cathode electron cloud, and the calculated values of γ are considered to be preliminary, and may be revised in the light of further experiments.

3.6 AUTOMATIC CONVERTER FOR A LANGMUIR PROBE

Igor Alexeff W. D. Jones

3.6.1 Introduction

In 1926, Mott-Smith and Langmuir[20] showed that, for a collector of any shape with a convex surface,

[20] H. M. Mott-Smith and I. Langmuir, *Phys. Rev.* **28**, 727 (1926).

the logarithm of the current taken from a Maxwellian distribution is a linear function of the voltage difference between the collector and the gas when the collector potential is such as to retard arriving electrons. For a cylindrical collector, such as a wire, operated at negative potentials, the relation takes the form,

$$\ln i = \frac{eV}{kT_e} + \text{constant}, \qquad (1)$$

where e is the electronic charge, V is the potential of the collector with respect to the gas, k is Boltzmann's constant, and T_e is the temperature of the electron distribution. The constant appearing in the equation depends upon the dimensions of the collector and the drift current of the electrons in the sheath surrounding the collector. A plot of log i vs the collector potential would accordingly give a straight line having a slope of e/kT_e for negative potentials.

3.6.2 Automatic Converter

A circuit has been devised which allows the characteristics of a Langmuir probe to be continuously displayed on an oscilloscope. Figure 3.32 shows the circuit which has been used to monitor continuously the electron temperature in a spherical discharge tube. The output of the logarithmic voltage converter[21] is fed into the vertical input of an oscilloscope, while the probe potential is fed into the horizontal input of the oscilloscope. The superposition of these two voltages gives, in effect, a plot of the logarithm of the probe current vs the probe potential. By using a double-beam oscilloscope, the probe potential can be fed into both the horizontal and vertical inputs of the second beam to give a calibration of the horizontal voltage sweep in terms of the vertical.

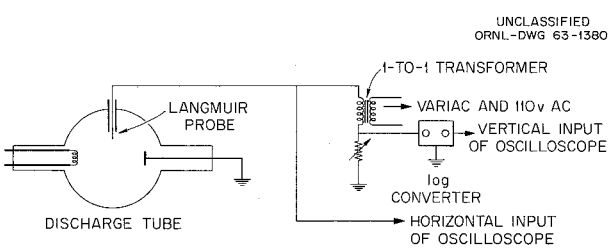

Fig. 3.32. Circuit for Continuous Monitoring of Electron Temperature in a Spherical Discharge Tube.

Figure 3.33 shows a typical plot of log i vs V, obtained by use of the circuit shown in Fig. 3.32. Since a 60-cycle alternating potential was applied to the probe, a plot of log i vs probe potential was obtained for both positive and negative probe potentials. For the purpose of comparison, Fig. 3.34 shows the results of simultaneous measurements of probe current and probe potential, made by use of dc potentials immediately after the data in Fig. 3.33 were obtained. In Fig. 3.34 an arbitrary positive-ion-current correction of 0.05 ma has been included. The lower curve of Fig. 3.33 shows the characteristic departure from linearity, due to failure to correct for positive-ion current. The extreme horizontal portions of the plot can be attributed to the fact that the current collected by a Langmiur probe saturates for large negative and positive probe potentials.

The electron temperature obtained from the slope of the Langmuir plot given in Fig. 3.33 is 3.5 ev, as compared with a value of 2.7 ev obtained from the data in Fig. 3.34. The agreement of these two values can be considered to be quite good, in view of the inherent uncertainty associated with information obtained from Langmuir probe data.

[21] Logarithmic Voltage Compressor model C-7A, Kane Engineering Laboratories, 845 Commercial Street, Palo Alto, Calif. This is a very compact, inexpensive, battery-operated device having a linear dynamic response for 0.1 to 100 v input. Operation from direct current to one megacycle is possible.

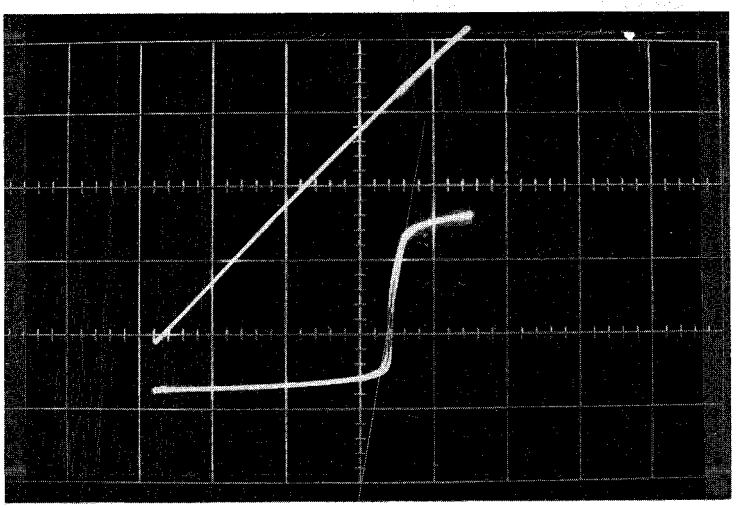

UNCLASSIFIED
PHOTO P-61719

XENON AT 17μ Hg

UPPER TRACE:
VERTICAL SCALE: 40v/cm
HORIZONTAL SCALE: 40v/cm

LOWER TRACE:
VERTICAL SCALE: 0.1 v/cm
(0.05 v CORRESPONDS TO A FACTOR OF *e* CHANGE IN PROBE CURRENT)
HORIZONTAL SCALE: 40v/cm

Fig. 3.33. Langmuir-Probe Plot Obtained by Use of the Automatic Converter.

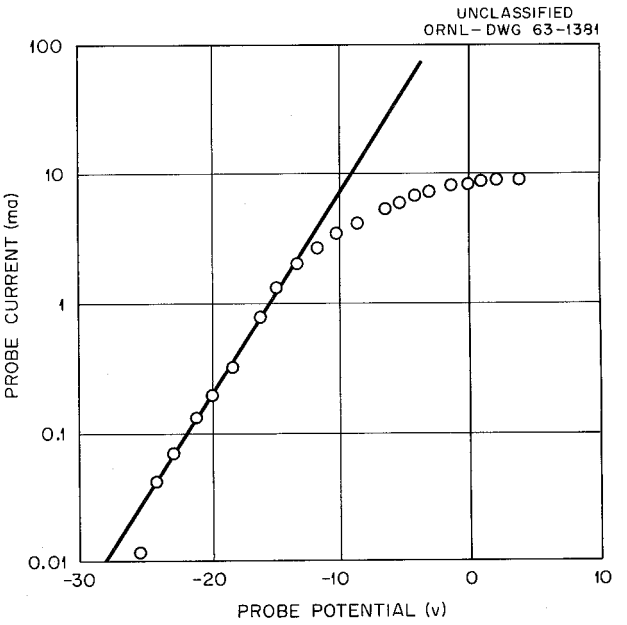

Fig. 3.34. Langmuir-Probe Plot Constructed from Simultaneous Measurements Made of Probe Current and Probe Potential.

4. Vacuum Arc Research

4.1 HIGH-DENSITY DEUTERIUM ARC ANALYSIS

R. A. Gibbons T. F. Rayburn

The high-density ($10^{14}/cm^3$) deuterium arc operated in the Gas Arc Facility has been shown to have a very highly ionized (~98%), essentially nonradiating plasma confined to the magnetic-field lines passing through the face of the cathode. Measurements and calculations based on the plasma properties reported earlier[1] indicated that the electrons and ions had well-defined temperatures with Maxwell-Boltzmann velocity distributions. Ideal-plasma calculations also indicated that there was a negligible potential drop along the plasma column. Consequently, the plasma seemed well suited to calculation of one-dimensional plasma-particle flows out of the plasma across potential sheaths at the anode and cathode. Using the balance of power, these calculations yielded equations for the plasma space potential, the electron temperature, and the power flow to the arc electrodes. These are expressed as functions of the arc current and voltage, the ion current and temperature, and the electron density, all of which have been independently measured. The electron temperature derived from the Langmuir-probe measurement on a particular arc was 45 ev. For the same arc the calculated electron temperature was 31 ev. Use of the lower electron temperature gave a power flow to the anode which was in good agreement with the measured value, while the higher temperature gave a power flow which was 50% too high. Generally the calculated anode powers are in good agreement with the measured values over a broad range of arc parameters.

[1]C. L. Cocke, Jr., *et al.*, *Thermonuclear Div. Progr. Rept. Oct. 31, 1961*, ORNL-3239, p 58.

4.1.1 Arc Potential Distribution

From ideal-plasma calculations of plasma resistivity,[2] the deuterium-arc plasma has a negligible potential drop along the magnetic field, as shown in Fig. 4.1. The plasma space potential is determined by the electron flow to the anode. An observed electron-drift velocity along the magnetic field which is smaller than the free-diffusion drift, $N\bar{v}/4$, requires an electron-retarding potential at the anode. This potential is easily calculable as $V = T_e(\ln I_0 - \ln I_e)$, where T_e is the electron temperature, I_0 is the free-diffusion electron current, $eAN\bar{v}/4$, and I_e is

[2]L. Spitzer, *Physics of Fully Ionized Gases*, p 86, Interscience, New York, 1956.

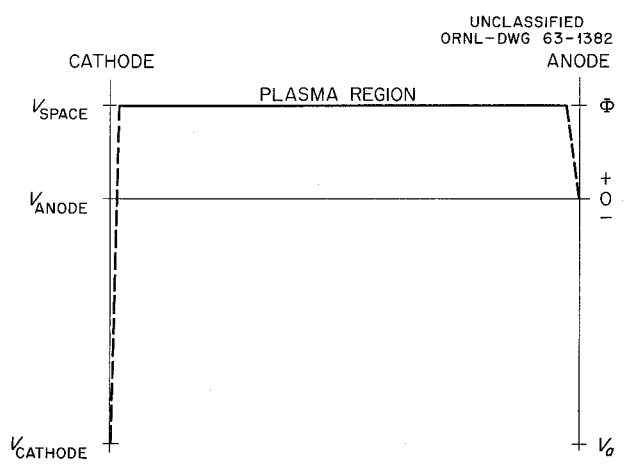

Fig. 4.1. Deuterium-Arc Potential Distribution.

the actual electron current. The deuterium-arc plasmas always have space potentials which are positive relative to the anode, as shown.

4.1.2 Electron Temperature from Plasma Power Balance

The power balance in the plasma can be used to calculate the electron temperature as a function of measurable parameters, using the calculated plasma space potential. The input power is the product of the primary electron current from the cathode (the arc current minus the ion current) and the voltage drop into the plasma (the arc voltage plus the space potential). The deuterium-arc plasma power output is primarily through charged-particle flow across the electrode sheaths.

For a Maxwell-Boltzmann distribution of charged-particle velocities with a temperature T, the power flow out of a plasma across a retarding potential V is

$$P_v = (2T + V)I_0 \exp(-V/T) ,$$

where I_0 is the free-diffusion current flux of particles, $eAN\bar{v}/4$. Assuming equal ion flow to both electrodes and employing the power flow formula above, power balance in the plasma gives a transcendental equation for the electron temperature,

$$T_e = \frac{\frac{1}{2}[I_a V_a - I_{0i}(4T_i + 2V_i + V_a)]}{(I_a + I_{0i})[1 + \exp(-V_a/T_e)] + I_{0i}[\ln(I_{0e}) - \ln(I_a + I_{0i})]} ,$$

where the subscripts a, e, and i denote arc, electron, and ion, respectively, and V_i is the deuterium ionization potential. The value of T_e is easily found by iteration starting with the experimental value. An arc with a calculated electron temperature of 31 ev yielded a Langmuir-probe temperature of 45 ev. The probe introduced an appreciable visible perturbation of the plasma and yielded an ion-density estimate which was high by about a factor of 2.

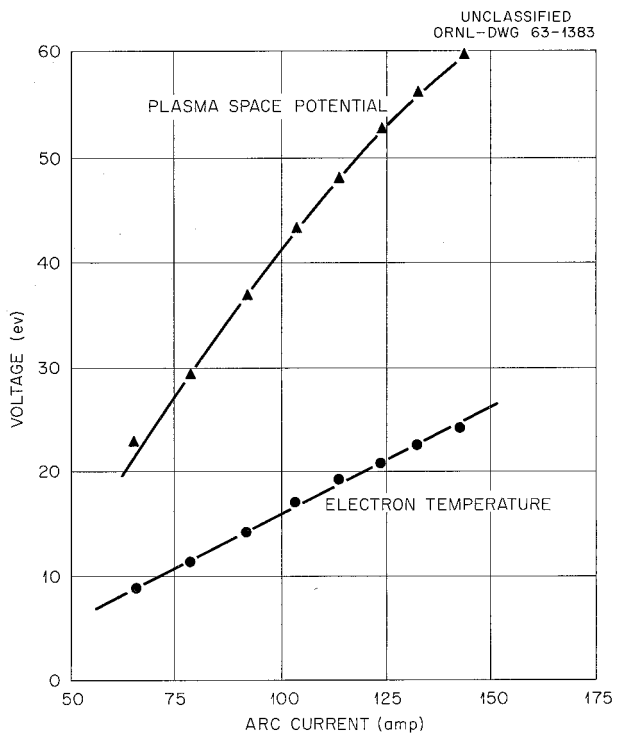

Fig. 4.2. Plasma Space Potential and Electron Temperature.

4.1.3 Electrode Power

Using the same approach, the power flow from the plasma to the electrodes can be calculated as a function of the arc parameters. The calculated and measured values of anode power have been found to agree well over a broad range of arc parameters. For one set of arc conditions, Fig. 4.2 shows the calculated plasma space potential and electron temperature as functions

of arc current. Figure 4.3 shows the corresponding calculated and measured values of anode power. The measured cathode power was about 20% below the calculated value.

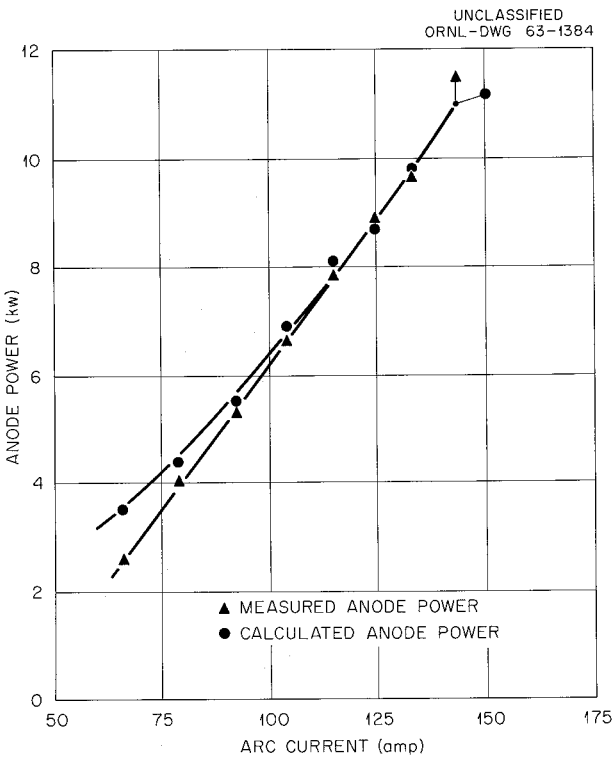

Fig. 4.3. Comparison of Calculated and Measured Anode Power.

4.2 SPECTROSCOPIC INVESTIGATIONS OF THE GAS-FED, MAGNETICALLY CONFINED, HIGH-CURRENT, CARBON ARC – THE QUESTION OF ION TEMPERATURE

J. R. McNally, Jr. M. R. Skidmore

4.2.1 Introduction

Doppler-broadened spectral lines indicative of ion temperatures up to 2.5×10^6 and 5×10^6 °K have been reported[3–5] for magnetically confined carbon arcs 8 and 16 ft long respectively. These results were based on the spectral-line profiles which were essentially Gaussian in shape for observations made transverse to the arc axis. Observations made approximately parallel to the arc axis revealed non-Gaussian and narrower line profiles near the cathode of the 16-ft-long arc. The ion "temperature" was reported to increase quadratically with the distance from the anode in a given arc, but the maximum temperatures were closely proportional to the actual length of a given arc. Although the different carbon-ion species gave essentially the same transverse ion-temperature parameter in an 8-ft-long carbon arc, the gas-fed carbon arcs gave significantly different temperature parameters for ions of different charge states. In addition, transverse-electric-field heating was proposed to provide preferential heating in the plane perpendicular to the arc axis (and the magnetic field).[5] It was recognized, however, that hot ions could escape readily along the flux lines and thus account in part for a local depletion of hot ions. The present report discusses the observed temperature parameters in terms of turbulence phenomena and a possible resonance type of heating at the ion-cyclotron frequency.

4.2.2 Turbulence

Similar charge- and mass-dependent effects have been reported elsewhere, notably in the Alpha, Zeta, and Stellarator discharges. The carbon arc shows a less marked dependence and hence may be somewhat better thermalized. It is customary in astrophysical research to express such nonthermal situations in terms of a turbulence relation,[6] which is valid for Gaussian distributions,

$$T_{\text{obs}} = T_{\text{th}} + Mv_{\text{tu}}^2/2k \ , \qquad (1)$$

where v_{tu}^2 is the velocity field due to turbulence. The turbulence term incorporates any actual oscillatory mass motion or other nonthermalized-ion heating; however, a *directed* mass flow would be exhibited as a spectral line shift (e.g., the "slant" effect[5]). A nonresonance, fluctuating

[3] J. R. McNally, Jr., and M. R. Skidmore, *Thermonuclear Div. Semiann. Progr. Rept. Oct. 31, 1962,* ORNL-3392, p 47.

[4] J. R. McNally, Jr., and M. R. Skidmore, *Thermonuclear Div. Semiann. Progr. Rept. Apr. 30, 1962,* ORNL-3315, p 45.

[5] J. R. McNally, Jr., and M. R. Skidmore, to be published in *Applied Optics.*

[6] See, for example, A. Unsöld, *Physik der Sternatmosphären,* Springer-Verlag, 1955.

electric field introduces a Z^2/M- and frequency-dependent term: under certain conditions[7] ($E \perp B$ and no damping) the turbulence term is dependent primarily on M.

Jones and Wilson[8] suggested that the mass-dependent relation best fits the Zeta data, whereas Zaidel *et al.*[9] have pointed out that a Z dependence fits the Brisish data at least as well as a dependence on Z^2/M or M. Hirschberg and Palladino[10] chose Z^2/M to fit the data of the B-65 Stellarator discharge, but again close inspection of their data reveals that a Z or Z^2 fit cannot be excluded. Although the data on Alpha suggests possibly an M and Z or Z^2 dependence, Zaidel *et al.*[9] have not specified the empirical form best suited to their data.

4.2.3 Radio-Frequency Spectra from the Carbon Arc

A Panoramic receiver coupled to the photoelectric output from a Jaco-Ebert 50-cm spectrometer showed a very broad noise spectrum up to 23 Mc/sec in the light emitted by the carbon arc. In addition, the top or bottom of the arc gave a pronounced signal at 120 kc, which decreased monotonically to 70 kc when the central field of the 10-ft solenoid was reduced from 8300 to 3600 gauss. This latter oscillation is believed to be related to the "slant" effect (due to a precessional drift of ions with bunching about the arc column) which has a rotational drift frequency in this range.[11] Magnetic and electrostatic probe studies also have revealed significant noise structure in the megacycle range.[12]

The presence of a noise spectrum in the spectral emission and in the probe studies suggests that the oscillating electric fields productive of light noise and radio spectra may induce irreversible ion heating. A resonance coupling could occur at the ion-cyclotron frequencies ($\sim 13Z/A$ Mc at 8300 gauss, where A is the atomic weight) such that ion-bunching oscillations at the cyclotron frequencies would enhance electron pigging action at this frequency and thus permit resonance transfer of energy from electrons to ions and vice versa.

4.2.4 Resonance Ion-Cyclotron Heating

The ion energy attainable in an electric field that is oscillating at the ion-cyclotron frequency is of the form[13]

$$E_i = \tfrac{1}{2}\left[Mv_0^2 + Zev_0 t\xi_0 \cos\phi + \frac{Z^2e^2\xi_0^2 t^2}{4M} + \frac{Z^2e^2\xi_0^2}{4M\omega_i^2}\sin^2\omega_i t + \frac{Z^2e^2\xi_0^2 t}{4M\omega_i}\sin 2\omega_i t + \frac{Ze\xi_0 v_0}{M\omega_i}\sin\omega t\cos(\omega t+\phi)\right], \quad (1)$$

where $Mv_0^2/2$ is the initial kinetic energy of the ion, ξ_0 is the amplitude of the electric field oscillating at the ion-cyclotron frequency ω_i, Z is the effective charge of the ion, and ϕ is a phase angle. The exact dependence of E_i on M and Z is not obvious from this expression. The second term may add to or subtract from the initial energy, but if the coefficient is sufficiently large, net energy may be gained by the ion regardless of the phase angle. The third term is probably of major importance in resonance radio-frequency heating of electrons in magnetic fields.[14]

---

[7] P. C. Thonemann, *Optical Spectrometric Measurements of High Temperatures*, p 56, University of Chicago Press, Chicago, 1961.

[8] B. B. Jones and R. R. Wilson, IAEA Conference on Plasma Physics and Controlled Nuclear Fusion Research, Salzburg, September 1961, Paper CN-10/57.

[9] A. N. Zaidel, O. V. Konstantinov, and G. M. Malyshev, *Soviet Phys. – Tech. Phys. (English Transl.)* **7**, 265 (1962).

[10] J. G. Hirschberg and R. W. Palladino, *Phys. Fluids* **5**, 48 (1962).

[11] P. M. Griffin, J. R. McNally, Jr., and G. K. Werner, *Temperature, Its Measurement and Control in Science and Industry* (ed. by F. G. Brick Wedde), vol 3, p 651, Reinhold, New York, 1962.

[12] J. E. Francis, Jr., and R. F. Stratton, oral discussions, 1963.

[13] J. G. Linhart, *Plasma Physics*, Interscience, New York, 1960.

[14] R. A. Dandl, oral discussions, April 1963.

The expression (1) may also be written

$$E_i = Mv_0^2/2\left[1 + Z\omega t\cos\phi + \frac{Z^2\omega^2t^2}{4} + \frac{Z^2\omega^2}{4\omega_i^2}\sin^2\omega_i t + \frac{Z^2\omega^2 t}{4\omega_i}\sin 2\omega_i t + \frac{Z\omega}{\omega_i}\sin\omega_i t\cos(\omega_i t + \phi)\right],$$

where ω is a measure of the heating rate and is simply $e\xi_0/Mv_0$. Thus, if $\omega = \omega_i$ and $t = 1/\omega_i$ there will be significant heating contributions from the various terms, some of which will oscillate in time. This suggests the advisability of time studies of sections of the line profile to ascertain any fluctuations at ω_i or $2\omega_i$. If $\omega = \omega_i$, the required amplitude of the electrostatic field is $\xi_0 = Bv_0/c \leq 8000(10^7)/3\times 10^{10} = 2.7$ esu = 800 v/cm. This is significantly higher than the macroscopic field of the arc ($E_r \approx -100$ v/cm) being of the order of the interionic fields. It is possible that the individual filaments[15] may undergo fluctuations of several tens of volts and, since r is of the order of a millimeter, give rise to quite large local fields. The large size of the Larmor orbit of the ions might then require all filaments to oscillate in phase and/or the time scale to be extended somewhat.

No definite conclusions can be reached at this time on the feasibility of resonance heating of ions in the carbon arc at the ion-cyclotron frequencies. Alternatively, it is possible that irreversible heating via collisions and the radial electrostatic fields may be adequate to account for a mean ion energy several times the radial potential differences.

The carbon ions (C^+, C^{2+}, and C^{3+}) were believed to be reasonably well thermalized in an 88-in.-long, non-gas-fed, carbon arc studied earlier[16,17] because the observed ion temperatures agreed within about 10% of each other. However, the rapid resonance charge-transfer processes among the different carbon-ion species may have accounted in part for this apparent equalizing of ion energies so that the individual ion species rapidly lost their specific charge identity. In contrast, the gas-fed arcs[17,18] do reveal a strongly charge-dependent ion temperature, though not as marked as in other discharges.[8-10] Figures 4.4 and 4.5 show the observed and theoretical (Gaussian-fitted) line profiles for N^+ and N^{3+} in an 8-ft-long, nitrogen-fed, carbon arc confined by a magnetic field of 8000 gauss. The line profiles are closely Gaussian except for an excess of very fast ions in the wings of the N^+ profile. No dependence of the observed ion temperature on the mass of the ion has yet been distinguished from observations on helium, carbon, nitrogen, and argon ions, suggesting that possibly a Z or Z^2 dependence might give an appropriate interpretation of the data. If this is the case, the thermal and turbulence terms might be expressed as

$$T_{obs} = 0.5\times 10^6 + 10^6 Z$$

or

$$T_{obs} = 1.2\times 10^6 + (0.3\times 10^6)Z^2$$

from the data[17,18] for N^+ (1.5×10^6 °K), Ar^+ (1.4×10^6 °K), C^{2+} (2.5×10^6 °K), N^{2+} (2.5×10^6 °K), and Ar^{2+} (2.6×10^6 °K) for a 96-in. arc observed about 88 in. from the anode. Data for C^+ (2.0×10^6 °K) and N^{3+} (2.5×10^6 °K) have not been used because of suspected extraneous influences (see above on carbon resonance charge-exchange mechanism).

Elucidation of the actual dependence of observed ion temperature on the basis of studies of higher ion stages as well as the development of a correct interpretation of the mechanism for heating in the carbon arc seems warranted. The coexistence of very "hot" ions with relatively cooler electrons (~40,000°K excitation temperature) indicates the presence of a vigorous ion-heating mechanism to offset the rapid classical heating loss to the colder electrons. If the turbulence is due to radial electric-field fluctuations and insufficient ion-ion collisions to

[15] G. K. Werner *et al.*, *Thermonuclear Proj. Semiann. Rept. Jan. 31, 1960*, ORNL-2926, p 44.

[16] J. R. McNally, Jr., and M. R. Skidmore, *Thermonuclear Div. Semiann. Progr. Rept. Apr. 30, 1962*, ORNL-3315, p 45.

[17] J. R. McNally, Jr., and M. R. Skidmore, to be published in *Applied Optics*.

[18] J. R. McNally, Jr., and M. R. Skidmore, *Thermonuclear Div. Semiann. Progr. Rept. Oct. 31, 1962*, ORNL-3392, p 47.

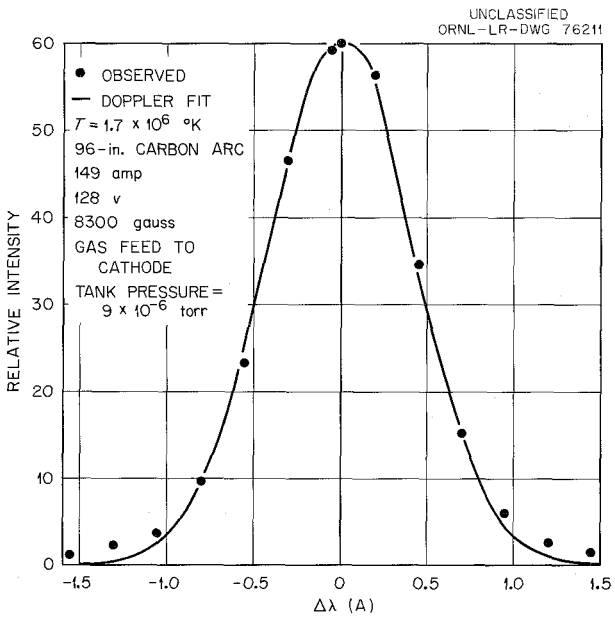

Fig. 4.4. Line Profile of N^+ λ 3955 A.

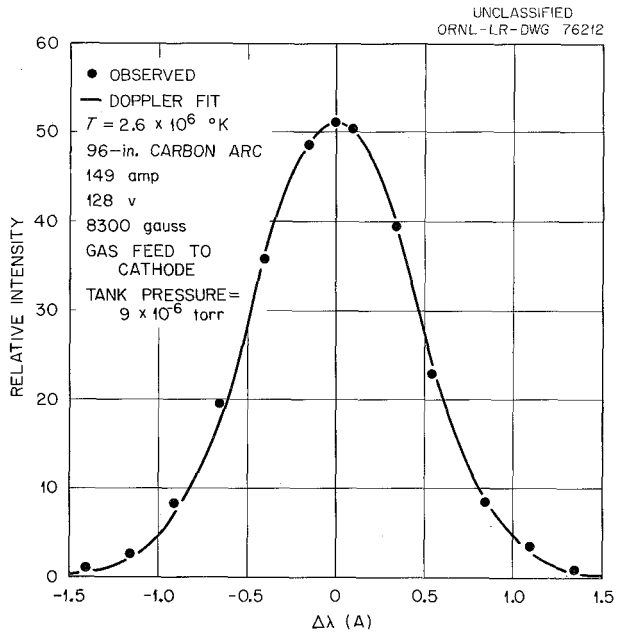

Fig. 4.5. Line Profile of N^{3+} λ 3479 A.

thermalize the distribution, it is probable that observed "temperatures" are not meaningful, even separately for each ion class; hence, until more is known about the mechanisms it seems appropriate to refer to the observed ion temperatures as turbo-thermal temperatures.

4.2.5 Future Work

Experiments with deuterium gas feed in a 20-ft-long carbon arc are contemplated, because of the possibly important collisional phenomena even in a turbulent discharge. Neutron detection will probably be marginal, since the turbo-thermal temperature may only be about 4×10^6 °K for D^+.

4.2.6 Acknowledgments

Acknowledgment is made to J. E. Francis, Jr., for contributions on the study of the radio-frequency spectra in the spectral signals.

5. Cross Sections

5.1. DISSOCIATION OF H_2^+ IN HYDROGEN GAS

C. F. Barnett J. A. Ray R. M. Warner

During the past six years various investigators have published the results of their measurements of the dissociation cross section of H_2^+ in hydrogen gas in the energy range 10 to 200 kev. The absolute cross sections were in disagreement by a factor of 3 or 4, and indications are that the measurements made at ORNL in 1957[1] were low by a factor of 2. The cross section has been remeasured and reevaluated in an attempt to determine if any experimental errors existed in the previous work.

A schematic diagram of the apparatus is shown in Fig. 5.1. Ions were accelerated to energies of 40 to 600 kev by a conventional accelerator and were passed through a magnetic analyzer. The H_2^+ beam was collimated and entered a differentially pumped gas cell where dissociating collisions occurred. The proton and H_2^+ beams emerging from the gas cell were passed through a parallel-plate electrostatic analyzer and then detected by means of a Faraday cup.

Dissociation collisions involving an energetic H_2^+ and a gas molecule follow the Franck-Condon principle, which implies that an electronic transition takes place so quickly that the nuclei have no time to move an appreciable distance. Thus the H_2^+ ions are excited from the stable ground state $^2\Sigma_g$ to a repulsive state during the interaction. Classically, the potential energy of the repulsive state is divided equally between the ions and atoms and is distributed isotropically in the center-of-mass system of the colliding particles. The imparting of 4 to 6 v of energy at angles up to 90° to the direction of travel results in inelastic scattering accompanying the collision. This inelastic scattering dictates that the exit aperture of the gas cell be made much larger than the entrance. The gas-cell geometry was changed from a 0.030-in. entrance, 0.125-in. exit, and 4.75-in. length to a 0.010-in. entrance, 0.150-in. exit, and 2-in. length to ensure that all particles were being collected. No detectable differences in cross sections were noticed when the geometry of the gas cell was changed.

The spatial extent of the proton beam at the detector was large due to the inelastic scattering. A Faraday cup was constructed with a grounded entrance aperture in the form of a 0.032 × 1.5 in. slit. The collector cup and bias electrodes were constructed in similar shape, and such geometry provided easy saturation of the bias potentials. The detector was driven at a constant rate across the beam, with the current output from the collector electrode being fed into a current integrator.

Gas streaming out of the large-exit aperture implies end connections to the geometric length of the gas cell in determining the target thickness *nl*. The target thickness was determined by measuring the attenuation of a proton beam as the pressure in the target chamber was increased. From previous work the electron capture cross section is known, so that *nl* can be calculated from the usual exponential attenuation relation. Then, without changing the gas flow, the proton beam was replaced by H_2^+, and the proton and H_2^+ components were measured. The total beam available for dissociation was given by the sum of H^+, H_2^+, and H_2^0, where the magnitude of the H_2^0 was calculated from a knowledge of the electron capture cross section of H_2^+ and the target thickness. Also the assumption was made that in the energy region of interest the electronic transitions were to the repulsive level $^2\Sigma_u$, resulting in a proton and hydrogen atom.

[1] C. F. Barnett, *Proc. U.N. Intern. Conf. Peaceful Uses At. Energy, 2nd, Geneva 1958* **32**, 398 (1959).

UNCLASSIFIED
ORNL-DWG 63-1385

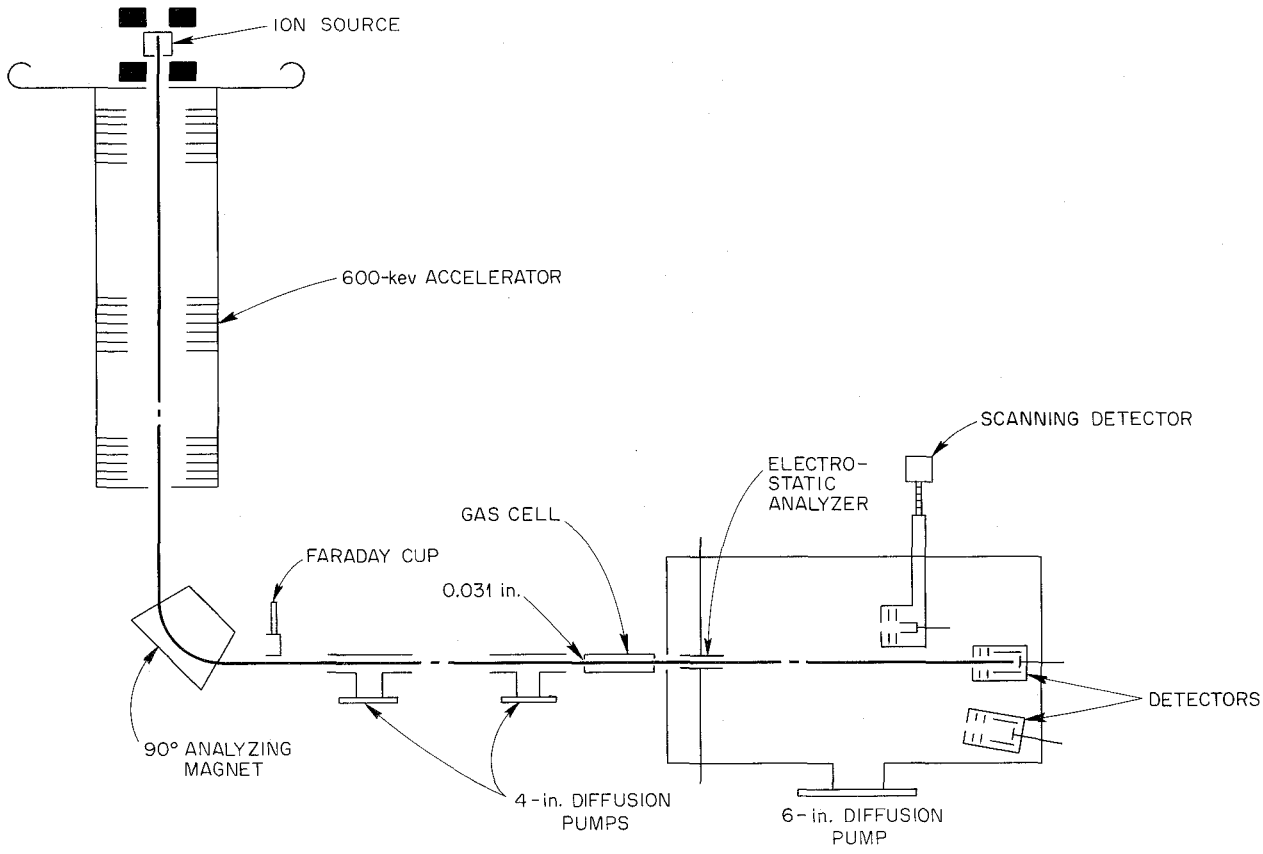

Fig. 5.1. Schematic Diagram of Apparatus Used in Dissociation Cross-Section Experiments.

The suggestion had been made that the cross section for dissociation of H_2^+ might depend on the degree of vibrational excitation of the H_2^+ ion, and this may be a possible explanation for the discrepancies of different investigators in the value obtained for this cross section. To determine if the type of ion source produced H_2^+ ions in different average vibrational levels that would influence the cross section, a radio-frequency ion source was interchanged with a Phillips ionization type source (PIG). The results are shown in Fig. 5.2, in which the proton production cross section from H_2^+ ions originating in a PIG source is compared with that of ions originating in an rf source, both given as a function of energy. There is a tendency for the cross section to be lower when ions come from a PIG source; however, the values are within the experimental accuracy, which is ±10%.

UNCLASSIFIED
ORNL-DWG 63-1386

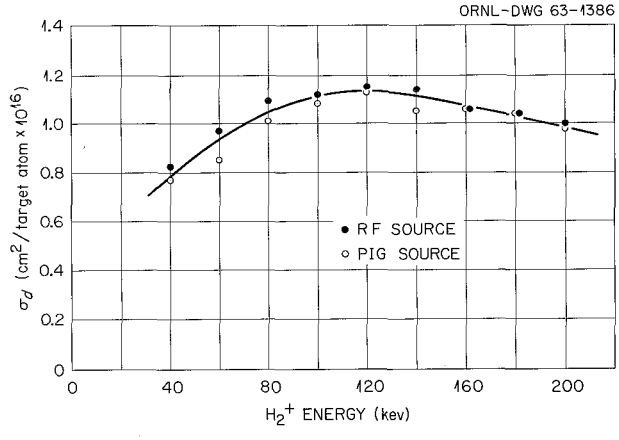

Fig. 5.2. Dissociation Cross Section of H_2^+ in H_2 Gas as a Function of Particle Energy. Comparison of cross section of H_2^+ from rf and PIG source.

The probability that an H_2^+ ion would be produced in a given vibrational level by electron impact on H_2^0 can be determined by calculating the overlap of the wave functions for the initial vibrational level of the H_2 molecule and the final vibrational level of the ion. For example, impacts of electrons with H_2 molecules in the second vibrational level may result in H_2^+ ions more highly excited, on the average, than if they had been produced from H_2^0 in the ground vibrational level. Since hydrogen diffuses through palladium in the atomic form, the possibility exists that on recombining at the palladium surface the H_2 molecules will be formed in some states of vibrational excitation. Accordingly, an experiment was performed to see if anything could be gained by using this artifice. Using a PIG source, a palladium leak was interchanged with a mechanical leak to admit H_2 gas to the ion source. The results obtained are shown in Fig. 5.3, where the ratio of the proton production cross sections obtained with the two leaks is plotted as a function of energy. There was no essential difference in the cross section when either of the leaks was used.

Further investigation revealed that two sources of error were present in the earlier cross-section measurements. Both sources of errors arose in determining the areal target thickness. The target thickness was usually measured at 60 or 100 kev, and since the electron capture cross section is a steep function of energy in this range, one must know the proton energy precisely. The PIG sources normally operate at a low pressure and with a 7.5-kev potential between the anode and cathode. With these operating conditions, ions were formed on different equipotential lines, and the energy spread of the ions from the source was 0 to 7.5 kev. Failure to know the ion energy within these limits can result in a factor of 1.8 in the measurement of the dissociation cross section. The other error occurred in the region in front of the dissociating cell. When protons suffer an electron-capture collision, essentially no scattering takes place, and all collisions before the H_2^+ beam entered the gas cell will be detected by the particle detectors. However, in dissociating collisions, internal potential energy is converted to kinetic energy with a resulting divergence of the dissociated particles. Therefore, all dissociating collisions in these regions will not be detected, and the resulting cross section will be small. These difficulties have been eliminated by (1) using an rf source or operating the PIG source at a higher gas flow with small anode-to-cathode potentials and (2) reducing the entrance aperture of the gas cell to 0.010 in. to minimize any pressure increase exterior to the gas cell. With these corrections, the cross section for proton production was redetermined, and it is shown as a function of energy in Fig. 5.4. Also shown are the values obtained by investigators[2] at other laboratories. There is a clustering within ±10% of the cross-section values except for the measurements of Fedorenko, which are higher than the average values by 50 to 80%. The values obtained by Schmid are consistently higher than the average.

Riviere and Sweetman[3] have found that the higher vibrational levels (v = 18, 17) of H_2^+ are relatively about five times more populated when H_2^+ is formed from the dissociation of H_3^+ than when H_2^+ is formed in a source. They have also compared the dissociation cross section (for proton production) of H_2^+ in hydrogen gas in the two cases: H_2^+ from an ion source, and H_2^+ formed

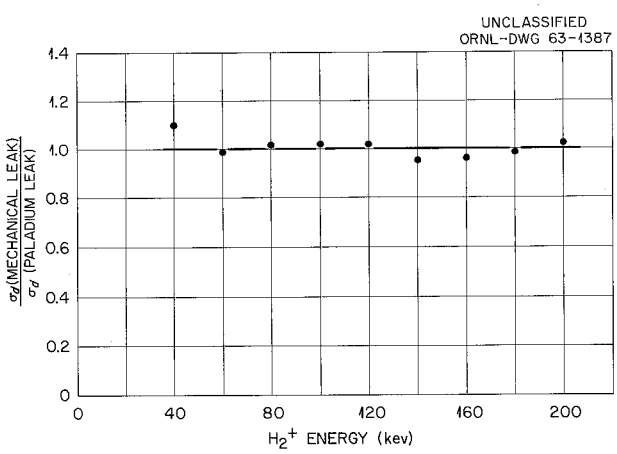

Fig. 5.3. Ratio of the Dissociation Cross Section of H_2^+ Produced in a PIG Source with a Mechanical Leak to That Produced with a Palladium Leak.

[2]G. W. McClure, "Charge Exchange and Dissociation of H^+, H_2^+, and H_3^+ Ions Incident on Hydrogen Gas," to be published in *Physical Review*; D. R. Sweetman, *Proc. Roy. Soc. (London)* **A256**, 416 (1960); A. Schmid, *Z. Physik* **161**, 550 (1961); N. V. Fedorenko *et al.*, *JETP* **36**, 267 (1959); J. Guidini, *Compt. rend* **253**, 829 (1961).

[3]A. C. Riviere and D. R. Sweetman, *Phys. Rev. Letters* **5**, 560 (1960).

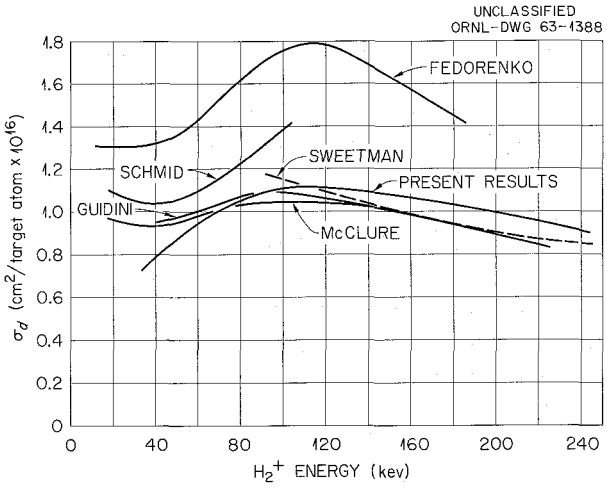

Fig. 5.4. Dissociation Cross Section for Proton Production of H_2^+ in Hydrogen Gas. Comparison of the present results with data of Schmid, Fedorenko, McClure, Sweetman, and Guidini.

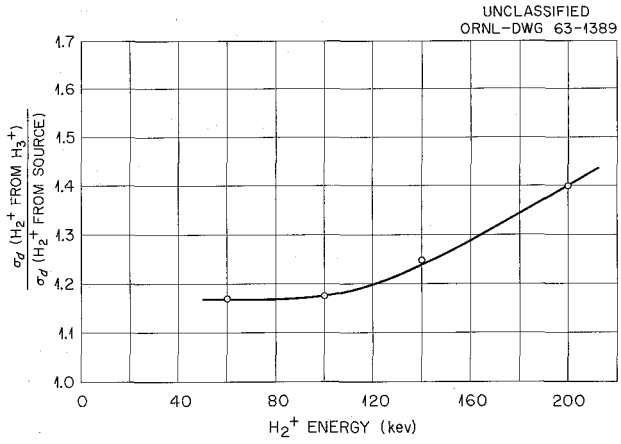

Fig. 5.5. Ratio of the Dissociation Cross Section of H_2^+ Produced by H_3^+ Dissociation to That Produced from a PIG Source.

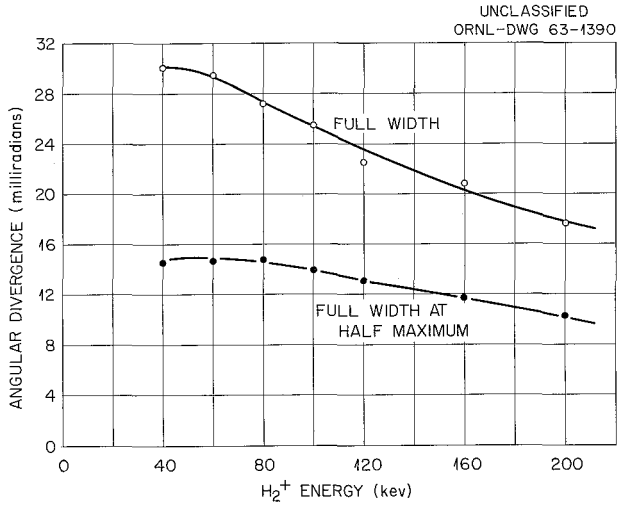

Fig. 5.6. Angular Divergence of H^+ Resulting from the Dissociation of H_2^+ in Hydrogen Gas.

from H_3^+. They found[4] that in the energy range 280 to 670 kev the dissociation cross section is 7% higher for H_2^+ ions formed from H_3^+ than it is when the H_2^+ ions were taken directly from their ion source.

This experiment has been repeated here in the energy range 40 to 200 kev. Our ratios of the proton production cross section for H_2^+ from H_3^+ are shown in Fig. 5.5. At the lower energies the cross section is 16% greater, while at 200 kev the cross section is 40% greater. These differences are considered to be outside the experimental error and suggest a larger effect than was observed by Riviere and Sweetman. Apparently, vibrational levels do indeed have considerable influence on the magnitude of the dissociation cross section.

The angular divergence of the proton beam from the dissociation of H_2^+ in hydrogen is shown in Fig. 5.6. Two curves are plotted as a function of energy: (1) the total angular full width of the beam, and (2) the angular width at half maximum amplitude. An elementary calculation can be made for the angular spread if a Gaussian distribution is assumed for the scattered particles.

The rms angle about the direction of the primary beam is given by $\overline{\Delta\theta^2} = \overline{\Delta E}/E$, where $\overline{\Delta E}$ is the average energy given to the H^+ particle and E is the H_2^+ particle energy.

The average $\overline{\Delta E}$ calculated in this manner is 4.5 v, suggesting that in this energy range most of the dissociating collisions result from a transition from the $^2\Sigma_g$ state to the repulsive $^2\Sigma_u$ state, which results in H^+ and H^0 particles.

[4] A. C. Riviere and D. R. Sweetman, *Proc. Phys. Soc.* **78**, 1215 (1961).

5.2 DISSOCIATION OF H_3^+ AND HeH^+ IN HYDROGEN GAS

In a similar manner the dissociation cross section for H_3^+ in hydrogen gas has been measured; the results are shown in Fig. 5.7. The cross section for both proton formation and H_2^+ formation is shown as a function of energy. The cross section for proton production is a factor of 2 greater than that for H_2^+ production. Measurements of the angular divergence indicated a full-width angular spread of 47 milliradians at 40 kev, decreasing to 35 milliradians at 200 kev.

Preliminary measurements have been made on the dissociation cross section for the helium hydride ion, HeH^+. Results indicate that the HeH^+ ion was strongly attenuated in passing through a gas, the principal reaction being electron capture that forms the unstable HeH molecule. The probability of formation of either He^+ or H^+ is small for energies of 100 kev. Additional measurements are being made to determine the absolute cross section.

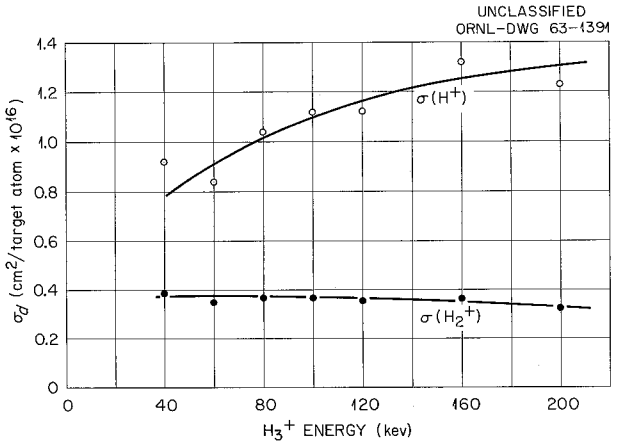

Fig. 5.7. Dissociation Cross Section of H_3^+ in Hydrogen Gas for the Production of Protons and H_2^+.

5.3 FORMATION OF NEUTRAL ATOMIC HYDROGEN BEAMS

C. F. Barnett Mozelle Rankin
J. A. Ray

To complement the present knowledge of energetic hydrogen-atom formation from electron capture by protons, the production of H^0 from dissociating collisions of H_3^+ and H_2^+ has been studied up to energies of 450 kev. Electron-capture collisions result in essentially no scattering during the collision process; however, the dissociating collisions can be accompanied by directional changes. Any H^0 beam formed in this manner will possess an inherent angular divergence, regardless of the initial beam divergence. This angular divergence has been measured to determine the feasibility of injection of fast neutral beams into a magnetic-mirror geometry.

When an H_3^+ traverses a thick[5] gaseous target, it can be dissociated in any of the following primary ways:

$$H_3^+ + H_2 \longrightarrow H_3^0 \rightarrow 3H^0 \qquad \sigma_1$$
$$\longrightarrow H_2^+ + H^0 \qquad \sigma_2$$
$$\longrightarrow H_2^0 + H^+ \qquad \sigma_3$$
$$\longrightarrow 2H^+ + H^0 + e \qquad \sigma_4$$
$$\longrightarrow 3H^+ + 2e \qquad \sigma_5$$
$$\longrightarrow 2H^0 + H^+ \qquad \sigma_6$$

The secondary particles can undergo subsidiary reactions, where again we disregard the fate of the target molecule:

$$H_2^0 + H_2 \longrightarrow 2H^0 \qquad \sigma_7$$
$$\longrightarrow H^+ + H^0 + e \qquad \sigma_8$$
$$\longrightarrow 2H^+ + 2e \qquad \sigma_9$$
$$\longrightarrow H_2^+ + e \qquad \sigma_{10}$$
$$H_2^+ + H_2 \longrightarrow H_2^0 \qquad \sigma_{11}$$
$$\longrightarrow 2H^0 \qquad \sigma_{12}$$
$$H_2^+ + H_2 \longrightarrow H^+ + H^0 \qquad \sigma_{13}$$
$$\longrightarrow 2H^+ + e \qquad \sigma_{14}$$
$$H^+ + H_2 \longrightarrow H^0 \qquad \sigma_{15}$$
$$H^0 + H_2 \longrightarrow H^+ + e \qquad \sigma_{16}$$

The reactions refer only to the energetic reaction products. The first six of the reactions

[5]A thick target is one in which the initial ion or its reaction products undergo several collisions.

occur at the initial H_3^+ energy E_0, while reactions seven through fourteen occur at $\frac{2}{3}E_0$ and fifteen and sixteen at $\frac{1}{3}E_0$.

One can write five coupled differential equations that predict the change of each of the five beam components as the target gas is varied in density or length. They are as follows:

$$\frac{dH_3^+}{d(nl)} = -(\sigma_1 + \sigma_2 + \sigma_3 + \sigma_4 + \sigma_5 + \sigma_6)H_3^+ , \quad (1)$$

$$\frac{dH_2^+}{d(nl)} = \sigma_2 H_3^+ + \sigma_{10} H_2^0 - (\sigma_7 + \sigma_8 + \sigma_9 + \sigma_{10})H_2^+ , \quad (2)$$

$$\frac{dH_2^0}{d(nl)} = \sigma_3 H_3^+ + \sigma_{10} H_2^+ - \sigma_7 H_2^0 , \quad (3)$$

$$\frac{dH^0}{d(nl)} = (\sigma_1 + \sigma_2 + \sigma_4 + \sigma_6)H_3^+ + (\sigma_7 + \sigma_8)H_2^0 + (\sigma_{12} + \sigma_{13})H_2^+ + \sigma_{15}H^+ - \sigma_{16}H^0 , \quad (4)$$

$$\frac{dH^+}{d(nl)} = (\sigma_3 + \sigma_4 + \sigma_5 + \sigma_6)H_3^+ + (\sigma_8 + \sigma_9)H_2^0 + (\sigma_{13} + \sigma_{14})H_2^+ + \sigma_{16}H^0 - \sigma_{15}H^+ . \quad (5)$$

Analytical solutions have been obtained for these equations, with the H^0 component being described as

$$H^0 = Ue^{-Ax} + Ve^{-Bx} + We^{-Dx} + e - \frac{Q}{R-A} \times (e^{-Ax} - e^{-Rx}) - \frac{S}{R-B}(e^{-Bx} - e^{-Rx}) - \frac{Y}{R-D}(e^{-Dx} - e^{-Rx}) - \frac{Z}{R}(e^{-Rx} - 1) , \quad (6)$$

where $x = nl$ and the constants are combinations of the 16 cross sections. Inspection of Eqs. (1–5) reveals that the H_3^+ component decays as a simple exponential as the gas thickness is increased, but both H_2^+ and H_2^0 are described by the difference of two exponentials, with the magnitude of each component increasing to a maximum and then decreasing to zero. The equations predict that at large gas densities the H_3^+, H_2^+, and H_2^0 components will approach zero, and then from either Eq. (4) or (5) one finds that the ratio of H^+ to H^0 is given by the ratio of the electron-capture to the electron-loss cross section. This result is the same as if H^+ or H^0 of appropriate energy was incident on the gas chamber.

An experimental check of the production of H^0 according to these relations has been carried out. The apparatus used in the measurements was similar to that described in the H_2^+ dissociation cross-section experiments. Since the gas target pressure was increased to several microns, the exit aperture was replaced by a 0.005-in. movable slit. Some of the H^0 beam was formed from two or more dissociating collisions; so the H^0 beam had a large spatial spread at the detector. A detector was constructed which consisted of a negative biased plate surrounded by a 6-in.-long cylinder 2.5 in. in diameter. Secondary electrons were liberated from the plate and collected by the cylinder. A transverse magnetic field at the detector entrance prevented any secondary electrons from escaping. The detector was calibrated by measuring the secondary-electron yield from proton bombardment and applying the usual correction for the secondary-electron yield which is higher for neutral hydrogen atoms than for protons.

To ensure that this detector was 100% efficient, the 0.005-in. movable slit was replaced with a 6-in. liquid-nitrogen-cooled tube, whose axis coincided with the path of the beam. The tube was placed exterior to the gas-cell exit, and the liquid nitrogen provided sufficient pumping of water vapor to prevent a pressure increase in the detector region. With this geometry the magnetic detector was replaced with the movable-slit detector described previously. The pressure in the gas cell was measured and continuously monitored by an alphatron pressure gage, which was calibrated with a mercury manometer.

The number of H^0 atoms formed per incident 60-kev H_3^+ or H_2^+ is plotted as a function of target thickness of water vapor in Fig. 5.8. For energies of 60 kev the number of atoms per ion increased monotonically to a plateau as the gas pressure was increased. For energies of 400 kev the H^0 yield was found to reach a maximum and then to slowly decrease to an equilibrium value. The gas-cell thickness at which maximum H^0 production was obtained was relatively insensitive to the incident-particle energy. Agreement between the experimental values and those predicted by Eq. (6) is unsatisfactory. Evaluation of Eq. (6) gives only the variation of H^0 with gas

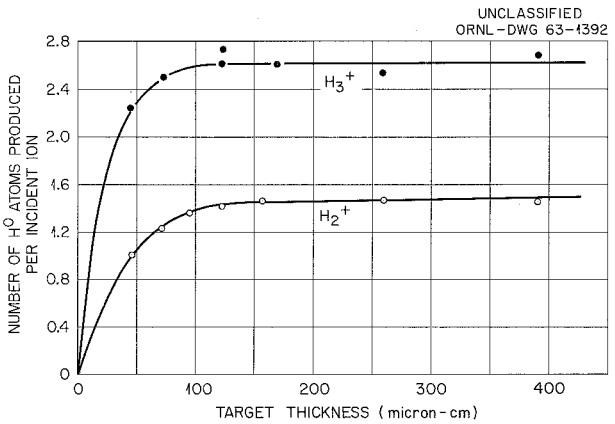

Fig. 5.8. Production of H^0 by the Dissociation of 60-kev H_3^+ and H_2^+ in Water Vapor as a Function of Target Thickness.

thickness. The predicted target thickness for maximum production of 100-kev H_3^+ in hydrogen was 260 micron-centimeters, whereas the experimental value was 450 micron-centimeters. This discrepancy of nearly a factor of 2 probably arises from insufficient knowledge of the 16 cross sections needed in evaluating Eq. (6).

The maximum number of H^0 atoms produced as a function of velocity is shown in Fig. 5.9 for both H_3^+ and H_2^+ in hydrogen and in Fig. 5.10 for water vapor. In each of the cases the curves may be characterized by an equation of the form $F(H^0) = Ae^{-Bv}$, where A and B are constants for each gas and v is the particle velocity. From Fig. 5.9 one sees that at the lowest velocity, corresponding to an energy of 60 kev, the number of atoms produced per incident H_3^+ was greater than three. This discrepancy arises from the inaccuracies incurred in measuring the secondary-electron emission coefficient. For energies of 20 kev the beams from the accelerator were unstable and of low intensity. The reproducibility of the coefficient was 20% at this energy, and the error bars shown in Fig. 5.10 represent the reproducibility of the data at low energies. For energies greater than 100 kev the reproducibility is within 5%. In any event, the production of H^0 in hydrogen was more efficient than in water vapor. This higher efficiency was probably the result of resonance-like collisions between the molecular ions and hydrogen molecules.

By moving the slit detector over the spatial extent of the H^0 beam, the angular divergence was

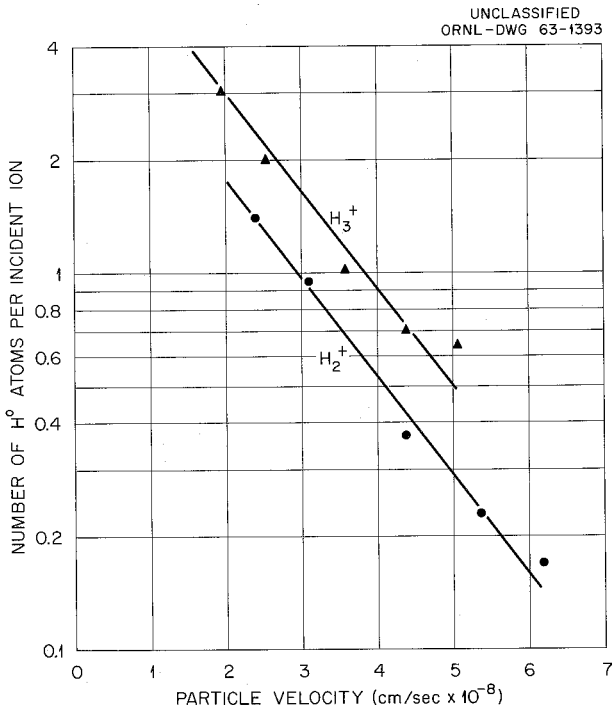

Fig. 5.9. Production of Neutral Particles on Passing H_3^+ and H_2^+ Through Hydrogen.

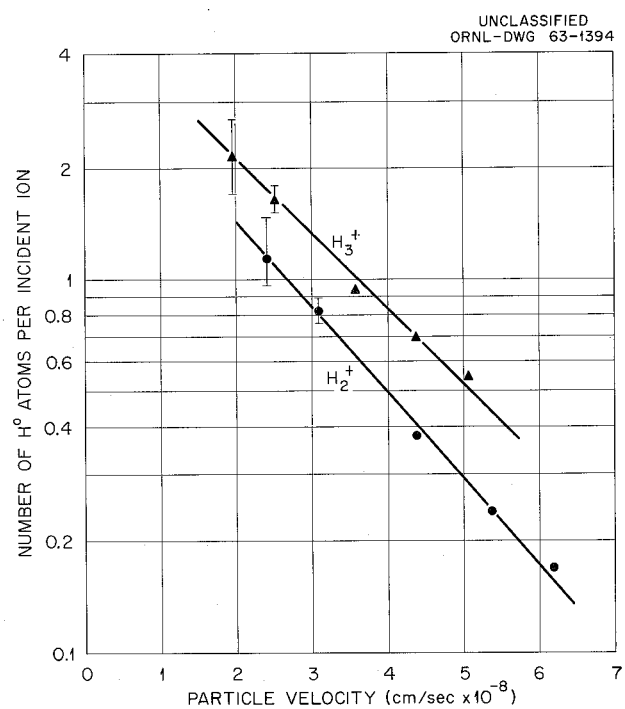

Fig. 5.10. Production of Neutral Particles on Passing H_3^+ and H_2^+ Through Water Vapor.

measured; the results are shown in Fig. 5.11. The amplitude for full width and for full width at half maximum of an H^0 beam is plotted as a function of target thickness for a 60-kev H_3^+ beam in water vapor. At low pressures where only single collisions occurred, the divergence was a minimum; at higher pressures where multiple collisions occurred, the divergence increased. As the energy of either the H_3^+ or H_2^+ was increased, the divergence of the H^0 beam decreased.

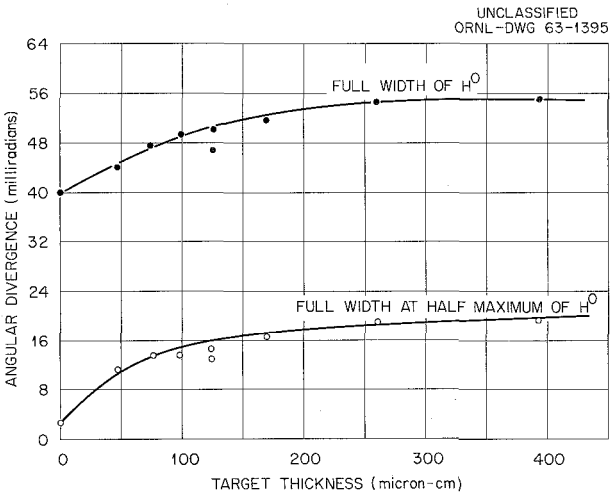

Fig. 5.11. Angular Divergence of H^0 as a Function of Target Thickness. H^0 produced by passing 60-kev H_3^+ through water vapor.

5.4 PRODUCTION OF H_2^+ IN HIGH-VIBRATIONAL LEVELS

Since the upper vibrational levels are about five times more densely populated when H_2^+ is formed from H_3^+ dissociated, it seemed highly desirable to investigate the properties of the resulting H_2^+ beam. A beam such as this could then be injected into DCX-1, and protons could be trapped efficiently by Lorentz ionization. Preliminary investigations included the determination of the angular divergence of the H_2^+ beam and the fraction of H_2^+ formed as a function of H_3^+ energy and target thickness.

Measurements were made in the apparatus used for production of H^0 from H_3^+ and H_2^+. The variation of the fraction of H_2^+ formed per H_3^+ ion as a function of target thickness is shown in Fig. 5.12 for 60-kev H_3^+ traversing water vapor. The shape of the curve was the same as that predicted from the solution of Eq. (3) with a fraction of 0.14 obtained at a target thickness of 50 micron-centimeters. The amplitude for full width at half maximum is shown in Fig. 5.13 as the gas pressure was increased. The nearly constant value of 8 milliradians indicates that the H_2^+ was formed from a single collision (i.e., $H_3^+ \rightarrow H_2^+ + H^0$). The cause for the slight decrease in beam width as the target thickness was increased is unknown at the present time. This angular

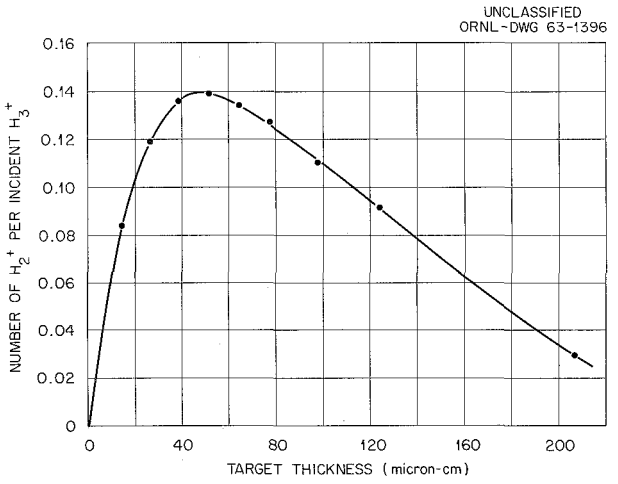

Fig. 5.12. Number of H_2^+ per Incident 60-kev H_3^+ Ion as a Function of Target Thickness.

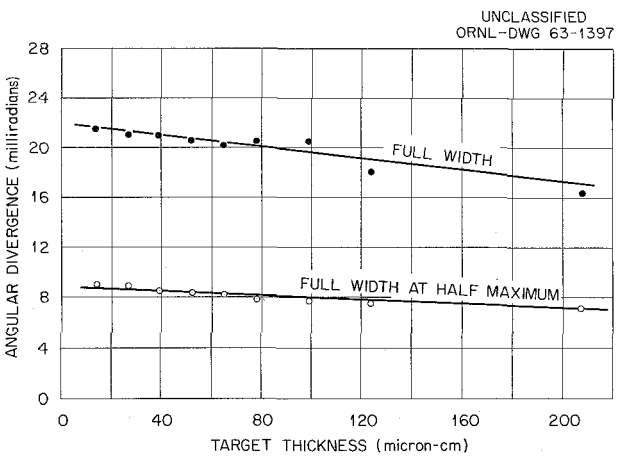

Fig. 5.13. Angular Divergence of H_2^+ as a Function of Target Thickness. H_2^+ ions produced from the dissociation of 60-kev H_3^+ ions in water vapor.

divergence indicated that less than 1 v of potential energy was given to the H_2^+ particle. The fraction of H_2^+ produced as a function of H_3^+ energy is shown in Fig. 5.14. The fraction of H_2^+ decreased from 0.14 at 60 kev to 0.105 at 400 kev.

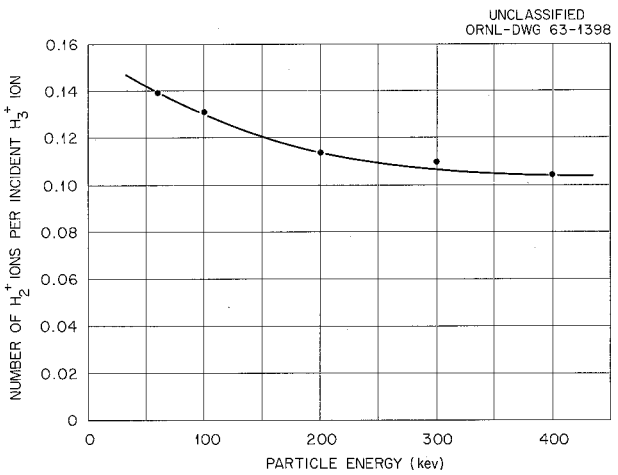

Fig. 5.14. Number of H_2^+ Ions Formed per Incident H_3^+ Ion as a Function of H_3^+ Energy. H_3^+ ions passing through water vapor.

5.5 DESIGN AND FABRICATION OF CROSSED-BEAM APPARATUS

One of the difficulties encountered in measuring atomic cross sections is the noise obtained from background collisions with residual gas molecules. A crossed-beam technique is frequently used in which an ion beam intersects an atom beam. By amplitude modulation of one of the beams and the use of a phase-sensitive detector amplifier, the magnitude of the desired reaction can be determined. In some reactions of interest to thermonuclear research, the signal-to-noise ratio is still too small to be useful with these modulation techniques. In an attempt to increase the signal-to-noise ratio, a high-vacuum chamber has been designed and is now being fabricated. The design parameters are such that the base pressure in the collision region will be of the order 10^{-10} to 10^{-11} torr. The vessel consists of an inner and outer vacuum region, with the inner region being pumped with cryo-titanium techniques. The outer chamber is 2 ft in diameter and 8 ft long.

Reactions to be studied include the dissociation of H_2^+ and H_3^+ by electrons, protons, and photons. The molecular ions will be produced by the present accelerator, while the electron, proton, and photon sources will be in one end of the outer vacuum chamber, and the beams will be projected down the axis of the chambers. A uniform external magnetic field will aid in collimating the charged beams.

Performance tests have been conducted on the new metal-gasket-sealed Consolidated Vacuum Corporation and N.R.C. (National Research Corporation) ultra-high-vacuum, 6-in. oil diffusion pumps to determine the pump configuration most suitable for the outer vacuum region. These tests were made both with and without the use of the manufacturer's zeolite trap and with water and refrigeration coolant on the baffle immediately above the pump. When the zeolite trap was used, a base pressure of 5×10^{-10} torr was attained with the Consolidated system, and 1×10^{-9} torr with the N.R.C. system.

With the zeolite trap removed, the base pressure of the N.R.C. pump and baffle was 1 to 2×10^{-9} torr with and without $-40°C$ refrigerant on the baffle. The Consolidated pump and baffle obtained a minimum pressure of 6×10^{-8} torr with water cooling on the baffle and decreased to 4.5×10^{-9} torr when the baffle was refrigerated. These tests indicate that a base pressure of 10^{-9} torr should be readily obtainable in the outer vacuum system with the use of the N.R.C. pump and water-cooled baffle.

5.6 PHOTOIONIZATION OF ATOMIC HYDROGEN

M. R. C. McDowell[6]

The photoionization cross section for atomic hydrogen has been obtained by use of the formula

$$\sigma_{n,l}(\nu) = 7.906 \times 10^{-18} \frac{g_{bf}(n,l)}{nE_{pb}} \left(\frac{\rho^2}{1+\rho^2}\right)^2 \text{cm}^2 ,$$

where E_{pb} is the photon energy in rydbergs, $\rho^2 = (1/n^2)\ E_{el}$, $E_{el} = [E_{pb} - (1/n^2)]$ rydbergs, and $g_{bf}(n,l)$ is the bound free Gaunt factor[7] for state n and level l.

[6]Consultant from Royal Holloway College, London, England.

[7]W. J. Karzas and R. Latter, *Astrophys. J. Suppl. Ser.* **55**, 167 (1962).

The average cross section for state n is obtained from the average Gaunt factor $\overline{g}_{bf}(n)$ for that state, where

$$\overline{g}_{bf}(n) = g_{bf}(ns) + \frac{3g_{bf}(np) + 5g_{bf}(nd) + \ldots + [2(n-1)+1]g_{bf}[n,2(n-1)+1]}{\Sigma_l(2l+1)} .$$

Values for this expression are tabulated by Karzas and Latter.

5.7 IONIZATION OF EXCITED STATES OF HYDROGEN BY ELECTRON IMPACT

A. D. Stauffer[8] M. R. C. McDowell[9]

Problems arising in the study of injection of fast protons into magnetic-mirror devices have led to a considerable interest in beams of neutral hydrogen atoms having a significant fraction of their total content in highly excited states. Experiments on electrostatic-field dissociation[10] of hydrogen and on magnetic-field dissociation[11] have been reported. It is of interest to examine whether electron-impact ionization of the excited states of atomic hydrogen would give a comparable yield of protons.

Detailed quantum-mechanical calculations of the cross section for the process

$$e + \mathrm{H}(nl) \longrightarrow e + \mathrm{H}^+ + e \qquad (1)$$

would be possible, at least to Born's approximation, and are at present under investigation. However, for present purposes sufficient accuracy can be achieved by using Bethe's approximation, modified to allow for the effects of the identity of the scattered and ejected electrons.

Peterkop[12] has shown that the cross section for process (1) may be expressed as

$$Q_{nl \to c}(E_i) = \frac{1}{2}\int_0^E \frac{kc}{q}\, d\epsilon \iint \sigma(\epsilon, E-\epsilon)\, \hat{dk}\, \hat{dc} , \qquad (2)$$

where

$$(\epsilon, E-\epsilon) = \frac{1}{4}\left| f(k,c) + g(k,c) \right|^2 + \frac{3}{4}\left| f(k,c) - g(k,c) \right|^2 , \qquad (3)$$

in which k, c, and q are the momenta of the ejected, scattered, and incident electrons, $f(k,c)$ is the direct and $g(k,c)$ the exchange amplitude for ejection into the continuum with momentum $k(c)$ the scattered (ejected) electron with momentum $c(k)$ and energy $(E - \epsilon)$.

Clearly,

$$f(c,k) = g(k,c) , \qquad (4)$$

and use of the symmetry of $(\epsilon, E-\epsilon)$ yields

$$Q_{nl \to c}(E_i) = \int_0^{E/2} \frac{kc}{q}\, d\epsilon \iint \hat{dk}\, \hat{dc}\, \sigma' , \qquad (5)$$

where

$$\sigma' = |f(k,c)|^2 + |f(c,k)|^2 - 2Re\,[f(k,c)f^*(c,k)] . \qquad (6)$$

In the nonexchange limit we have

$$Q_{nl \to c}(E_i) = \int_0^{E/2} \frac{kc}{q}\, d\epsilon \iint \hat{dk}\, \hat{dc}\, |f(k,c)|^2 , \qquad (7)$$

which differs from the usual Born approximation in that the upper limit on the integral over ejection energies is $\frac{1}{2}E$ and not $E = (E_i - I_{nl})$, I_{nl} being the ionization potential of the nlth state. This has the effect of reducing the calculated cross section in the region of the Born peak by about a factor of 2 and leaving it almost unaltered in the region of validity of the Born approximation, and is thus rather better than the Born approximation.

---

[8]Royal Holloway College, London, England.

[9]Consultant from Royal Holloway College, London, England.

[10]A. C. Riviere and D. R. Sweetman, *Proc. V. Intern. Conf. Ionization Phenomena in Gases*, vol II, p 1236, North-Holland Publishing Co., Amsterdam, 1962.

[11]S. Kaplan, G. A. Paulitas and R. V. Pyle, *Phys. Rev. Letters* **7**, 96 (1961).

[12]R. Peterkop, *Proc. Phys. Soc. (London)* **77**, 1220 (1961).

Now with Bethe's approximation[13] (putting E_i in rydbergs and letting α denote the fine-structure constant),

$$Q_{nl \to c}(E_i) = \frac{1}{\pi\alpha E_i} \int_0^{E/2} \frac{a_{nl}(W)}{I_{nl} + W} \log \frac{4E_i}{I_{nl} + W} \, dW \,, \qquad (8)$$

where $a_{nl}(W)$ is the photoionization cross section of H(nl) at $h\nu = (W + I_{nl})$ in rydbergs. Photoionization cross sections may readily be obtained from the tabulated Gaunt factors,[14] since

$$a_{nl}(W) = a^0_{nl}(W) g_{nl,c}(W) \,, \qquad (9)$$

where $g_{nl,c}(W)$ is the Gaunt factor and $a^0_{nl}(W)$ is the classical approximation to $a_{nl}(W)$,

$$a^0_{nl}(W) = \frac{25\pi n}{3\sqrt{3}} (1 + n^2 W)^{-3} a_0^2 \,. \qquad (10)$$

[13] M. J. Seaton, *Atomic and Molecular Processes* (ed. by D. R. Bates), chap. 11, Academic Press, London, 1962.

[14] W. J. Karzas and R. Latter, *Astrophys. J. Suppl.* **6**, 167 (1961).

The photoionization cross sections are given in Figs. 5.15 *a*, *b*, and *c*.

We have computed $Q_{nl \to c}(E_i)$ as given by Eq. (8) for nl = 1*s*, 2*s*, and 2*p*, together with the

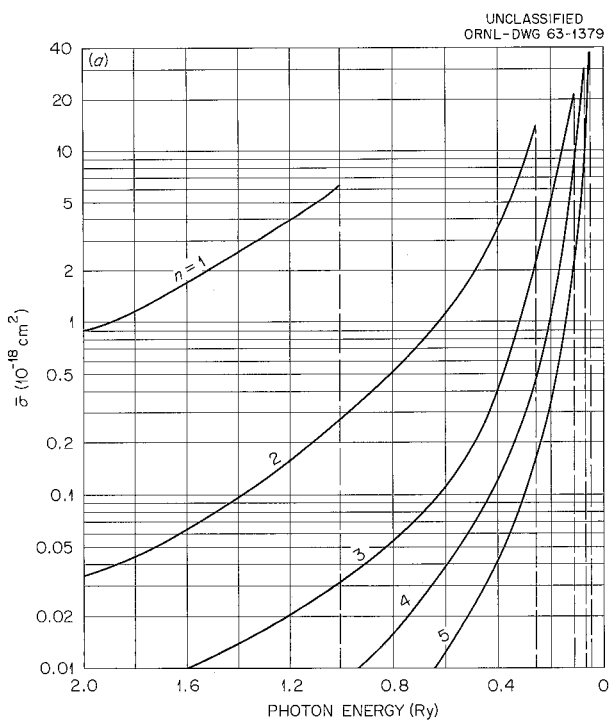

Fig. 5.15*a*. Photoionization Cross Sections, Atomic Hydrogen (n = 1 to 5).

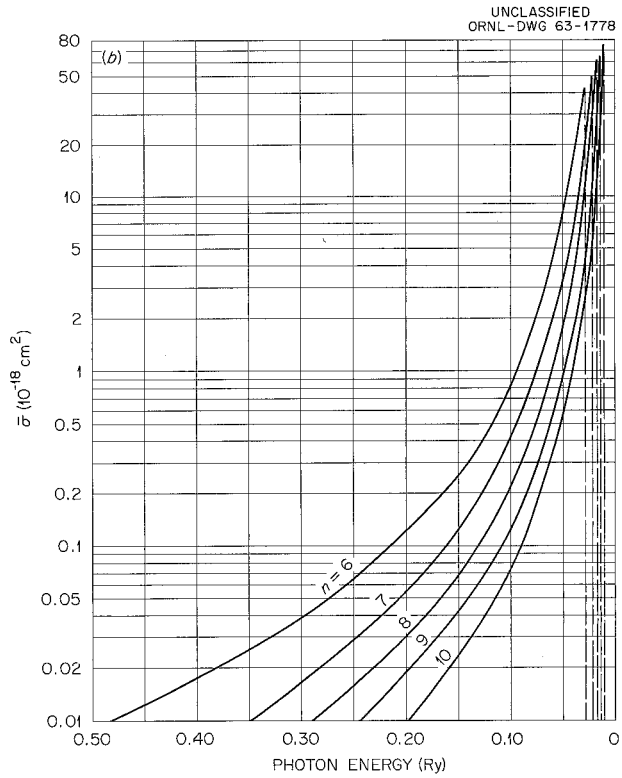

Fig. 5.15*b*. Photoionization Cross Sections, Atomic Hydrogen (n = 6 to 10).

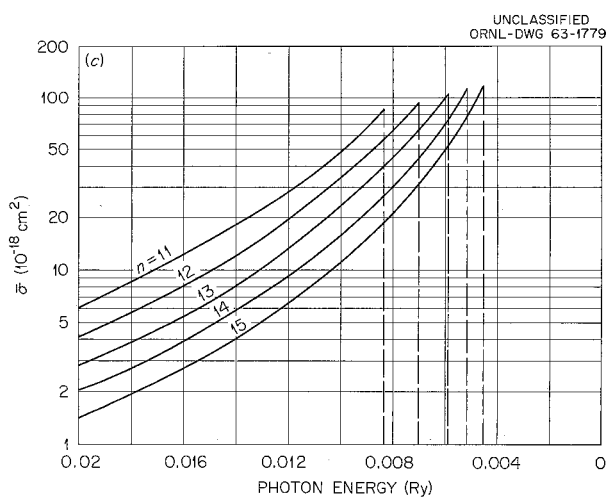

Fig. 5.15*c*. Photoionization Cross Sections, Atomic Hydrogen (n = 11 to 15).

weighted average over l, $Q_n^*(E_i)$, for $3 \leqq n \leqq 15$. It was found by a least-squares fit that for $n \geqq 5$ the photoionization cross section was adequately represented by

$$a_n^*(W) = c_n(W + I_{nl})^m , \qquad (10^{-18}\ \mathrm{cm}^2) , \qquad (11)$$

where $c_n = cn^{\epsilon}$, with $c = 7.90$, $\epsilon = -4.94$, and $m = -2.96$. With this simple form for $a_{nl}^*(W)$, Eq. (8) becomes

$$Q_n^*(E_i) = \frac{1}{\pi\alpha E_i}\frac{c_n}{m}\left\{\left(\frac{E_i + I_{nl}}{2}\right)^m \left[\log\left(\frac{8E_i}{I_{nl} + E_i}\right) + \frac{1}{m}\right] - I_{nl}^m\left[\log\left(\frac{4E_i}{I_n}\right) + \frac{1}{m}\right]\right\} . \qquad (12)$$

The results are shown in Table 5.1 for $E_i \leqq 15.0$ rydbergs, for $3 \leqq n \leqq 15$. For $n < 5$, the results were computed directly from Eq. (8) by numerical integration.

We may compare our results with the experimental evidence and with the results of other more elaborate calculations for the 1s case (Fig. 5.16).[15] Thus our modified Bethe-Born approximation is surprisingly good in the region of the maximum but tends to underestimate by about a third at higher energies. For $n = 2s$, $2p$ the Born approximation has been evaluated by Swan,[16] and his results are compared with ours in Fig. 5.17. Assuming that our result is again reliable near the maximum, the Born approximation gives an overestimate there by almost a factor of 5.

It has been usual for astrophysical purposes to estimate ionization cross sections by Thomson's[17] impulse approximation,

$$Q_c = \frac{4n_0}{I_{nl}E_i}\left(1 - \frac{I_{nl}}{E_i}\right)\pi a_0^2 , \qquad (13)$$

where in this case $n_0 = 1$. However, this approximation is invalid for $n >> 1$ and, indeed, in general when it predicts a cross section much greater

[15] S. Geltman, M. Rudge, and M. J. Seaton, *Proc. Phys. Soc. (London)* **81**, 375 (1963).

[16] P. Swan, *Proc. Phys. Soc. (London)* **A68**, 1157 (1955).

[17] J. J. Thomson, *Phil. Mag.* **6**(23), 449 (1912).

Table 5.1. Calculated Ionization Cross Sections in Units of πa_0^2 at Impact Energy of E_i in rydbergs and Averaged over l for $3 \leqq n \leqq 15$ in Atomic Hydrogen

n	E_i								
	0.1	0.2	0.5	1.0	1.5	2.0	5.0	10.0	15.0
3	8.7	21.3	18.1	11.8	8.91	7.21	3.56	2.03	1.46
4	46.3	50.6	30.8	18.9	14.0	11.2	5.38	3.03	2.15
5	105	80.5	44.3	26.5	19.3	15.4	7.29	4.07	2.88
6	167	114	59.8	35.2	25.5	20.2	9.48	5.27	3.72
7	228	147	75.3	43.8	31.6	25.0	11.6	6.42	4.52
8	292	183	91.7	52.9	38.0	30.0	13.9	7.63	5.30
9	362	220	110	63.1	45.2	35.6	16.4	8.98	6.30
10	425	257	126	72.0	51.5	40.4	18.5	10.1	7.10
11	495	297	145	82.1	58.5	45.9	20.9	11.5	8.01
12	572	340	164	92.7	66.0	51.7	23.5	12.8	8.96
13	644	380	182	103	73.0	57.1	25.9	14.1	9.85
14	725	425	203	114	80.8	63.2	28.6	15.5	10.9
15	800	467	222	124	88.1	68.8	31.1	16.9	11.8

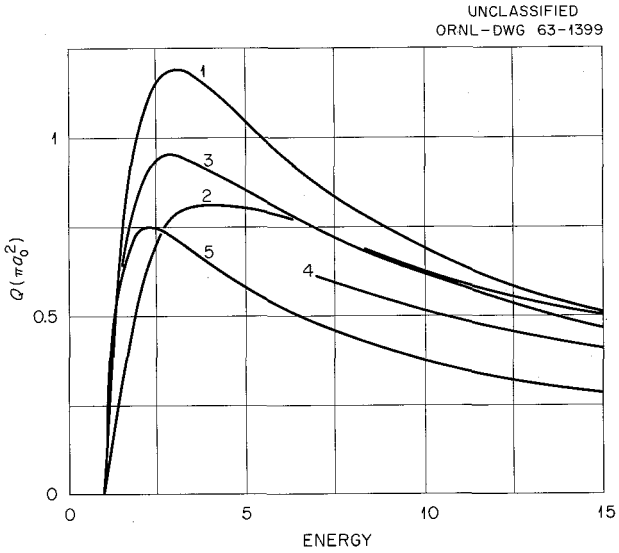

Fig. 5.16. Ionization of H(1*s*) by Electron Impact. Curve 1, Born approximation; curve 2, Born exchange; curve 3, experiment by W. Fite and R. T. Brackmann, *Phys. Rev.* 112, 1141 (1958); curve 4, experiment by E. W. Rothe *et al.*, *Phys. Rev.* 125, 582 (1962); curve 5, this paper.

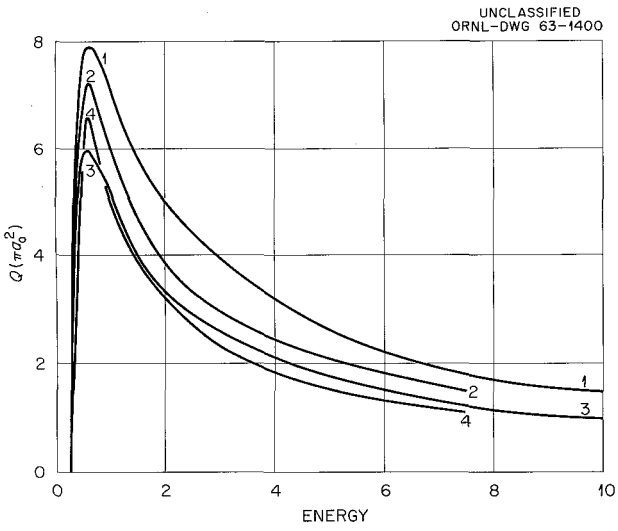

Fig. 5.17. Cross Sections for $e + H(2s,2p) \rightarrow e + H^+ + e$. Curve 1, this paper, 2*s*; curve 2, $\frac{1}{5}\, Q_{2s}$, Born approximation by P. Swan, *Proc. Phys. Soc. (London)* A68, 1157 (1955); curve 3, this paper, 2*p*; curve 4, $\frac{1}{5}\, Q_{2p}$, Born approximation by P. Swan, *Proc. Phys. Soc. (London)* A68, 1157 (1955).

than r_n^2, where r_n is the mean orbital radius[18]. It predicts a maximum cross section of I_n^{-2}; that is,

$$(Q_c)_{\max} = n^4(\pi a_0^2) \tag{14}$$

at $E_i = 2I_{nl}$, whereas our approximation gives a maximum at $E_i \approx 2.3I_{nl}$,

$$\frac{(Q_n^*)_{\max}}{(Q_c)_{\max}} \approx \frac{0.916}{n^{1.02}} \,. \tag{15}$$

Thus for $n > 10$, our maximum cross section for a given n is at least an order of magnitude less than the Thomson result.

Close to threshold we may write $E_i = I_{nl} + W_0$, $W_0 << I_{nl}$, and obtain

$$Q_{nl}(W_0) \approx \frac{1}{\pi\alpha}\frac{a_{nl}(0)}{I_{nl}^2} \times W_0\left[\log 2 + \left(\frac{3}{8} - \log 4\right)\frac{W_0}{I_{nl}} + \ldots\right] \tag{16}$$

and

$$Q_c(W_0) \approx \frac{4W_0}{I_{nl}^3}\left(1 - \frac{2W_0}{I_n} + \ldots\right), \tag{17}$$

so that near threshold,

$$Q_{nl}(E_i) \approx (\log 2)\,(4\pi\alpha)^{-1}\, a_{nl}(0)\, I_{nl} Q_c\,(E_i)\,. \tag{18}$$

In Fig. 5.18, the ratio Q_n^*/Q_c for $1 \leqq n \leqq 6$ is plotted as a function of the logarithm of E_i, measured in units of I_n. It is clear that the results do not substantiate the hypothesis that Q/Q_c is a unique function of (E_i/I_n).

It is well known that the photoionization cross section for $He^+(nl)$ at frequency ν is related to that for hydrogen at frequency $\nu/4$ by

$$a_{nl}^{He^+}(h\nu) = \frac{1}{z^2}\, a_{nl}^{H}\left(\frac{h\nu}{z^2}\right), \tag{19}$$

with $z = 2$. Thus, for a hydrogen-like ion of nuclear charge z, our result predicts

$$Q_{nl}^{z}\,(z^2E_i) = \frac{1}{z^4}\, Q_{nl}^{H}\,(E_i)\,, \tag{20}$$

[18]This was pointed out to us in a conversation with M. J. Seaton.

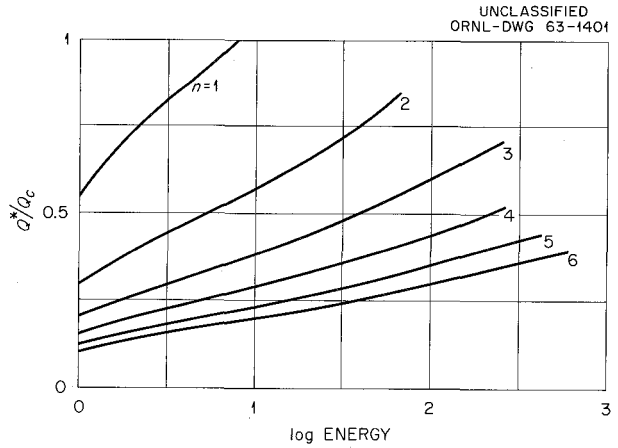

Fig. 5.18. Ratio of Q_n^* to the Thomson Cross Section Against Logarithm of Energy, in Units of I_{nl} for $e + H(n) \rightarrow e + H^+ + e$, $1 \leq n \leq 6$, Where the Numbers on the Curves Give the Value of n.

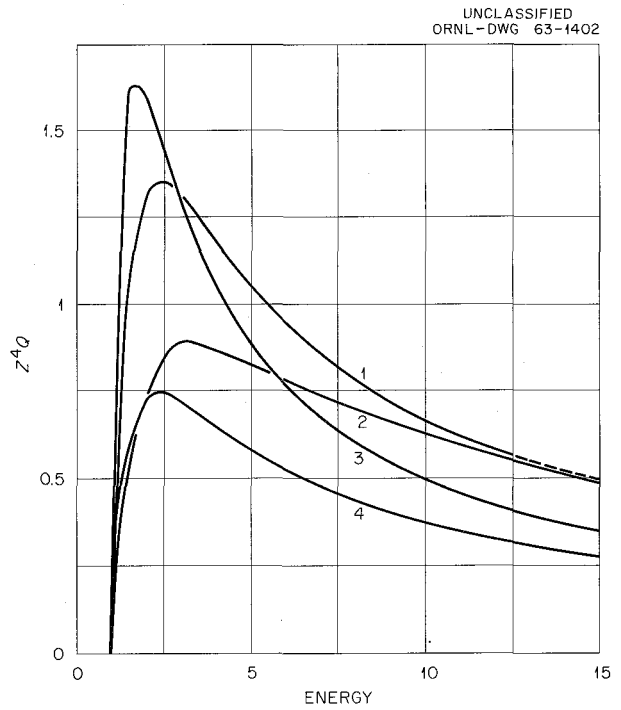

Fig. 5.19. $z^4 Q_{1s \rightarrow c}$ for Electron Ionization of He^+ Against Energy in Units of I_{He^+}. Curve 1, Coulomb-Born approximation: A. Burgess, *Astrophys. J.* 132, 503 (1960); curve 2, experiment by K. T. Dolder, M. F. A. Harrison, and P. C. Thonemann, *Proc. Roy. Soc. (London)* A264, 367 (1961); curve 3, this paper with coulomb correction; curve 4, this paper, uncorrected.

but this takes no account of the strong coulomb attraction when $z \neq 1$. Geltman[18] suggested that a coulomb correction factor of the form $1 + 1/E_i\sqrt{Q_{nl}}$ will be adequate at large E_i, while for E_i small, one would expect a coulomb factor $\approx 2\pi/E_i^{1/2}$. In Fig. 5.19, cross sections obtained from Eq. (20) are compared with and without this coulomb correction, with the coulomb-Born calculations of Burgess,[19] and with the experimental results of Dolder *et al.*[20] for $He^+(1s)$. As Dolder *et al.* found, the coulomb effect is rather small when reduced variables are employed, and Geltman's suggested correction is much too large. We would, however, expect that a correction of the form $(1 + E_i^{-1}Q_n^{-1/2})$ would be satisfactory for large n and $E_i \lesssim 10$.

To conclude, we notice that since $(Q_n^*)_{max}$ varies approximately as n^3 and if more than 0.1% of a beam of hydrogen atoms are in states with $n > 10$, there will be a marked effect on the effective ionization cross section for very slow electrons: for 1% of the beam in such states, $Q_{effective} \approx 10\pi a_0^2$, and for 10% of the beam in such states, $Q_{effective} \approx 100\pi a_0^2$. Effective rate coefficients for thermal electrons would be 10^{-8} cm^3/sec and 10^{-7} cm^3/sec, respectively, so that this process would be at least as effective as electric-field ionization when the thermal-electron density exceeded 10^4/cm^3.

[19] A. Burgess, *Astrophys. J.* **132**, 503 (1960).

[20] K. T. Dolder, M. F. A. Harrison, and P. C. Thonemann, *Proc. Roy. Soc. (London)* **A264**, 367 (1961).

6. Production, Acceleration, and Injection of Ionic and Atomic Beams

6.1 HIGH-CURRENT ION-BEAM INJECTION

R. C. Davis E. C. Moore
R. R. Hall O. B. Morgan
G. G. Kelley R. F. Stratton
D. C. Weaver[1]

The efforts of this group continued to be divided between injecting an ion beam into DCX-2 and doing basic studies on producing high-current beams.

The DCX-2 injection system has been performing very satisfactorily since the installation of the accelerator tube that uses epoxy skirts[2] in October 1962. Several minor modifications were made in the tube to minimize the involuntary shutdowns due to external discharges. These discharges have not been completely eliminated, but they now occur with time periods of from 30 min to several hours for operating parameters of 0 to 100 ma total current at 600 kv.

The amount of H_2^+ ion current injected into DCX-2 is still limited to approximately 60 ma, even though the total current has been 150 ma and could be greater if the H_2^+ component injected into the machine showed any appreciable increase. This problem has been investigated with the High-Intensity-Beam Facility. This facility[3] is very similar to the DCX-2 injection system except that there is no intense transverse magnetic field. The results, although not complete, are almost identical with those found in DCX-2. The earlier beam analyses from the duoplasmatron ion source were made at 50 to 100 kv by utilizing an *einzel* lens and a transverse magnetic field and were limited by the lens to total currents of 100 ma or less. The present analysis is made at 600 kv by utilizing a magnetic lens and focusing the desired space-charge neutralized-beam components through a limiting aperture.

Although the above techniques should not affect the beam analysis from the source, the earlier work was repeated for currents up to 100 ma. The results of these tests were very similar to the original analysis. For example, with 100 ma of total current and optimized source parameters, current ratios of 60 ma of H_2^+, 30 ma of H^+, and 10 ma of H_3^+ were obtained; with 60 ma of total current up to 40 ma of H_2^+ can be obtained. However, when the total current is increased from 100 ma to 150 ma, there is essentially no change in the H_2^+ ion current focused through the $1\frac{5}{8}$-in. aperture.

A thorough investigation of the reason for the lack of change in H_2^+ ion current when the total current is increased from 100 ma to 150 ma has been delayed because of several complications. The accelerator tube being used does not have x-ray shielding included inside the electrodes as does the tube being used on DCX-2. Therefore the x-ray intensity in the vicinity of the tube is much greater than on DCX-2, and this may be the reason the tube is more unstable at high currents. Before shielding is added, an attempt will be made to determine the source and energy of these x rays. The equipment for doing this is ready and is waiting for operating time with the 600-kv power supply. The second complication is that as the total current is increased the accountability as determined calorimetrically decreases until only about 78% of the power is accounted for at 150 ma. This appears to be because of beam losses above the first analyzing cone and will require a modification of this cone. If this proves to be the case,

[1]On loan from Y-12 Plant.

[2]R. C. Davis *et al.*, *Thermonuclear Div. Semiann. Progr. Rept. Oct. 31, 1962,* ORNL-3392, p 50–51.

[3]*Ibid.*, p 51–53.

then the H_2^+ beam component that is being analyzed is correct, and the reason for the injected-current limitation is a decreased relative production of H_2^+. A variety of ion-source modifications are being built and will be evaluated at total currents above 100 ma.

An effort has been made to maximize the H_3^+ ion current from the duoplasmatron. By using the 100-kv laboratory facility with an *einzel* lens and a transverse magnetic field, total currents up to 100 ma were analyzed. The ion-source[4] parameters that were varied were pressure, electrode spacing, and anode and intermediate electrode aperture sizes. The most important parameter was the source pressure. The optimum source pressure was 500 to 700 μ, as indicated by a thermocouple gage mounted on the filament assembly, depending weakly on the other source parameters. The optimum H_3^+ production found is indicated in Table 6.1.

Table 6.1. Composition of 100-kev Hydrogen Ion Beam from Duoplasmatron Source, Optimized for H_3^+

Total Current (ma)	H^+ (ma)	H_2^+ (ma)	H_3^+ (ma)
89.0	32.5	20.0	36.5
48.5	15.0	6.5	27.0
27.5	6.0	3.5	18.0

A gun for injecting electrons along field lines into DCX-2 has been built, and some preliminary tests have been made on the long solenoid. The gun consists of a circular oxide filament 3 in. in diameter with a 1/8-in. cross section. The electrons are extracted through a 3-in.-diam slot with a 1/4-in. cross section spaced 1/4 in. from the filament. There is also a second slot with a slightly larger cross section spaced 1/4 in. from the first slot. The filament and both extraction apertures are insulated so that a variety of electrical potential arrangements can be tested. In the preliminary tests the gun delivered up to 5 amp of electrons at 1500 ev. The gun will be tried soon in DCX-2, and, if the results are significant, more effort will be devoted to improving the performance.

Some preliminary tests have also been made with the duoplasmatron as an electron gun. Currents up to 1 amp of electrons at 15 to 20 kev were extracted, with no indications of an upper limit in current. The electron current extracted was approximately 2.5 times the arc current in the source. Since the source can be operated continually in excess of 10 amp arc current, the current limitation is determined by the current density that can be handled in the extraction region. This current density, j(amp/cm^2), is determined by the formula

$$j = \frac{5.44 \times 10^{-8}\ \Phi^{3/2}}{M^{1/2}\ Z^2},$$

where Φ is the applied potential difference in volts, M is the mass number in amu, and Z is the effective spacing between electrodes in centimeters (empirically Z has been found to be equivalent to the real spacing plus the radius of the extraction aperture). Since potential gradients of 200 kv/cm can be maintained in the extraction region, the extracted currents that can be obtained are very great. As a typical example, with 200 kv/cm and Φ = 50 kv, $j \cong 100$ amp/cm^2. To explore the problems involved in injecting electrons or ions along field lines into DCX-2, a source is being constructed that will be mounted in a stray field of 1 to 2 kilogauss and the electrons or ions will be injected into the machine through the 40-kilogauss mirror field.

6.2 ION-SOURCE DEVELOPMENT

C. W. Blue N. H. Lazar
O. D. Matlock

6.2.1 General Description

The ion-source work reported in ORNL-3315, Sec 5.3, has been continued in tank D of the Beta Tank Facility. The source was redesigned to operate at high positive potential and adapted to a modified calutron unit. This allowed the use of an electron dumping system that could be built from existing parts. The essential parts of the source and the electrical supplies are shown in

[4] O. B. Morgan *et al.*, *Thermonuclear Project Semiann. Progr. Rept. July 31, 1960*, ORNL-3011, p 57.

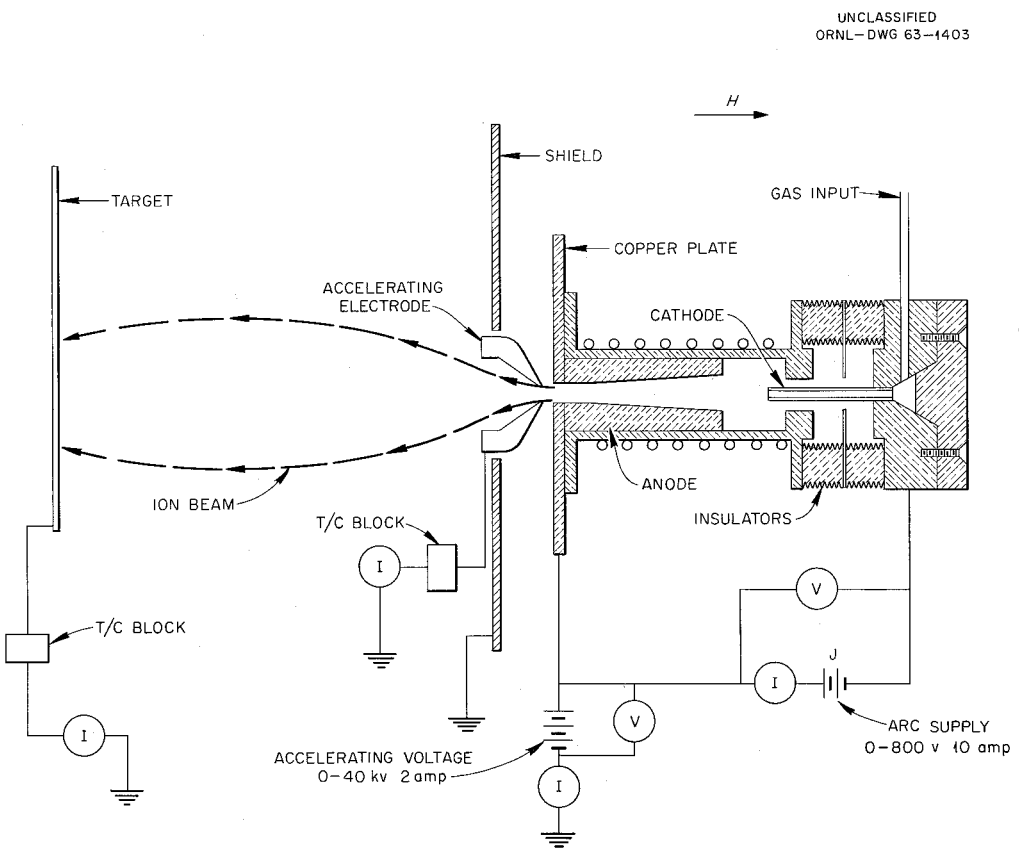

Fig. 6.1. Hollow Cathode Ion Source.

Fig. 6.1. The hollow cathode is of tungsten: 0.205-in. OD with 0.040-in. wall thickness. The cathode holder is of water-cooled copper mounted off the anode holder by the two insulators. Gas feed is through the cathode to increase efficiency of operation. The hollow anode is of carbon approximately 4 in. in length. Its inside diameter tapers from 7/16 to 1/4 in. This taper improves the stability of the arc. The accelerating electrode is also of water-cooled copper. The large grounded shield through which the accelerating electrode is mounted suppresses electron oscillations along the magnetic-field lines. The shield and the target are both water cooled. The target is located 10 in. from the accelerating electrode.

6.2.2 Operation of the Arc

Before striking the arc, the gas feed (hydrogen) is adjusted to approximately 75 micron-liter/sec. The arc is initially struck by introducing argon into the anode region. The voltage-current characteristics of the arc are negative for higher hydrogen-gas feed rates (>75 micron-liter/sec) but positive for the lower feed rates. Typical arc conditions are 450 v and 4 amp with 50 micron-liter/sec of hydrogen and a tank pressure of 4×10^{-6} mm Hg.

6.2.3 Operation of the Ion Source

On application of high potential, the ions that diffuse from the plasma within the anode are accelerated and collected on the target. The diffusion rate of ions is a function of the plasma density and temperature, and to prevent ions from striking the acceleration electrode this rate must

not exceed the space-charge-limited ion current for a paralled beam, given by

$$I = \frac{1.71 \times 10^{-7} V^{3/2}}{(Z/r_0)^2 A^{1/2}}, \qquad (1)$$

where

V = accelerating potential in volts,
Z = accelerator spacing,
r_0 = initial beam radius,
A = mass number of extracted ions,
I = ion current in amperes.

It is therefore desirable to operate the arc with a density as low as possible.

An ion current of 0.300 amp has been obtained for V = 30 kv, Z = 3/32 in., and r_0 = 1/8 in. Arc conditions were 4 amp at 450 v. The current to the accelerating electrode was less than 0.010 amp. Power measurements to the target and accelerating electrode were made both electrically and calorimetrically. When the target was biased to prevent secondary electrons from leaving it, the power measurements were in excellent agreement. Increasing the accelerating potential did not change the ion current, showing that the output was limited by the ion-diffusion rate. However, when the voltage was decreased below 26 kv, the current to the accelerating electrode increased, indicating the ion flow to be in excess of the value predicted by Eq. (1). Arc conditions were kept constant. The space charge and the focusing effect of the magnetic field gave the ion beam a "football" shape, as indicated in Fig. 6.1.

No attempt has been made to determine the H^+ and H_2^+ ratio of the ion beam. Gas efficiency would be 45% if the beam were 100% H^+ and higher than this for appreciable molecular-ion fractions.

The present work includes scaling down the dimensions of the source for reduced ion output and increased efficiency. Also, the use of copper anodes and thoriated-tungsten cathodes is being evaluated.

[5]On loan from Y-12 Plant.

[6]R. L. Knight *et al.*, *Thermonuclear Div. Semiann. Progr. Rept. Apr. 30, 1962*, ORNL-3315, p 62.

[7]J. N. Luton, Jr., *Thermonuclear Div. Semiann. Progr. Rept. Oct. 31, 1962*, ORNL-3392, p 73.

6.3 NEUTRAL-SOURCE DEVELOPMENT

E. L. Earley[5] V. J. Meece
W. L. Stirling

An assembly drawing of the neutral-source assembly has been previously published.[6] The assembly mounts in a 10-in.-ID stainless steel cylinder (Fig. 6.2), which serves both as vacuum-chamber wall and as spool mount for the magnetic-field coil.[7] A base pressure of 4×10^{-7} torr has been achieved in the region of the high-voltage bushing.

Forty kilovolts are easily maintained in high-voltage testing without either ion-source or converter arc running.

Both arcs have been run, but not at the same time. The ion-source arc experiences insulation difficulties between the cathode holder and ion-source anode cooling-water lines in the region of the fringing field of the solenoid. Preliminary tests with nylon sleeving over a 1-ft section of the water lines in the fringe-field region have yielded satisfactory operation.

Insulation difficulties have also arisen between the anode and cathode of the converter arc. The breakdown is along the inner surface of the insulator which connects these two electrodes. A new design with a longer path length from cathode to anode will soon be tested.

6.4 NEGATIVE IONS

O. C. Yonts

A grid ion source has been modified to serve as a source of negative ions. The source is stable and well behaved to outputs of approximately 12 ma of Cl^- ions. Above this point, output is unstable owing to excessive electron drain to walls of the vacuum tank. Short bursts of Cl^- ions in excess of 30 ma have been obtained. The source also produces 1 ma of N^- ions.

Negative chlorine ions have also been observed in the mode II discharge.

UNCLASSIFIED
ORNL-DWG 63-1404

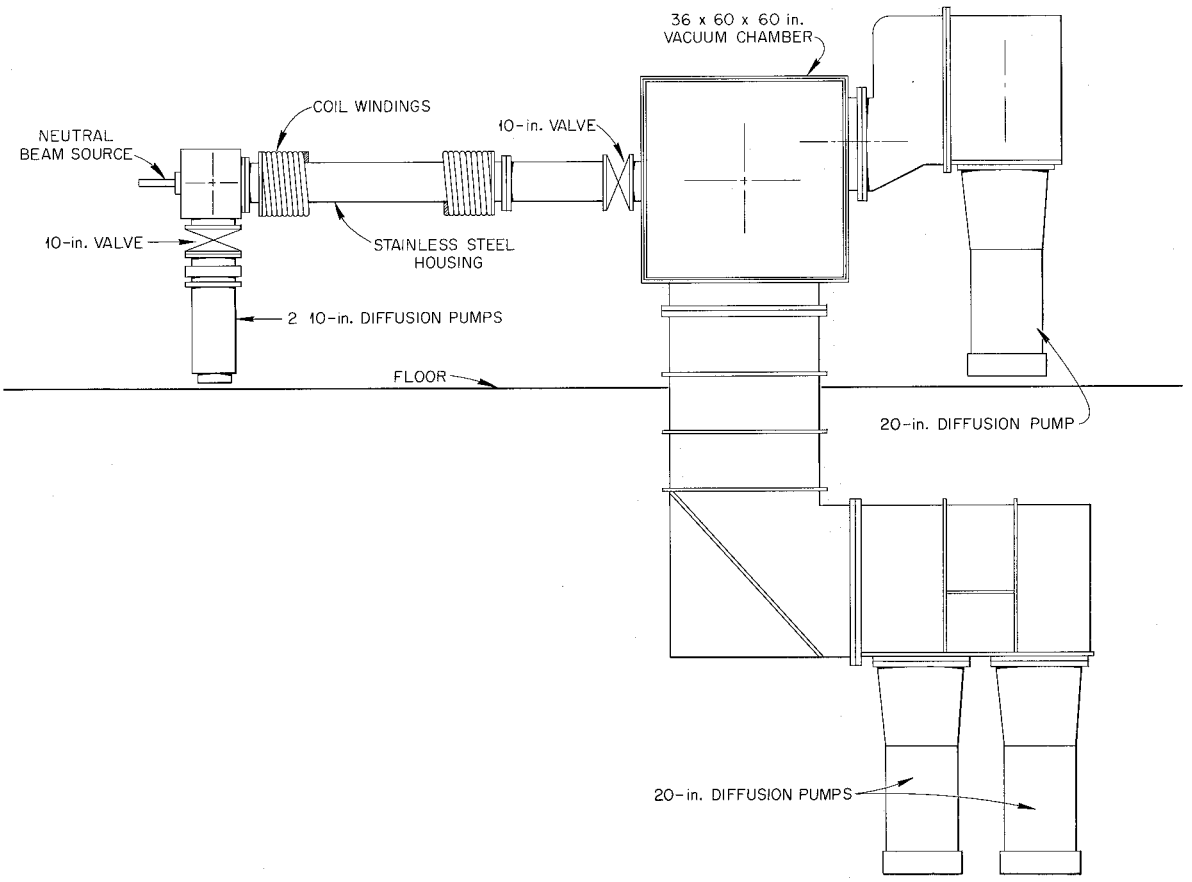

Fig. 6.2. Vacuum Assembly for Neutral-Beam Experiment.

7. Plasma Theory and Computation

7.1 INSTABILITY MECHANISMS

T. K. Fowler

In reviewing stability literature, the following simplified description of velocity-space instabilities was achieved. All electrostatic instabilities, whatever the velocity distribution, are caused by bunching, known to be the two-stream mechanism.[1] Bunching of streams is best understood in the "wave frame," where the electric potential does not oscillate ($Re\omega = 0$). Then, at the threshold for growth, the potential is static, and the dynamics can be obtained from conservation laws. If in the wave-frame stream j has velocity v_j, density n_j, particle mass and charge m_j and q_j, the density change Δn_j and velocity change Δv_j on encountering a charge clump of density ρ, dimension k^{-1}, are, by continuity and energy conservation,

$$\Delta n_j \cong \left(\frac{-\Delta v_j}{v_j}\right) n_j \,, \tag{1}$$

$$m_j v_j \Delta v_j \cong q_j \frac{4\pi\rho}{k^2} . \tag{2}$$

Combining, with $\omega_{pj}^2 = 4\pi q_j^2 n_j/m_j$, the total charge change in streams is

$$\sum_j q_j \Delta n_j = \sum_j \frac{\omega_{pj}^2}{k^2 v_j^2} . \tag{3}$$

The inequality expresses the instability condition that the response exceed the cause. Equation (3) is just the multistream dispersion relation at threshold (in the frame in which the potential is static). To obtain Penrose's instability condition for an arbitrary distribution $G(v)$ (projected onto the direction of $\vec{k}$),[2] we simply sum all streams, density $nG(v)\,dv$, where n is the total density and $\int dv\, G = 1$, except that we omit particles nearly at rest in the wave frame. Let w be the wave-frame velocity as seen from the laboratory, and exclude $|v - w| < \epsilon$. We interpret the excluded interval as "trapped" particles,

$$m\epsilon^2 = \left|\frac{4\pi\rho}{k^2}\right| . \tag{4}$$

With energy less than the potential barrier, they are thrown off potential hills into valleys, and thus essentially all their charge contributes toward neutralizing ρ, a stabilizing effect in opposition to bunching. Adding responses, the requirement that the response exceed the cause yields the instability condition

$$\left(\int_{w+\epsilon}^{\infty} + \int_{-\infty}^{w-\epsilon}\right) \frac{\omega_p^2}{k^2(v-w)^2}\, \rho\, G(v)\, dv - 2n\epsilon\, G(w)\, |q|\, \rho/|\rho| > \rho \,. \tag{5}$$

For small ρ and, hence, by (4), small ϵ, Eq. (5) is independent of ρ. By (4),

$$2n\epsilon\, G(w)\, |q| \frac{\rho}{|\rho|} = \rho\, \frac{\omega_p^2}{k^2}\, \frac{2G(w)}{\epsilon} . \tag{6}$$

With this substitution, in the limit ϵ, $\rho \to 0$, Eq. (5) can be written (omitting ρ),

$$\frac{\omega_p^2}{k^2} P \int dv \frac{G'(v)}{v - w} > 1 \,, \tag{7}$$

[1] J. D. Jackson, *J. Nucl. Energy, Pt C* **1**, 171 (1960).

[2] O. Penrose, *Phys. Fluids* **3**, 258 (1958).

which is the form given by Penrose.[1] His criterion for choosing the wave frame, namely, $G'(w) = 0$, is the condition that the bunching response be an extremum.

The pinch mechanism responsible for all (or most) magnetic velocity-space instabilities, discussed by Furth,[3] can be derived similarly. Pinching is the antithesis of bunching. Whereas like charges repel, so that streaming charges respond in phase to a disturbance, as in Eqs. (1) to (3), transverse-streaming current elements are attracted by current in the same sense; they speed up, thin out, and, hence, respond out of phase (stabilizing). Conversely, "trapped" current piles up (destabilizing). From the particle viewpoint, the current interaction between pairs of particles (for example, electrons) relatively at rest but streaming with speed u is the result of noncancellation of the $\vec{u} \times \vec{B}$ magnetic interaction, which is just $(-u^2/c^2)(e\vec{E}_\perp)$, where $\vec{E}_\perp$ is the laboratory transverse electric field between pairs. In the wave frame, the dynamics of the response of particles to the magnetic correction is again given by conservation laws, as in Eqs. (1) to (3). In short, with a change of "coupling constant," $e^2 \to (-u^2/c^2)e^2$, the Penrose condition applies to the magnetic interaction for an arbitrary, transverse (to the main stream) velocity distribution to the extent that the transverse current is a negligible source of $\vec{B}$. The interesting case is the single-humped function, stable electrostatically. Let $G(v) \sim \exp - v^2/v_t^2$. With the magnetic coupling constant [whence $\omega_p^2 \to (-u^2/c^2)\omega_p^2$], Eq. (7) yields the pinch instability criterion in terms of which Furth interpreted magnetic instability criteria. Since $G'(0) = 0$, $w = 0$ and the result is

$$\left(\frac{-u^2}{c^2}\right) \omega_p^2 P \int dv \frac{G'(v)}{v} = \frac{1}{2} n \left(\frac{8\pi}{k^2}\right) \left(\frac{e^2}{mc^2}\right) \frac{2u^2}{v_t} > 1 \ . \quad (8)$$

7.2 BOUNDS ON INSTABILITY GROWTH RATES

T. K. Fowler

A method is being explored for placing rigorous bounds on the growth rates of instabilities predicted by the Vlasov equation. Both electrostatic and magnetic interaction among particles is allowed, and all instability modes are treated simultaneously. As it is not necessary to make simplifying assumptions, such as spatial uniformity, instabilities arising from finite size and gradients in field, density, temperature, etc., are incorporated, along with velocity-space instabilities of all kinds. The equilibria which can be treated must be time-independent, but otherwise they can be quite realistic. For example, both electric and magnetic fields of plasma or external origin may exist in equilibrium, and proper boundary conditions can be employed, though this sometimes adds to the labor. The principal conclusions so far are:

1. Growth in the linearized theory is never faster than exponential, which justifies the customary use of the Laplace transform in conventional stability analysis. Furthermore, usually the rate is no faster than the plasma frequency. This general result was proved for the special case of infinite, uniform plasmas by Backus.[4]

2. The growth rate approaches zero uniformly as stable equilibrium is approached. For example, one bound on the streaming instability growth rate vanishes linearly with the streaming speed.

The method is an application of a previously reported theorem on exponential growth employing Lyapunov functions.[5] Let vector ψ denote collectively the distribution and field perturbations, f, $\vec{E}$, $\vec{B}$, and denote the linearized Vlasov equation by $\partial\psi/\partial t = P\psi$. If operator H is Hermitian, positive definite is a certain scalar product, denoted by (,), such that boundedness in time of (ψ, ψ) is a satisfactory criterion for stability, (ψ, ψ) grows no faster than $\exp 2\gamma t$, where the growth rate ψ satisfies the bound

$$2\gamma \leqq \operatorname*{Max}_{(\text{all } \psi)} \frac{d(\psi, H\psi)/dt}{(\psi, H\psi)} = \operatorname*{Max}_{(\text{all } \psi)} \frac{(\psi, [HP + P^+H]\psi)}{(\psi, H\psi)} . \quad (1)$$

The bound is double-variational, of the minimax type. Upon maximizing on ψ and minimizing on H,

[3] H. P. Furth, *Phys. Fluids* **6**, 48 (1963).

[4] G. Backus, *J. Math. Phys.* **1**, 178 (1960).

[5] T. K. Fowler, *J. Math. Phys.* **4**, 559 (1963); *Thermonuclear Div. Semiann. Progr. Rept. Oct. 31, 1962*, ORNL-3392, p 60.

the bound approaches the true maximum growth rate with arbitrary precision.

For any H, maximizing on ψ gives a rigorous bound (possibly infinite), though not necessarily the best. Our results to date have employed $F \equiv (\psi, H\psi)$, closely related to the lowest order terms of the free energy appropriate to a stable state "close to" the equilibrium in question; namely,

$$F = \frac{1}{2} \sum_j \int d\vec{x}\, d\vec{v}\, f_j^2 \left(\frac{-\partial h_j}{\partial \epsilon_j} \right)^{-1} + \frac{1}{8\pi} \int d\vec{x} (\vec{E}^2 + \vec{B}^2) \quad . \quad (2)$$

The sum runs over particle species, subscripted j. The quantity h_j is a function of equilibrium single-particle energy,

$$\epsilon_j = \frac{1}{2} m_j v^2 + V(\vec{x}) \ ,$$

and possibly other variables. The quantity h_j is chosen so that $\partial h_j / \partial \epsilon_j < 0$, whereby the first term of (2) is positive, but otherwise it is arbitrary. If $\partial f_0^j / \partial \epsilon_j < 0$, f_0^j being the equilibrium, the best choice is $h_j = f_0^j$.

Now, F would be invariant as f, $\vec{E}$, $\vec{B}$ change in time if, in the Vlasov equation, $\partial f_0^j / \partial \vec{v}$ were replaced by $(\partial h_j / \partial \epsilon_j)(\partial \epsilon_j / \partial \vec{v})$. Thus the actual time variation of F arises only from a corrected version of the term representing action of the field perturbations on equilibrium particles,

$$\frac{q_j}{m_j} \left(\frac{\partial h_j}{\partial \epsilon_j} \frac{\partial \epsilon_j}{\partial \vec{v}} - \frac{\partial f_0^j}{\partial \vec{v}} \right) \left(\vec{E} + \frac{1}{c} \vec{v} \vec{B} \right) . \quad (3)$$

The contribution of (3) to the bound has the dimensions of the plasma frequency ω_{pj}, and Eq. (1) takes the form

$$\frac{1}{F} \frac{dF}{dt} = \sum_j \omega_{pj} U_j \ . \quad (4)$$

The dimensionless quantities U_j are always bounded over all ψ. After some manipulations employing Schwarz' inequality, the U_j prove to be bounded by a sum of a few terms of the form

$$U < \sum k \frac{|a|\,|b|}{a^2 + b^2} = \sum_{(\text{all } a, b)} \frac{1}{2} k \quad , \quad (5)$$

where a depends on f_j and b depends on a field component. As a typical case, consider a streaming instability in which one species has the distribution $f_0 \sim \exp - (\epsilon + u p_z)/T$, where u is the streaming speed and p_z is the canonical momentum in the streaming direction (no force in that direction). Then, $k = u/v$ with $v = (2T/m)^{1/2}$. The magnetic interaction contribution is lower by a factor v/c.

The rigorous bound applies to disturbances of arbitrary spatial variation. To correlate growth rate and wavelength, the variation over ψ can be limited to a subspace of perturbations with bounded logarithmic space derivative ($\equiv$ wavelength). However, the result is a valid bound only as long as ψ remains within the chosen subspace, that is, only as long as allowed wavelengths do not couple to shorter wavelengths, generally not known. Employing such techniques, with choices for H different from (2), we have found for long wavelengths bounds characterized by natural periods other than ω_p, for example, transit times across the plasma.

7.3 STABILITY INVESTIGATION OF INHOMOGENEOUS PLASMAS

Ya'akov Shima

The method of constants of motion for investigating the stability of plasmas involves the consideration of a three-dimensional integral equation.[6] In cases of sufficient symmetry this integral equation can be reduced.[7] We have considered a plasma, situated in a constant magnetic field in the z direction, whose distribution function f_0 depends on the following three constants of motion: v_z, $v_\perp$, and $p_\theta = r v_\perp \sin(\phi - \theta) + \frac{1}{2} r^2 \omega_c$. ($r, \theta, z$ and $v_\perp$, ϕ, v_z are, respectively, the cylindrical coordinates of x, y, z and v_x, v_y, v_z spaces.) The resulting reduced one-dimensional integral equation is of the form

$$\rho(r) = \int_0^\infty K(r, r'') \rho(r'') r''\, dr'' \ . \quad (1)$$

[6] T. K. Fowler, *Plasma Stability Analysis Employing Equilibrium Constants of Motion*, ORNL-3123 (1961).

[7] Ya'akov Shima and R. G. Alsmiller, *Thermonuclear Div. Semiann. Progr. Rept. Apr. 30, 1962*, ORNL-3315, p 68.

The kernel K depends on f_0, p (the Laplace transform parameter used in solving the Vlasov equation), k_z, and l. The last two parameters come from the eigenfunctions $e^{ik_z Z}$ and $e^{il\theta}$ used in reducing the three-dimensional integral equation.

In order to investigate Eq. (1), it was found useful to expand $\rho(r)$ in terms of the complete set of eigenfunctions $J_l(kr)$,

$$\rho(r) = \int_0^\infty h(k) J_l(kr) k \, dk \, . \tag{2}$$

The resulting integral equation for $h(k)$ is then

$$h(\kappa) = \int_0^\infty G(\kappa, k) h(k) k \, dk \, , \tag{3}$$

where

$$G(\kappa, k) = \iint K(r, r'') J_l(\kappa r) J_l(k r'') \, r \, dr \, r'' \, dr'' . \tag{4}$$

We considered a particular distribution function f_0

$$f_0(\vec{x}, \vec{v}) = n \frac{b}{2\pi} e^{-ap_\theta - bv_\perp^2} \delta(v_z) \, ,$$

whose space dependence is

$$\int f_0(\vec{x}, \vec{v}) \, d\vec{v} = n e^{-r^2/R_0^2} \, ,$$

$$\frac{1}{R_0^2} = \epsilon(1 - \epsilon) b \omega_c^2 \, ,$$

$$\epsilon = \frac{a}{2b\omega_c} \, .$$

The kernel $G(\kappa, k)$ has then the following form:

$$G(\kappa, k) = \frac{\omega_0^2}{\omega_c^2} \frac{1}{2\epsilon(1-\epsilon)} \frac{1}{k^2 + k_z^2} e^{-1/4R_0^2(\kappa^2 + k^2)} \left\{ \int_{-\infty}^0 dx \, e^{p'x} g(x) I_l \left[\frac{1}{2} R_0^2 \kappa k \, f(x) \right] - 2 I_l \left(\frac{1}{2} R_0^2 \kappa k \right) \right\} \, , \tag{5}$$

where

$$p' = \frac{p}{\omega_c} \, , \quad \omega_0^2 = \frac{4\pi n e^2}{m} \, ,$$

$$f(x) = \sqrt{1 - 4\epsilon(1-\epsilon) \sin^2 x/2} \, ,$$

$$g(x) = \left(2p' - 2il\epsilon + \frac{k_z^2}{b\omega_c^2} x \right) \left(\frac{1 - \epsilon + \epsilon e^{-ix}}{f(x)} \right)^l \, ,$$

I_l = the modified Bessel Function.

It is easy to show that for the two limiting cases where the plasma becomes infinite ($a = 0$ and $a = 2b\omega_c$) the kernel G reduces to

$$G(\kappa, k) = \frac{1}{k} F(k) \, \delta(\kappa - k)$$

and $F = 1$ is the usual dispersion relation.

An interesting case is the long wavelength limit where $R_0 k \ll 1$. Using the formula

$$I_l(y) \sim 1/l!(y/2)^l$$

for $y \ll 1$, the kernel G becomes separable in κ and k;

$$G(\kappa, k) \sim \frac{\omega_0^2}{\omega_c^2} \frac{1}{2\epsilon(1-\epsilon)} \frac{1}{l!} \frac{1}{k^2 + k_z^2} \times e^{-1/4R_0^2 k^2} \left(\frac{kR_0}{2} \right)^l e^{-1/4R_0^2 \kappa^2} \left(\frac{\kappa R_0}{2} \right)^l D \, , \tag{6}$$

$$D = \int_{-\infty}^0 dx \, e^{p'x} \left(2p' - 2il\epsilon + \frac{k_z^2}{b\omega_c^2} x \right) \times (1 - \epsilon + \epsilon e^{-ix})^l - 2 \, , \tag{7}$$

and the corresponding dispersion relation is

$$\frac{1}{D} = \frac{\omega_0^2}{\omega_c^2} \frac{1}{2\epsilon(1-\epsilon)} \frac{1}{l!} \left(\frac{R_0}{2} \right)^{2l} \times \int_0^\infty \frac{k \, dk}{k^2 + k_z^2} k^{2l} e^{-1/2R_0^2 k^2} \, . \tag{8}$$

The right side of Eq. (8) is always positive and varies linearly with the density $n[\omega_0^2 = (4\pi n e^2/m)]$.

The stability investigation of the inhomogeneous plasma has thus been reduced in the long wavelength limit to a solution of a usual dispersion equation.

7.4 EFFECT OF A FINITE BOUNDARY ON ION-CYCLOTRON INSTABILITIES

G. K. Soper[8] E. G. Harris[9]

Unstable oscillations of an infinite plasma in a uniform magnetic field have been investigated by Harris,[10] and unstable cyclotron oscillations of a finite cylindrical shell of cold plasma have been investigated by Burt and Harris.[11] In this work, the general dispersion relation is derived for still another geometry, a plasma slab. A zero-order velocity distribution function of the form $f_0(v_\perp, v_z) \sim \delta(v_z) \exp(-v_\perp^2/\alpha_\perp^2)$ is employed such that the particles have a temperature (velocity) spread in the x and y (infinite) directions and zero spread in the z direction. With this type of distribution function the equations of motion can be solved by using the Maxwell equations, the Vlasov equations in the x and y directions, and the hydrodynamic equations in the z direction. This derivation is made in the first case for no external magnetic field and in the second case for a uniform magnetic field in the positive z direction. In the absence of the external field, three unstable modes exist. One of these is found in the infinite plasma case. The other two involve charges on the plasma surface. It was found that the boundary considerations reduced the Landau damping decrement in the region of long wavelength oscillations.

7.5 IMPURITY RADIATION FROM NON-MAXWELLIAN SPHERICAL PLASMAS

S. Cuperman

The influence of non-Maxwellian free-electron energy distributions on the steady-state de-excitation radiation of not completely stripped impurity ions persisting in homogeneous spherical plasmas is investigated. As in an earlier paper,[12] following an astrophysical method due to Thomas and co-workers,[13] the equation of radiative transfer and that giving the rate of change of the impurity atomic populations, taking into account all radiative and collisional processes involved, are simultaneously solved for arbitrary free-electron distributions. As a result, the simple energy-loss formula for a two-level impurity atom, calculated without the assumption of Boltzmann atomic distributions, but using Maxwellian distributions for free electrons, which was previously found,[14] is corrected to be valid for arbitrary free-electron energy distributions.

To test the importance of the correction introduced, two slightly different free-electron distributions characterized by the same average energy $\bar{E}$ are used: a Druyvesteyn one and a Maxwellian one. When the corresponding energy losses N_D and N_M are calculated, it is found that while insignificant differences occur up to values $\chi_{12} \equiv \frac{3}{2}E_{12}/\bar{E} \cong 1$ (E_{12} is the transition energy), a very strong decrease of the ratio N_D/N_M follows. For $\chi_{12} = 5$ this ratio is already 10^{-2}, while for $\chi_{12} = 10$, it gives 10^{-8}.

The above examples emphasize the fact that for the same average energy of the free electrons, the intensity of radiation and thus the energy loss from a plasma through de-excitation radiation is strongly dependent on the shape of the distribution function of those electrons. The critical value $\chi_{12} \cong 1$, for which the effect becomes considerable, is not a fixed one but corresponds to the two particular distributions chosen. Thus, unless the correct distribution of the electronic plasma is known, no good estimation of the energy loss or spectroscopic information from line intensities can be obtained.

7.6 BEAM-ELECTRON INTERACTION IN DCX-1

C. O. Beasley E. G. Harris[15]

It has been noted previously[16] that an electron stream through the low-density plasma in DCX-1

[8]Oak Ridge Graduate Fellow.

[9]Consultant from the University of Tennessee.

[10]E. G. Harris, *J. Nucl. Energy, Pt C* **2**, 138 (1961).

[11]P. Burt and E. G. Harris, *Phys. Fluids* **4**, 1412 (1961).

[12]S. Cuperman, F. Engelmann, and J. Oxenius, *Phys. Fluids* **6**, 108 (1963).

[13]R. N. Thomas and R. G. Athay, *Physics of the Solar Chromosphere*, Interscience, New York, 1961.

[14]S. Cuperman, F. Engelmann, and J. Oxenius, *Phys. Letters* **2**(2), 71 (1962).

[15]Consultant from the University of Tennessee.

[16]J. L. Dunlap *et al.*, *Thermonuclear Div. Semiann. Progr. Rept. Oct. 31, 1962*, ORNL-3392, p 10.

seems to quiet those oscillations at the ion-cyclotron frequency ω_{c_i} which are present in the absence of the stream. It has been suggested that the stabilization results from damping by the transport of electric-field energy to the walls. It is here shown that the lowest-frequency modes of the Harris instability, a possible source of oscillations in DCX, are indeed stabilized. However, other higher-frequency modes are always introduced. Such additional instabilities with the stream present are observed experimentally (see Sec 1.4, this report).

That stabilization may be achieved by energy streaming is seen from the following argument. We expand the electric field in a Fourier series,

$$E(\vec{x}, t) = \sum_k E_{k_0} e^{i\vec{k}\cdot\vec{x} + i\bar{\omega}_{\vec{k}} t} , \tag{1}$$

where

$$\bar{\omega}_{\vec{k}} = \omega_{\vec{k}} - i\gamma_{\vec{k}} \tag{2}$$

is the complex frequency determined from the dispersion relation. The energy density associated with the kth mode is

$$\mathcal{E}_{\vec{k}} = \frac{1}{8\pi} |\vec{E}_{\vec{k}}|^2 . \tag{3}$$

This energy moves in space with the group velocity

$$\vec{V}_{\vec{k}} = \frac{\partial \omega_{\vec{k}}}{\partial t} . \tag{4}$$

To take into account the flow of energy, we write

$$\frac{\partial \mathcal{E}_{\vec{k}}}{\partial t} + \vec{V}_{\vec{k}} \left(\frac{\partial \mathcal{E}_{\vec{k}}}{\partial t} \right) = 2\gamma_{\vec{k}} \mathcal{E}_{\vec{k}} . \tag{5}$$

Now, if the characteristic length of the plasma is L, Eq. (5) is approximately written

$$\frac{\partial \mathcal{E}_{\vec{k}}}{\partial t} = \left(2\gamma_{\vec{k}} - \frac{V_{\vec{k}}}{L} \right) \mathcal{E}_{\vec{k}} . \tag{6}$$

If the term in parentheses is negative, as might be the case with a sufficiently large group velocity, the plasma is stable to that mode.

The dispersion relation for our situation may be considered to be a generalization of the two-stream type of Burt and Harris,[17]

$$1 = \frac{\alpha \omega_{p_e}^2}{(\omega - kv)^2} + \frac{\beta \omega_{p_e}^2}{\omega^2} + \frac{(m_e/m_i)\, \omega_{p_e}^2}{\left(\omega - \omega_{c_i}\right)^2} = f(\omega) , \tag{7}$$

where ω_{p_e} is the electron-plasma frequency, m_e and m_i the masses of electron and ions, l the mode in question ($l = 1, 2, 3, \ldots$), v the velocity of the electron stream, and k the wave number of the electron stream. We take k to be larger than the reciprocal of the width of the plasma. The parameters α and β are the fractions of the total number of electrons in motion and at rest respectively;

$$\alpha + \beta = 1 . \tag{8}$$

Thus we have incorporated into the dispersion relation not only the streaming between the ions and background electrons but also the additional streaming caused by the electron beam. A plot of $f(\omega)$ for typical parameters might be that shown in Fig. 7.1. Real roots, or correspondingly real ω, occur when the line $f(\omega) = 1$ crosses $f(\omega)$. Conversely, if the singularities occur too near each other, ω has an imaginary root and hence an instability.

For the case of no electron beam ($\alpha = 0$) in DCX-1, the mode with $l = 1$ is unstable if $\omega_{p_e} > \omega_{c_i}$. However, as α becomes larger, β becomes smaller, and the curve around $\omega = 0$ rises more steeply, until finally $f(\omega)$ again intersects $f(\omega) = 1$. Thus a reduction in the fraction of electrons at rest causes stabilization of that mode.

Such a result is subject to the condition that kv be large enough that an instability does not occur between the poles at kv and $l\omega_{c_i}$. It is indeed this latter effect which always causes instabilities of higher modes. The necessary conditions for the presence of these additional instabilities are that (1) it be necessary for β to be sufficiently small ($\beta \ll 0.5$) for stabilization of the $l = 1$ mode to occur, and (2) there exist higher l modes. Both conditions are satisfied.

---

[17] P. Burt and E. G. Harris, *Phys. Fluids* **4**, 1412 (1961).

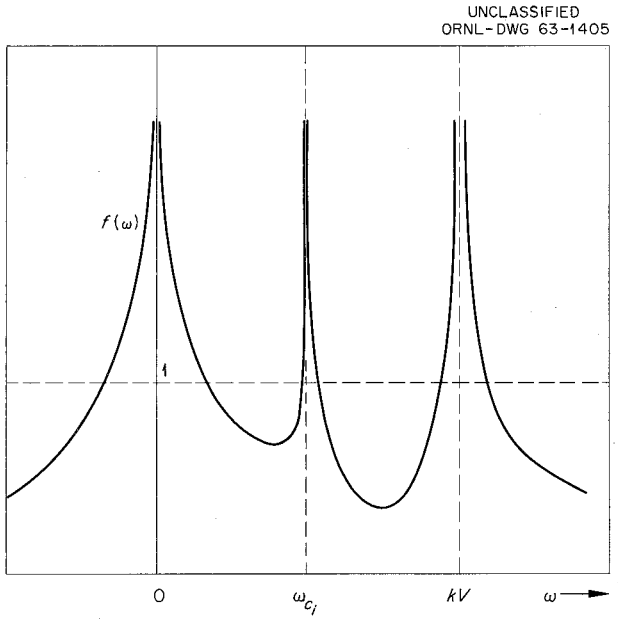

Fig. 7.1. Graphic Solution of the Dispersion Relation.

Solutions to the dispersion relation (6) were found numerically for a variety of the parameters. In all cases of interest, that is, unstable cases with $0 < Re\ \omega < \omega_{c_i}$ (interaction with the electrons at rest), we find that

$$V_k/L < 2\gamma_k \ . \tag{9}$$

Thus the only stabilizing mechanism when $\beta \neq 0$ is the one mentioned previously, that of the change of relative densities of moving electrons and electrons at rest.

Thus the theory is able to describe the stabilization of certain modes and the onset of additional instabilities. Apparently, as long as electrons are present, streaming or not, these instabilities will exist.

7.7 RELATIVISTIC EFFECTS ON PLASMA-DENSITY MEASUREMENTS BY PHASE-SHIFT ANALYSIS

H. W. Graben

In experiments such as those in the Physics Test Facility,[18] the kinetic energy of some electrons is comparable to the rest mass energy, mc^2. Hence, relativistic effects could play an important role in the analysis of these "hot" plasmas.

The index of refraction has been calculated for plane, transverse waves having frequencies large compared with the plasma frequency and with the electron-cyclotron frequency. The relativistic Vlasov equation and Maxwell's equations are solved in the usual manner to obtain an expression for the index, n in the form

$$n^2 = 1 - (\omega_p^2/\omega^2)\ C(T)\ , \tag{1}$$

where $C(T)$ is a function of temperature only. For $T = 0$, Eq. (1) becomes the customary cold-plasma relation with $C(T)$ equal to unity.

For the case of no external magnetic field, an approximate expression (to the first order in ω_p^2/ω^2) for $C(T)$ is obtained in the form

$$C(T) = 4\pi \int_0^\infty \frac{f_0(p)p^2\ dp}{(1+p^2)^{1/2}}, \tag{2}$$

where the (dimensionless) electron-momentum distribution function has the normalization

$$4\pi \int_0^\infty f_0(p)p^2\ dp = 1. \tag{3}$$

This expression for $C(T)$ has been evaluated for two forms of f_0. For the Boltzmann function in relativistic form, that is,

$$f_0^{\mathrm{I}} = \frac{\alpha e^{-a(1+p^2)^{1/2}}}{4\pi K_2(a)}\ , \quad a \equiv mc^2/T\ , \tag{4}$$

we obtain

$$C(a) = K_1(a)/K_2(a)\ , \tag{5}$$

where K_n is the Bessel function of the second kind of imaginary argument. Employing a delta-function distribution of the form

$$f_0^{\mathrm{II}} = \frac{\delta(p - p_0)}{4\pi p^2}\ , \tag{6}$$

the expression for $C(a)$ becomes

$$C(a) = 1/(1 + 3/2a)\ , \tag{7}$$

where a is related to p_0 by $(1 + p_0^2)^{1/2} - 1 = 3/2a$.

[18] W. B. Ard *et al.*, "Investigation of the Electron-Cyclotron Plasma in the Physics Test Facility," this report, sec 3.1.

A numerical evaluation[19] of $C(T)$, applicable to transverse waves with polarization parallel to an external magnetic field, has also been performed for a distribution function of the form

$$f_0^{\mathrm{III}} = \frac{\delta(p_\perp - p^*)}{4\pi K_1(a) p_\perp} e^{-a(1+p_z^2)^{1/2}} , \qquad (8)$$

with $p^{*2} = 2/a$.

The results of these three calculations are presented in Fig. 7.2. These results indicate that microwave phase-shift measurements of the plasma density based on the cold-plasma relation for the index of refraction tend to be too small, particularly at high temperatures ($T > mc^2$).

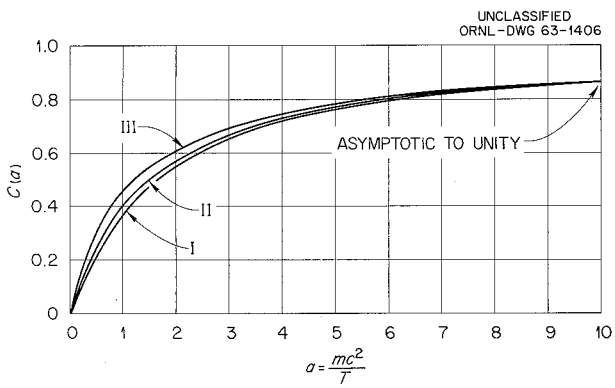

Fig. 7.2. Theoretical Values of $C(a)$ as a Function of the Reduced Temperature for Distributions I, II, and III, Defined in the Text.

7.8 DCX-1 STUDIES

Mozelle Rankin D. A. Griffin J. L. Dunlap

A number of trajectories have been determined for H^+, H_2^+, and H_3^+ beams in connection with studies by the DCX-1 group of Lorentz dissociation and neutral-beam injection. These same studies have entailed calculations of several parameters of the magnetic containment field, calculations of performance characteristics (S curves) for a variety of initial assumptions, and density determinations for precessing H^+ orbits.

7.9 DCX-2 PERFORMANCE CURVES

Mozelle Rankin T. K. Fowler

The previously reported[20] computation of DCX-2 performance curves employing Fokker-Planck equations for ions and electrons has been improved. The simplified expression for mirror loss of particles has been replaced by the more accurate formula recommended by Bing and Roberts.[21] New results, together with old results for comparison, are shown in Fig. 7.3. (Symbols are defined in previous reports.[20]) The increase in critical current (position of a maximum in dI/dn) reflects a smaller factor of increase in the magnitude of the loss term. The fact that the Bing-Roberts loss term becomes very large for an effective mirror ratio near unity has little influence here. The effective reduction in mirror ratio for ions when the space potential is positive is significant only if the potential difference approaches the ion energy.

Table 7.1 compares new and old results for the plasma potential ϕ, the mean ion and electron energies, $E_{\mathrm{av}}^{\pm}$, inside the machine, and the mean energies of escaping particles $E_{\pm}$. The term α is the ratio of neutral density inside the plasma to plasma density, a measure of burnout. The quantity $\alpha = 10^{-5}$ corresponds to the uppermost point on the performance curves (new results); $\alpha = 0.2$ corresponds to the lower bend in the curve (critical current). Other values of α correspond to intermediate points.

---

[19]Acknowledgment is made to R. D. McCulloch (ORGDP) for programming the calculations.

[20]T. K. Fowler and Mozelle Rankin, *J. Nucl. Energy, Pt C* **4**, 311 (1962); *Thermonuclear Div. Semiann. Progr. Rept. Oct. 31, 1962*, ORNL-3392, p 64.

[21]G. F. Bing and J. E. Roberts, *Phys. Fluids* **4**, 1039 (1961).

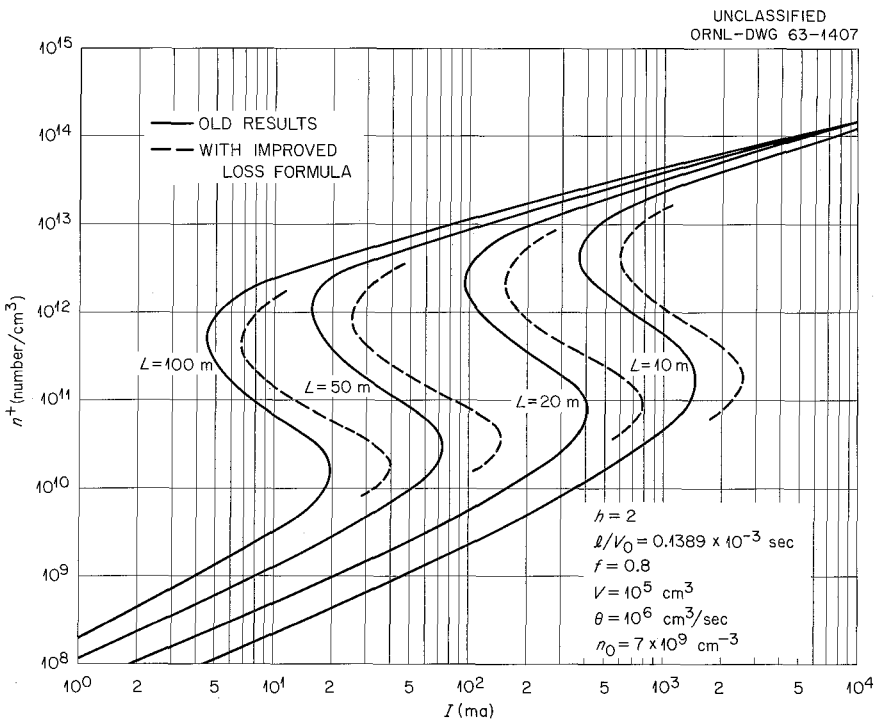

Fig. 7.3. Trapped-Ion Density vs Injected 600-kev H_2^+ Ion Current (Path Length as a Parameter).

Table 7.1. Plasma Potential and Energies at *Different Degrees of Burnout*

For each value of α, the upper line gives old results and the lower line gives results using the improved loss formula of Bing and Roberts.[21] The molecular-ion energy at injection is 600 kev.

α	ϕ (kev)	E^+_{av} (kev)	E^-_{av} (kev)	$\bar{E}_+$ (kev)	$\bar{E}_-$ (kev)
10^{-5}	15.77	175	10.8	86	25.4
	24.05	179	9.4	102	30.5
10^{-4}	4.82	180	4.66	102	8.64
	7.7	174	3.80	100	10.4
10^{-3}	1.36	201	2.18	139	2.95
	2.54	194	1.66	130	3.65
10^{-2}	0.303	226	1.14	183	0.960
	0.784	218	0.760	171	1.29
0.1	0.03	257	0.776	236	0.254
	0.20	244	0.374	214	0.438
0.2	0.012	267	0.749	254	0.152
	0.120	252	0.305	228	0.311

8. Magnetics and Superconductivity

8.1 CURRENT-CARRYING CAPACITY AND TRANSITION STATE OF SUPERCONDUCTING SOLENOIDS

W. F. Gauster D. L. Coffey

8.1.1 Discussion of the Models of Montgomery and of Chandrasekhar and Hulm

Solenoids wound with high-field superconducting wire (for instance, NbZr) display maximum currents I_m and maximum fields H_m which are in general considerably less than the critical current I_c of a short piece of the same wire exposed to a homogeneous transversal field of equal strength H_m ("degradation effect").[1] Montgomery[2] and Chandrasekhar and Hulm[3] suggested models for predicting I_m and H_m of high-field superconducting solenoids. Both models consider a linear relation between the field H and the coil current I ("load line") which is assumed to be identical with that of a nonsuperconducting solenoid with the same dimensions:

$$H = \Phi I \ . \tag{1}$$

For the case of a rectangular coil cross section (inside radius a_1, outside radius $a_2 = \alpha a_1$, and length $2b = 2\beta a_1$) and uniform turn density (n turns per cm^2), Eq. (1) can be written as

$$H = a_1 \phi(\alpha,\beta) I \ . \tag{2}$$

Another assumption of both models is the relation

$$I_m = I(H_m) = I_c(H_m) - I_d(H_m) \tag{3}$$

between the critical values of the coil current I and a current I_d induced in the solenoid ("diamagnetic" or "shielding" current), and the "short sample quenching current" I_c at the critical field value H_m.

For the shielding current I_d in a wire of radius r, Montgomery assumes

$$I_d(H) = \frac{\pi r^2}{F'(\alpha,\beta)} H = f(\alpha,\beta) H \tag{4}$$

[ref 2, Eq. (2)], whereas Chandrasekhar and Hulm's assumption is

$$I_d(H) = KG(H)H \tag{5}$$

[ref 3, Eq. (1)]. The term $G(H)$ varies monotonically from unity at low fields to zero at high fields, reflecting the shape of the magnetization curve for a hard superconductor (Fig. 1 of ref 3), and K is a constant determined by the requirement that at very low fields the flux is completely excluded from the wire. This leads to the value

$$K = \frac{10d}{4\pi}, \tag{6}$$

where d is the distance between two successive turns of one layer. If the solenoid is very tightly wound and if the insulation thickness of the wire is much smaller than its radius r, then $d = 2r$.

[1] S. H. Autler, p 324 in *Proceedings of the International Conference on High Magnetic Fields, Cambridge, Mass., Nov. 1–4, 1961*, (ed. H. Kolm *et al.*), MIT Press and Wiley, New York, 1962; J. K. Hulm, B. S. Chandrasekhar, and H. Riemersma, *High Field Superconducting Magnets*, Westinghouse Research Lab, Sc. paper 62-108-278-P3 (Aug. 8, 1962).

[2] D. B. Montgomery, *Appl. Phys. Letters* 1(2), 41 (1962) and Nat. Magnet Lab. Rep. AFOSR-3015 (July 1962).

[3] B. S. Chandrasekhar and J. K. Hulm, *Appl. Phys. Letters* **2**, 43–44 (1963).

From Montgomery's model it follows that high-field superconductor coils of similar geometrical shape (α and β constant) wound with identical wire type and equal distances between turns, but with different inside radii a_1, should display for any field H the same shielding current I_d [see Eq. (4)], and therefore there should exist a unique coil quenching characteristic $I_m(H_m)$ for α and β constant (Fig. 8.1). If the short sample characteristic $I_c(H)$ of the wire and one quenching point (H_{mI}, I_{mI}) of a solenoid with the inside radius a_{1I} are known, the maximum current I_{mII} of a geometrically similar coil at a critical field H_{mII} can be found [Eqs. (3) and (4)] by

$$I_{mII} = I_c(H_{mII}) - I_d(H_{mII}) \tag{7}$$

$$= I_c(H_{mII}) - I_{dI}\frac{H_{mII}}{H_{mI}}.$$

The inside radius of the second coil is [Eq. (2)]

$$a_{1II} = a_{1I}\frac{I_{mI}(H_{mII})}{I_{mII}(H_{mI})}. \tag{8}$$

Equations (7) and (8) allow a check of Montgomery's model with experimental data. Experiments with a set of geometrically similar coils did not verify the expected data.[4]

Chandrasekhar and Hulm's model leads to a unique $I_m(H_m)$ curve (Fig. 8.2) for all coils wound with identical wire type and insulation dimensions, since K and $G(H)$, and therefore $I_d(H)$ [see Eq. (5)], are the same for all these coils. Solenoids with identical load factor $\Phi = a_1\phi(\alpha, \beta)$ should display identical critical currents I_m and critical fields H_m. This yields a criterion for an experimental check of that model.

8.1.2 Currents and Fields in an Infinitely Long Ideal Superconductor Solenoid

The following ideal case shall be considered:[5] An infinitely long solenoid is wound with ideal superconducting wire (p layers, each layer has n turns/cm). The wire cross section is rectangular, and the insulation between turns is infinitely small

[4] Z. J. J. Stekly, oral communication.

[5] B. S. Chandrasekhar, W. F. Gauster, and J. K. Hulm, "Degradation Factor and Diamagnetic Currents in Supermagnets" (to be published).

UNCLASSIFIED
ORNL-DWG 63-1408

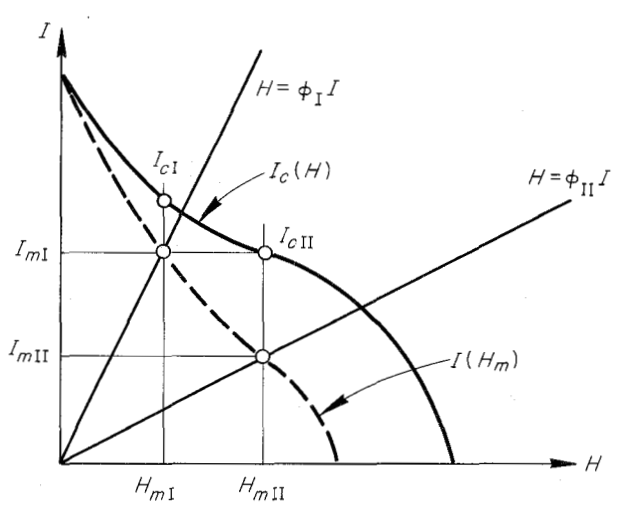

Fig. 8.1. Short Sample Characteristic and Coil Quenching Characteristic Based on Montgomery's Model.

UNCLASSIFIED
ORNL-DWG 63-1409

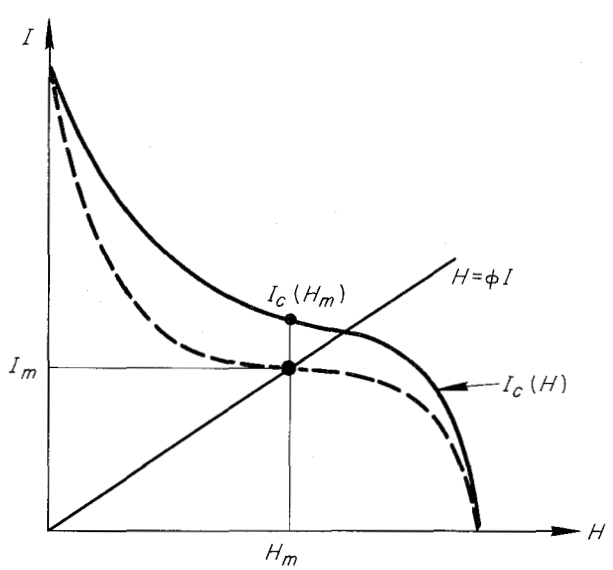

Fig. 8.2. Short Sample Characteristic Based on Chandrasekhar and Hulm's Model.

(Fig. 8.3). In the wire, only surface currents are possible (Meissner effect). In the outside layer I flows only at the inner surface ($I_{1o} = 0$, $I_{1i} = I$). In the second layer $I_{2o} = -I$ and $I_{2i} = +2I$. In the inside layer (number p) $I_{po} = -(p - 1)I$ and $I_{pi} = +pI$. The field inside the solenoid is

$$H_0 = \frac{4\pi}{10} pnI \ . \tag{9}$$

Therefore the field inside an ideal superconducting long solenoid is the same as that on a nonsuperconducting coil having the same number of turns.

In this case the coil quenching current is determined by the condition

$$H_0 = H_c \ , \tag{10}$$

and therefore the quenching current is

$$I_m = \frac{10}{4\pi pn} H_c \ , \tag{11}$$

For an infinitely long ideal superconductor solenoid with circular wire cross section, Eq. (9) holds with good approximation if the insulation between adjacent turns of each layer is thin and if the wire radius r is small compared with the coil radius. The quenching current I_m, however, will be somewhat smaller than indicated by Eq. (11), because of the distortion of magnetic-field lines (Fig. 8.4). An analytical solution is possible but complicated.

UNCLASSIFIED
ORNL-DWG 63-1410

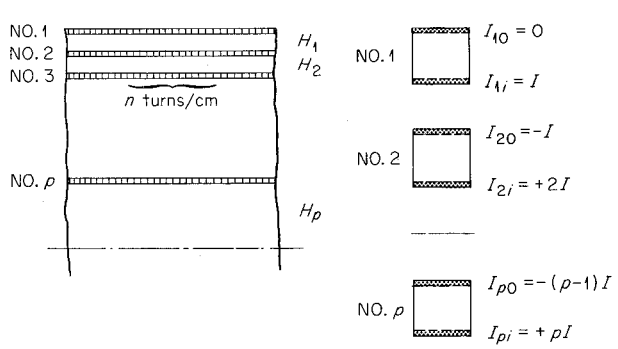

Fig. 8.3. Infinitely Long Soft-Superconductor Solenoid (Ideal Case).

UNCLASSIFIED
ORNL-DWG 63-1411

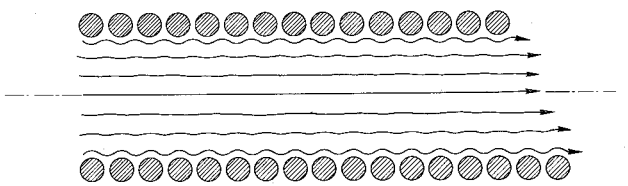

Fig. 8.4. Distortion of Magnetic-Field Lines Due to Circular Wire Cross Section.

8.1.3 Experiments with a Lead Solenoid (Quenching Current and Transition State)

To verify the considerations of the previous section, several experiments were made. A solenoid 3 in. long with a diameter of $\frac{2}{3}$ in. was wound with a single layer of 45 turns of 0.060-in.-diam Pb wire (99.9% pure). In order to produce a practically homogeneous field inside this coil, the solenoid was extended on both ends to an overall length of 8 in. by means of NbZr windings. Their number of turns per unit length was the same as that of the lead windings. Since the experiments were performed at the temperature of liquid helium at atmospheric pressure, the critical field strength of the lead wire was close to 550 gauss. Equation (11) yields a critical current $I_m = 74$ amp if rectangular wire cross section (Fig. 8.3) is assumed.

The normal resistance R_n at 4.2°K of the lead coil was measured in an external magnetic field of about 1 kilogauss to be 156 microhms, which corresponds to a ratio of about 1:1700 to the resistance at room temperature. Figure 8.5 shows the value R/R_n as a function of the current. The first trace of resistance was found at 69 amp, indicating a short tail of the resistance curve. This curve, smoothly extrapolated to zero, yields a coil quenching current of 70 amp. The influence of the circular wire cross section and of the insulation thickness ($d/r = 0.066/0.060$) on the quenching current is apparently small. The experimental value for H_m is between 500 and 520 gauss.

It is of interest to compare this experimental result with an application of Chandrasekhar and Hulm's model to this case. Equation (1) becomes

$$H = \frac{4\pi}{10d} I \ . \tag{12}$$

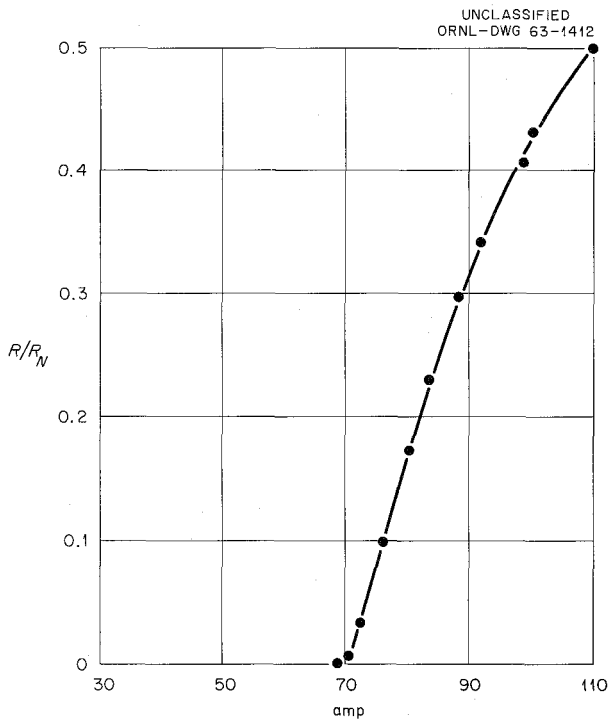

Fig. 8.5. Resistance of a Single-Layer Lead Solenoid in Intermediate State (With Nb-Zr End Compensation).

For the short sample quenching current in a transversal homogeneous field, Silsbee's rule yields

$$I_c = 5r(H_c - 2H) . \qquad (13)$$

By substituting Eqs. (12) and (13) in Eq. (3) and considering for this case $G(0) = 1$, a predicted maximum field strength

$$H_m = \frac{H_c}{2 + (d/\pi r)} \qquad (14)$$

is obtained. The corresponding value of 204 gauss is much smaller than the observed maximum field strength. It is suggested that Eq. (3), on which the models of Montgomery and Chandrasekhar and Hulm are based, cannot be used in the described ways.[5]

Other experiments were made with the same arrangement, however, by leaving the NbZr windings floating and energizing only the lead winding. On each turn of this winding thin copper wires were soldered for measuring the individual turn voltages. At 70 amp only five turns on each end of the lead winding showed voltage drops, indicating that these two parts went into intermediate state; 35 turns of the lead winding remained superconducting. With increased currents, partial resistance was restored to all turns. Figure 8.6 shows the individual turn resistances at a current of 85 amp. Similar experiments are being continued in order to elucidate the complex performance of soft and high-field superconducting solenoids.

8.1.4 Conclusion

Montgomery's model for predicting the degradation effect of superconducting solenoids leads to a unique coil quenching characteristic if geometrically similar solenoids are considered. Chandrasekhar and Hulm's model leads to one unique coil quenching characteristic for all solenoids with identical wire type and turn distance; coils with identical load factor should display identical values I_m and H_m. Experiments do not verify these predicted results. An analysis of the surface currents in an ideal superconducting infinitely long solenoid demonstrates possible forms of shielding currents.[5] Experiments with lead coils with and without NbZr end-effect compensation agree with the expected values of maximum currents and fields. Measurements of individual turn resistances show the behavior of the soft superconductor solenoid in the intermediate state.

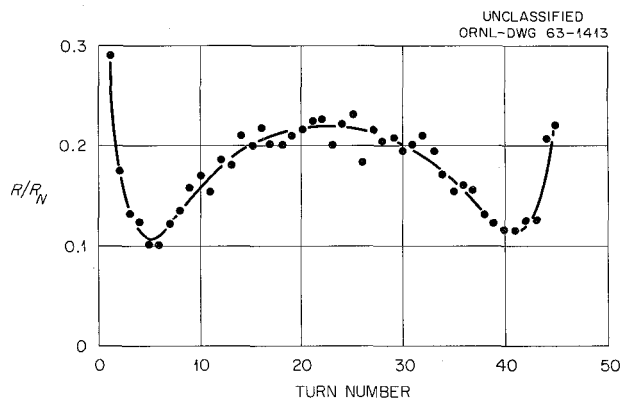

Fig. 8.6. Turn Resistances of a Single-Layer Lead Solenoid in Intermediate State (I = 85 amp) (Without End Compensation).

8.2 SOFT-SUPERCONDUCTOR PROXIMITY EFFECTS

W. F. Gauster J. E. Simpkins
P. A. Thompson

Theory and experiments concerning proximity effects of soft superconductors were presented in the previous report.[6] The experiments were made with a loop of a 99.999% tin wire 20 mils in diameter. The diagnostics consisted in the measurement of the resistance ratio R/R_n, where R stands for the sample resistance in intermediate state and R_n for the resistance in normal state at 3.91°K, that is, very close to the critical temperature of 3.72°K. Figure 7.18 of the cited report shows the intermediate-state resistance curve; however, it is very difficult to decide whether this curve starts with a rather long tail from the calculated critical current I_{sc}, or from a higher current value. This uncertainty is a result of the limits of the sensitivity of the instrumentation for measuring the voltage drop across the sample (10^{-8} v).

By means of another type of diagnostics, namely magnetic-field measurements, it seems to be possible to remove this uncertainty about the start of the intermediate state. Meissner and Heidenreich[7] measured the field between the two superconducting leads of a long, straight current loop in superconducting and normal states. Since at that time the intermediate state of soft superconductors was unknown, no measurements were made in the region of interest of this present study. In the superconducting state the ratio between magnet field and current must, as a result of the Meissner effect, be larger than that in the normal state. Therefore it was expected that the field-current curve should start with a higher slope for the superconducting region and change to a lower slope in the normal state, connected by some sort of transition curve during the intermediate state.

Figure 8.7*a* shows the cross section of the superconducting loop and the bismuth magnetometer. Tentative results of early measurements are indicated in Fig. 8.7*b*. Since the distance between the two tin wires is not exactly known, the current value I_{sc} where the intermediate state should start

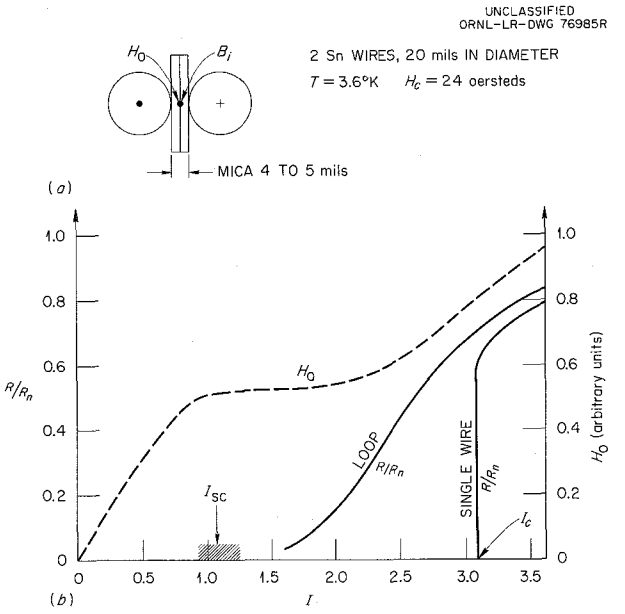

Fig. 8.7. SC–N Transition of "Long Loop."

can be calculated only approximately. The curve representing the measured value H_0 shows a "plateau," apparently starting with I_{sc}, which should indicate that this calculated value I_{sc} is actually the beginning of the intermediate state. The R/R_n values were again very low for currents somewhat larger than I_{sc}; however, these magnet-field measurements seem to indicate that a very flat tail starts at the precalculated value.

A model to explain the behavior in the intermediate state has not been proposed yet. For the much simpler case of a wire in a homogeneous external transversal field, Rinderer's model[8] explains to a good approximation the R/R_n characteristic. The high inhomogeneity of the field produced by the second wire of the loop makes it necessary to alter drastically that simple model. More experiments are being done in order to elucidate this problem.

8.3 CRYOGENIC CURRENT INPUT APPARATUS

R. L. Brown

Improvements have been made on the current input apparatus described in the last progress re-

[6] W. F. Gauster *et al.*, *Thermonuclear Div. Semiann. Progr. Rept. Oct. 31, 1962*, ORNL-3392, pp 81–85.

[7] W. Meissner and F. Heidenreich, *Physik. Z.* **37**, 449–70 (1936).

[8] L. Rinderer, *Helv. Phys. Acta* **29**, 365 (1956).

port.[9] Since previous experience had shown that it was difficult to make reliable bushings for large conductor cross sections through the bottom of a nitrogen container, the original design achieved precooling to 77°K by means of six Dewars symmetrically arranged about the top of the helium Dewar.[10] Further developmental work showed, however, that feedthrough insulators of a special kind were able to withstand repeated exposure to large temperature changes. These insulators have a bore somewhat larger than the diameter of the conductor, which is soldered only to the bottom end of the insulator (Fig. 8.8). The conductor can contract or expand independently from the insulator, which is now not subjected to undue strains. The

[9] R. L. Brown, D. L. Coffey, and W. F. Gauster, *Thermonuclear Div. Semiann. Progr. Rept. Oct. 31, 1962*, ORNL-3392, p 77.

[10] *Ibid.*, Fig. 7.13.

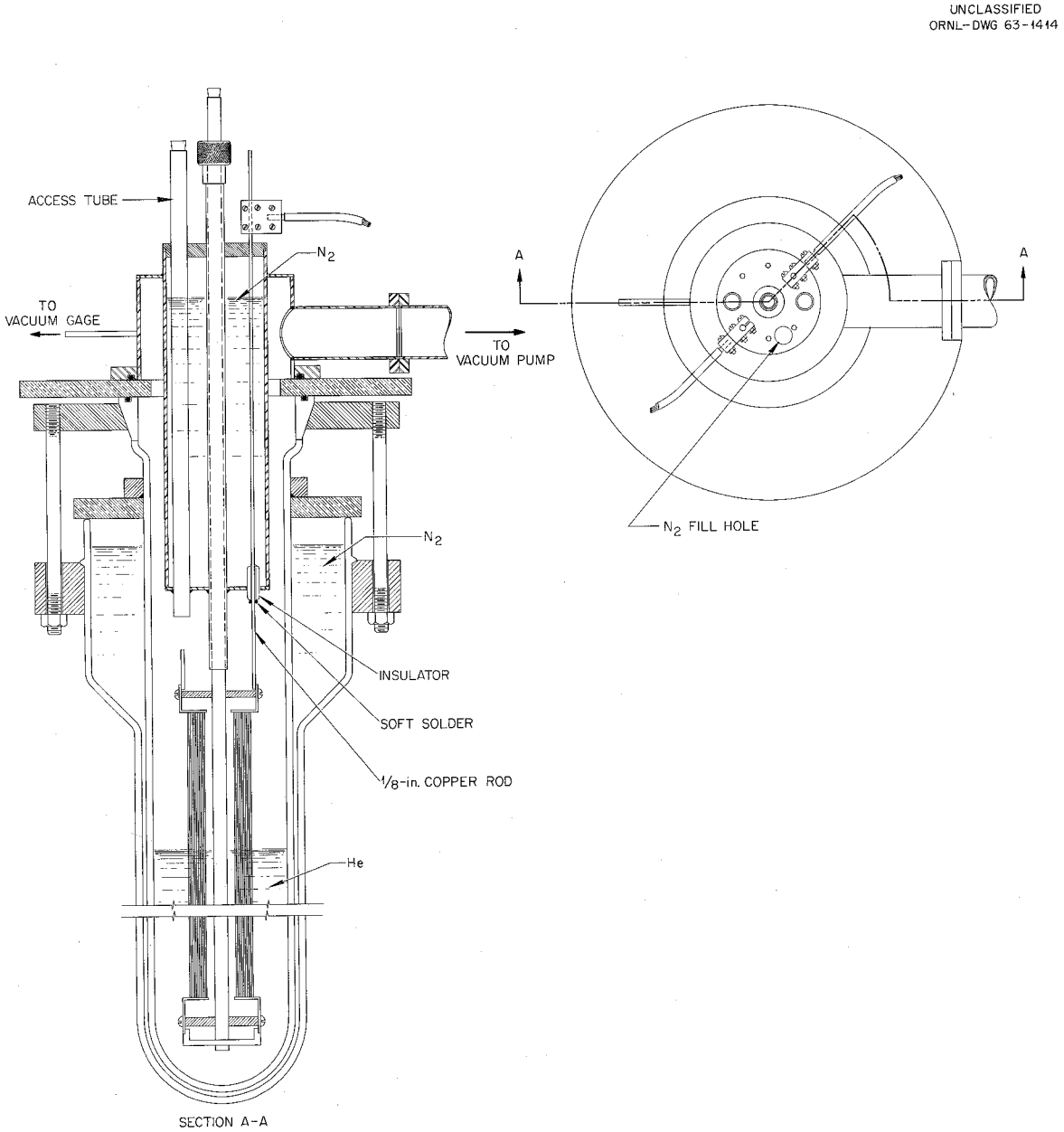

Fig. 8.8. Current Input Apparatus.

soldering of the insulator flange to the container bottom must be done by heating up slowly and uniformly, preferably by furnace soldering.

The head of the current input apparatus was completely redesigned, and by use of a nitrogen container with bushings of the described kind (Figs. 8.8 and 8.9) helium pumping for achieving temperatures below 4.2°K is now possible.

The redesigned head was tested separately by replacing the Dewar with a glass cylinder which was evacuated. A current of 200 amp was passed through two leads ($\frac{1}{8}$-in. round copper), which were shorted together just below the insulators. Only about 1 in. of liquid nitrogen was lost per hour. This loss was nearly the same with no current flowing, since the conductor cross section is relatively large. The small evaporation rate of nitrogen is achieved by making the upper part of the head double-walled, which extends the length of the heat path from the flange to the liquid-

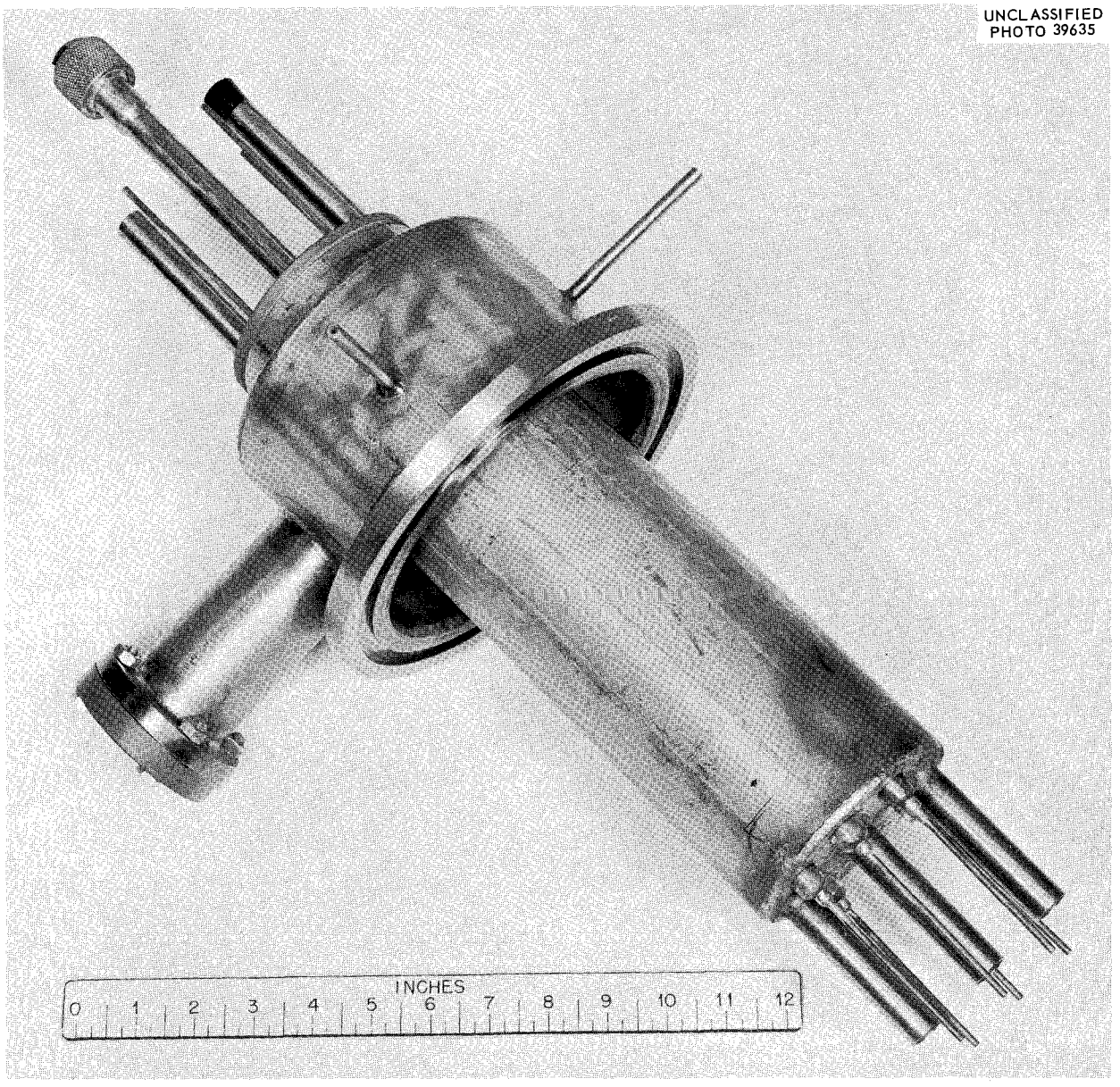

Fig. 8.9. Photograph of Current Input Apparatus.

nitrogen container. Without this measure, the O-ring seal often became too cold and leaked, and also excessive outside frosting occurred.

8.4 METALLURGY OF SUPERCONDUCTING MATERIALS

R. E. Clausing[11] E. E. Barton[11]
M. L. Picklesimer[11] G. R. Love[11]

The development of inexpensive, reproducible, and reliable superconducting magnets is currently of great importance to the problem of controlled fusion and to modern technology in a wide sense. The Metals and Ceramics Division is conducting a series of investigations into the metallurgy of superconductors.[12] Part of this work is in support of the Thermonuclear Project. The investigations combine the practical problems of production and inspection of conductors (which are of immediate interest to the Thermonuclear Project) with a more basic investigation of superconducting alloys and phenomena. Even the more basic investigations in this study are intended to supply information essential to the establishment of manufacturing procedures capable of producing a uniform, high-quality product from one lot to the next.

Among the problems expected in the manufacture of large-volume high-field superconductors are several of immediate and major interest related to the metallurgy of superconductors. Since hundreds of thousands of miles of wire will be required for a single large-volume magnet, perhaps the most obvious problem is the joining of lengths of superconducting wire to other superconductors or to normal conductors without impairing the current-carrying capacity of the circuit. This requires that the contact resistance be made very low, or zero. Several joint designs and materials are being investigated for metallurgical quality and current-carrying capacity.

Another problem is that of quality control and inspection of wire during and after wire manufacture. In the manufacture of large coils and in the present metallurgical study, it is of utmost importance to know the quality of the test wires. For research purposes many test specimens must be cut from one length of wire, and they must be comparable in composition, cold work, diameter, and cross section. The first attempt to provide a rapid and simple method for quality control resulted in the construction of a device to measure continuously the resistance of a $\frac{1}{4}$-in. increment of wire for lengths of wire up to 5000 ft. The measurement is performed by passing the wire at carefully controlled speeds through four sliding contacts which are weighted to give an approximately constant contact load. The contacts are electrically connected to a milliohmmeter using the familiar four-lead method of measuring resistance. The resistance is recorded on a strip chart recorder, and the chart speed is known relative to the wire speed. The combined error in the measuring and recording system is no greater than 2% of the instantaneous value of wire resistance (nominally 0.3 ohm).

Test wires of commercially produced tantalum and Nichrome V were examined by the equipment. In no case was the variation in resistance observed to be as much as 2%, and the reproducibility for any given length was at least ±1%. One lot of commercially produced Nb-Zr superconducting wire was examined and was found to have no variation in 50 ft greater than instrumental error. A second lot, from another manufacturer, was found to exhibit variations in resistance as great as 10%, with a reproducibility of at least 1%. Since a part of the variation could have been due to a surface film (oxide scale, die lubricant, etc.), the test wire was pickled to remove 0.00025 in. from the diameter (5% reduction in area) and the resistance was again measured over the same length. The second determination showed the same variations at each point along the wire, although offset from the original value by about 5% (due to the decreased cross section). This illustrates that the observed variations were due to varying properties in the wire. The variations should reveal defects such as (1) a decrease in cross section; (2) nicks, folds, laps, longitudinal grooves, and cracks; (3) tensile fractures in the core; and/or (4) compositional variations across the diameter and/or along the length.

The survey equipment has been used to select a number of short samples which have significantly higher or lower resistance for testing for superconducting properties and for later destructive examination to determine the cause of the resistance variation.

[11] Metals and Ceramics Division.

[12] M. L. Picklesimer, E. E. Barton, and G. R. Love, "Metallurgy of Superconducting Materials," pt. 1, chap. 11 in *Metals and Ceramics Div. Ann. Rept., May 31, 1963*, ORNL-3740 (in press).

Other metallurgical problems receiving attention include the development of a method for the preparation of homogeneous Nb-Zr alloys, development of anodizing methods for metallographic determination of elemental segregation in these alloys (both macro- and microsegregation), the kinetics of phase transformations in the Nb-Zr alloys, and experimental studies to determine the site and velocity of propagation of the superconducting-normal interface in short wire specimens. These investigations are all well begun. The progress, which through May 1963 has been reported elsewhere,[12] is briefly summarized below.

A study of segregation in alloys was made because homogeneous materials are required for both physical metallurgy studies and the superconducting-property determinations. A casting technique was developed which eliminates macrosegregation and produces only microsegregation in the casting process. Homogenization studies showed that this microsegregation can be eliminated in most of the alloys of the Nb-Zr system by annealing at 1400°C for times ranging from 4 to 24 hr. A metallographic technique was developed for making quantitative analysis of the composition of the alloys over regions ranging from 0.5 μ to several centimeters in diameter. Preliminary tests indicate that this technique can detect zirconium variations of about 1% in alloys ranging from 20 to 50% zirconium.

Studies of the transformation kinetics and morphologies of Nb-Zr alloys showed that the $\beta \rightarrow \beta_1 + \beta_2$ reaction produces a pearlitic structure with interlamellar spacings ranging from 0.1 μ to a few hundred angstroms as the temperature of transformation is decreased. No transformation to the equilibrium α-Zr + Nb structure occurred in one week at 400, 500, or 600°C. Time-temperature-transformation diagrams were determined for alloys containing 25 to 40% Zr. Composition had little effect on the incubation period for the transformation, but did affect the time for completion of the transformation. Cold work accelerated both the beginning and completion of transformation. The nose of the TTT diagram is at about 700°C and is independent of composition.

Although these latter investigations may seem somewhat removed from the problem of understanding the basic principles of superconductivity or the immediate problems of producing experimental magnets, they will establish a firm foundation on which to build the procedures and processes for commercial production of large quantities of uniform wire. A thorough understanding of the alloy systems involved will be required for an optimization of the required properties and for establishment of production processes with adequate quality control.

8.5 MICROMAGNETOMETERS FOR LOW TEMPERATURE

J. E. Simpkins P. A. Thompson

In order to investigate the effects of mutual proximity on current-carrying superconducting wires, it is necessary to measure the magnetic field between two wires.[13,14] Since the expected effects would be most easily measured for small ratios of separation to radius and since other considerations indicated a wire diameter of about 20 mils, the space available for the magnetometer is a few mils or less. Furthermore, to minimize any possible end effects from using superconducting samples of a short finite length, it is desirable for the magnetometer to make readings localized to the middle of the sample length. Other general requirements are that the magnetometer be mechanically resistant to cycling between room temperature and liquid-helium temperature, that it have an impedance which can be matched to necessary amplifying equipment, and that it have a large signal-to-noise ratio.

Three types of magnetometers were considered for the proximity investigations: flip coils, Hall-effect elements, and magnetoresistive elements. One of the earliest investigators to use flip coils was Meissner.[15] Even his 1.5-mm coils would be too large in the present case; however, there is undeniable attractiveness in the absolute calibration of such coils, which would only be limited by the precision of measurement of their physical dimensions at liquid-helium temperature. Commercially available indium arsenide Hall-effect elements have been used at liquid-helium temperatures for periods of up to six months without deleterious

[13] W. F. Gauster *et al.*, *Thermonuclear Div. Semiann. Progr. Rept. Oct. 31, 1962*, ORNL-3392, p 81.

[14] W. F. Gauster *et al.*, "Soft-Superconductor Proximity Effects," this report, sec 8.2.

[15] W. Meissner and F. Heidenreich, *Physik. Z.* **37**, 449 (1936).

effects.[16] They have such advantages as indicating the direction of the field and giving approximately zero output signal for zero field. Their disadvantage again is size; since they respond to fields parallel to the thin dimension, they are, for usable sensitivity, necessarily large in the other dimensions.[17,18] The third type of magnetometer, the magnetoresistive type, has the disadvantages of not indicating field direction, of giving a large signal for zero field, and of having a signal with a quadratic field dependence in the range of interest. The very real advantage of magnetoresistive magnetometers is that they may be made extremely thin with field sensitivity perpendicular to this thin dimension. Since size was such a dominant factor, further investigation was restricted to magnetoresistive elements, specifically those made from bismuth, since it shows the greatest sensitivity.[19]

Investigation has been conducted into the fabrication and testing of bismuth magnetometers made from short extruded or Taylor-process[20] wires and vacuum-deposited films. An additional type using a small boule of bismuth attached to 1-mil V-shaped leads has been suggested by Shiffman.[21] Others have successfully used for magnetometers extruded bismuth wires several mils in diameter wound into noninductive spirals[22] and very thin extruded wires pressed down and cut into fractional mil-sized strips.[23]

In the work of this report two major problems have been encountered in all bismuth magnetoresistive elements: (1) maintaining the integrity of wires or of substrates (for films) upon cycling between room and liquid-helium temperatures and (2) making and maintaining low-noise electrical contacts. The specific problems with extruded wires were that the larger, more convenient size (nominal 5-mil diameter) is too large to put directly between the superconducting samples and that the necessary current and potential contacts add even more to the size. One-mil wires, on the other hand, were too fragile and unreliable even when mounted in mica strips. The Taylor-process wires[24] also proved to be so delicate that it was necessary to mount them on mica strips, which then provided a convenient method by which to support the assembly. The glass on the ends of the probe was etched off with hydrofluoric acid, and connections were made with gold leaf and silver epoxy. These connections were no thicker than the glass-encased wire, both of which were sandwiched between the mica strips; however, no combination of gold leaf and/or silver epoxy proved entirely reliable after repeated immersions in liquid helium. Moreover, the active length of the probe (that between the potential contacts) had to be a few centimeters, adding to the difficulties of aligning the finished magnetometer between the superconducting samples. A final problem with the Taylor-process wires was the uncertainty of the actual wire size, making it almost impossible to predict the resulting impedance of a given assembly.

By far the most promising method for fabricating reliable bismuth magnetometers at present seems to be vacuum-deposited thin films – especially for probe assemblies less than 2 mils (50 μ) thick. Therefore the latter half of the present report period was devoted to thin-film studies.

Magnetometers made from suitable magnetoresistive material (here bismuth exclusively) have their own peculiar difficulties, some of which have yet to be satisfactorily overcome. For instance, it is reported[25] that very thin films (probably less than a few thousand angstroms) should show competing effects (in a magnetic field) of increasing resistance from normal bulk magnetoresistivity and of decreasing resistance from geometrical considerations of thinness and nonuniformity. By thickness control, which will be discussed at some length presently, it is possible to prevent to some extent this complication. Furthermore, several authorities

[16] Representative of Cryogenic Products Department of Linde Company at Physics Show of American Physical Society at January 1963 meeting in New York, private communication.

[17] H. Kronick, *IBM J.* **12**, 252 (1958).

[18] D. Roshon, *Rev. Sci. Instr.* **33**, 201 (1962).

[19] P. Kapitza, *Proc. Roy. Soc. (London)* **A119**, 358 (1928).

[20] J. Strong, *Procedures in Experimental Physics*, p 312, Prentice-Hall, Englewood Cliffs, N. J., 1938.

[21] C. A. Shiffman, *Rev. Sci. Instr.* **33**, 206 (1962).

[22] H. Laquer, Los Alamos Scientific Laboratory, private communication.

[23] A. Meshkovsky and A. Shalnikov, *J. Phys.* **11**, 1 (1947).

[24] These "fibers" were fabricated by C. Burlow, Department of Physics, Louisiana State University.

[25] J. M. Reynolds, consultant, Louisiana State University, private communication.

have shown that bismuth becomes superconducting,[26] or at least not magnetoresistive,[27] when the normal crystalline structure is replaced by an amorphous one, which may easily result from depositing on a too-cool substrate[28] or from depositing too slowly.[29] However, it has been found that defective films can be transformed to the proper uniformly smooth structure by annealing them above their melting point. Some workers[30] insist that a bismuth oxide jacket must be sputtered around the desired film to prevent its breakup upon melting; others maintain[31] that a sufficiently strong coating is formed automatically whenever bismuth is heated in the presence of air. In our work the former method has so far proved unsuccessful; use of the latter method, just barely begun, shows very promising results.

Two problems previously encountered in other types of bismuth magnetometers are especially troublesome in films: methods of making electrical connections and choice of substrates. Mica as thin as 2 or 3 μ has been used for substrates, but it is exceedingly delicate to handle. Commercially available microscope-slide cover glasses (about 150 μ) have proved to be the most convenient for test deposits. Cover glasses about 75 μ thick should provide usable substrate and cover "sandwiches."

Since thin-film bismuth magnetometers were well known (in theory, if not in practice), the really original aspect of the present work was the design of the masks used to deposit the films. The specific design considerations were: (1) that there should be a small active area, (2) that the portion of the film to which the electrical connections would be made should be as nearly insensitive to magnetic field as possible, (3) that the shape of the film should be such that the finished "sandwich" would be uniform in thickness, and (4) that some method should be provided for the accurate determination of the active area of the magnetometer, even when obscured by the superconducting samples. To accomplish these aims, layer depositing with multiple masks was indicated; Fig. 8.10 shows the schematic arrangement, Fig. 8.11 shows the mask designs, and Figs. 8.12–8.14 show the the actual masks. The active-area slit in mask No. 1 is 25 $\mu \times 1000\ \mu$; the gold deposited by mask No. 2 renders the rest of the bismuth magnetically insensitive. The gold from mask No. 3 provides sufficient thickness for making electrical connections. (In actual practice, thus far, only one thick coat of gold applied with mask No. 2 has been used.) Finally, the "7-mm" fiducial mark executed with modest care on the art work, which was over six times actual size for all three masks, became highly precise upon reduction to the size of the contact-print-size negatives.

In order to reduce "undercut" during the photoetching process and to minimize "shadows" during actual depositing with the masks, it was desirable to make the masks from a material which would be as thin as possible but still capable of maintaining its shape and supporting its own weight. Further, ease of etching limited the choice for all practical purposes to copper and aluminum.

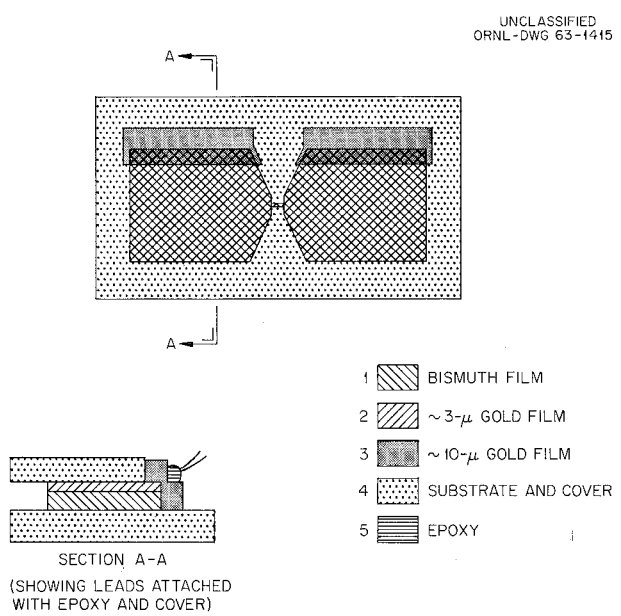

Fig. 8.10. Schematic Diagram of Multilayer-Deposited Magnetometer. Thickness and width of active area greatly exaggerated for clarity.

[26] See, for instance, D. Shoenberg, p 239 in *Superconductivity*, Cambridge University Press, 1938.

[27] P. Kapitza, *Proc. Roy. Soc. (London)* **A119**, 430 (1928).

[28] W. Buckel, pp 53–57 in *Structure and Properties of Thin Films* (ed. by C. Neugebauer *et al.*), Wiley, New York, 1959.

[29] H. Levinstein, *J. Appl. Phys.* **20**, 306 (1949).

[30] A. Colombani and P. Huet, pp 253–62 in *Structure and Properties of Thin Films*, (ed. by C. Neugebauer *et al.*), Wiley, New York, 1959.

[31] A. Meshkovsky and A. Shalnikov, *J. Phys.* **11**, 1 (1947).

UNCLASSIFIED
PHOTO 39730A

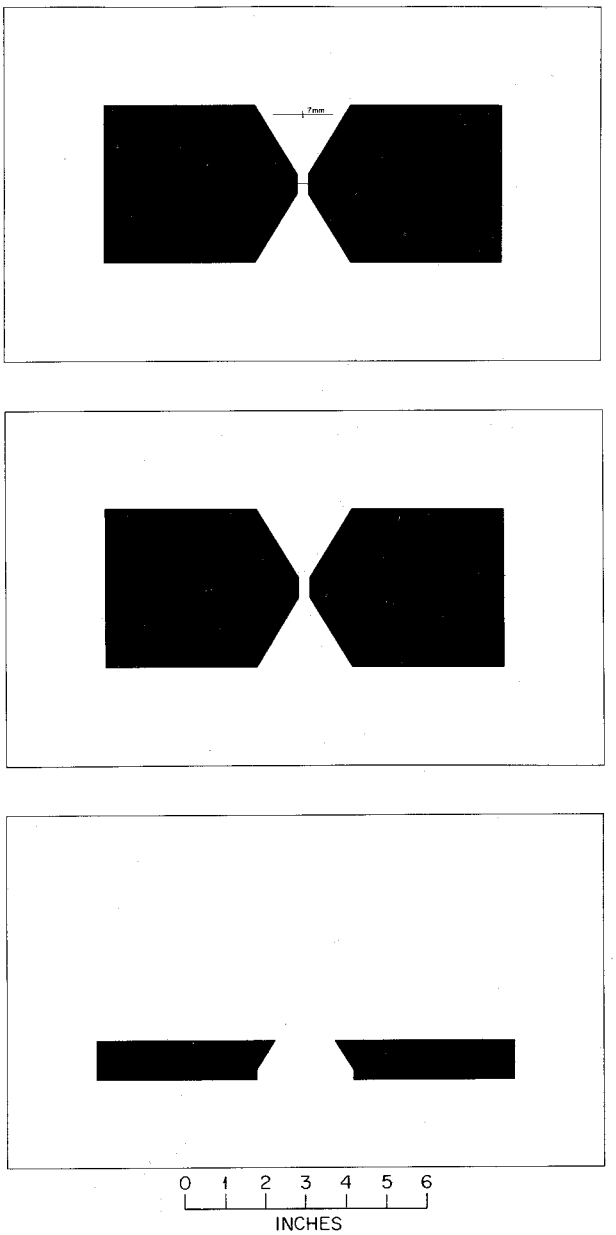

Fig. 8.11. Art Work from Which Contact Negatives Were Made.

Since aluminum sputters away at a slower rate than copper in the nitrogen-ion bombardment[32] used to clean the substrates during the depositing process, it would have been the better choice of material; however, only copper sheets of reasonable flatness for the desired thickness (1 mil or less) could be obtained, and even these were unbelievably "wavy" and "bumpy" compared to the 25-μ slit to be etched in them. It was necessary, in fact, to press the flattest obtainable sheets of copper between large parallel blocks (used in lieu of steel optical flats) on a 50-ton press to make usable blanks. The resulting smooth copper blanks were covered with Kodak Photo Resist (KPR)[33] (which was applied by dipping and allowed to dry at room temperature for 25 hr), exposed to ultraviolet light through the appropriate mask for 15 min, soaked in acetone for 5 min (to facilitate removal of unexposed KPR after development), developed for 5 min in KPR developer (full strength), spray-rinsed in 50% KPR developer—50% KPR thinner, soaked again in acetone for 5 min, and dried, and the resulting nonresistant portions were etched through with a ferric chloride solution. The Photo Resist coating was then dissolved with trichloroethylene.

Upon completion, the masks could indeed hold their shape, but it was necessary to mount them in $\frac{1}{16}$-in. brass plates and to reinforce them with pieces of wire so that they would not droop under their own weight (see Fig. 8.13) when heated by the deposition process. In all, some dozen masks were made and discarded before a completely satisfactory set was obtained.

Upon completion of the masks, the most time-consuming part of the program began – the actual vacuum deposition of the films. It would be hard to estimate how many finished probes, partial probes, test plates, and thickness-control glasses have been deposited, as almost all the pitfalls of film making have been rediscovered. It is possible that probes by the dozen will have to be made before a sufficient number of optimized magnetometers are produced. In all cases it has been found necessary to chemically clean the surface for deposition with either concentrated nitric acid or a solution of chromic-sulfuric acid, followed by rises in distilled water and acetone to remove surface contaminants. After placement in the vacuum depositer, any remaining monolayers of contaminant were removed by about 15 min of ion bombardment at 45 to 50 μ of nitrogen with a 3- to 5-kv glow discharge drawing about 100 ma.

Base pressures for long enough mean free paths for the depositing atoms are given variously from

[32] J. Strong, *Procedures in Experimental Physics*, p 163, Prentice-Hall, Englewood Cliffs, N. J., 1938.

[33] Kodak Photo Resist (KPR) and associated developer and thinner manufactured by Eastman Kodak Company, Rochester, N. Y.

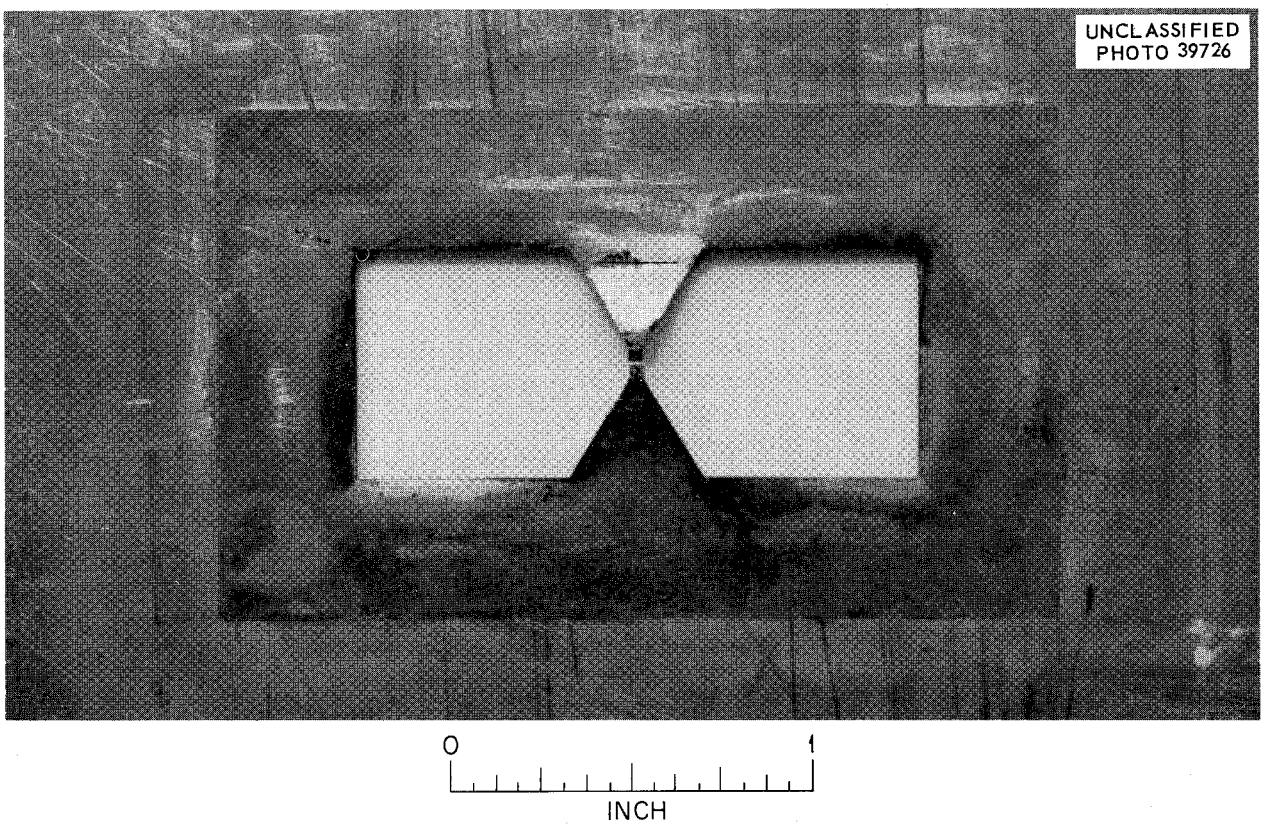

Fig. 8.12. Substrate Side of Mask No. 1 Mounted in $\frac{1}{8}$-In. Brass Plate.

5×10^{-5} to 10^{-3} torr;[34,35] however, the resulting structure of the deposited film depends upon the nature of the residual gas. In actual practice, base pressures between 2×10^{-5} and 5×10^{-6} torr were attainable with reasonable care in the cleaning of the inside of the vacuum chamber.

The experiments of Levinstein indicate that the rate for deposition of bismuth films should be as high as possible. The original arrangement of the vacuum depositer used provided a distance of about 40 cm from heater to substrate. At this distance the rate was so slow that what appeared to be an oxide coating accompanied all deposits over a few thousand angstroms thick. Then, following the suggestion of Roshon, the heater was moved to 10 cm from the substrate; at this distance severe radiant heating of the mask, substrate, and associated supporting parts occurred until a radiation shield was installed. This shield consisted of a sheet of tantalum about 3 cm from the heater with a small collimating slit cut in it. With this arrangement it was possible to deposit films several microns thick without appreciable heating and without the resulting "oxide" coating. In the most recent phase of the program, however, relatively thin films were desired for studying the effects of heat treatment; since this treatment would correct for amorphous structure and since the short heater-substrate distance then being used led to rather poor uniformity of deposition, this distance was once more increased, according to the formula of Tolansky,[36] to 35 cm – this time, however, using the heat shield.

The distance from the heater to the substrate affects the rate of deposition perhaps no more than does the type of heater element used. Tolansky[37] makes the point that for extreme purity of deposit the substrate should "see" as large a ratio as

[34] D. Roshon, *Rev. Sci. Instr.* **33**, 201 (1962).

[35] H. Levinstein, *J. Appl. Phys.* **20**, 306 (1949).

[36] S. Tolansky, *Multiple Beam Interferometry*, p 28, Clarendon Press, Oxford, 1948.

[37] *Ibid.*, p 27.

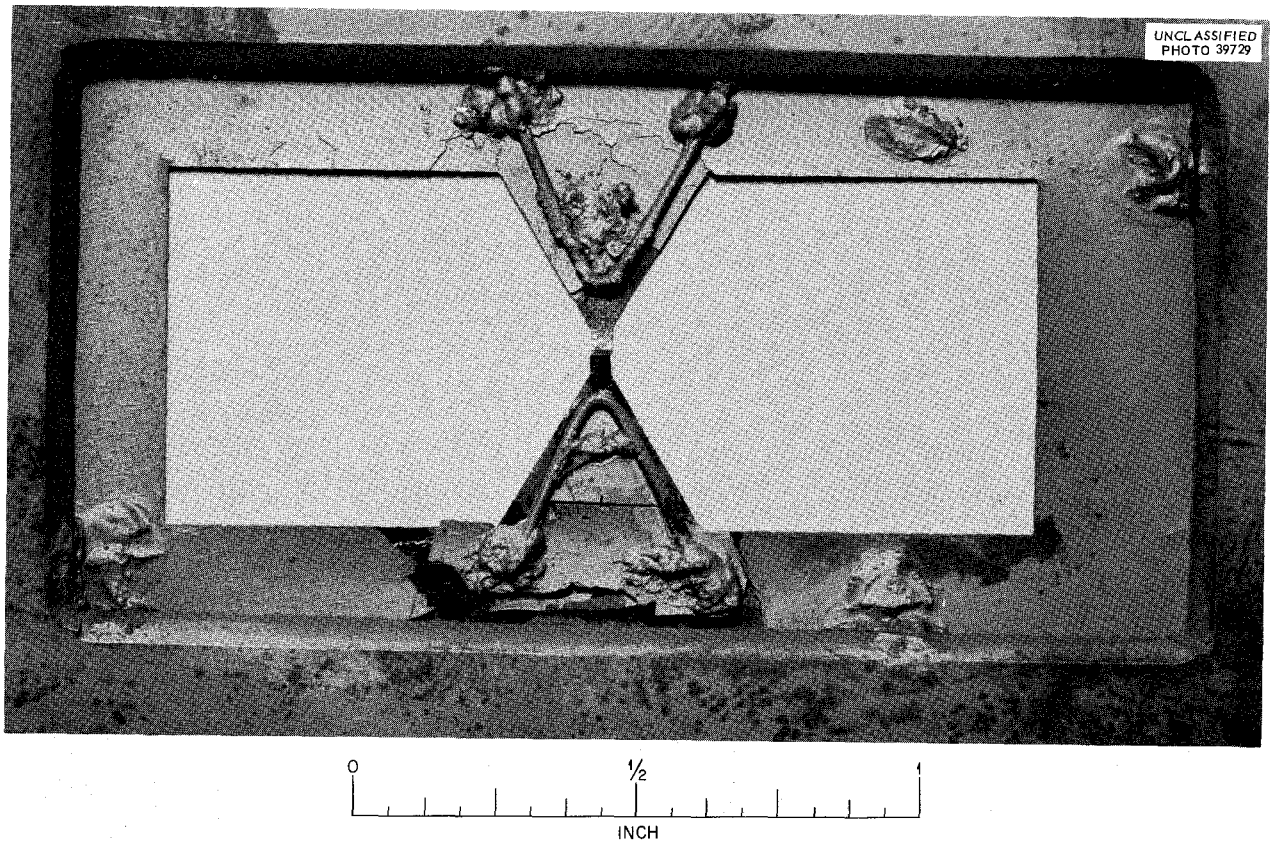

Fig. 8.13. Heater Side of Mask No. 1 After Some Three Months of Use Showing Buildup of Bismuth and Effects of Wear. Note "vees" of copper wire which reinforce weak portions of mask.

possible of material to be deposited to heater material, since the latter may attain temperatures high enough to emit particles by some process. For this condition it has been found sufficient to use either a strip of the heater material (usually tungsten, tantalum, or molybdenum) with its sides bent up to retain the molten bismuth or a boat of V-shaped cross section, both of which have only thin edges of the heater material not covered by bismuth and therefore "visible" to the substrate. In the case of gold or aluminum (the latter used for the multiple-beam interferometry described below), it was found that the method given by Strong[38] of hanging small loops of deposit material on a spiral tungsten filament admirably met the high-ratio criterion, since the material "wetted" and flowed all over the tungsten before actually beginning to deposit.

Having chosen the heater-substrate distance and the type of heater, one need only vary the current through the heater to control the rate of deposition. This, however, is far from being an exact science. Useful rules of thumb were developed during the studies, but exactly reproducible conditions were never achieved. In the final analysis, measurement of thickness is necessary, either during the process or after the deposit has been removed from the vacuum chamber. Five different methods of film-thickness monitoring or measuring have been considered, and three of these were tried, with varying degrees of success.[39] Probably the first method that would occur to one for measuring thin sheets of metal would be the use of a standard micrometer. These normally will read to 0.001 in. (25.4 μ) and with a vernier to 0.0001 in. (2.54 μ); dial micrometers can be read by interpolation to

[38] J. Strong, *Procedures in Experimental Physics*, p 163, Prentice-Hall, Englewood Cliffs, N. J., 1938.

[39] K. Greenland *et al.*, *Vacuum* **2**, 216 (1952).

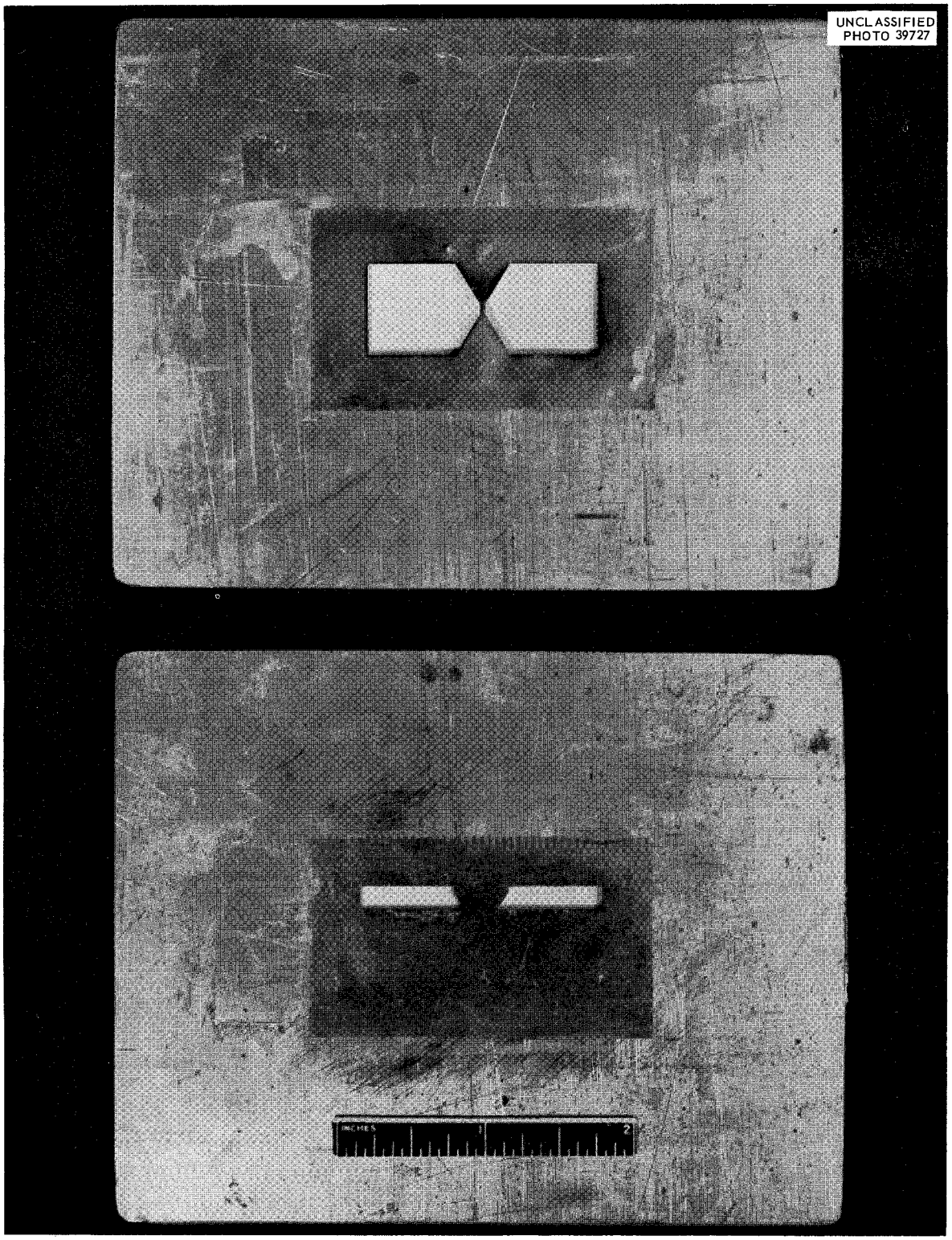

Fig. 8.14. Substrate Side of Masks No. 2 and 3 (Mounted in Brass Plates).

even smaller fractions. However, since these instruments rely on physical contact for measurement, they exert enough pressure to be destructive to the surface. In the case of certain films several microns thick, it has been possible to place a cover glass over the surface and make a thickness determination of moderate accuracy. The second most direct method of measuring thickness, which is widely used, is weighing of a known area. There is no limit, other than the sensitivity of the balances employed, to the range of thicknesses that can be inferred from this method; however, there is the fundamental question of the meaning of thickness for a nonuniform deposit.[40] Delicate balances have been constructed[41] which could be put right into the vacuum depositer, thereby making it possible to monitor "thickness" during depositing. Owing to the odd shape of the desired deposit and to nonuniform distribution resulting from the close heater-substrate separation, this method was deemed unreliable for the present study; however, it may be used for process monitoring at a future date. Another way of monitoring during actual depositing is afforded by changes in resonance of a thin diaphragm as the deposit builds up on it. Such an instrument is commercially available and might prove useful.

The final two methods of thickness determination, both of which have been used during this study, are usually performed with a microscope. Most good microscopes, such as the Bausch & Lomb metallurgical model used here, have fine adjustment of the stage calibrated to a micron or so. By focusing first on the top of the substrate and then on the top of the deposit, it should be possible to make a direct reading of film thickness without any corrections. Unfortunately, however, the process is strongly subjective, and even the average of many readings taken by several observers often turns out to be quite different from the more exact method next discussed.

The final method considered is that of Fizeau fringes, which occur for surfaces separated by an integral number of wavelengths of the illuminating light. Details of rather sophisticated improvements in the method are discussed at length by Tolansky.[42] Not only can this method be used under proper conditions to measure films up to several microns with high precision, but also there is at least one commercially available instrument working on this principle that monitors thickness during deposition. Multiple-beam interferometry was the variation employed during the present study. For films up to about 5000 A the thickness has been estimated to a few hundred angstroms by simply putting an optical flat (or a piece of ordinary picture glass) on a film-substrate intersection, illuminating it with 5461-A green light passed by a suitable filter from a mercury discharge lamp, and alternately pressing different parts of the glass until fringes appear perpendicular to the intersection. The thickness of the film is then the fraction of the fringe (half the 5461-A wavelength) shifted in going from the film to the substrate. For more precise determinations or measurements on films several microns thick ($1\ \mu = 10{,}000$ A), the metallurgical microscope is used with special partially reflecting interference plates, a monochromatic light source (5080 A), and a filar-micrometer eyepiece. In either case, the method of fringe shifts is not always possible and is seldom routine. For easily counted fringes it is necessary to have a continuous transition from film to bare substrate. Further, to avoid the ambiguities of phase shift[43] and to intensify the fringes by providing more contrast, it is desirable to deposit an additional layer of aluminum or silver over the film-substrate transition. Although this additional coating can correct for abrupt transitions, it obviously cannot be applied to films which are to become parts of finished probe assemblies.

As this report period came to an end, two rather distinct sets of potentially usable films had been deposited: the first (Fig. 8.15 is a sample), deposited at a rather high rate to a depth of some microns in order to form a crystalline structure, and the second (Fig. 8.16), deposited somewhat more slowly and thinly to be used in determining the efficacy of heat treatment. Besides these two groups, three individual probes of more or less unknown origin were subjected to rather extensive tests. The deposition data on all the probes are given in Table 8.1. Electrical measurements were attempted on only some of the probes, and in some

[40] L. Holland, *Vacuum Deposit of Thin Films*, p 220, Wiley, New York, 1958.

[41] P. Clegg and A. Crook, *J. Sci. Instr.* **29**, 201 (1952).

[42] S. Tolansky, *op. cit.*, especially chap. II.

[43] O. Heavens, *Optical Properties of Thin Solid Films*, p 107, Butterworths, London, 1955.

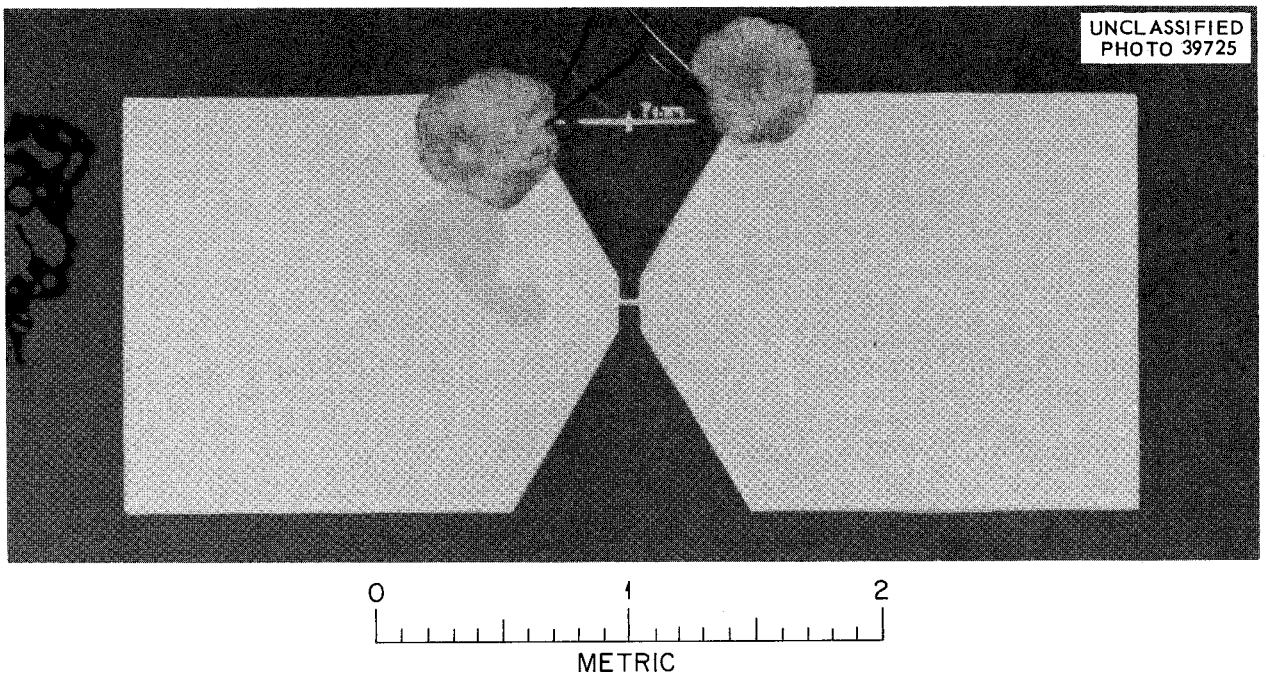

Fig. 8.15. Finished Probe on 2.5-μ Mica Substrate Consisting of 13 μ of Bismuth Deposited Through Mask No. 1 and 3 μ of Gold Through Mask No. 2. Leads are 40 AWG copper attached with silver epoxy; assembly covered with another 2.5-μ sheet of mica.

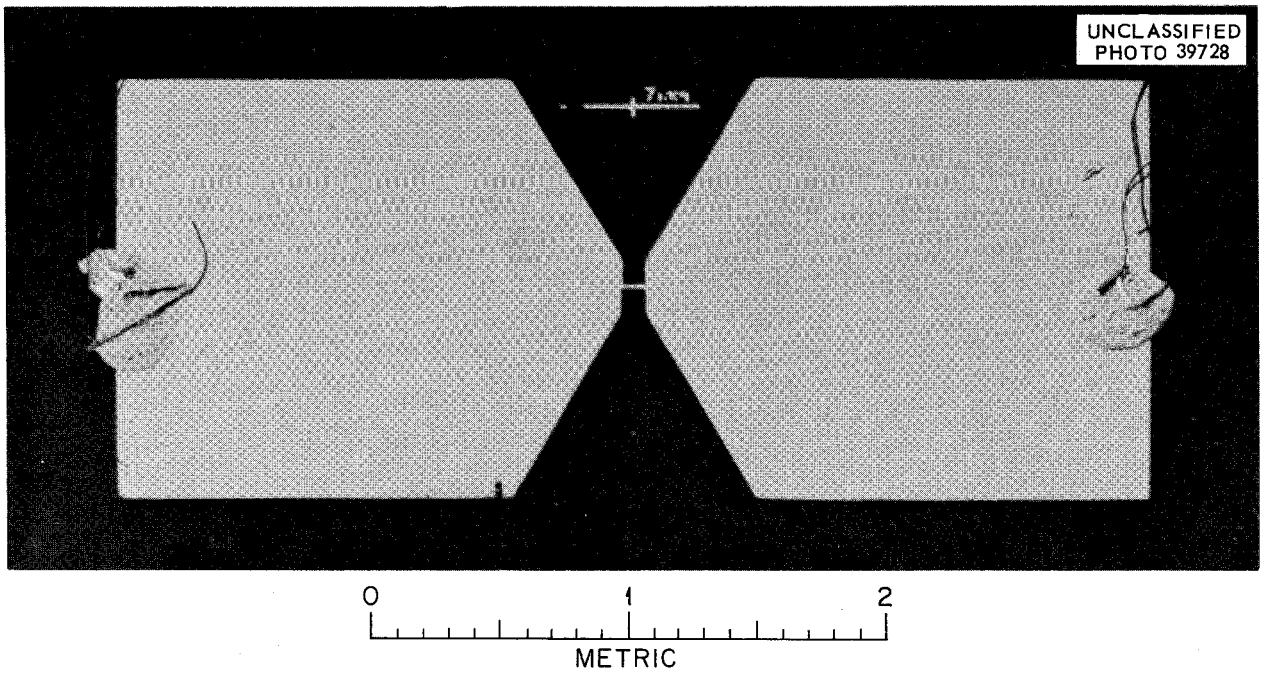

Fig. 8.16. Thin Probe Arranged for Testing Prior to Heat Treatment. 2000 A of bismuth through Mask No. 1 on 150-μ glass substrate; electrical leads attached with silver paste.

Table 8.1. Deposition Information

Probe Number	Distance from Heater to Substrate (cm)	Substrate Material	Chamber Pressure (torr)	Deposition Time (sec)	Thickness	Type of Contacts
1	10	Mica	5×10^{-6}	60	12.0 μ	*a*
2	10	Mica	5×10^{-6}	60	12.5 μ	*a*
3	10	Mica	5×10^{-6}	60	6.1 μ	*a*
4	10	Mica	5×10^{-6}	60	13.3 μ	*a*
5	10	Mica	5×10^{-6}	15	<1 μ	*a*
6	10	Mica	5×10^{-6}	60	15.5 μ	*a*
7	10	Mica	5×10^{-6}	60	10.4 μ	*a*
8	10	Mica	5×10^{-6}	60	5.6 μ	*a*
9	10	Mica	5×10^{-6}	60	11.7 μ	*a*
10	10	Glass	2×10^{-5}	15	5,080 A	*b*
11	10	Glass	2×10^{-5}	10	3,300 A	*b*
12	10	Glass	1×10^{-5}	5	2,030 A	*b*
13	10	Glass	1×10^{-5}	20	1,550 A	*b*
14	10	Glass	1×10^{-5}	30	3,040 A	*b*
15	10	Glass	1×10^{-5}	30	6,600 A	*b*
16	10	Glass	1×10^{-5}	60	17,700 A	*b*
17	35	Glass	2×10^{-5}	120	7,110 A	*b*
18	35	Mica	2×10^{-5}	60	7,620 A	*b*
19	35	Glass			~8 μ	*c*
20	10	Mica	8×10^{-6}	60	2 μ	*c*
21[d]	35	Glass			< 1 μ	Silver epoxy to bismuth film

[a]Copper leads attached with silver epoxy to approximately 3-μ gold film deposited on "land" areas of bismuth film.

[b]Copper leads attached directly to bismuth film "land" area with silver epoxy.

[c]Silver epoxy to gold film (as above).

[d]Annealed at 300°C for approximately 5 min.

cases instrumental troubles (especially excess noise resulting from bad mismatch between probe and amplifier) prevented useful data from being obtained. Table 8.2 lists the available information on resistance; change of resistance with field (magnetoresistive); and figure of merit[44] α, the fractional change of resistance divided by the square of the applied field (since the response is quadratic in the region of interest). The thickness of the first set and the three odd ones (those indicated in microns) was determined by microscope-stage calibration and is somewhat in doubt, although the measurements have not yet been repeated by the fringe-shift method. All the films in the second set were measured after the acquisition of the special microscope and were estimated to a tenth of a fringe shift. The 1.5-kilogauss field indicated in Table 8.2 was that of a magnetron horseshoe magnet equipped with rather large pole pieces; the 50-gauss field was from a square Helmholz pair and may have been changed by as much as 10% by stray fields from DCX-2, etc. It should be noted that No. 21 was one of three that

[44]C. Shiffman, *Rev. Sci. Instr.* **33**, 206 (1962).

Table 8.2. Results of Tests on Magnetoresistivity

Probe Number	R_0 at 300°K (ohms)	$\Delta R/R_0$ at 300°K in 1.5-kilogauss Field	α at 300°K	R_0 at 77°K (ohms)	$\Delta R/R_0$ at 77°K in 50-gauss Field	α at 77°K	R_0 at 4.2°K (ohms)	$\Delta R/R_0$ at 4.2°K	α at 4.2°K
1	2.43	7.5×10^{-3}	3.3×10^{-9}				7.69	3.15×10^{-4} at 50 gauss	1.26×10^{-7}
10		1.02×10^{-3}	4.5×10^{-10}						
11	118	7.6×10^{-4}	3.4×10^{-10}	385					
13	380						907	6.01×10^{-6} at 50 gauss	6.0×10^{-4}
15	71.4	6.86×10^{-4}	3.0×10^{-10}	348					
16	17.5	8.41×10^{-4}	3.7×10^{-10}	54					
17	45.1	7.78×10^{-4}	3.5×10^{-10}	152					
18	41.2	1.11×10^{-3}	5.0×10^{-10}	135					
19	1.37	1.46×10^{-2}	6.5×10^{-10}	0.93	1.29×10^{-3}	4.3×10^{-7}	0.83	1.2×10^{-3} at 30 gauss	1.4×10^{-6}
20	8.57				1.87×10^{-4}	6.2×10^{-8}			
21	14.9	2×10^{-3}	9.3×10^{-10}				51.9	1.67×10^{-4} at 50 gauss	6.7×10^{-8}

were heat treated; since the other two had gold deposited on the bismuth, they alloyed below the melting temperature of bismuth and had to be discarded.

Many subjective impressions have already been formed from the work. Thick films are usually magnetoresistive, but have such a low impedance that the voltage drop is too low for desired sensitivity; thin films may not always be magnetoresistive and are usually of too high an impedance to match the inputs of available amplifiers; films of the proper impedance can be made, and if they are not magnetoresistive, they can be made so by proper heat treatment. Obviously, much work needs to be done to achieve the desired end of producing completely reliable, micron-size magnetometers for low temperatures.

8.6 THERMAL PROTECTION OF WATER-COOLED MAGNET COILS

J. N. Luton, Jr.

In a previous report[45] tests with thermoswitches[46] for protecting large water-cooled magnet coils were described. Several switches were mounted on a piece of a hollow conductor and were exposed to rapidly or slowly changing temperatures.

In practice, thermoswitches are mounted near the outlet of each water path of the coil to be protected, on either side of the electrical connection to the adjacent path. It seemed desirable to study the question of proper switch location under well-reproducible thermal transient conditions.

Figures 8.17 and 8.18 show the test arrangement. Water paths I and II are joined electrically and thermally by soldering the hollow conductors at J. Thermal switches are mounted at locations S_1 and S_2. The water flow in tube II is kept constant, whereas that in tube I can be quickly varied in the following way: With valve V_s open, water flows in parallel through the throttle valves Th_1 and Th_2. When valve V_s is quickly closed by means of a solenoid, the water flows through Th_1 only, and

[45] R. L. Brown, *Thermonuclear Div. Semiann. Progr. Rept. Jan. 31, 1961*, ORNL-3104, p 97.

[46] Fenwall Inc. Catalog No. 32410-0, 93°C, 2.5 amp, 115 v ac, 1200 v ground insulation.

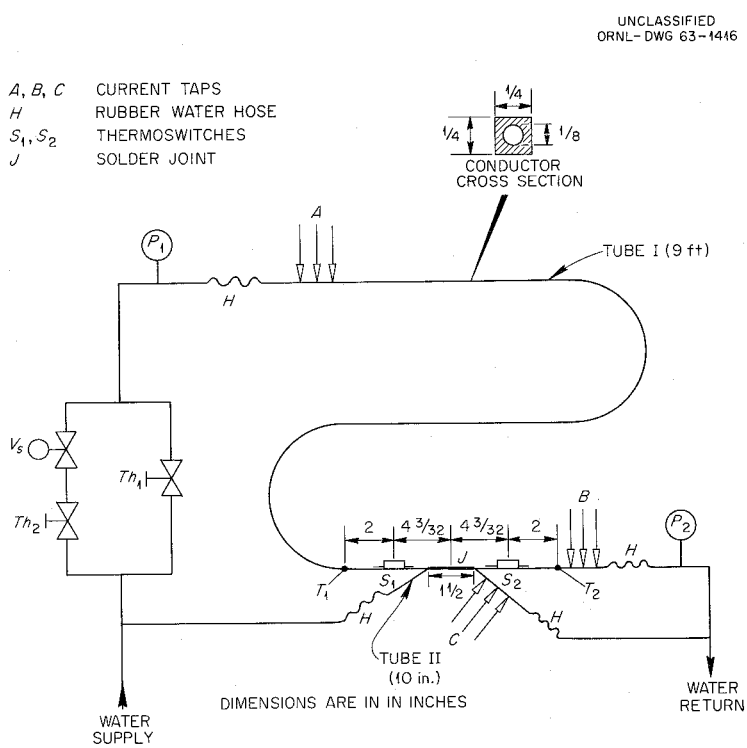

Fig. 8.17. Schematic of Test Arrangement.

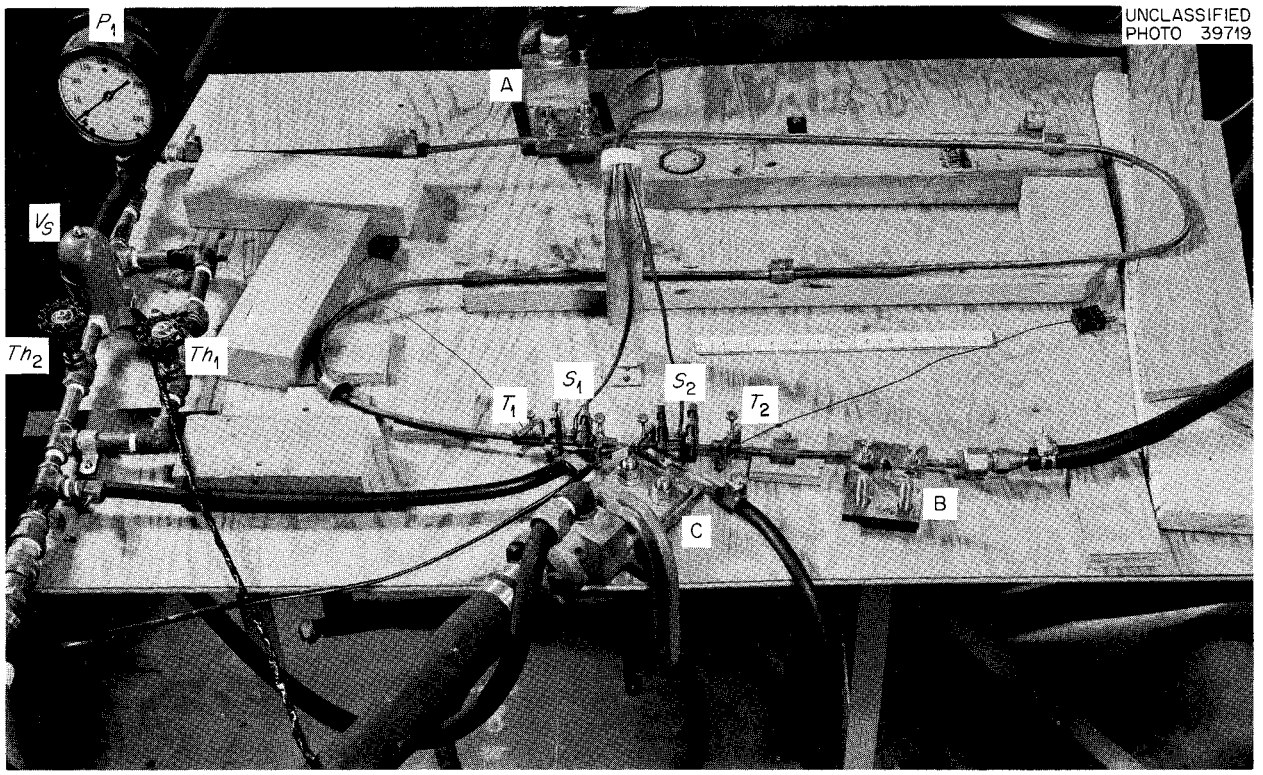

Fig. 8.18. Photo of Test Apparatus.

the pressure (read on pressure gage P_1) is reduced to a value p_1, which is determined by the setting of Th_1.

Current leads were first connected to points A and B. Measurements showed that thermoswitches S_1 and S_2 were exposed to practically the same temperature. In this way it was possible to ascertain that the operation of the switches was nearly identical.

Then the current lead connected at B was moved to C. This arrangement allows the test conductor to be heated while the electrical joint is cooled by the water flushing through the short conductor, thus simulating an actual pancake whose hot end is soldered to the cold end of the adjacent pancake. Switch S_1 was located near the solder joint on the current-carrying portion of the conductor; S_2 was the same distance from the joint, but on the inactive portion of the conductor.

The water-valve arrangement allowed the system to be brought up to some "warm" condition, representing normal operation of the coil, and then to have a "fault" of specified magnitude suddenly applied by closing the solenoid valve V_s. The thermal switches were connected to ohmmeters, and the time between solenoid closure and switch operation was measured. Thermocouple T_1, located at the point assumed to be the hottest, was also read as each switch tripped.

Typical test results are shown in Fig. 8.19. The broken curves represent the response time of switches S_1 and S_2 vs p_1. The two solid lines indicate the conductor hot-spot temperature at the time S_1 and S_2 tripped. These data clearly show that a switch located at S_1 gives better protection than one at S_2. In both cases temperatures which might damage insulation are approached as p_1 is reduced drastically. Under the most severe conditions ($p_1 = 0$, $I \neq 0$), the trip times of S_1 and S_2 seemed to approach a minimum of about 2 and 10 sec, respectively.

The maximum temperature that could be reached before S_1 tripped was 290°C, obtained by setting the current at the maximum value (4400 amp) and then stopping the water flow entirely. However, when S_2 was employed, it was found that at low values of p_1, even with the smallest current obtainable (2100 amp), the temperature exceeded the

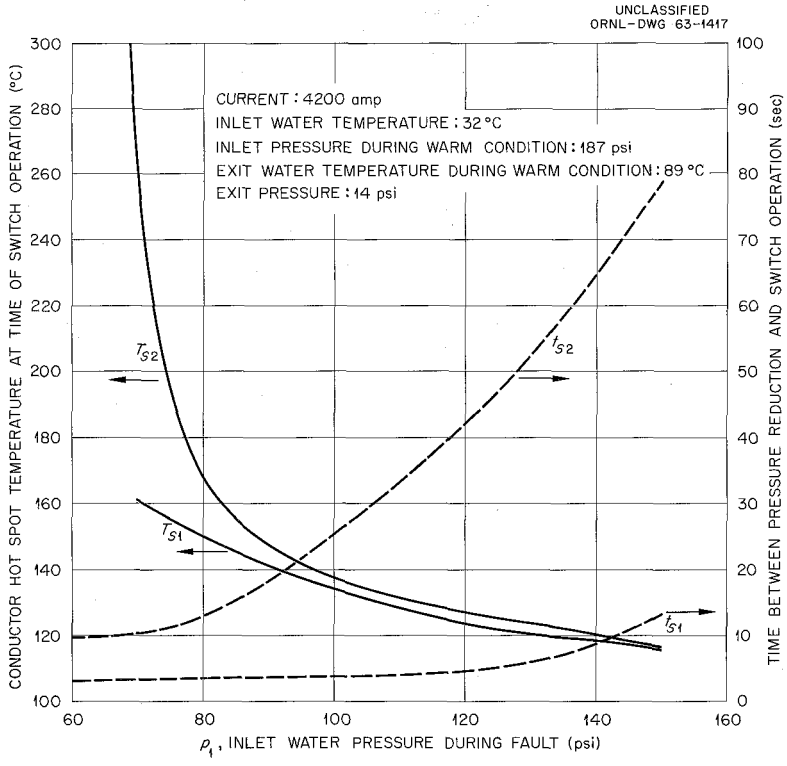

Fig. 8.19. Response of Thermal Switches.

meter range (400°C). When currents larger than 2700 amp were used, the wooden plate on which the conductor was mounted was ignited before S_2 operated. In most actual coils the current density will be smaller than in this test, and the right location of the thermal switches might or might not be mandatory. At any rate, however, these tests show clearly that it is preferable to mount the thermal-protective devices in direct contact with a current-carrying portion of the conductor, several conductor widths upstream from the electrical connection to the adjacent water path.

8.7 EXTENDED WORK ON NEW COMPUTER PROGRAMS FOR CALCULATING MAGNETIC PROPERTIES OF CURRENT SYSTEMS

8.7.1. Program Based on Gaussian Integration of Elliptic Integrals

M. W. Garrett[47] C. E. Parker

In previous reports[48] the zonal harmonic code for calculating magnetic properties of current systems was described. Although the code will calculate axial force and mutual inductance, as well as the other magnetic quantities (B_z, B_r, A, rA, and $\partial B_r/\partial z$), there are some limitations because of the convergence. To circumvent this limitation, another code based on elliptic integrals was written to calculate the force and mutual inductance between coils. The basic expression was derived by Jones[49] and called to our attention by Garrett. It gives the mutual inductance between a loop and a thin solenoid in terms of elliptic integrals (first, second, and third kind).

Using this expression and incorporating a Gaussian numerical integration in radial depth, a code was written to give the force and mutual inductance between two thick coils. The values of force were valid even when the coils approached each other.

[47] Consultant, Swarthmore College, Swarthmore, Pa.

[48] M. W. Garrett, *Computer Programs Using Zonal Harmonics for Magnetic Properties of Current Systems with Special Reference to the IBM 7090*, ORNL-3318 (Nov. 19, 1962); C. E. Parker, *Thermonuclear Div. Semiann. Progr. Rept. Oct. 31, 1962*, ORNL-3392, p 66.

[49] J. V. Jones, *Proc. Roy. Soc. (London)* **63**, 192 (1898).

Somewhat later, Garrett pointed out that all the magnetic quantities (B_z, B_r, A, rA, and $\partial B_r/\partial z$) could be incorporated into the routine with very little additional work. Subsequently, this was done, and the answers were compared with the zonal harmonic calculations. The agreement was excellent (six decimal places).

Still later it was decided to include a routine for tracing lines of flux, since the only method available was rather cumbersome. In addition, the flux lines could be followed through the windings, since the fields could be calculated everywhere in space. Garrett had previously used extrapolation and interpolation procedures in some of his work, and his scheme was used for the code.

After several difficulties were overcome, the routine worked very well. Subsequently, it was used to calculate the flux lines in several operating systems.

In addition to the code described above, another routine for general line tracing (based on differences) is being written. When the routine is completed, it will trace flux, axial field (B_z = constant), and total field ($|B|$ = constant) lines.

9. Vacuum Systems, Techniques, and Material Studies

J. D. Redman[1] D. M. Richardson[1]
R. A. Strehlow[1]

9.1 HIGH-VACUUM FLANGE TEST OF A BAKEABLE ALUMINUM WIRE SEAL

9.1.1 Introduction

In cooperation with the Engineering and Design Section of the Thermonuclear Division, a series of tests of bakeable flange-gasket assemblies has begun. The study was designed to determine the reliability and reproducibility of flange closure as a function of flange and gasket design for optimum performance in the high-vacuum region. Test results of a homemade aluminum alloy O-ring gasket are described in this report. The 86-mil wrought alloy was type 1100-0 temper with a specified minimum of 99% aluminum and a maximum of 1% iron and silicon. The wires were formed into $10\frac{1}{8}$-in.-diam welded rings and were tested between plain flange surfaces with a 32-μin. rms finish. Quality of the seals, monitored with a helium mass analyzer as a function of torque, bolt stress, and gasket strain, was determined for multiple closures and thermal cycles from room temperature to 250°C for pressures down to 1.5×10^{-8} torr. Bolt loading and instantaneous gasket stress were determined by micrometer measurements of bolt elongation and change in the effective bolt length. Data obtained from hardness tests and direct-thrust compression tests were used to evaluate seal quality as related to stress, strain, and yield strength of the gasket material.

9.1.2 Test Facility and Procedure

The test facility, shown in Fig. 9.1, consisted of a 12-liter test chamber pumped by a 6-in., DC-705-filled NRC No. HS6-1500 diffusion pump with a liquid-nitrogen baffle. The test chamber, formed by "spool" and "hat" flange components joined at the test flanges, was sealed by a 30-mil, $10\frac{3}{4}$-in.-diam, gold O-ring to a 3.5-liter water-cooled base flange spool assembly. The gold O-ring, a shear-deformation type, was found to seal with a bolt loading of 40 ft-lb for the three closures tested and thermal cycling to 150°C. With the gold gasket seal insulated, the test chamber was designed to be baked to at least 400°C with a removable furnace heated by a 3.5-kw Calrod heater fixed equatorially to the inside of the furnace wall and insulated with 2 in. of Marinite. Temperatures were monitored on the outside wall of the "hot" assembly and in 1-in.-deep thermocouple wells in the test flange and gold-gasket-sealed base flange. The base pressure of the system, as measured by a Bayard-Alpert glass-enveloped gage located in the spool assembly beneath the test chamber, was 1.5×10^{-8} torr.

The aluminum gaskets were tested between $11\frac{1}{2}$-in.-diam flanges which were $\frac{7}{8}$ in. thick and were drilled to accommodate eight $\frac{1}{2}$-in. bolts. In some tests, sixteen bolts were simulated by adding eight C clamps stressed to an equilibrium tension with the standard bolts as determined by the maximum torsional stress without bolt relaxation. Standard type 304 stainless steel, grades 2 and 3, $\frac{1}{2}$-in. 13NC hexagonal-head bolts and type 304 stainless steel nuts were used without washers or lubrication.

The test procedure consisted in determining the lowest bolt loading that would produce a seal for initial and successive joint closures at room temperature and with thermal cycling to 250°C. The quality of the seal was determined by flooding the plastic-bagged test flange area with helium and

[1]Reactor Chemistry Division.

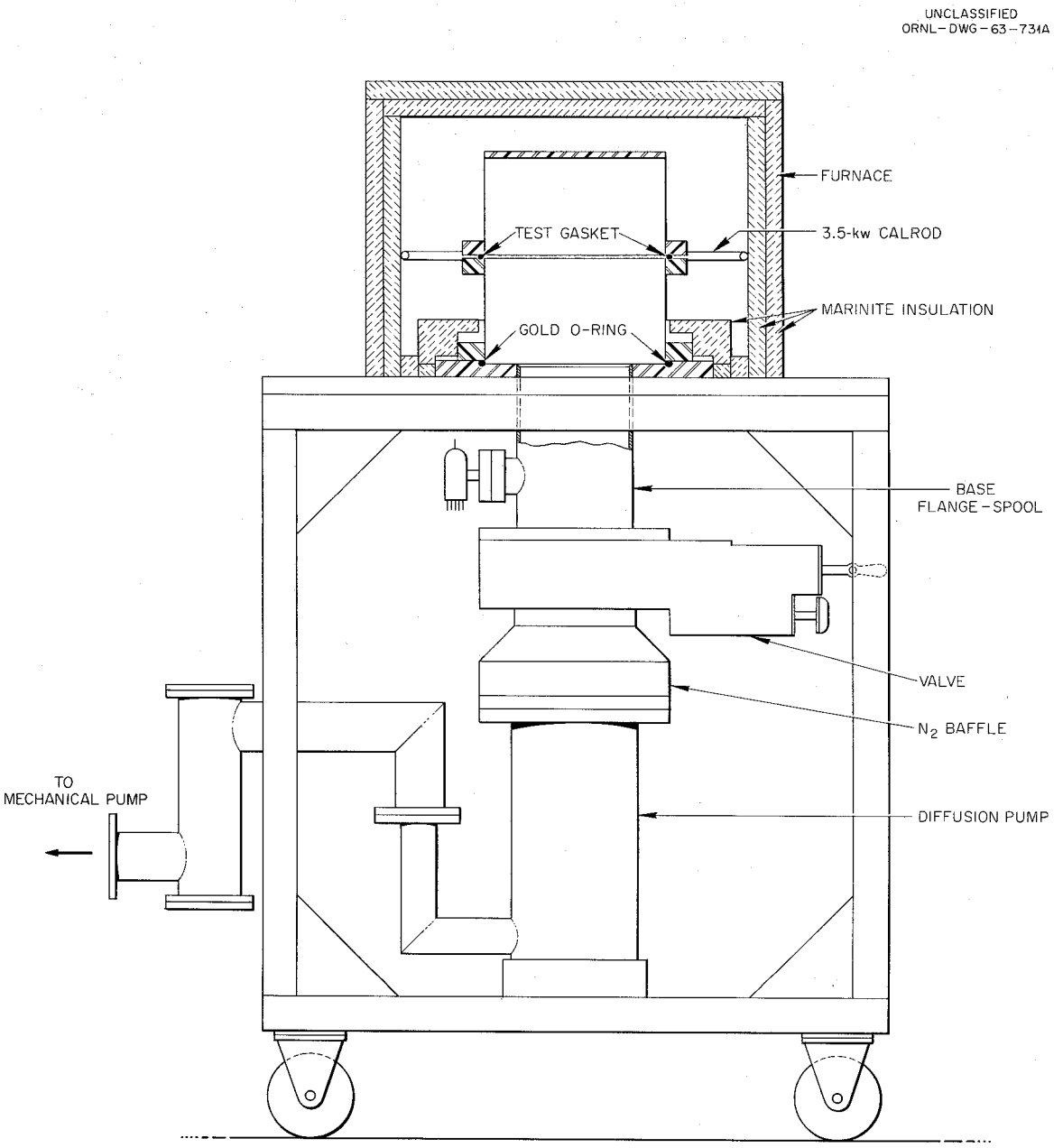

Fig. 9.1. High-Vacuum Flange Test Facility.

measuring the leak rate with a Veeco model MS9 leak detector. The leak rate was also monitored periodically during baking by sweeping the furnace interior with helium. Four bolts chosen for elongation measurements, spaced alternately around the eight-bolt flange, were machined to a 10° cone on the end, and the heads were finished smooth and level. Micrometer measurements of the four bolts for a given average bolt stress had a variation of ±0.0002 in. Measurements of gasket deformation were made by measuring the distance across the two flanges at points 90° apart around the flange on the bolt circle with a precision of ±0.002 in. Bolt stress was applied with calibrated torque wrenches, which were checked periodically for accuracy.

9.1.3 Test Results

The results from eight gaskets tested for quality of closure as a function of bolt loading and gasket deformation for a variety of operating conditions are shown in Figs. 9.2 and 9.3. Also, a number of gaskets were prepared for hardness and compressive strain tests which were performed by the Y-12 Metallurgical Services Section; results of these tests are included in Figs. 9.2 and 9.3. Since the test flange assembly was designed for ½-in.-diam bolts, most of the tests were limited to a bolt torque of 75 ft-lb, which produced a total stress of 63,500 psi per bolt for 75% of allowable loading of the type 304 stainless steel, grade 2 bolt. In test AC 8 a maximum torque of 85 ft-lb was used for 85% of allowable loading.

It was found (Fig. 9.4) that when the flange coupling was loaded sufficiently to seal, there was a gasket deformation of 27.5 ± 3.5 mils. Deformation values cited are transient (instantaneous) and not permanent. Measurements of the gasket deformation made at the conclusion of each test were generally 3 or 4 mils lower than the final instantaneous value measured under load. In order to obtain the force necessary to deform the gasket sufficiently, a bolt loading of 75 ft-lb for eight bolts was adequate in some cases. In others, a seal was not obtained until the gasket was annealed during the baking cycle. Between gaskets there was a variation of ±3 to ±6 mils from the average deformation as a function of torque and a variation of torque for the same deformation of ±20%. Torque values are nominal only, since a variation of ±30% has been observed by others for the stressing of commercial nuts and bolts.[2] To obtain a deformation of 31 mils, the maximum necessary for leak-tight sealing, a bolt torque of 115 ft-lb may be required for eight bolts, assuming the deformation-torque relation to remain essentially linear. This would require a bolt stress 115% greater than that available with the type 304 stainless steel, ½-in. 13NC, grade 2 bolt.

Bolt elongation measurements permitted calculation of axial force per unit stress area of the stressed bolts according to Hooke's law and were related to the gasket loading area for the corresponding compressive stress on the deformed gasket. Stress-strain curves in Fig. 9.2 compare experimental data points from the bolt-loaded flange tests, prior to baking, with those obtained from direct-thrust compressive strain tests. The direct-thrust tests were made on a typical gasket by use of a tensile-compression machine with a 1-in. ram, and a strain gage for correlating instantaneous deformation. The data from the tensile-compression machine showed a definite yield point at 28 mils instantaneous deformation, corresponding to a yield strength of 6.9 tons/in.^{2}. The data in the lower region of the direct-thrust curve are insufficient to indicate definitely a primary yield point. The gasket material, initially an O-temper with a yield strength of 5000 psi,[3] was strain hardened with cold working to a high temper. In the three graphs shown in Fig. 9.3, changes in the average stress of the test gaskets were correlated with temper and strain hardening as a function of torque.

The hardness tests (performed on gaskets prepared in the test cell by cold working from 0 to 75 ft-lb of torque, by heat treating only, and by

[2] J. K. Salisbury (ed.), *Kent's Handbook of Mechanical Engineering*, vol 2, 12th ed., pp 10–57, Wiley, New York, 1950.

[3] Lyman Taylor (ed.), *Metals Handbook*, vol 1, 8th ed., p 936, American Society for Metals, 1961.

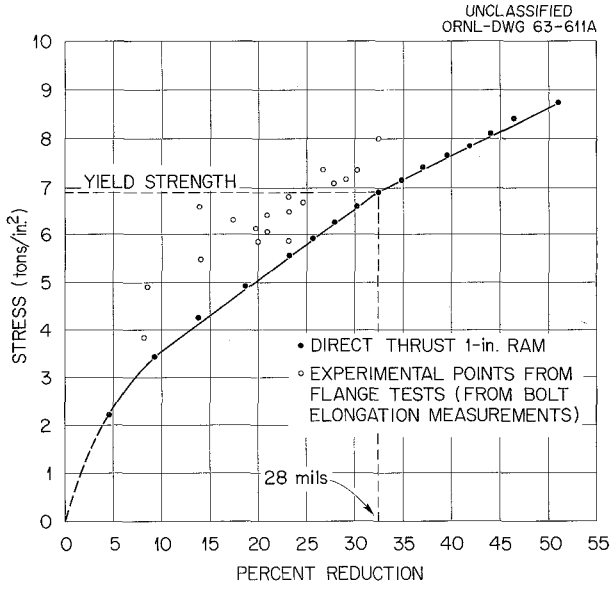

Fig. 9.2. Comparison of Stress-Strain Curves for Direct-Thrust Test and Bolt-Loaded Flange Tests of 0.086-in. Aluminum Wire Gasket.

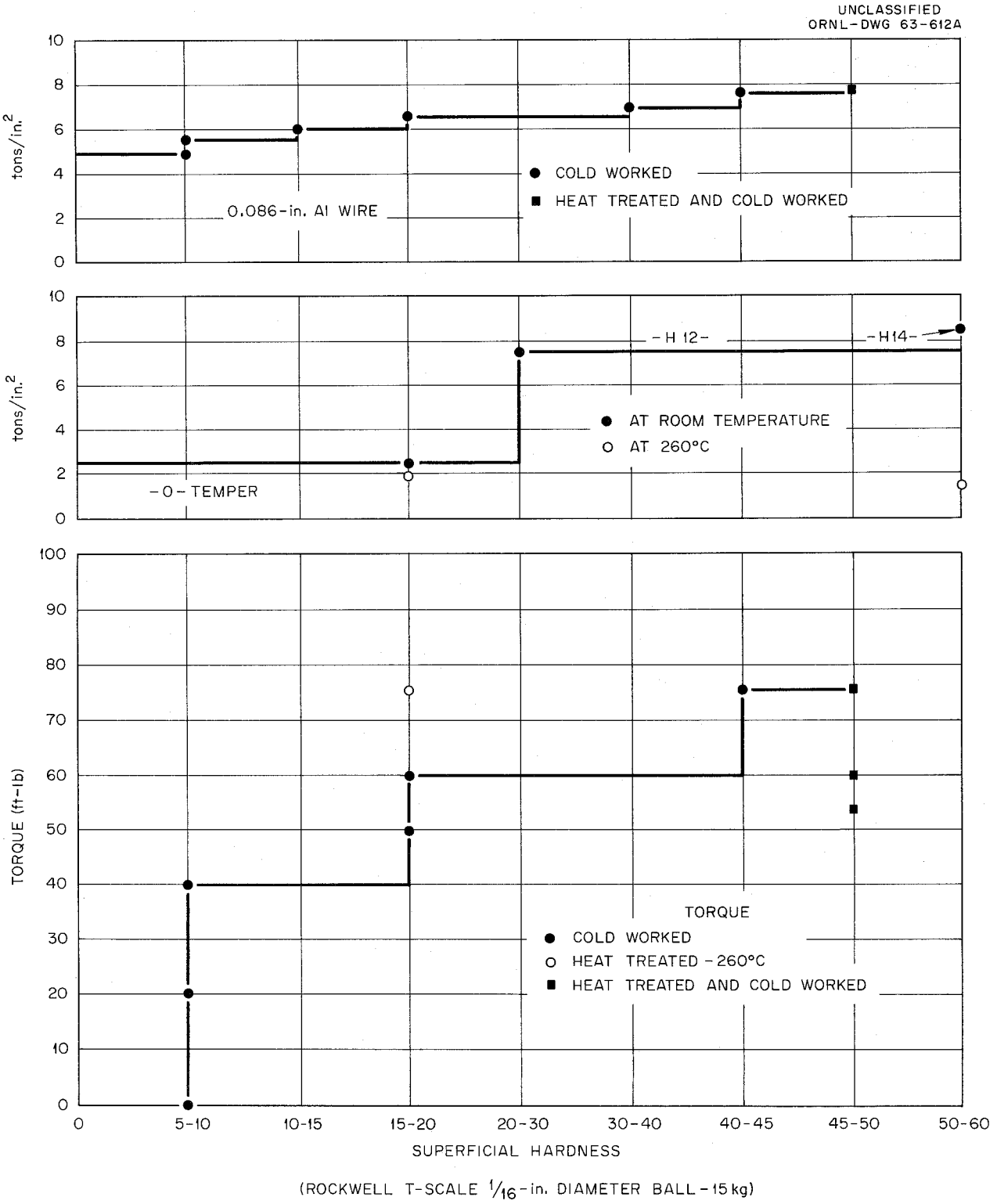

Fig. 9.3. Stress on Gasket Near the Yield Point as Related to Strain Hardening.

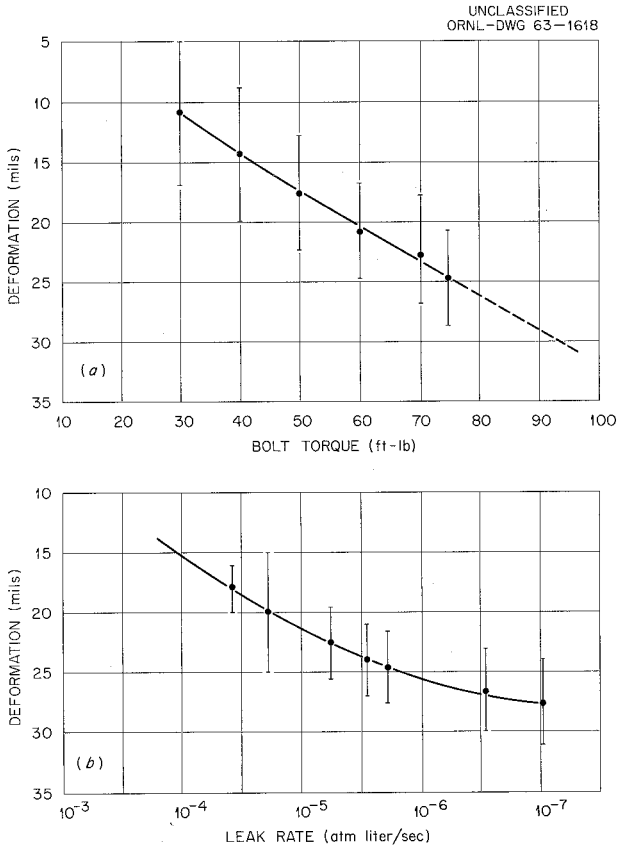

Fig. 9.4. (*a*) **Gasket Deformation as a Function of Bolt Loading vs Helium Leak Rate;** (*b*) **Helium Leak Rate as a Function of Gasket Deformation.**

heat treating followed by cold working) were superficial hardness tests on the Rockwell T-scale with a $\frac{1}{16}$-in.-diam ball with a 15-kg load. Due to the softness of the material the hardness numbers were reliable only for comparative purposes, but were sufficient to show that the cold-worked gasket strain-hardened under 75 ft-lb of bolt loading to a temper corresponding to the H12 temper of the alloy.[4] Aluminum 1100 with an H12 temper has a yield strength of $7\frac{1}{2}$ tons/in.^{2}, which was approximately the stress necessary for the 28-mil gasket deformation shown in Fig. 9.2. Gaskets annealed by the flange-test baking cycle had the lower temper and a yield strength of 1 to 2 tons/in.^{2}, as determined by the residual axial bolt force after baking. When annealed gaskets were restressed, they again became strain-hardened.

[4]H. R. Voorhees and J. W. Freeman, *The Elevated Temperature of Aluminum and Magnesium Alloys*, ASTM Tech. Publ. No. 29 (1960).

Test gasket AC 8 was thermally cycled for a total baking time at 250°C of 72 hr. For this test, eight new 304 stainless steel, $\frac{1}{2}$-in. 13NC bolts were installed. No evidence of thread relaxation or permanent deformation of either set of bolts could be observed. A graphic history of this gasket, which was typical in many respects, is shown in Figs. 9.5 and 9.6. Prior to baking, the gasket failed to seal because of a leak at the weld, which subsequently sealed near 135°C during the initial bake. Initially the creep strain in the gasket was 4 mils per bake or 3.5%/hr and required that the bolts be restressed prior to each bake. After six 4-hr baking periods and about 65% reduction in gasket thickness, the creep strain diminished to an average of 2.0%/hr during baking. Eventually, due to the increase in area of the gasket in contact with the flange surfaces, the critical stress of $7\frac{1}{2}$ tons/in.^{2} necessary to seal the strain-hardened gasket could not be maintained by eight bolts loaded to 85 ft-lb. Eight C-clamps were installed alternately with the eight bolts about the flange, and stress was applied so that similar axial loading was maintained on both classes of bolts. The 16 bolts were restressed to 85 ft-lb for each thermal cycle in the primary creep region, and stress on the gasket was maintained between $7\frac{1}{2}$ and 9 tons/in.^{2}. In the minimum or secondary creep area there was less strain hardening, because very little bolt restressing was necessary and the yield point remained below the diminishing stress value. After 72% reduction of the gasket thickness, there was no further bolt restressing. Small, almost immeasurable, creep continued, which was apparent in a bolt relaxation

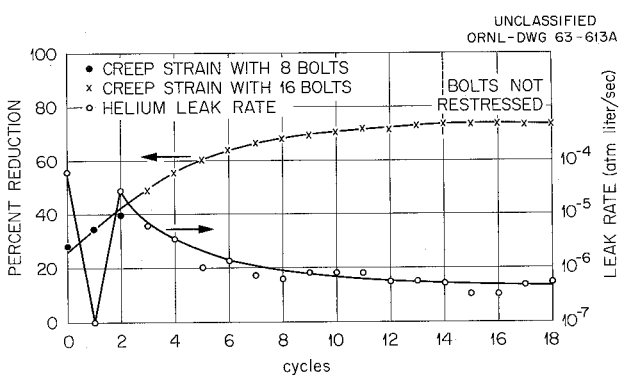

Fig. 9.5. Creep Strain and Leak Rate as a Function of Thermal Cycling Between Room Temperature and 250°C.

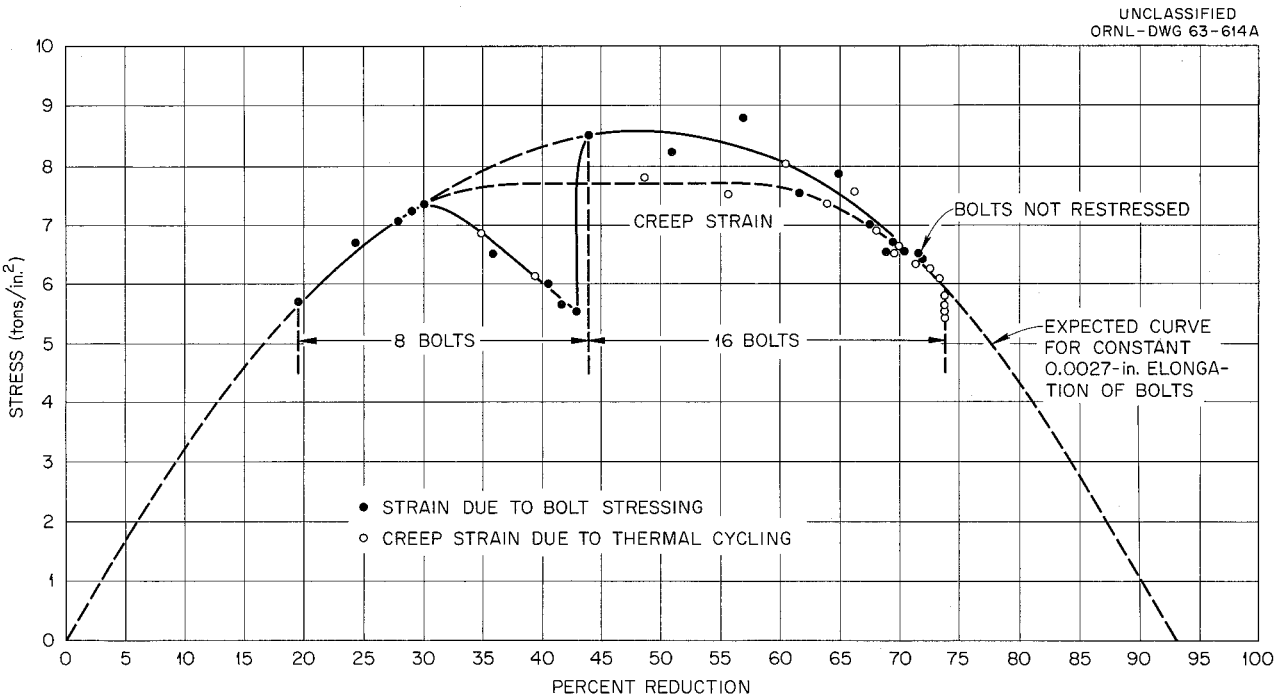

Fig. 9.6. Stress-Strain History of Test Gasket AC 8 (0.086-in. Aluminum Wire).

of about 3.5 mils in seven cycles and a slowly increasing leak rate. If the bolts were restressed to maintain a constant stress on the gasket, the stress-strain data points should fall along the broken curve in Fig. 9.6. The test was concluded after 18 cycles, assuming the seal would fail when the stress had decreased to a value lower than the yield point of the fully annealed gasket.

If thermal cycling of AC 8 were to be continued, the gasket would creep either with a continuation of the final creep rate or at an accelerated creep rate to failure. In the case of the former, the creep would be expected to continue until the closure failed because the increasing gasket area would be so large that there would be insufficient bolt loading capability. If the curve in Fig. 9.6 is projected to the yield strength of the fully annealed alloy, 5000 psi, the curve intersects this value at 87.5% reduction or 10.7 mils. Stress calculation for this area with the axial loading force of the bolts and for the average elongation values also yields 5000 psi, if there were no bolt relaxation. Actually, restressing is required since the gasket creeps and bolt relaxation occurs.

9.1.4 Summary and Discussion

In the tests which were limited to only one baking time and temperature variable, it is apparent that the sealing characteristics of the nominal 10-in.-diam gasket were related to the mechanical properties of the aluminum material. For a leak-tight seal of the 86-mil O-ring between flat flange surfaces, procedure and bolt loading requirements such as bolt size, grade, and number must satisfy two conditions: (1) The bolt force available must be sufficient to seal prior to thermal cycling and also be sufficient to overcome strain hardening corresponding to at least an H12 temper. (2) The force must be adequate to maintain a seal through the creep strain region of the gasket during thermal cycling. The first condition was satisfied by loading the flange until the yield point of the strain-hardened gasket, about $7\frac{1}{2}$ tons/in.^{2}, was reached. The yield point for the O-temper alloy is $2\frac{1}{2}$ tons/in.^{2} and was reached with about 5% reduction of the gasket. This reduction was insufficient for sealing. Under additional stress, the O-temper alloy strain-hardened to an H12 temper which has a

yield strength of $7\frac{1}{2}$ tons/in.^{2}. Direct-thrust compression tests showed that the yield point of the cold-worked material occurred after a (32.6 ± 4.5)% (28 ± 4 mils) reduction for a stress of 6.9 tons/in.^{2}. A stress-strain curve for the average of the experimental points indicated a 28-mil deformation for a stress of $7\frac{1}{2}$ tons/in.^{2}. Stress values obtained from the bolt tension as measured by elongation per unit area of instantly deformed gasket were in good agreement with the direct compression test values and the reported yield strength for the H12 temper alloy.

The maintenance of a seal during thermal cycling is complicated by the bake-cycle-dependent creep strain of the gasket. In the primary or steeper region of the creep curve, bolt relaxation following baking required restressing the bolts prior to each bake to maintain a constant stress of $7\frac{1}{2}$ to 9 tons/in.^{2}. Greater bolt loading was required than prior to baking to overcome the increasing effective area of the gasket until reaching the secondary creep region, where there was less strain hardening and successively lower yield points.

A projection of the data indicates that a leak-tight seal can be maintained, if the gasket does not perforate, until the applied stress drops below the yield point of the fully annealed gasket. Assuming a continuance of the average minimum creep rate of 0.6 mil/cycle for a constant bolt loading stress, corresponding to the average maximum bolt elongation of 0.0027-in., a 5000-psi gasket stress would be reached after 77 mils deformation (90% reduction) or a total of about thirty-eight 4-hr bake cycles. The experiment has shown that at least eighteen 4-hr 250°C bakes can be performed with a bolting assembly capable of producing a maximum stress of $7\frac{1}{2}$ to 9 tons/in.^{2} for a 60% (69 mils) gasket reduction. Assuming a bolt strain of 0.133% (the average in these tests), it is possible to determine the stress area of a bolt with the necessary axial stress potential from Hooke's law for the deformed cross-sectional area of the gasket;

$$A_{\text{bolt}} = \frac{SA_G L_B}{Y \Delta l_B} ,$$

where

S = stress on gasket, 18,000 psi,

A_G = cross-sectional area of the gasket per bolt for a 10-in.-diam O-ring,

$L_B/\Delta l_B$ = 1/bolt strain,

Y = modulus of elasticity for type 304 stainless steel, 2.9×10^7 psi.

An approximation of torque for a given bolt tension can be obtained from the equation,

$$T \text{ (in.-lb)} = KDS ,$$

where K is the torsional constant, which is about 0.2 for the lowest coefficient of friction (0.15 for dry-driven semifinished bolts); D is the bolt diameter; and S equals the bolt tension or clamping force for type 304 stainless steel bolts with a 75% safe loading of 63,700 psi. There is variation in the coefficient K, depending on thread condition and erosion of the flange surfaces by the bolt head and nut. Bolts with the necessary stress area for 8- and 16-bolt assemblies are listed in Table 9.1.

Table 9.1. Comparison of Bolt Requirements for Flange Closure and Recommended Bolts

	Bolt Stress Area (in.^{2})	Torque (ft-lb)
8-bolt assembly	0.3180	115[a]
16-bolt assembly	0.1540	85[a]
$\frac{9}{16}$-in. 12NC bolt	0.1820	110
$\frac{3}{4}$-in. 10NC bolt	0.3340	265

[a]Based on experimental evidence.

For convenience in determining instantaneous cross-sectional area of the gasket during testing, the effect of slip-plane friction between the gasket and flange surfaces was neglected. Under compression that part of the gasket touching the flange surfaces is prevented from expanding laterally due to friction, and a bowing in the middle occurs. The degree of bowing, and consequently the stress, is proportional to the coefficient of friction. In a paper[5] on friction in plain-strain compression tests, stress-compression strain is reported in the region of 7 to 13 tons/in.^{2} as a function of interfacial friction of fully annealed aluminum wire.

[5]H. Takahashi and J. M. Alexander, *J. Inst. Metals* **90**, 72 (1962).

The coefficient of friction with no lubrication was 0.8 ± 0.07, depending on the surface conditions. Frictional effects of air oxidation and freshly polished surfaces were reported observed. Also, there was a marked increase of friction with increased die pressure and an accumulation of metallic debris with no lubrication, which resulted when lubricated in lower friction. This work suggests the possible significance of frictional conditions in high-vacuum flange closure studies.

9.1.5 Acknowledgments

Acknowledgment is made to the Metallurgical Service Section of the Y-12 Plant for carrying out hardness and compression tests; to J. F. Potts and H. Watts of the Engineering and Design Section of the Thermonuclear Division for assistance in design, fabrication, and procurement of test components; and to H. C. Boyd of the Y-12 R.E.D. Mechanics Group for assistance in performing the tests.

9.2 GASEOUS DESORPTION AT LOW PRESSURES AND LIQUID-NITROGEN TEMPERATURES

The fact that physical adsorption is one of the more important factors in high-vacuum technique has been recognized by many workers in the field of ultrahigh vacuum.[6–9] A study of the possible base-pressure limitation due to Van der Waals adsorption has been initiated at this laboratory. Studies of the base-pressure limitation in a 15-ft^3 vacuum chamber, the entire surface of which was cooled with N_2, were carried out in the pressure range of 2×10^{-10} to 2×10^{-8} torr over the temperature interval of 80 to 115°K. The facility is schematically shown in Fig. 9.7. Two Veeco RG-75 enveloped ion gages were used to monitor the pressure change after N_2 flow was stopped. There was an effective pumping area from this inner liner to the outer region of about 10-cm^2 effective area. The area of the liner was 3×10^4 cm^2. The outer vacuum region was pumped by a 6-in., MCF-700, CVC diffusion pump. One of the two ion gages was located with its orifice immediately in contact with a hole of about the same size in the liner, while the other was suspended inside the liner in such a way that it faced a large area of the inner surface. For the observations reported here, the two ion gages agreed to within ±0.02 of full scale. Before the experiments were conducted, a vapor deposition of molybdenum was carried out, giving an average molybdenum coverage of 0.3 mg/cm^2. A typical desorption curve is shown in Fig. 9.8, where pressure is plotted vs time. The indicated temperatures were determined by comparing stainless-steel-sheathed Chromel-Alumel thermocouples with liquid nitrogen at atmospheric pressure as a temperature reference. Thermocouple outputs were obtained with a Hewlett-Packard

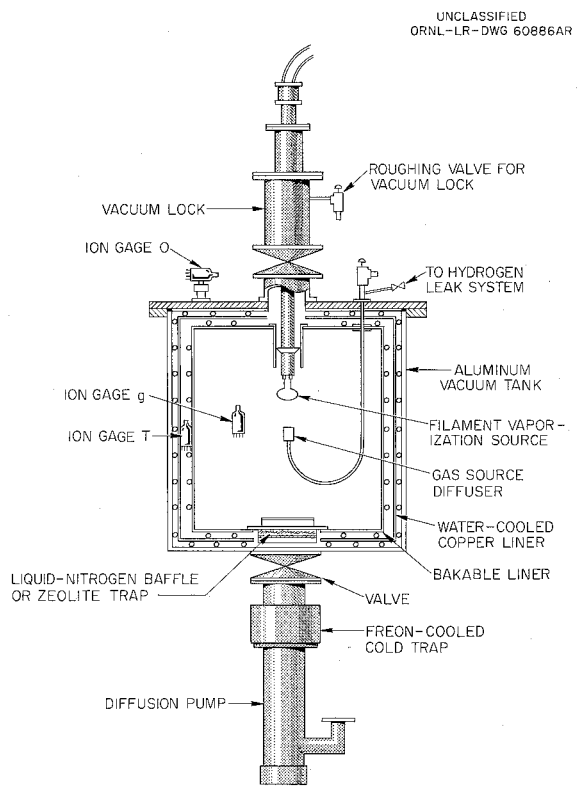

Fig. 9.7. Ultra-High-Vacuum Test Facility.

[6] S. Dushman, *Scientific Foundations of Vacuum Technique*, 2d ed., p 376 ff, Wiley, New York, 1962.

[7] D. Alpert, "Production and Measurement of Ultrahigh Vacuum," *Encyclopedia of Physics* (ed. by S. Flugge), vol 12, p 632, Springer-Verlag, Berlin, 1958.

[8] V. A. Malyshev, *Soviet Phys. – Tech. Phys.* **7**(2), 258–60 (1962).

[9] B. A. Buffham, P. B. Henault, and R. A. Flinn, "A Theoretical Evaluation of the Sticking Function in Cryopumping," and P. G. Smeaton, G. Carter, and J. H. Leck, "Thermal Desorption of Argon in an Ionization Pump," *Transactions of the Ninth National Vacuum Symposium* (ed. by F. H. Bancroft), pp 205, 491, MacMillan, New York, 1962.

microvoltmeter which measured voltages smaller than 1 μv. The terminal 6 in. of the thermocouple sheath was in close mechanical contact with the outside of the copper liner. The warming rate was 0.5°/min initially, decreasing to 0.25°/min after the first hour. Warming characteristics are shown in Fig. 9.9.

The desportion characteristics shown in Fig. 9.8 were obtained when the base pressure in the system was of the order of 1×10^{-9} torr or lower. At higher base pressures, for example, after the admission of a quantity of methane into the system, behavior was observed of which Fig. 9.10 is typical. It will be noticed that there was a significant drop in pressure corresponding to the time of N_2 turnoff and that the pressure rise began immediately.

Application of the Arrhenius relation to the experimental data yielded the heats of desorption

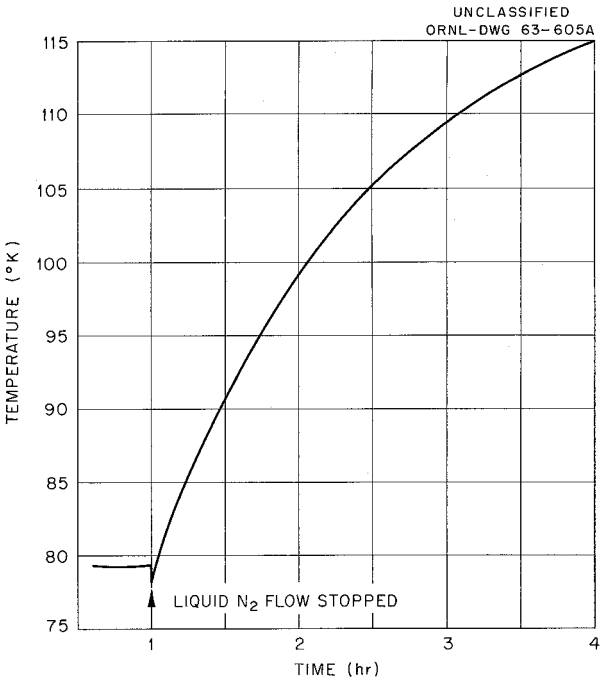

Fig. 9.9. Liner Temperature During Warmup.

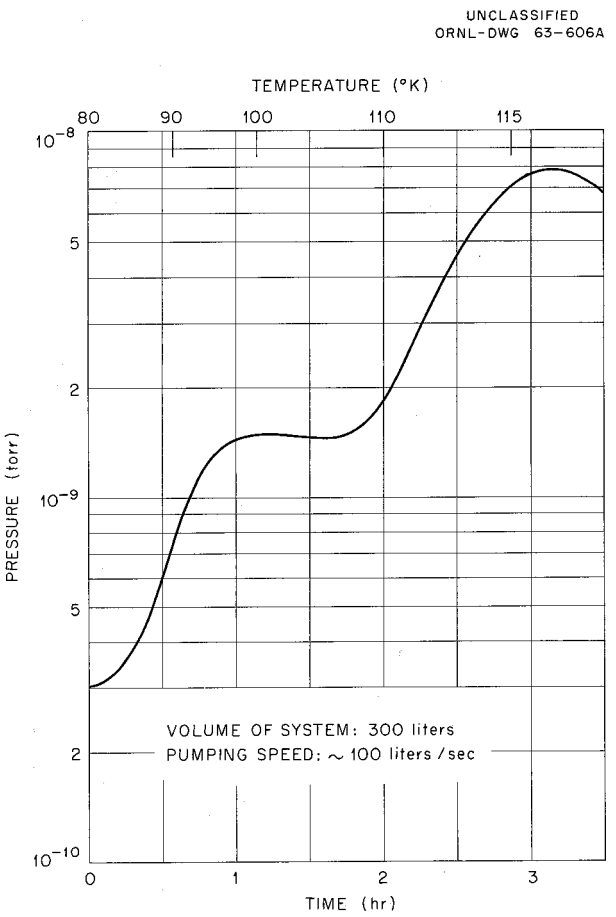

Fig. 9.8. Typical Desorption from Low Base Pressure, Pressure vs Time.

listed in Table 9.2. Independent mass spectroscopic information[10] obtained on the similar liner system of the DCX-1 experiment has indicated that the primary desorption was of methane. The second desorption peak (Q = 7 kcal/mole) has not yet been characterized. Ice at these temperatures has the vapor-temperature behavior shown in Fig. 9.11 and should not be expected to be measurable at temperatures below about 130°K. Table 9.2 includes data obtained for the heats of desorption of three gases on platinum, silver, and iron surfaces for comparison purposes.

Graphical integration of the desorption curves obtained in this work have indicated that the amount of gas desorbed is of the order of 10^{13} molecules/cm^2 or less. Since this is but a small fraction of a monolayer ($>3 \times 10^{15}$ molecules/cm^2), a Henry's law isotherm (the amount adsorbed is proportional to the gas pressure) rather than a Langmuir relation is expected to hold. One derivation of a Henry's law isotherm follows:

[10] E. R. Wells, ORNL Thermonuclear Division, private communication.

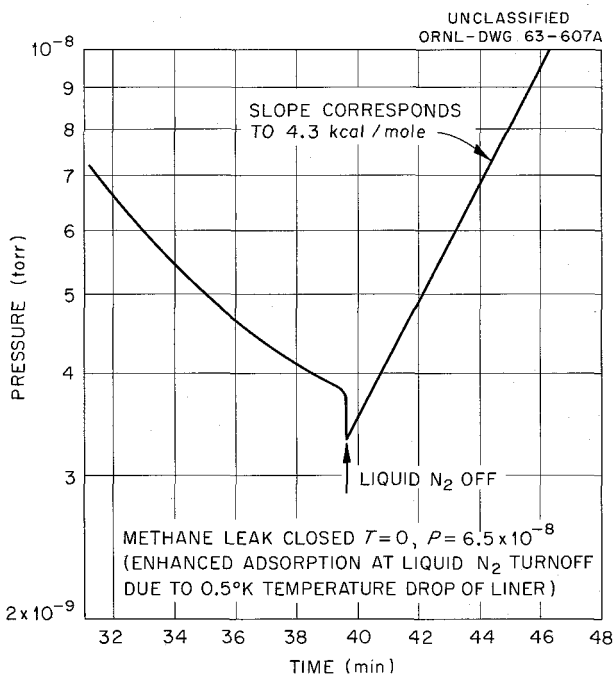

Fig. 9.10. Desorption Curve from High Pressure (Methane).

Table 9.2. Heats of Desorption of Selected Gases (kcal/mole)

Gas	Mo (This Work)	Ag[a]	Pt[a]	Fe[a]
CH_4	4.3			
Ar	3.5	3.5	3.3	3.2
CO	3.0	3.2	3.6	3.4
N_2		3.6	3.4	3.1
H_2	2.2			

[a]M. H. Armbuster and J. B. Austin, *J. Am. Chem. Soc.* **66**, 159 (1944).

The surface concentration in molecules/cm^2, Γ_1, is defined as the product of the collision rate with the wall, ν (molecules cm^{-2} sec^{-1}), and the residence time, τ (sec);

$$\Gamma_1 = \nu\tau \; ; \qquad (1)$$

from kinetic theory

$$\nu = \tfrac{1}{4} n v_a \, , \qquad (2)$$

where n, the molecular density, and v_a, the average molecular speed, are given by

$$n = 9.656 \times 10^{18} P/T \text{ cm}^{-3} \, , \qquad (3)$$

$$v_a = 14.551\sqrt{T/M} \text{ cm/sec} \, , \qquad (4)$$

where P is the pressure in torr, T is the absolute temperature in °K, and M is the molecular mass number. The quantity τ can be shown to be related to Q, the energy of adsorption, by

$$\tau = \tau_0 \exp Q/RT \, , \qquad (5)$$

where τ_0 is of the order of 6×10^{-13} sec and R is the Boltzman constant in units consistent with those of Q.

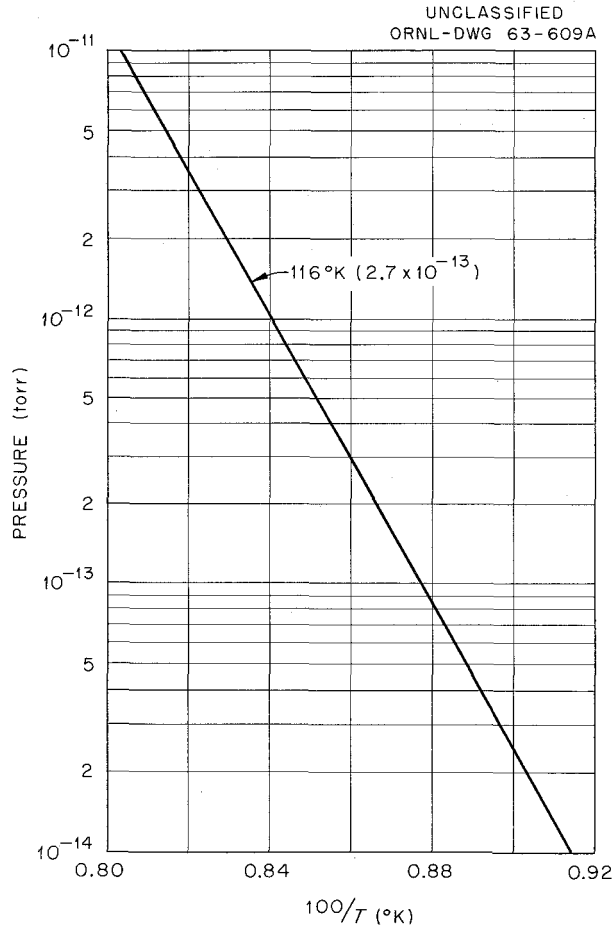

Fig. 9.11. Vapor Pressure of Ice (125 to 110°K).

The isotherm is then

$$\Gamma_1 = \frac{1.4 \times 10^{23} P \tau}{(MT)^{1/2}}$$

$$= 8 \times 10^{10} P(MT)^{-1/2} \exp Q/RT \ . \quad (6)$$

In the Henry's law region no variance of Q with surface coverage is expected. This derivation assumes perfect gas behavior for the adsorbed film, where the film pressure is given by Eqs. (7) and (8);

$$\pi = \Gamma_1 kT \ , \quad (7)$$

$$\pi = 1.8 \times 10^{-6} (T/M)^{1/2} P \exp Q/RT \ . \quad (8)$$

However, for the application of this isotherm we may simply write

$$\Gamma_1 = \beta P \exp Q/RT \ , \quad (9)$$

or

$$\Gamma_1 \approx 2 \times 10^{-9} P \exp Q/RT \text{ molecule/cm}^2 \ , \quad (9a)$$

where β is a weak function of temperature, or stated differently

$$\left| \frac{d \ln \beta}{dT} \right| \ll \left| \frac{d(Q/RT)}{dT} \right| = Q/RT^2 \ . \quad (10)$$

When the isotherm (9) is applicable to the conditions present in a vacuum system, the base pressure achievable will be given as a function of the surface coverage and an exponential term involving the heat of adsorption of the species present in the system. The gases normally found in vacuum systems involving oil diffusion pumps include CH_4, H_2, CO, CO_2, Ar, N_2, and H_2O. The equilibrium surface coverage at partial pressures in the 10^{-9}-torr range for H_2, Ar, and CO are estimated, by using Eq. (9), to be much smaller than those for H_2O, CO_2, or CH_4. Experimentally, in numerous systems operating in this pressure range with large surface areas held at temperatures near 80°K, methane has been observed to be a dominant species. As seen from Fig. 9.11, water may be neglected.

The following relations may be derived from Eq. (9):

$$\left(\frac{\partial \log P}{\partial T} \right)_{Q,\Gamma} = \frac{Q}{2.3RT^2} \ , \quad (11)$$

$$\left(\frac{\partial \log P}{\partial Q} \right)_{T,\Gamma} = -\frac{1}{2.3RT} \ , \quad (12)$$

$$\left(\frac{\partial \log P}{\partial 1/T} \right)_{Q,\Gamma} = \frac{Q}{2.3R} \ . \quad (13)$$

Equation (11) shows the change in pressure with temperature for a given coverage of specified gas and adsorbent. Equation (12) shows the expected influence of a change in Q on the pressure (as would accompany a deposition of a different metal). Equation (13), of course, is the Clausius-Clapeyron relation.

The change of thermocouple output with temperature is only a slowly varying function of temperature in the range up to 110°K (ranging from 16.8 to 20 μv/deg). Consequently, the change in T can be quite precisely determined, even though the starting temperature is not fixed. The importance of calibration of the test thermocouple in the determination of Q is indicated by Eq. (14):

$$(\partial Q/\partial T)_{\Gamma,P} = Q/T \ . \quad (14)$$

The probable maximum uncertainty in T was about 3°K or about 0.2 kcal/mole. The estimated uncertainty in ΔT was ±0.3°K.

In the estimation of the heats of adsorption, it may be necessary to graphically determine and define a base pressure, substracting it from the desorption peak except when the base pressure is known to be predominantly the same gas as that which is desorbing. The pressure was monitored with enveloped gages which were normally not outgassed for some time previous to the determination of a gaseous desorption to minimize the possibility of significant gage pumping of CO or other gases present.

The lowest surface concentrations were observed (by graphical integration of the area under the pressure-time curve) after the operation of a filament which resulted in a temperature rise in the system of 3 or 4°K. The filament was operated at

a power level of less than 2 kw for some 30 min. From the stability of the voltage-current characteristics of the filament, it was clear that no metal evaporation was occurring. This was borne out by the observation that the addition of a small flux of hydrogen gas yielded essentially the characteristic pumping time constant for the liner system. During the operation of the filament, desorption may have occurred by electron bombardment, as well as the expected thermal desorption. One should expect significant interaction between electrons and gas molecules adsorbed by Van der Waals forces even at electron energies lower than those necessary for electronic excitation in the gas molecule. Photodesorption of the gas molecules can also be expected to occur. (It should be noticed that the exponential term for this isotherm includes translational, vibrational, rotational, and electronic energy of the adsorbed gases relative to the gas-phase molecules.)

10. Further Speculations on Very High Energy Injection into a Magnetic Mirror

J. R. McNally, Jr. Mozelle Rankin E. D. Shipley

A speculative calculation was presented in the last semiannual report[1] with the aim of looking into the gains that might accrue to a DCX-1-like device working at 30 kilogauss and an injection energy (H_2^+) of 3 or 6 Mev. Two factors combined to make the idea look attractive: a breakup factor greatly increased over the figure at 600 kev because of Lorentz dissociation, and, simultaneously, a greatly decreased rate of charge-exchange loss.

The main loss mechanism for the trapped protons was assumed in the earlier calculation to arise from energy degradation from stopping-power effects; that is, by ionization and excitation of the background gas. It was indicated, however, that plasma-potential effects should introduce a more serious energy-degradation mechanism for the ions. We have now included in the calculation the energy losses caused by heating of cold, free electrons and have computed performance curves according to the method of Fowler and Rankin,[2] using their Fokker-Planck code.

Although the plasma-exponentiation condition is attainable more easily than at lower injection energies, the Lorentz trapping is so large that exponentiation no longer plays a dominant role in the early stages of plasma growth. Eventually, however, as the electron density increases, the protons lose energy more rapidly via heating of the cold electrons with the result that the charge-exchange rate increases, and exponentiation becomes progressively more difficult to maintain; in fact, it may be that the DCX-1 injection energy is somewhat more advantageous because of the smaller temperature difference between the two distributions of protons and electrons. It appears that very high energy injection might permit the attainment of proton densities that are two or more orders of magnitude larger than the $10^8/cm^3$ currently reached in DCX-1.

It should be noted that the computations to date are still incomplete inasmuch as cyclotron (and bremsstrahlung) radiative losses by the electrons have not been included; again, it appears that the present energy of DCX-1 may be more advantageous than an energy of 6 Mev. The lower mean energy of the electrons and the weaker magnetic field in DCX-1 both introduce reduced electron-cyclotron radiative losses. In order for the DCX-1 approach to be really superior to the very high energy injection approach, the exponential condition must not only be attained in DCX-1 but maintained to high plasma densities.

Plasma instabilities productive of a volume increase of the trapped plasma have been observed[3] in DCX-1. These instabilities should be more amenable to study if the trapping rate for protons were dependent essentially on the beam current and not on the neutral-gas density

[1] J. R. McNally, Jr., *Thermonuclear Div. Semiann. Progr. Rept. Oct. 31, 1962*, ORNL-3392, pp 89–93.

[2] T. K. Fowler and Mozelle Rankin, *J. Nucl. Energy, Pt C* **4**, 311 (1962).

[3] J. L. Dunlap *et al.*, *Thermonuclear Div. Semiann. Progr. Rept. Oct. 31, 1962*, ORNL-3392, pp 1–10.

or the plasma density – such is the case when Lorentz trapping is the primary trapping mechanism. In addition to obtaining this improved condition for study of instabilities and the associated spreading, the very high energy injection method also introduces a velocity distribution for the trapped protons (due to selective trapping away from the symmetry orbit plus significant energy degradation), which may reduce the severity of instabilities for a given plasma density.

Acknowledgments

Acknowledgment is gratefully made to C. F. Barnett, J. L. Dunlap, T. K. Fowler, D. A. Griffin, and Herman Postma.

11. Design and Engineering: Notes

11.1 CORROSION-EROSION TESTS ON INTERNALLY COOLED COPPER CONDUCTORS

Joe Lewin

Some additional tests to determine corrosion-erosion rates in copper tubing were conducted. The experimental arrangement was similar to that reported earlier,[1] except that removable sections of tubing were in the coolant circuit downstream of the heated tubes. Thus, weight loss could be determined at various time intervals.

The weight-loss samples were $\frac{1}{8}$-in.-diam copper tubes with $\frac{1}{16}$-in.-diam internal passages. Other tubing of the same diameters was in the coolant circuit and was used to make photomicrographs of the inside surface of the coolant passages.

Initial results indicate a high initial rate of weight loss, corresponding to an early roughening of the inside surfaces, which remain unchanged thereafter. The rate of weight loss shows a gradual increase with both increasing flow velocity and increasing coolant temperature in the nonboiling range of temperatures.

[1] Joe Lewin, *Thermonuclear Div. Semiann. Progr. Rept. Apr. 30, 1962*, ORNL-3315, p 85.

12. Design and Engineering: Service Report

J. F. Potts, Jr.

The activities of the Engineering Services Group are generally reported incidentally with the research efforts of other groups of the Thermonuclear Division. The Group executes or coordinates engineering design, shop fabrication, building operations, and maintenance.

Design activities are summarized as follows:

Jobs on hand 11-1-62 on which work had not started	3
New jobs received	210
Total jobs	213
Jobs completed	186
Jobs in progress	13
Backlog of jobs, 4-30-63	14
Total drawings completed for period (does not include drawings for use in reports, slides, etc.)	392
Overtime (draftsmen, man-days)	0

New experimental systems on which design effort has been concentrated are the apparatus for cross-section measurements and the scale-up of microwave heating experiments. Notwithstanding this, the preponderance of design effort continued on modification or extension of existing facilities. Design activity did increase during this interval over the previous reporting interval.

Shop fabrication for the period is summarized as follows:

Jobs requiring 16 man-hours or less	222
Jobs requiring up to 1200 man-hours	378
Jobs requiring up to 2000 man-hours	1
Jobs of miscellaneous character in plating, carpenter, electrical, and millwright shops	105
Jobs by outside contractors	0
Average manpower (per week)	26.3

Publications, Papers, and Traveling Lecture Program

PUBLICATIONS

OPEN LITERATURE

Author(s)	Title of Article	Journal
Igor Alexeff, R. V. Neidigh, and E. D. Shipley	An Optimum Energy for Plasma Confinement	*Phys. Fluids* **6**, 450 (1963)
Igor Alexeff, R. V. Neidigh, W. F. Peed, and E. D. Shipley	Hot Electron Plasma by Beam-Plasma Interaction	*Phys. Rev. Letters* **10**, 273 (1963)
Igor Alexeff and R. V. Neidigh	Observations of Ionic Sound Waves in Plasmas: Their Properties and Applications	*Phys. Rev.* **129**, 516 (1963)
W. B. Ard, M. C. Becker, R. A. Dandl, H. O. Eason, A. C. England, and R. J. Kerr	Neutron Production from a Steady State Electron-Heated Deuterium Plasma	*Phys. Rev. Letters* **10**, 87 (1963)
R. J. Mackin, Jr., and P. R. Bell	High-Energy Injection: An Approach to Controlled Fusion	*Nucleonics* **20**, 58 (1962)
T. K. Fowler	On Integrating the Vlasov Equation	*J. Nucl. Energy: Pt C* **4**, 375 (1962)
T. K. Fowler and Mozelle Rankin	Plasma Potential and Energy Distributions in High-Energy Injection Machines	*J. Nucl. Energy: Pt C* **4**, 311 (1962)
J. R. McNally, Jr., J. E. Francis, Jr., M. R. Skidmore, P. M. Jenkins, and D. A. Griffin	Preliminary Spectroscopic Results on a Very Long, High-Current Magnetically Confined Vacuum Carbon Arc	*J. Opt. Soc. Am.* **53**, 495 (1963)
P. M. Griffin, J. R. McNally, Jr., and G. K. Werner	Ion Energy Evaluation from Spectrum Line Contours	*Temperature, Its Measurement and Control in Science and Industry* (ed. by F. G. Brickwedde), vol 3, Pt 1, p 651, Reinhold, New York, 1962
J. R. McNally, Jr.	Lorentz Theory of Zeeman Effect	*Encyclopaedic Dictionary of Physics* (ed. by J. Thewlis), p 860, Pergamon, London, 1962
E. R. Wells and Herman Postma	A Temperature Cycling Technique for Obtaining 10^{-9} torr in Large Vacuum Chambers	*Transactions National Vacuum Symposium, Oct.–Nov. 1962, Los Angeles* (ed. by G. H. Bancroft), p 266, MacMillan, New York, 1962

J. S. Luce	The DCX Program	*Progress in Nuclear Energy* (ed. by C. L. Longmire, J. L. Tuck, and W. B. Thompson), vol 2, p 120, MacMillan, New York, 1963

ORNL REPORTS

Author(s)	Title	Number	Date
Mozelle Rankin and T. K. Fowler[1]	DCX-2 Performance Curves	ORNL-3387	1-14-62
R. M. Warner and C. F. Barnett	Results of Performance Tests Conducted on the Consolidated Vacuum Corporation and the N.R.C. Corporation Ultra-High-Vacuum Oil Diffusion Pumping Assemblies	ORNL TM-567	4-5-63

PAPERS PRESENTED AT SCIENTIFIC AND TECHNICAL MEETINGS

American Physical Society, Atlantic City, N.J., Nov. 28–Dec. 1, 1962

W. B. Ard, M. C. Becker, R. A. Dandl, H. O. Eason, A. C. England, and R. J. Kerr, "Electric Dissociation of Deuterium in a Plasma Heated at the Electron-Cyclotron Frequency."

P. R. Bell, J. S. Culver, R. C. Davis, S. M. DeCamp, J. C. Ezell, R. A. Gibbons, G. G. Kelley, N. H. Lazar, R. J. Mackin, Jr., O. B. Morgan, R. F. Stratton, and A. J. Wyrick, "Initial Experiments with DCX-2."

R. A. Dandl, "Experiments on the Electron-Cyclotron-Heated Plasma in a Magnetic Mirror."

J. L. Dunlap, G. R. Haste, Herman Postma, and E. R. Wells, "RF-Correlated Phenomena in the DCX-1 Plasma."

T. K. Fowler,[1] "Plasma Stability and Lyapunov Functions."

R. A. Gibbons, "Analysis of the ORNL High-Density Arc."

C. E. Nielsen,[2] J. L. Dunlap, R. S. Edwards, and Herman Postma, "Recent Observations of High-Frequency Activity in DCX-1."

Herman Postma, G. R. Haste, J. L. Dunlap, and R. G. Reinhardt, "Energy Analysis of the Escaping Particles from the DCX-1 Plasma."

Y'akov Shima, "Stability of Inhomogeneous Collisionless Plasmas."

Symposium Clinical Radioisotope Scanning, Oak Ridge, Tenn., Oct. 22–26, 1962

C. C. Harris, P. R. Bell, J. E. Francis, Jr., M. M. Satterfield, J. C. Jordan, and J. P. Murray, Jr., "Collimators for Radioisotope Scanning."

C. C. Harris, M. M. Satterfield, P. R. Bell, J. C. Jordan, and J. E. Francis, Jr., "Data Recording for Radioisotope Scanning."

C. C. Harris, P. R. Bell, J. C. Jordan, J. E. Francis, Jr., and M. M. Satterfield, "An Automatic Electronic Method of Analyzing Radioisotope Scan Records – The Rescanner."

American Physical Society, New York, Jan. 23–26, 1963

W. F. Gauster, J. E. Simpkins, and P. A. Thompson, "Soft Superconductor Proximity Effects."

---

[1]Physics Division.

[2]Consultant, Ohio State University.

American Institute of Electrical and Electronics Engineers, Winter General Meeting, New York, Jan. 27–Feb. 1, 1963

A. H. Snell, "Controlled Fusion Today."

W. F. Gauster, "Development of Superconducting Magnets."

Society of Nuclear Medicine, SE-SW Meeting, New Orleans, Mar. 22–24, 1963

C. C. Harris, P. R. Bell, M. M. Satterfield, and J. C. Jordan, "Further Development in Data Extraction from Scan Records by the Recording Densitometer or 'Rescanner'."

C. C. Harris, P. R. Bell, M. M. Satterfield, and J. C. Jordan, "On the Relationship Between Collimators and Isoresponse Patterns in Air and in Water."

Society of French-Swiss Physicists, Lausanne, Switzerland, Mar. 22, 1963

W. F. Gauster, "Development of Superconducting Magnets."

American Physical Society, Southeastern Section, University of Tennessee, Knoxville, Apr. 4–6, 1963

A. H. Snell, "Controlled Fusion Today."

Deutsche Physikalische Gesellschaft, Bad Nauheim, Germany, Apr. 5, 1963

W. F. Gauster, "Magnetic Fields for Experimental Plasma Physics."

Institution of Electrical Engineers, London, England, Apr. 8, 1963

W. F. Gauster, "Application of Superconducting Materials."

Annual Sherwood Theoretical Meeting, University of California, E. O. Lawrence Radiation Laboratory, Berkeley, Calif., Apr. 8–9, 1963

T. K. Fowler,[1] "A Unified View of Streaming Instabilities."

American Physical Society, Division of Plasma Physics, Washington, D.C., Apr. 22–25, 1963

Igor Alexeff, "Direct Measurement of Ionic Sound-Wave Velocity."

T. K. Fowler,[1] "Bounds on Plasma Instability Growth Rates."

R. V. Neidigh, Igor Alexeff, W. F. Peed, and E. D. Shipley, "Hot Electron Plasma by Beam-Plasma Interaction."

C. E. Nielsen,[2] "Ion Clusters in Beams and Plasmas."

Herman Postma, "Experimental Properties of a 300-kev Plasma Stored in a Magnetic Mirror."

TRAVELING LECTURE PROGRAM

The Traveling Lecture Program is conducted in cooperation with the Oak Ridge Institute of Nuclear Studies as a part of the AEC's program of disseminating scientific and technical information to universities, particularly those in the South. Lectures delivered by ORNL personnel present unclassified information to university undergraduate and graduate students and members of the faculty. The lectures serve to stimulate interest in research in the university departments and also to assist the teaching staff

[1]Physics Division.

[2]Consultant, Ohio State University.

in expanding the scope of instruction offered under their regular curricula. Through such personal contacts, ORNL staff members are also able to observe departmental activities at the universities. Listed below are members of the Thermonuclear Division who participated in the Traveling Lecture Program during the academic year 1962–1963.

Igor Alexeff	University of Houston, Apr. 8, 1963 "Plasma as a Compressible Fluid."
N. H. Lazar	Virginia Polytechnic Institute, Jan. 15, 1963 "Progress Toward the Generation of a Thermonuclear Plasma by Injection and Trapping of High-Energy Particles."
P. M. Griffin	Baylor University, Apr. 29, 1963 "The Spectroscopy of High Temperature Plasmas."
	The University of Texas, Apr. 30, 1963 "The Spectroscopy of High Temperature Plasmas."

ORNL-3472
UC-20 – Controlled Thermonuclear Processes
TID-4500 (20th ed., Rev.)

INTERNAL DISTRIBUTION

1. I. Alexeff
2. R. G. Alsmiller
3. W. B. Ard
4. C. F. Barnett
5. C. O. Beasley
6. M. C. Becker
7–12. P. R. Bell
13. D. S. Billington
14. E. P. Blizard
15. C. W. Blue
16. G. E. Boyd
17. R. L. Brown
18. R. E. Clausing
19. D. L. Coffey
20. F. L. Culler
21. J. S. Culver
22. S. Cuperman
23. R. A. Dandl
24. R. C. Davis
25. S. M. DeCamp
26. J. L. Dunlap
27. H. O. Eason, Jr.
28. R. S. Edwards
29. A. C. England
30. J. C. Ezell
31. J. L. Fowler
32. T. K. Fowler
33. J. E. Francis, Jr.
34. J. H. Frye, Jr.
35. W. F. Gauster
36. R. A. Gibbons
37. H. W. Graben
38. P. M. Griffin
39. W. R. Grimes
40. E. Guth
41. C. C. Harris
42. G. R. Haste
43. R. E. Hill
44. A. S. Householder
45. H. C. Hoy
46. R. P. Jernigan, Jr.
47. W. D. Jones
48. G. G. Kelley
49. M. T. Kelley
50. R. L. Knight
51. J. A. Lane
52. C. E. Larson (K-25)
53. N. H. Lazar
54. G. F. Leichsenring
55. J. Lewin
56. R. S. Livingston
57. J. N. Luton, Jr.
58. J. R. McNally, Jr.
59. W. D. Manly
60. O. D. Matlock
61. K. Z. Morgan
62. O. B. Morgan
63. R. V. Neidigh
64. M. L. Nelson
65. J. Neufeld
66. C. E. Parker
67. W. F. Peed
68. H. Postma
69. J. F. Potts
70. M. Rankin
71. J. D. Rather
72. J. A. Ray
73. R. G. Reinhardt
74. D. M. Richardson
75. P. W. Rueff
76. W. K. Russell
77. H. E. Seagren
78. Y. Shima
79. E. D. Shipley
80. M. R. Skidmore
81. M. J. Skinner
82–91. A. H. Snell
92. W. L. Stirling
93. R. F. Stratton, Jr.
94. R. A. Strehlow
95. J. A. Swartout
96. E. H. Taylor
97. P. A. Thompson
98. R. M. Warner
99. H. L. Watts
100. A. M. Weinberg
101. E. R. Wells
102. T. A. Welton
103. G. K. Werner
104. W. L. Wright

105. A. J. Wyrick
106. O. C. Yonts
107. Gale Young
108. W. P. Allis (consultant)
109. W. H. Bostick (consultant)
110. F. E. Dunnam (consultant)
111. J. W. Flowers (consultant)
112. M. W. Garrett (consultant)
113. E. G. Harris (consultant)
114. D. E. Harrison (consultant)
115. W. Heckrotte (consultant)
116. R. Hefferlin (consultant)
117. G. W. Hoffman (consultant)
118. V. W. Hughes (consultant)
119. R. K. Jaggi (consultant)
120. D. W. Kerst (consultant)
121. E. W. McDaniel (consultant)
122. M. R. C. McDowell (consultant)
123. D. R. Montgomery (consultant)
124. C. E. Nielsen (consultant)
125. W. B. Pardo (consultant)
126. J. M. Reynolds (consultant)
127. F. F. Rieke (consultant)
128. H. S. Robertson (consultant)
129. D. J. Rose (consultant)
130. L. P. Smith (consultant)
131. P. M. Stier (consultant)
132. C. H. Weaver (consultant)
133. J. D. Tillman (consultant)
134–163. Thermonuclear Division Library
164. Reactor Division Library
165. Biology Library
166–167. Central Research Library
168. Laboratory Shift Supervisor
169–193. Laboratory Records Department
194. Laboratory Records, ORNL RC
195–196. ORNL – Y-12 Technical Library Document Reference Section

EXTERNAL DISTRIBUTION

197. S. C. Brown, Massachusetts Institute of Technology
198. M. B. Gottlieb, Princeton University
199. H. Grad, New York University
200. J. M. B. Kellogg, Los Alamos Scientific Laboratory
201. A. C. Kolb, Naval Research Laboratory
202. J. A. Phillips, Los Alamos Scientific Laboratory
203. R. F. Post, University of California, Lawrence Radiation Laboratory
204. A. Simon, General Atomic, San Diego, California
205. L. Spitzer, Princeton University
206. E. Teller, University of California, Lawrence Radiation Laboratory
207. C. M. Van Atta, University of California, Lawrence Radiation Laboratory
208. R. W. McNamee, Union Carbide Corporation
209–210. Research and Development Division, AEC, ORO (1 copy each to H. M. Roth and R. B. Martin)
211–212. Controlled Thermonuclear Branch, AEC, Washington (A. E. Ruark)
213. L. D. Smullin, Massachusetts Institute of Technology
214–816. Given distribution as shown in TID-4500 (20th ed., Rev.) under Controlled Thermonuclear Processes category (75 copies – OTS)